# INTEGRATION OF INDIUM GALLIUM NITRIDE WITH NANOSTRUCTURES ON SILICON SUBSTRATES FOR POTENTIAL PHOTOVOLTAIC APPLICATIONS

HO JIAN WEI

NATIONAL UNIVERSITY OF SINGAPORE
2014

# INTEGRATION OF INDIUM GALLIUM NITRIDE WITH NANOSTRUCTURES ON SILICON SUBSTRATES FOR POTENTIAL PHOTOVOLTAIC APPLICATIONS

HO JIAN WEI
*(B.Eng.(1st Hons), NUS)*

A THESIS SUBMITTED

FOR THE DEGREE OF DOCTOR OF PHILOSOPHY
NUS GRADUATE SCHOOL FOR INTEGRATIVE SCIENCES AND ENGINEERING

NATIONAL UNIVERSITY OF SINGAPORE
2014

# DECLARATION

I hereby declare that the thesis is my original work and it has been written by me in its entirety. I have duly acknowledged all the sources of information which have been used in the thesis.

This thesis has also not been submitted for any degree in any university previously.

Ho Jian Wei

29 September 2014

# ACKNOWLEDGEMENTS

There are many people who have given me invaluable aid in the course of my Ph.D. journey and made this much more palatable. I would like to take this opportunity to express my sincerest gratitude to them. First, I would like to thank my supervisors, Professor Chua Soo-Jin and Professor Andrew Tay, for their guidance, encouragement and support which were instrumental in making this work possible. I have gained much from the fruitful discussions I had with them, not only within the realms of my research work, but also in terms of personal development. They have provided many opportunities in enhancing both the depth and breadth of my research.

I also greatly appreciate the help from the other members of my Thesis Advisory Committee (TAC). Professor Choi Wee Kiong, who is the TAC Chairman, has provided a much needed perspective and played a significant role in steering my research direction. I am truly humbled by his attitude towards life. Dr Zang Keyan has imparted valuable knowledge on MOCVD to me, supported my research and shared her experience in navigating research life. Dr Liu Hong Fei has inspired me greatly in my work. His dedication to research and academic finesse is admirable. I benefitted greatly from the many technical discussions I had with him.

Next, I would like to thank the staff at the Center of Optoelectronics (COE) in NUS, namely, Ms Musni Bte Hussain and Mr Tan Beng Hwee, for their help in administrative matters. I also greatly appreciate the friendship and support of my fellow students in COE. Special mention goes to Dr Wee Qixun who has mentored me and taught me much about the growth and characterization of III-nitrides.

I am grateful for the opportunity to perform part of my research work at the Institute of Materials Research and Engineering (IMRE), A*STAR and would like to thank many of the IMRE staff who have helped me in the training and operation of equipment there. This includes Mr Jarrett Dumond, Dr Tanu Suryadi Kustandi, Dr Liu Hong, Ms Tan Hui Ru, Ms Teo Siew Lang, Ms Doreen Lai, Mr Lim Poh Chong and Mr Eric Tang. I am also indebted to my ex-colleagues and ex-laboratory mates at Lab 10 who have provided much needed support in the course of my work.

In addition, I would also like to acknowledge the help from the Singapore-MIT Alliance of Research and Technology (SMART) for providing me temporary access to its high-resolution X-ray diffraction (HR-XRD) equipment. I would like to thank Dr Abdul Kadir and Dr Kohen David Alexandre for operation and meaningful discussions of the machine. Next, I would like to thank Dr Michael Heuken from AIXTRON SE for providing me substrates for MOCVD growth.

I am immensely grateful to the NUS Graduate School for Integrative Sciences and Engineering (NGS) for providing me with a Scholarship and support for this Ph.D. work. NGS and her staff have been extremely helpful in ensuring the well-being of students. I truly appreciate their support.

Last but not least, I would like to thank my family, fiancée and friends for their love, unwavering support and understanding while I was both physically and/or mentally absent during my Ph.D. journey.

# TABLE OF CONTENTS

# SUMMARY

Nanostructured growth of InGaN on Si substrates targeting photovoltaic applications was performed in this work. The technique mitigates the challenges plaguing InGaN heteroepitaxy on Si which result in inadequate quality high In content InGaN. The integration of InGaN with nanostructures on Si will facilitate development of monolithic InGaN/Si tandem solar cells which combine the bandgap tunability of InGaN and low-cost, wide availability of Si. Two growth approaches are proposed, namely, (A) nano selective area growth (nano-SAG) of InGaN through a nanoporous mask fabricated on Si substrate, or Scheme A, and (B) nanoheteroepitaxy of InGaN on Si nanopillars, or Scheme B.

Nanopatterning techniques based on Step and Flash™ Imprint Lithography (S-FIL™), a form of wafer-scale nanoimprint lithography, were first developed. These are classified according to the two Schemes: (A) Fabrication of uniform, tunable aspect ratio nanoporous $SiN_y$ masks on AlN/Si(111) substrates by combining S-FIL™ with angled metal deposition, and (B) Fabrication of Si nanopillar arrays of variable patterns and adjustable aspect ratio by combining S-FIL™ with metal-catalyzed electroless etching (MCEE). To ensure a manageable scope, only Type A templates were selected for subsequent growth.

A metalorganic chemical vapour deposition (MOCVD) study of InGaN films on bare AlN/Si(111) substrates was then performed to examine preliminary growth conditions. Substrate pre-annealing in $H_2$ at 1000°C was critical for epitaxy. Further, phase separation and In droplet formation at low growth temperature *T* (655°C) may be suppressed by elevated reactor pressure *P* (300 Torr). However, while low *T* favors

higher In content *x*, crystal quality suffers. For $x > 0.2$, photoluminescence (PL) was absent. Nano-SAG at 780°C and 300 Torr was then performed on Type A templates to achieve InGaN nanopyramid array. Compared to the control film, the crystalline quality of nanopyramids is notably increased through dislocation confinement, bending, and filtering. Morever, higher *x* by an absolute 4.5% due to strain relaxation, and a four-fold increase in internal quantum efficiency to 17.5% are achieved. Average reflectance is also reduced from 23.6 % to 8.3% due to light trapping.

The impact of *T*, *P*, growth duration and V/III ratio on *x*, morphological, structural and PL qualities of the InGaN nanopyamids was subsequently studied. Lower *T* permits higher *x*, but $T < 750$°C are correlated with polycrystalline deposits, In droplet formation and structural degradation. Alternatively, lowering *P* at a moderately high *T* (~ 775°C), increases *x* due to enhanced mass transport, without as significant degradation. This also enhances growth rate and improves size uniformity. The nanopyramids generally exhibit greater lattice tilt than the controls due to dislocation bending. Tilt increases with reduced *P* (increased *x*) but is slight. While lattice twist increases with *x*, it is offset by epitaxial lateral overgrowth. Compared to the controls, the nanopyramids consistently yielded higher *x*, lower average reflectance (< 9%) and a multi-fold increase in PL intensity with tunable emission from 3.05 eV to 1.93 eV. Larger nanopyramids and high V/III ratios in $N_2$ growth ambient are also advocated for improved morphological and structural properties. Lastly, functional InGaN/GaN MQW core-shell structures were successfully grown crack-free on InGaN nanopyramid array in contrast to the cracked control.

# LIST OF TABLES

# LIST OF FIGURES

# LIST OF SYMBOLS

| | |
|---|---|
| $F_{TD}$: | fraction of threading dislocations blocked by a mask template during selective area growth |
| $d$: | diameter of a pore in a nanoporous mask template |
| $p$: | periodicity of pores within a nanoporous mask template |
| $r$: | radius of a pore or cylinder |
| $\delta$: | radial distance away from the axis of a cylinder |
| $c$: | axial lattice parameter |
| $a$: | basal lattice parameter |
| $E_g$: | bandgap |
| $x$: | In composition in $In_xGa_{1-x}N$ |
| $b$: | bowing parameter |
| $T$: | temperature |
| $P$: | pressure |
| $\alpha$ and $\beta$: | Varshni parameters |
| $\nu$: | Poisson's ratio |
| $E$: | Young's modulus |
| $f$: | lattice mismatch |
| $a_s$: | unconstrained in-plane lattice constant of substrate |
| $a_f$: | unconstrained in-plane lattice constant of epilayer |
| $h_c$: | critical layer thickness |
| **b**: | Burgers vector |
| **u**: | dislocation line vector |

| | |
|---|---|
| $F_{in}$: | incident flux of In onto growth surface |
| $F_s$: | flux of In incorporated into InGaN |
| $F_m$: | flux of In incorporated into In metal droplets |
| $F_d$: | flux of In desorbed from growth surface |
| $\tau$: | residence lifetime of In on growth surface |
| $\tau_0$: | resident lifetime constant |
| $E_d$: | activation energy for In desorption |
| $k_B$: | Boltzmann constant |
| $P_b$: | bubbler pressure |
| $T_b$: | bubbler temperature |
| $P_{MO}$: | equilibrium vapour pressure of precursor in bubbler |
| *A and B*: | constants for calculation of $P_{MO}$ |
| $F_{MO}$: | molar flow rate of precursor |
| $Q_b$: | volume flow rate of carrier gas into bubbler |
| $R$: | molar gas constant |
| $P_{std}$: | pressure at standard conditions |
| $T_{std}$: | temperature at standard conditions |
| $R_g$: | growth rate |
| $k$: | rate constant |
| $\Delta G^*$: | activation free energy |
| $\boldsymbol{g}$: | vector in two-beam condition for TEM diffraction contrast imaging |
| $\lambda$: | wavelength |
| $d$: | inter-planar spacing |
| $\theta$: | angle between incident X-ray beam and atomic planes in XRD |

| | |
|---|---|
| $\omega$: | angle between incident X-ray beam and sample surface in XRD |
| $\chi$: | inclination/skew angle in a four-circle XRD diffractometer |
| $\phi$: | azimuthal angle in a four-circle XRD diffractometer |
| $\boldsymbol{k_i}$: | incident beam vector |
| $\boldsymbol{k_d}$: | diffracted beam vector |
| $\boldsymbol{S}$: | scattering vector |
| $c_0$: | relaxed axial lattice parameter |
| $a_0$: | relaxed basal lattice parameter |
| $I$: | photoluminescence intensity |
| $I_0$: | photoluminescence intensity at low temperature |
| $C_i$: | strength of $i^{th}$ non-radiative recombination channel |
| $E_{Ai}$: | activation energy of $i^{th}$ non-radiative recombination channel |
| $r_m$: | ratio of molar flow rate of TMIn to that of TMIn and TMGa |

# Chapter 1 Introduction

## 1.1. Current Status of Photovoltaics (PV) for Solar Energy Harvesting

Among all photovoltaic (PV) technologies, Si wafer based PV technology dominates the global market accounting for ~ 86% of total shipments [1] due to material abundance and mature processing technologies adapted from the microelectronics industry [2]. Out of this, monocrystalline Si (c-Si) technology account for ~ 40%. This typically employs single cell architectures with commercially available c- Si wafer based cell efficiencies approaching > 19%.

World record PV conversion efficiencies, on the other hand, are currently held by concentrating multi-junction (MJ) PV technologies based on direct bandgap III-V ternary or quaternary compound semiconductors comprising aluminium, gallium, indium, arsenic, and phosphorus, epitaxially grown by metalorganic chemical vapour deposition (MOCVD) or molecular beam epitaxy (MBE) on germanium or gallium arsenide substrates [3]. The present world record of 44.4% is achieved in an InGaP/GaAs/InGaAs triple-junction solar cell (surface area ~ 0.165 $cm^2$) under optical concentration (302×) [4, 5]. See Figure 1.1. Optical concentration onto minute cell areas is critical to improve the viability of III-V MJ PV technology due to the expensive and relatively low throughput nature of the growth process even with industrial MOCVD systems used in the light emitting diode (LED) industry [3]. From a materials viewpoint, however, large-scale terawatt deployment of this high efficiency PV technology is predicted to be restricted by the cost and availability of Ge or GaAs substrates [6]. The efficient use, recycling of these substrates, and/or the migration to less expensive, more abundant substrates may aid in the large-scale deployment of this technology.

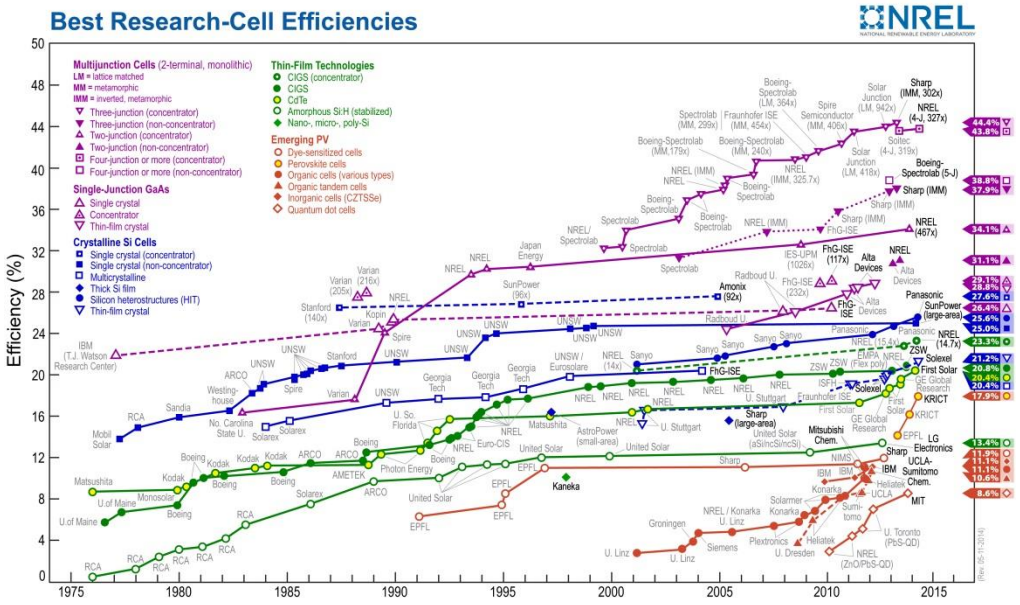


**Figure 1.1** Chart showing the best solar cell efficiencies. The current record efficiency of 44.4% is held by Sharp in a triple-junction concentrator solar cell. (Reprinted from ref. [4])

Multijunction or tandem solar cells are highly efficient because they are designed to judiciously divide the incident solar spectrum between each subcell for harvesting. This reduces the fundamental losses of transmission and thermalization associated with single energy gap solar cells [3]. As mentioned before, record efficiencies in excess of 40% (under optical concentration), almost double that of commercial high efficiency Si cells, have already been achieved and are still on the rise [4]. In fact, higher efficiency can theoretically be achieved by more optimal bandgap combinations and greater number of subcells within the tandem stack. Unfortunately, this is difficult to achieve in practice due to a lack of materials with suitable bandgaps and the same lattice constants. Careful management of the lattice mismatch is essential to avoid the generation of crystal lattice defects and dislocations which act as undesirable recombination centres, and adversely impact PV performance.

## 1.2. Motivation for Integration of InGaN with Nanostructures on Si in PV

The most common MJ III-V solar cells use the completely lattice-matched $Ga_{0.5}In_{0.5}P/Ga_{0.99}In_{0.01}As$/Ge triple junction structure [3]. However, the successful growth/integration of lattice-mismatched materials with more optimal bandgaps will further increase the efficiency of multijunction photovoltaics [7]. The InGaN/Si material system is highly promising as it combines the wide bandgap tunability of InGaN, and low-cost, wide availability of Si. However, lattice mismatch growth leads to the generation of structural defects that degrade device efficiency. Other challenges also exist in InGaN heteroepitaxy on Si, namely, large mismatch in thermal expansion, growth process limitations, and phase separation. Nanostructuring has been postulated to mitigate these issues. Hence, nanostructured growth of InGaN on Si substrate is pursued in this work. The integration of InGaN with nanostructures on the Si platform will facilitate the development of monolithic vertically integrated InGaN/Si tandem solar cells which are cost-effective, and possess broad solar absorption and high efficiency. In the following sections, the advantages of InGaN, Si as a substrate, potential of InGaN solar cells, and application of nanostructuring schemes are examined in greater detail.

### 1.2.1. Advantages of InGaN for PV Applications

The Group III phosphides and the Group III arsenide have conventionally been used in III-V MJ photovoltaics. Recently, the Group III nitrides have emerged as a very promising class of III-V compound semiconductors. These have led to significant progress in the semiconductor industry, such as in the industrial realization of InGaN/GaN-based violet, blue and green light emitting diodes (LEDs) and laser diodes [8, 9], as well as, in high efficiency and high voltage high electron mobility transistors (HEMTs), and high power electronics such as metal-oxide-semiconductor

field-effect transistors (MOSFETs) and metal-semiconductor field effect transistors (MESFETs). $In_xGa_{1-x}N$ is a ternary alloy belonging to the III-nitrides with a direct bandgap $E_g$ that can be tuned from 0.7 eV (in InN) to 3.4 eV (in GaN) by varying the indium composition $x$ from 1 to 0. The broad $E_g$ range covers nearly the entire solar spectrum as shown in Figure 1.2, favouring its application in full-spectrum photovoltaics [10, 11]. Materials with direct $E_g$ greater than 2.0 eV are attractive because more than half of the solar spectrum energy occurs above 2.0 eV. While the III-phosphides and III-arsenides can be combined to form semiconductors alloys with a wider range of bandgaps $E_g$ (up to ~2.5 eV in AlP), part of the $E_g$ range, including that of AlP, is indirect in nature. A consequence of indirect bandgaps is the lower optical absorption coefficients. The broad range of direct $E_g$ in $In_xGa_{1-x}N$ enables the incorporation of more subcells with more optimal $E_g$ combinations in tandem solar cells to reduce the fundamental losses of transmission and thermalization [12].

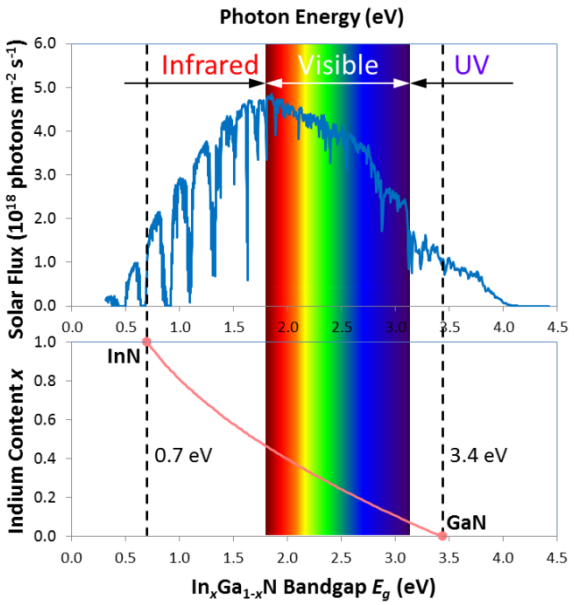


**Figure 1.2** Graphs showing the ASTM G173-03 reference solar spectrum (top) and the continuously tunable bandgap energies $E_g$ of $In_xGa_{1-x}N$ (bottom). The latter spans the UV, visible and infrared regions and covers majority of the solar spectrum.

Due to its direct $E_g$, $In_xGa_{1-x}N$ possesses a very high optical absorption coefficient of ~ $10^5$ $cm^{-1}$ at just 0.1 eV above the $E_g$. This is nearly an order of magnitude higher than that of GaAs [13] and offers the potential of very thin solar cell absorber layers which reduces the material and time required for growth. $In_xGa_{1-x}N$ is also characterized by low effective carrier masses and high carrier mobilities [10, 11, 14-16]. Further, the semiconductor alloy exhibits excellent radiation resistance [11] and strong phonon bottleneck effects that slow down hot carrier cooling [17]. Moreover, compared to conventional III-V multi-junction solar cells which typically combine III-phosphides and III-arsenides to access a broader range of $E_g$ combinations, the III-nitrides may be grown as a solitary alloy system due to its broadly tunable $E_g$. This simplifies and streamlines the growth process. The collective possession of the above traits makes $In_xGa_{1-x}N$ a very attractive material for full-spectrum photovoltaics.

### 1.2.2. Merits of Si as a Growth Substrate for InGaN PV Applications

Native GaN bulk substrates, typically grown by hydride vapour phase epitaxy or ammonothermal methods, are prohibitively expensive [18, 19]. Due to the high-cost, low-availability of these substrate, the III-nitrides are traditionally grown lattice-mismatched on sapphire or silicon carbide substrates. In recent years, however, there has been an interest to grow the material on Si substrates. Although growth remains lattice-mismatched, the cost benefits are substantial. While a 2” GaN wafer substrate costs at least US$2000, and a 2” sapphire substrate US$10, a 6” Si wafer with 9 times the area costs only US$12 [18]. Due to the abundance of Si and mature Si wafer production techniques fuelled by the established Si microelectronics industry, Si wafers of high crystalline quality and various specifications, e.g. in terms of doping type and concentration, lattice orientation, surface roughness and other electronic and mechanical properties, are widely available. Moreover, they may be realized in large sizes up to 12” in diameters. Such large sizes are suitable for large-scale batch

processing and growth, thus contributing to higher throughputs and lower effective costs per run. The wide availability and significant cost reduction potential are key benefits of adopting Si as a growth substrate for III-nitrides.

In the growth of InGaN on Si substrates for photovoltaic applications, we propose that the latter may conveniently serve as the bottom cell in InGaN/Si hybrid tandem solar cell architectures to harvest low energy photons (E < 1.12 eV). See Figure 1.3(a). The concept of high-efficiency monolithic InGaN/Si hybrid tandem solar cells has been mooted theoretically. Using realistic material parameters, it has been shown that double junction InGaN/Si tandem solar cells may achieve efficiencies of ~ 27% to 29% [20-22] even without optical concentration. In fact, for triple junction InGaN/InGaN/Si configurations with appropriate bandgap combinations, efficiencies in excess of 35% are possible [22]. See Figure 1.3(b). Efforts to realize such architectures have recently been reported [23-26]. However, progress is limited and further research and development, which is the subject of this work, is warranted.

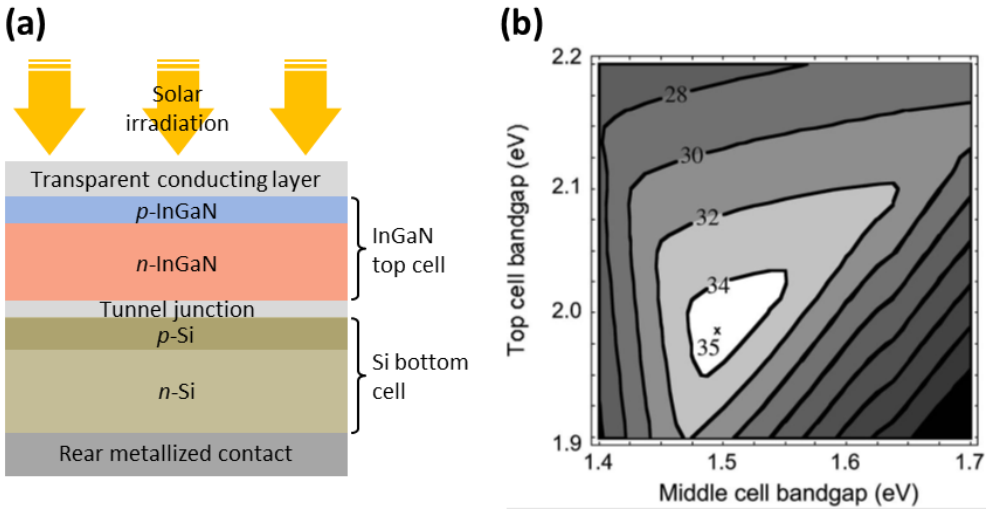


**Figure 1.3** (a) Schematic of a double junction InGaN/Si tandem solar cell consisting of a InGaN top cell and a Si bottom cell. (b) Isoefficiency plot of a triple junction InGaN/InGaN/Si solar cell as a function of the bandgaps of the two InGaN subcells. (Reprinted from ref. [22])

In addition, the establishment of the Si microelectronics industry has led to the development of mature processing techniques for integrated circuit (IC) fabrication. These include the major methods for doping, dielectric deposition, photolithography, wet and dry etching, and metallization, etc. The techniques have been adopted by the Si PV industry for fabrication of industry c-Si wafer solar cells which are known for their reliability and relatively high efficiencies. The realization of the Si bottom cell in the proposed InGaN/Si tandem solar cell may be expedited by drawing upon the knowledge in Si processing from the Si microelectronics and PV industries.

InGaN/Si tandem solar cells also possess one additional benefit over those based on traditional III-V materials. A low resistance ohmic junction is naturally formed at a *n*-$In_{0.46}Ga_{0.54}N$/*p*-Si interface [22]. Tandem cells can be designed to incorporate such an interface to avoid heavy doping or formation of a tunnel junction at the InGaN/Si interface. This characteristic arises because at $x \sim 0.46$, the conduction band of InGaN has the same energy relative to the vacuum level as the valence band of Si [24]. See Figure 1.4. In fact, the ohmic behaviour has been experimentally observed for *n*-InGaN/*p*-Si junctions [24, 27]. For other *x*, a tunnel junction may be necessary.

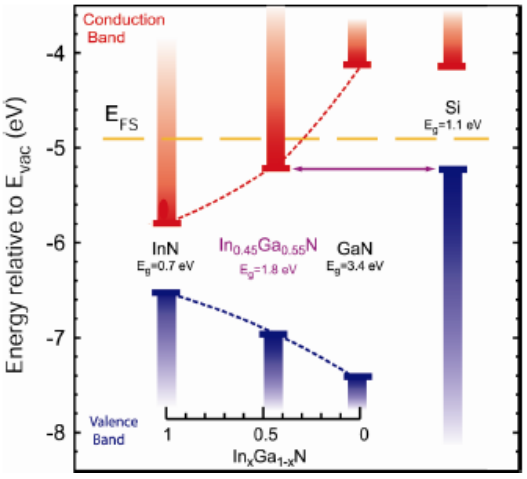


**Figure 1.4** Energy diagram showing the conduction and valence bands of InGaN as a function of In composition *x*. Those of Si are also shown for comparison. (Reprinted from ref. [24])

Si also bears other qualities that make it an excellent substrate. These include its mechanical stability which see it often used as a handle substrate for III-V MJ solar cells, and good thermal conductivity which allows it to dissipate heat efficiently. The latter is important as the rise in temperature under solar irradiation can impair photovoltaic performance. By combining the aforementioned merits of Si as a substrate and full-spectrum PV potential of InGaN, high efficiency tandem solar cells can be achieved at a lower cost for realistic large scale deployment.

### 1.2.3. Potential and Technical Barriers of InGaN Solar Cells

In the typical lattice-matched $In_{0.5}Ga_{0.5}P/In_{0.01}Ga_{0.99}As/Ge$ triple junction solar cell, conversion efficiencies of ~ 32% and ~ 40.1% under 1-sun and 135-suns, respectively, have been achieved [28]. However, current-matching which is required to maximize the efficiency of tandem cells is not realized due to restriction of materials selection to lattice matched materials. Further, future terrestrial multijunction solar cells will likely feature four to six junctions to increase the performance potential of multijunction technology (reduce thermalization and transmission losses) [7]. Work on 4-junction solar cells is already under way [29] and practical cell efficiencies up to ~ 47% under 500-suns AM1.5D illumination with a $E_g$ combination of ~ 1.9/1.4/1.0/0.7 eV have been projected [7].

To achieve the required $E_g$ combinations in multijunction photovoltaics, the conventional III-V approach draws upon the III-phosphides, III-arsenides, and possibly the dilute nitrides, as well as their alloys. Ultimately, the use of lattice mismatched materials is inevitable, and fabrication likely involves (1) metamorphic growth and/or (2) wafer-bonded, layer-transferred epitaxial technologies [7]. The use of multiple material systems and complex fabrication methods complicate this approach. Further, the largest direct $E_g$ available in the AlGaInAsP alloy system is

only ~ 2.2 eV which occurs in InGaP [30-32]. Larger $E_g$ (> 2.24 eV) are required for multijunction solar cells with six or more junctions [33]. This is overcome in the InGaN material system where the $E_g$ is direct and can be conveniently tuned from 0.7 eV to 3.4 eV by adjusting the In content without addition of other materials.

Simulation of 4-junction InGaN-based solar cells shows a power conversion efficiency of ~ 46.45% [34] which is close to that mentioned above (~ 47%). InGaN/Si tandem solar cells are promising because they also combine the cost-effectiveness of Si substrates. As discussed in Section 1.2.2, efficiencies of ~ 29% [20, 21] can be achieved for double junction structures even without optical concentration, while efficiencies in excess of 35% are possible for triple junction InGaN/InGaN/Si configurations with appropriate bandgap combinations [22].

InGaN solar cells possessing various device architectures such as *p*-GaN/*i*-InGaN/*n*-GaN heterojunction [35-38], *p*-*i*-*n* InGaN homojunction [39, 40], *p*-*n* InGaN homojunction [41], and InGaN/GaN multiple quantum wells [42-44], have been reported and show good photovoltaic effects. However, due to non-optimal bandgaps of low In content InGaN (high In content is correlated with poor structural quality), high densities of threading dislocations, stacking faults, phase separation, and other structural defects, power conversion efficiencies of these solar cells are relatively low [45]. The highest value, ~ 3.4% with 200 suns concentration [42], is achieved by MQW structures ($x$ ~ 0.17) where $In_xGa_{1-x}N$ wells are kept within the critical thickness thus minimizing dislocation generation, and phase separation is suppressed by elastic strain. Good quality high In content InGaN quantum wells remain difficult to achieve due to the large lattice mismatch involved, and the relatively low temperature required to preserve In content. These InGaN growth challenges are elaborated in Section 2.3. It is important to point out that due to the small well

thickness in MQW device structures, several tens of wells are required for sufficient light absorption. Maintaining good crystal quality over such a great number of wells may be difficult [46]. Further, piezoelectric polarization effects can also reduce the efficiencies of InGaN/GaN solar cells as the polarization-induced electric fields oppose carrier collection [47, 48].

In summary, the technical barriers associated with InGaN solar cells are related to both growth issues which affect structural quality, and polarization effects. These have inhibited the realization of high performance InGaN single and multijunction solar cells. However, the challenges can be mitigated by the nanostructuring approaches advocated in this work. This is discussed as follows in Section 1.2.4.

### 1.2.4. Relevance of Nanostructuring and its Benefits

Heteroepitaxy of high quality InGaN films with diverse In content and adequate thickness for PV applications is challenging because of thermal and lattice mismatch, compositional non-uniformity and phase separation, and temperature tradeoff between structural quality and In content. These challenges are compounded by Ga-meltback etching of Si and unintentional nitridation of Si during growth. InGaN growth issues are discussed in detail in Section 2.3. Nanostructuring in material growth offers two key benefits, namely, strain relaxation and dislocation reduction. By incorporating appropriate device architecture designs with suitable nanostructuring schemes, the challenges can be overcome. In this section, we discuss nanostructuring with respect to two Schemes, A and B, and how they can overcome the growth challenges. Other benefits are also outlined. Both Schemes employ nanopatterned substrates. However, while material growth is initiated from nano-scale *recessed* regions (nanopores) in Scheme A, Scheme B involves material growth

from *elevated* nano-scale areas (nanopillars). In both cases, nanostructures or coalesced epilayers can be attained.

#### 1.2.4.1. Nano Selective Area Growth (Nano-SAG or Scheme A)

Scheme A involves the selective area growth (SAG) of material into nanostructures by employing a nanoporous mask fabricated over the substrate. An illustration of the concept is depicted in Figure 1.5. Due to the use of pores with nano-scale dimensions (~ 10 nm to ~ 250 nm), Scheme A is termed nano selective area growth. This distinguishes it from traditional SAG using micron-sized features. The deposition of a buffer layer may be required prior to mask fabrication to prevent unwanted chemical reaction between the material to be grown and the substrate, or to improve the growth quality. The mask material is chosen to ensure good growth selectivity within the pores relative to the mask, and growth conditions are tuned to ensure growth is initiated from the nano-scale *recessed* regions and proceeds out to form nanostructures. Figure 1.5(a) shows nanostructures with emerged nanopyramidal tops. However, prismatic structures, e.g. nanorods, are possible depending on growth conditions [49]. If epitaxial lateral overgrowth (ELO) is enforced, a coalesced epilayer may be achieved as illustrated in Figure 1.5(b).

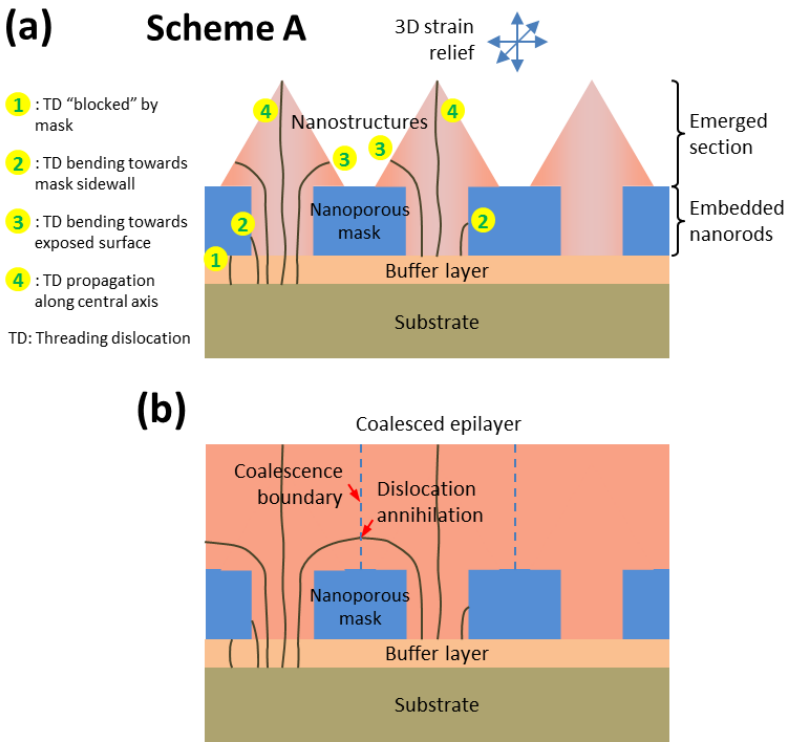


**Figure 1.5** (a) Schematic showing nano selective area growth (nano-SAG) of nanostructures through a nanoporous mask fabricated on the substrate. (Scheme A) The nanostructured morphology provides three-dimensional strain relief. Threading dislocation (TD) behaviour induced in nano-SAG acts to increase the volume of dislocation-free regions. (b) Schematic showing the coalesced epilayer arising from nano-epitaxial lateral overgrowth (nano-ELO). Dislocation bending and annihilation serve to reduce the TD density in the overgrown region.

### 1.2.4.2. Nanoheteroepitaxy on Nanopillar Substrates (Scheme B)

Like Scheme A, Scheme B involves the heteroepitaxy of nanostructures. However, no SAG mask is deposited prior to growth. Instead, the substrate is directly patterned to form an array of nanopillars or nano-scale *elevated* regions (mesas) where material growth is targeted. A conformal layer of buffer material may be deposited after patterning to prevent unwanted chemical reaction between the nanostructure material and the substrate during growth. See Figure 1.6(a). The aspect ratio, density, size and arrangement of the nanopillars may be designed to favor growth on their top surface. However, some depositions on the sides and recessed regions may be unavoidable. Figure 1.6(a) shows truncated nanopyramids being grown on the nanopillars [50]. However, prismatic nanostructures may also be possible [51]. In fact, high aspect ratio towers have been obtained in patterned substrate growth [52]. Further, in

principle, growth conditions may also be tuned to facilitate epitaxial lateral growth to obtain a coalesced epilayer. See Figure 1.6(b).

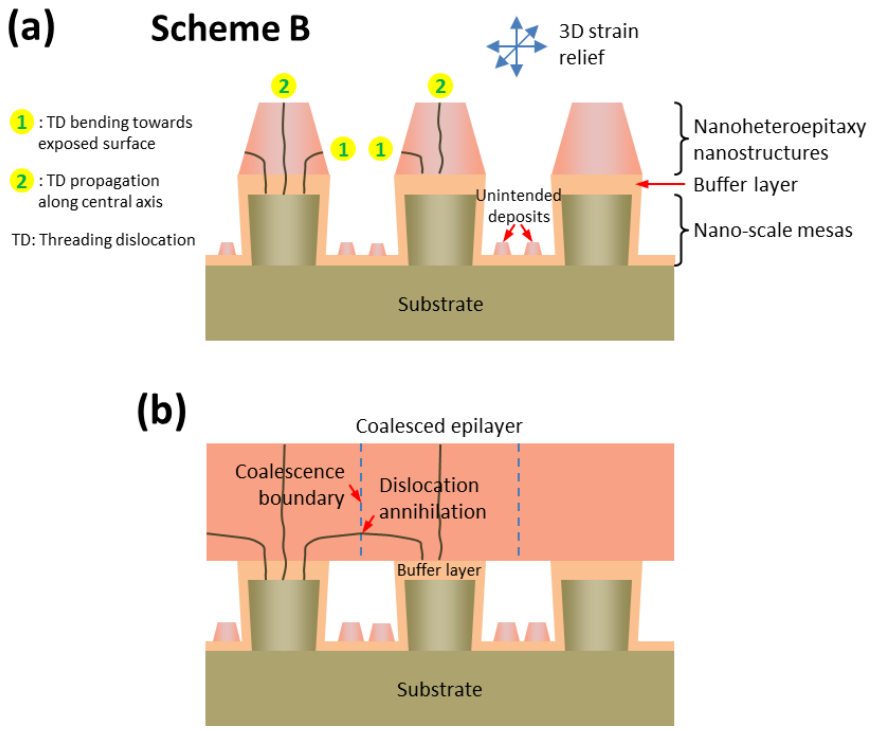


**Figure 1.6** (a) Schematic diagram showing nanoheteroepitaxy of nanostructures on nano-scale mesas or nanopillars patterned directly from the substrate. (Scheme B) Some unintentional growth may be present at the recesses of the pattern due to a lack of growth selectivity. The nanostructured morphology provides three-dimensional strain relief. Threading dislocation (TD) behaviour in a nanostructure acts to increase the volume of dislocation-free regions. (b) Schematic showing the coalesced epilayer arising from epitaxial lateral growth. Dislocation bending and annihilation serve to reduce the TD density in the overgrown region.

### 1.2.4.3. Benefits of Nanostructures

Dislocations are detrimental to PV device performance. Threading dislocations (TDs) may be generated at a lattice mismatched interface under energetically favorable conditions for relaxation of strain. High TD densities are common in III-nitride heteroepitaxy due to the extreme difference in lattice constants between the III-nitrides and the substrate, and within the III-nitrides. See Section 2.3.2. In Figure 1.5(a) and Figure 1.6(a), TDs are shown to occur at both the substrate/buffer and buffer/nanostructure interfaces with the TDs threading into the nanostructures.

However, for sufficiently small nanostructures with diameters in the 10 – 100 nm range or less, a reduction in interfacial mismatch dislocations is possible [53]. The size range depends strongly on the lattice mismatch and mechanical properties of the materials, and may extend to larger sizes for smaller lattice mismatches and more compliant nanostructure materials, and vice versa [54]. This is because the small size of the nanostructure allows it to deform in three dimensions. The stress and strain associated with the lattice mismatch at the heterojunction decays exponentially from the heterointerface. If the strain energy is less than the energy required for a defect to form, the nanostructure remains defect free [53-57]. See right nanostructure in Figure 1.5(a) and Figure 1.6(a). In the same vein, epilayer cracking (arising from a mismatch in coefficient of thermal expansion (CTE) between the material to be grown and the substrate) may be avoided with a nanostructure approach since this lowers the total strain energy. If the total strain energy of the nanostructure array is lower than the energy for formation of cracks, cracking is avoided.

Even if dislocations are introduced into a nanostructure, e.g. due to an exceedingly large mismatch, defective buffer, or poor starting growth interface, selective area growth can still serve to reduce them [58] as explained by the dislocation behavior summarized and numbered in Figure 1.5(a) and Figure 1.6(a). First, in Scheme A, the nanoporous mask template directly blocks threading dislocations (TDs) in the underlying layer from propagating into the *overgrown* region. For the *coalesced film*, assuming a random distribution of TDs in the buffer, the fraction $F_{TD}$ of TDs blocked by the template is given by the area fraction occupied by the template. For a hexagonal array of circular pores with diameter $d$ and periodicity $p$, $F_{TD}$ is given by

$$F_{\mathrm{TD}} \approx 1 - \frac{\pi d^2}{2\sqrt{3}p^2} \tag{1-1}$$

Hence, depending on the pattern dimensions and arrangement in the mask template, a significant fraction of TDs can be "blocked" at first pass by the template as in epitaxial lateral overgrowth (ELO) [59-61]. From Equation (1-1), adoption of a nanoporous mask template with smaller *d* will be beneficial for template filtering of TDs. In Scheme B, by facilitating pendeoepitaxy ("hanging" ELO) from growths on the mesas, reduction in TD densities can be achieved in the *coalesced film* too.

In Scheme A, bending of some TDs towards the sidewalls of the nanostructure within the pores and subsequent "exit" from the nanostructure act further to improve the structural quality of the nanostructures. Such a phenomenon was first calculated in the 1950s by Eshelby [62] for screw dislocations within a semi-infinite thin rod with radius *r* and a fixed end. According to him, the effect of free surfaces or image forces on a screw dislocation located at a distance $\delta$ more than 0.54*r* from the axis of the rod is sufficient to drive it out. The phenomenon was later numerically modeled and experimentally shown by Colby et al. for pyramidal tip GaN nanostructures grown on hydride vapour phase epitaxy (HVPE) GaN substrates [58]. The authors also added that within the pyramidal cap, for $\delta/r > 0$, the effective force per unit length is greater than the Peierls-Nabarro (P-N) force necessary to drive a TD out of GaN. As the pyramidal tip occurs throughout the growth process, TD filtering is facilitated all along, except for those TDs near the center of the nanostructure. Complete filtering of all underlying TDs was demonstrated for 50 nm and 80 nm diameter nanostructures [62]. The persistence of an axial TD to continue propagating axially may be explained by the attainment of a state of metastable equilibrium at the axial region.

Unfiltered, non-axial TDs which emerge with the nanostructure from the mask in Scheme A may similarly bend towards and terminate at the exposed free surface in order to relax the stress field associated with the TDs. The phenomenon is facilitated in pyramidal geometries as aforementioned and similarly for trapezoidal structures in Scheme B. This effectively reduces the TD density at the top part of the nanostructures and is even more pronounced for higher aspect ratios [63]. The dislocation reduction effect has been exploited in the III-nitrides for facet-controlled epitaxial lateral overgrowth (FACELO) for producing low TD density coalesced thin films [59, 64] as illustrated in Figure 1.5(b) and Figure 1.6(b). However, for the *coalesced film* arising from Scheme A, the mismatch strain energy is accommodated almost entirely by the epilayer since substrate compliance is effectively zero [56]. As such, it may be susceptible to cracking by thermal stress. For the *coalesced film* arising from Scheme B, a significant portion (~ half) of the mismatch strain energy is shared by the compliant substrate, and hence may be more resistant to cracking [55, 56]. To surmise, the propensity of SAG for dislocation reduction can significantly improve crystalline quality in heteroepitaxial nanostructures.

A well-known problem in the growth of InGaN is the existence of a thermodynamic solid phase miscibility gap over much of the alloy composition at typical growth temperatures (~700 to 800°C) which will be discussed in Section 2.3.3. This is attributed to the large difference in atomic spacing between GaN and InN [65, 66]. As a result, phase separation or compositional inhomogeneities are predicted and have been observed over a wide range of In composition $x$ for InGaN bulk films, except at low $x$ (close to GaN) or high $x$ (close to InN) [16, 67, 68]. However, it has been reported that $x$ can be increased without phase separation under strain relaxed conditions with the conventional approach of growing InGaN from the GaN end of the alloy [69]. As a nanostructured morphology is expected to favor strain relaxation

[57], an increase in *x* may be expected. The hypothesis is supported by a report from Kuykendall et al. in which complete composition tunability of InGaN was achieved with InGaN nanowires synthesized by halide chemical vapour deposition and indicated in Figure 1.7 [70].

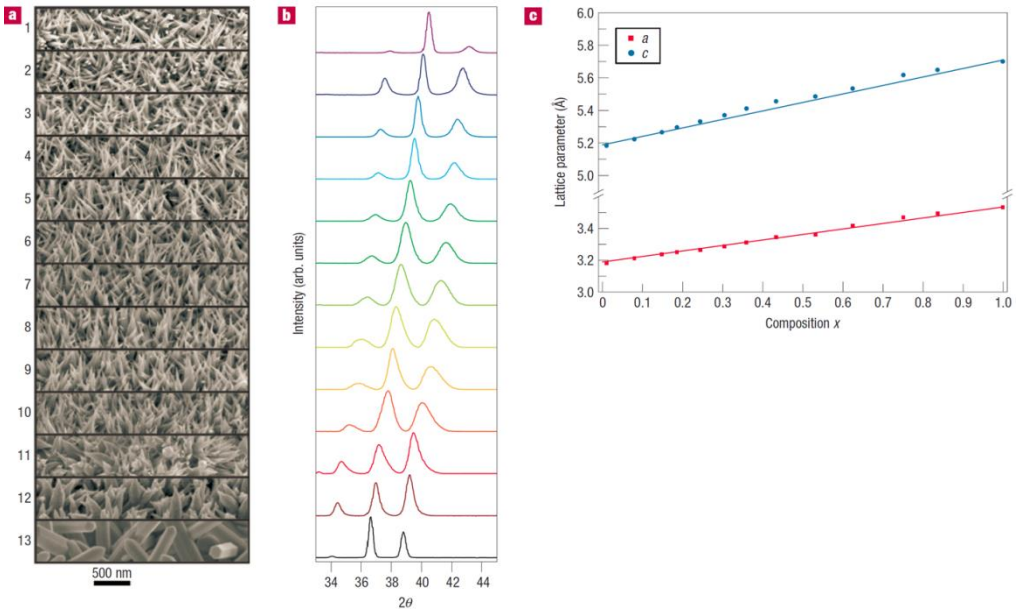


**Figure 1.7** Complete composition tunability of InGaN nanowires grown by halide chemical vapour deposition. (a) SEM of the nanowire morphology with increasing In composition from images 1 to 13. (b) Corresponding XRD scans showing the 100, 002 and 101 XRD peaks from left to right. Co $K_\alpha$ radiation ($\lambda$ = 1.79026 Å) was used as the X-ray probe. (c) Lattice constants *a* and *c* derived from XRD as a function of In composition. (Reprinted from ref. [70])

Recently, theoretical evidence showing that the nanowire configuration provides better strain release than thin films for complete compositional tunability of InGaN was obtained through atomic modeling [71]. These reports indicate that growth of InGaN as strain-relaxed nanostructures is a promising and valid approach to access a broader range of *x* without phase separation. Further, strain relaxed nanostructured morphologies may also mitigate undesired piezoelectric polarization effects characteristic of III-nitrides. Growth over semipolar or non-polar planes (see Section 2) exposed in nanostructures can also help circumvent polarization effects. Further, due to the high equilibrium vapour pressure of $N_2$ over InN, lower temperatures are

typically employed in InGaN growth to improve *x*, with the consequent reduction in structural quality [72]. This will be discussed in Section 2.3.4. This tradeoff may be mitigated by the nanostructured growth of InGaN. For instance, the increase in *x* favored by nanostructured growth may be used to offset the decline in *x* which would occur if increased growth temperature were employed to improve crystalline quality. The consequent improvement in crystalline quality of InGaN through nanostructuring schemes may also help to reduce the defect-related high background electron density which impedes *p*-type doping as discussed in Section 2.3.2. High concentration *p*-type doping will greatly advance the progress in InGaN-based solar cells.

A common approach to reduce reflection in solar cells is the application of optical coatings with refractive indices between that of the semiconductor and that of air [73]. However, an ideal coating would possess a continuously graded refractive index. Tapered semiconductor nanostructure arrays such as nanopyramids and nanocones with sharp tips can function as an effective medium with a gradual change in refractive index given by the weighted average of that of air and the material. Improved absorption over that of planar samples over a broad wavelength and incident angle range can be realized [74, 75]. For instance, GaN nanorod array on Si substrate can reduce reflection over the visible spectrum by a factor of about 3 to 4 [76]. Typically, as-grown III-nitride nanostructures are faceted. By tuning the growth conditions in nano-SAG, pyramidal structures can be achieved. Nanopyramid arrays can have excellent light-trapping properties as light reflected off a facet onto a neighboring facet can have another chance of absorption. In fact pyramidal texturing of surfaces is a widely used technique for reflection control in c-Si solar cells [77].

Nanostructures, such as nanorods, nanopyramids, may be grown in a core-shell PV device architecture for enhanced charge separation. Here, the junction envelopes the

nanostructure. Due to the small lateral dimensions of the nanostructure, photo-generated carriers are likely to lie in close proximity (within their diffusion length) to the junction space charge region where they can be separated and collected [78]. This reduces the sensitivity of the PV process to bulk defects which cause non-radiative recombination of photogenerated carriers before they can be collected. Undesired surface recombination effects may also be reduced [79, 80]. For instance, core-shell nanostructures utilizing "window" shells that exert a periphery surface field also reduce surface recombination which we have numerically shown to limit power conversion efficiencies in axial junction nanostructures [81]. Further, the height of core-shell nanostructures may be increased to improve absorption without removing the junction too far from the core and adversely impacting charge separation.

By growing the semiconductor material into nanostructures, the amount of material needed for absorption is reduced due to lower reflection and improved light trapping. That is, the material is more efficiently utilized. The quality of material required may also be relaxed in core-shell nanostructure device architectures because efficient charge separation and collection may be effected even with lower carrier lifetimes. The reduction in material consumption and relaxation of quality requirements can translate to lower material costs.

#### 1.2.4.4. Plausible InGaN/Si Tandem PV Device Structures

Two plausible InGaN/Si double junction tandem PV device structures based on Schemes A and B are shown in Figure 1.8. The working concept is similar to that already described in Section 1.2.2. A low electrical resistance, thin layer of AlN may be used as the buffer to prevent Ga meltback etching of Si during the growth of InGaN on Si as explained in Section 2.3.1.

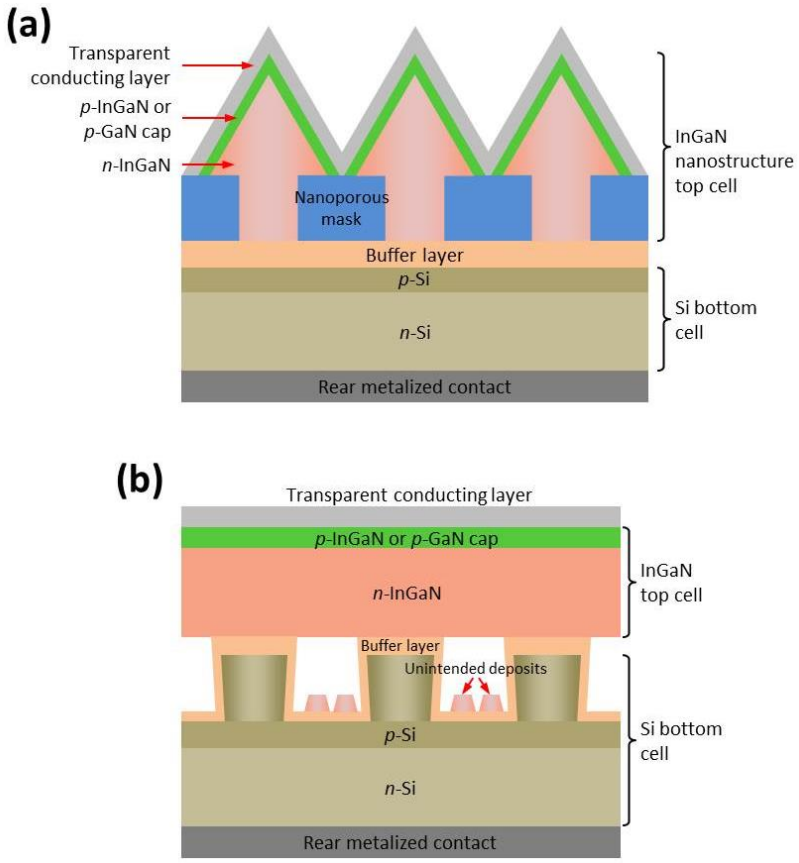


**Figure 1.8** Schematic diagram showing two plausible InGaN/Si tandem device structures based on Schemes A and B. The structure in (a) consists of a *p*-*n* junction top cell of core-shell InGaN nanostructures grown by nano-SAG (Scheme A) over a *p*-*n* junction Si bottom cell. In (b), the *p*-*n* junction top cell is formed by the coalesced InGaN epilayer grown via Scheme B over nanopillars of a *p*-*n* junction Si bottom cell. In both cases, the top and bottom contacts are formed by a transparent conducting layer and a metal layer respectively.

The top cell in Figure 1.8(a) is based on *p*-*n* junction core-shell InGaN nanostructures grown by nano-SAG (or Scheme A) over a *p*-*n* junction Si bottom cell. *p*- and *n*-type doping in InGaN can be achieved during growth by Mg and Si doping respectively. *p*-InGaN may be substituted by *p*-GaN with the advantages of more established *p*-type doping methods in GaN and a wider $E_g$ in GaN which allows it to serve as a window layer thus reducing front surface recombination. The strain associated with the lattice mismatch of GaN on InGaN is alleviated by nanostructuring, use of thin GaN layers or composition grading from InGaN to GaN. A conformal transparent conducting layer coats the top surface of the device and connects the nanostructure tops to form

the front contact. A metal layer deposited on the back surface of the Si substrate forms the back contact.

The coalesced InGaN epilayer arising from epitaxial lateral overgrowth in Schemes A and B may also be employed to form the top cell in InGaN/Si tandem solar cell architectures. Figure 1.8(b) shows such a device structure arising from Scheme B. Junction formation, doping and electrical contact concepts are similar to that described for Figure 1.8(a).

Due to the small contact area between the InGaN nanostructures and the underlying Si substrate in Scheme A, and between the InGaN epilayer and the underlying Si nanopillars in Scheme B, the series electrical resistance is inevitably larger than the thin film case. The impact of this on resistive power loss can be reduced by optimization of doping profiles (and hence conductivities) in the semiconductors in relation to dimensional and electrical properties considerations. It is important to note that while nanostructuring reduces contact area which increases resistive loss, the reduction can have a positive influence. In fact, a reduction in contact area between the lattice mismatched III-nitride and Si material system is beneficial as this improves the quality of the overgrown region, reduces the strain at the footprint of the nanostructures, and hence result in a lower dislocation density. The improvement in material quality from nanostructuring can improve electrical properties such as mobility and conductivity [82]. The benefits of a nanostructuring approach in general and specifically to the InGaN system have already been discussed in previous sections and offer an avenue to overcome InGaN material growth issues which have been plaguing the InGaN thin film community.

As discussed earlier, the region of InGaN nearest Si possesses higher TD and defect densities than regions away from the growth interface. The TDs and defects negatively influence the electrical properties of the device by presenting traps and non-radiative recombination centres. These hinder carrier transport and reduce device efficiency. However, it is important to note that these are inevitably generated in heteroepitaxial growth beyond the critical thickness and nanostructuring advantageously causes the rapid decay in TD and defect densities with distance away from the interface [53]. The undesirable effects of TDs and defects on charge separation are minimized by locating the active region (junction) away from the defects. Hence, taller nanostructures or thicker coalesced epilayers are advocated. In all, it is believed that the proposed InGaN/Si nanostructure schemes for photovoltaic applications are promising and worthy of pursuit.

In the preceding sections, the advantages of InGaN as a promising full spectrum photovoltaic material and of Si as both an excellent substrate and an established photovoltaic material were examined. The successful integration of the two materials will form a key step towards the development of monolithic InGaN/Si tandem solar cells which are cost-effective, and offer broad solar absorption and high conversion efficiencies. However, heteroepitaxy of high quality InGaN films with diverse In content and adequate thickness is difficult because of thermal and lattice mismatches, compositional non-uniformity and phase separation, and temperature tradeoff between structural quality and In content. These challenges are compounded by Ga-meltback etching of Si and unintentional nitridation of Si during growth. Two nanostructuring schemes, A and B, and appropriate device architectures were proposed and offer plausible solutions to overcome the aforementioned challenges.

## 1.3. Scope and Thesis Organization

The nanostructured growth of InGaN on Si substrate to improve InGaN quality forms the focus of this work. The primary objective is to achieve nanostructured growth of InGaN on nano-templated Si substrates under different conditions in MOCVD and examine their characteristics in comparison with that of InGaN grown on non-templated Si substrates. The nano-templated Si substrates may bear either dielectric nanomasks (Type A) or Si nanopatterns (Type B). As such, scalable nanopatterning techniques associated with Schemes A and B are also developed. This thesis consists of seven Chapters and these are summarized as follows.

Chapter 1 provides the introduction and motivation for the integration of InGaN with nanostructures on Si substrates for photovoltaic application. The relevance of nanostructuring to overcoming InGaN growth challenges is discussed. Further, the scope and thesis organization are outlined. In Chapter 2, a background of the III-nitrides is first provided. The growth challenges of InGaN and traditional mitigation methods are then discussed. A review of novel growth strategies and work-to-date on III-nitrides nanostructures is also presented.

In Chapter 3, the experimental methods employed in this work are described. These are Step and Flash$^{TM}$ Imprint Lithography (S-FIL$^{TM}$) for nanopatterning, MOCVD for III-nitride epitaxy, SEM and AFM for morphology characterization, XRD and TEM for structural characterization, and PL spectroscopy and reflectance spectroscopy for optoelectronic and optical characterization. In Chapter 4, nanopatterning techniques developed for the fabrication of growth templates on Si substrates are presented. These are classified into the two Schemes: (A) Fabrication of uniform, tunable aspect ratio nanoporous $SiN_y$ templates on AlN/Si(111) substrates, and (B) Fabrication of Si

nanostructure arrays of variable patterns and adjustable aspect ratio. To ensure a manageable scope, only Type A (nano-SAG) templates were selected for growth.

In Chapter 5, the results of a baseline growth study of InGaN thin films on unpatterned AlN/Si(111) substrates are presented. Pre-requisite growth conditions and effect of growth temperature and pressure on InGaN film properties are discussed. Derived results were used for nanostructured growth. The characteristics of InGaN nanostructure array grown via nano-SAG on Type A templates for a set of conditions is then presented and discussed in comparison with control AlN/Si(111) substrate. In Chapter 6, a comprehensive study on the influence of growth temperature, pressure and other conditions on the In content, morphological, structural and PL qualities of nano-SAG InGaN is presented. A proof-of-concept InGaN/GaN MQW nanopyramid array is also demonstrated. The results are discussed in relation to growth mechanism and relevance to photovoltaic applications. Finally, Chapter 7 summarizes and concludes this thesis. Some suggestions for future work are also proposed.

# Chapter 2 Background and Review of InGaN Growth

## 2.1. Introduction

In this Chapter, a background of the Group III-nitrides is first provided. Then, growth challenges of InGaN and traditional mitigation methods are discussed. A review of growth strategies and work-to-date on III-nitrides nanostructures is lastly presented.

## 2.2. Structure and Characteristics of Group III-Nitrides

InN, GaN and AlN are the three basic binary compound semiconductors of Group III nitrides used in semiconductor devices. These may be alloyed in various proportions to form ternary and even quaternary compound semiconductors to achieve specific properties. They can exist in zinc blende (or sphalerite) and wurtzite structures as seen in Figure 2.1. InGaN is a ternary alloy of InN and GaN.

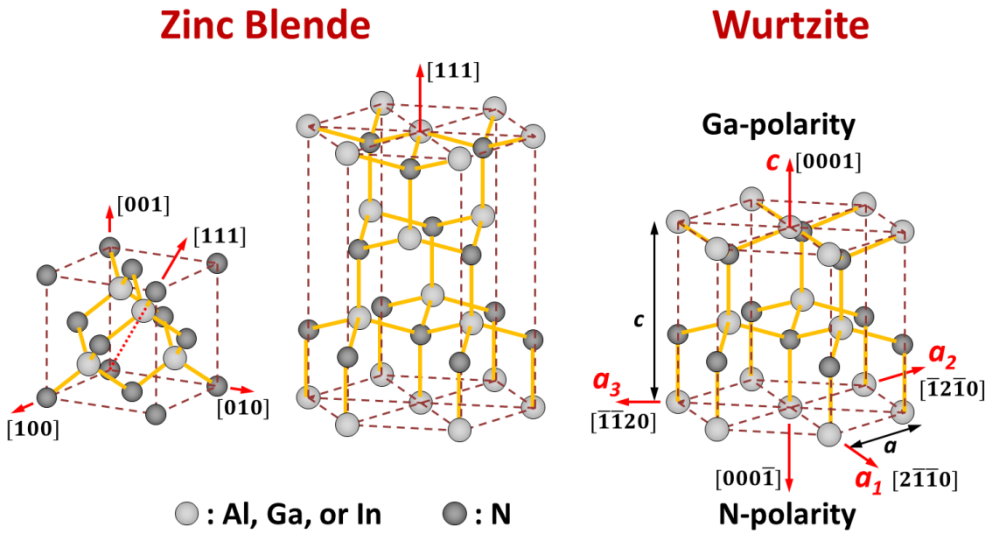


**Figure 2.1** Schematic showing the atomic structures of the Group III nitrides. Zinc blende (left) and wurtzite (right). The cubic zinc blende structure may be positioned to show the stacking of the (111) close-packed planes (middle). In the [0001]-oriented wurtzite structure, two surfaces may be distinguished, namely the “Ga-polar face” and “N-polar face”.

Under ambient conditions, wurtzite is the thermodynamically stable form. The zinc blende structure consists of two interpenetrating face-centered cubic sublattices, each formed by one type of atom, offset by a quarter of the distance along a body diagonal. Each atom is positioned at the center of a tetrahedron, with its four bonded atoms (of the other type) forming the four corners. The stacking sequence for the (111) close-packed planes is AaBbCcAaBbCc where the upper and lower case letters represent the Group III and V atoms respectively. In contrast, the wurtzite structure consists of two interpenetrating hexagonal closed-packed (HCP) sublattices, each formed by one type of atom, offset along the *c*-axis by 5*c*/8, where *c* is the axial lattice parameter. The basal lattice parameter is *a*. Like the zinc blende structure, each atom is tetrahedrally coordinated with four atoms from the other Group. However, the stacking sequence for the biatomic close-packed (0001) planes is AaBbAaBb in the [0001] direction as seen in Figure 2.2. A stacking fault (SF) arises when there is an error in stacking due to the insertion or removal of one close-packed layer. While the three-index (*h'k'l'*) Miller notation is used for the cubic zinc blende structure, a four-index (*hkil*) Bravais-Miler index is usually employed for the hexagonal wurtzite structure. The redundant index *i*, equals – (*h* + *k*), indicate the equivalency of planes such as (2$\underline{11}$0) and ($\underline{11}$20). For brevity especially in XRD, the index *i* may be dropped, and the four-index notation (*hkil*) abbreviated with three indices as (*hkl*), or (*hk.l*).

In this work, the III-nitrides are grown in the wurtzite structure. Thus, four-index and three-index notations when applied to the III-nitrides refer to the hexagonal system. Due to the lack of an inversion plane perpendicular to the *c*-axis in the III-nitride wurtzite structure, two unique nitride surfaces may be distinguished in the [0001]- or *c*-oriented III-nitride crystal typically obtained in growth. The (0001) surface, or the surface with a [0001] surface normal, bears Group III elements at the center of the "upright tetrahedrons" and is known as the "Ga-face" or possesses Ga-polarity. The

opposite surface with a [000$\underline{1}$] surface normal is the "N-face" or possesses N-polarity as seen in Figure 2.1. The distinction between the two surfaces is important because the III-nitrides exhibit significant polarization arising from spontaneous and piezoelectric polarizations. This greatly affects device performance. Even though spontaneous polarization is permitted in an ideal wurtzite structure, the values are considerably larger in the III-nitrides due to structural non-idealities (especially deviation of the *c*/*a* ratio from the ideal value of 1.633) [83, 84]. Further, large piezeoelectric coupling constants implies that the polarization effects are accentuated under in-plane strain. As the polarization is directed along or opposite the axial [0001] direction, there is a need to distinguish between the Ga- and N- polarity surfaces.

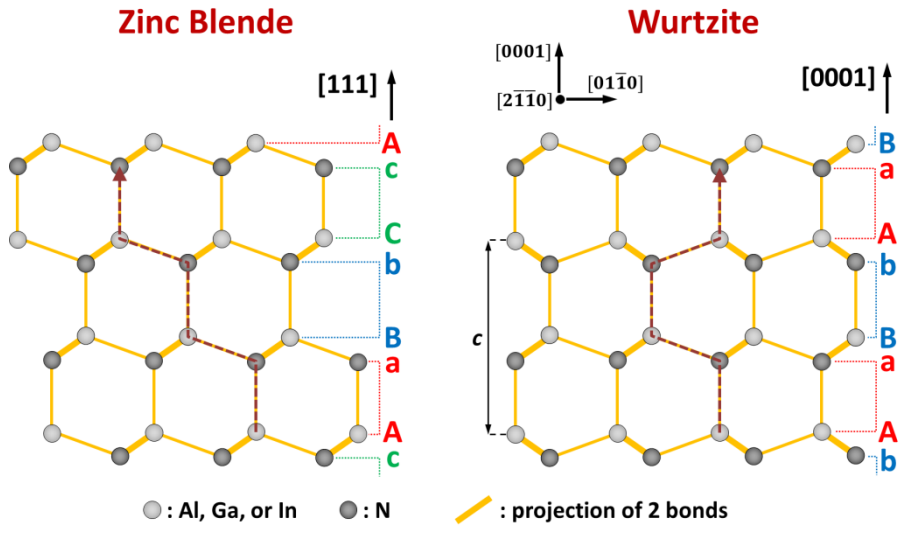


**Figure 2.2** Schematic showing the stacking sequence of the close-packed planes in zinc blende along the [111] direction (left) and wurtzite along the [0001] direction (right).

For growth on Si substrates, Si(111) is preferred due to its trigonal symmetry which favors epitaxial growth of the (0001) plane in III-nitrides. The typical epitaxial relationship between them is given in Figure 2.3(a). Depending on growth conditions, non-polar or semipolar planes may be exposed as illustrated in Figure 2.3(b). Growth on such planes may eliminate or reduce undesired polarization effects such as the

quantum-confined Stark effect (QCSE) in MQWs which reduces output power in LEDs [85] or polarization-induced electric field that impedes carrier collection in solar cells [47]. In III-nitride SAG, the semipolar {1101} planes are easily exposed due to their stability and slow growth rate, and can benefit LED or PV applications.

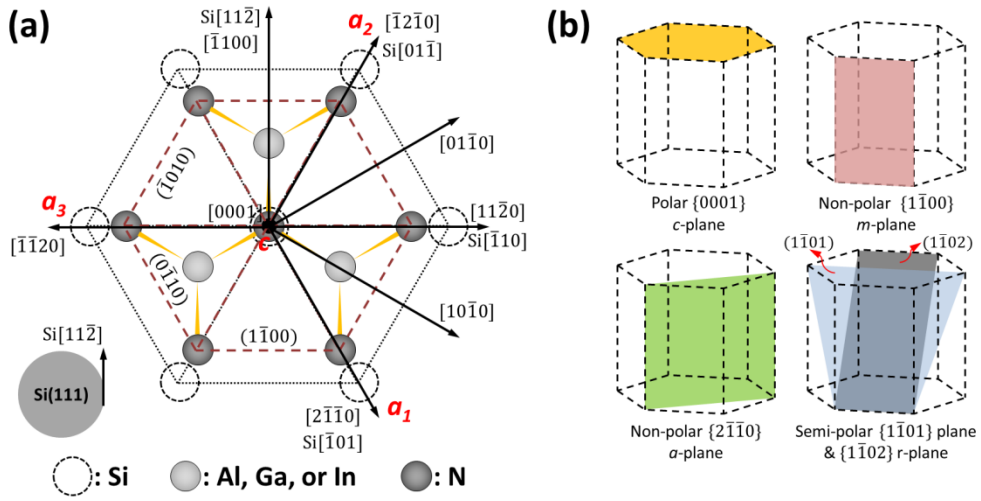


**Figure 2.3** Schematic showing (a) the typical epitaxial relationship of the III-nitrides on Si(111) substrate, and (b) common planes of the wurtzite structure in III-nitrides.

The bandgap $E_g$ of the ternary wurtzite $In_xGa_{1-x}N$ alloy as a function of indium composition $x$ is given by Vegard's Law and expressed in Equation (2-1).

$$E_g = xE_g^{\mathrm{InN}} + (1-x)E_g^{\mathrm{GaN}} - bx(1-x) \tag{2-1}$$

where $b$ is the bowing parameter taken as 1.43 [10], and $E_g{}^{\mathrm{GaN}}$ = 3.42 eV, and $E_g{}^{\mathrm{InN}}$ = 0.7 eV at room temperature. Figure 1.2 shows the relation between $E_g$ and $x$. The temperature dependence of the bandgap $E_g(T)$ can be expressed in Varshni form as

$$E_g(T) = E_g(0) - \frac{\alpha T^2}{T+\beta} \tag{2-2}$$

where $T$ is the temperature in K, $E_g(0)$ is the bandgap at $T$ = 0 K in eV, and $\alpha$ and $\beta$ are Varshni parameters in eV/K and K respectively [86]. The values of these parameters for the binary members of the wurtzite III-nitrides are shown in Table 2-1.

**Table 2-1** Bandgap $E_g(0)$ (eV) at $T$ = 0 K, and Varshni parameters $\alpha$ (meV/K) and $\beta$ (K) [87].

| **Parameters** | **InN** | **GaN** | **AlN** |
|---|---|---|---|
| $E_g(0)$ **(eV)** | 0.78 | 3.51 | 6.25 |
| $\alpha$ **(meV/K)** | 0.245 | 0.909 | 1.799 |
| $\beta$ **(K)** | 624 | 830 | 1462 |

The main epitaxy methods for the Group III nitrides are hydride vapour phase epitaxy (HVPE), plasma-assisted molecular beam epitaxy (PA-MBE), and metalorganic chemical vapour deposition (MOCVD). The advantage of HVPE is its capability of growing epitaxial thick GaN films with low defects at high growth rates and relatively low cost. High quality HVPE GaN templates or free-standing GaN substrates may be used for MOCVD and MBE to fabricate GaN-based devices with excellent performances. However, the growth of high quality InN and InN-containing InGaN layers in HVPE remains challenging due to the poor stability of InN and other growth challenges. In PA-MBE, the supply of N is assured through a plasma. Hence, lower substrate temperatures may be employed which may be helpful for increased In incorporation in InGaN. Further, an advantage of materials grown by MBE is its high purity since other elements (e.g. C) are not present in the sources. However, MBE is ceded in favor of MOCVD which has considerably better economics. MOCVD is capable of producing high purity, high quality materials with atomically abrupt interfaces for device applications. It is versatile and is suitable for large-scale production due to high growth rates and high yield. Hence, this growth method is employed in this work. For details, see Section 3.3. However, a notable conundrum exists for the growth of InGaN in MOCVD due to the use of $NH_3$. While low temperatures favor higher In incorporation in InGaN, the cracking efficiency of $NH_3$ to form N radicals for bonding suffers. This is discussed in Section 2.3.4.

## 2.3. Challenges in InGaN Growth and their Conventional Mitigation

Despite the benefits of InGaN for PV applications (See Section 1.2.1), its growth is markedly more challenging than that of other III-nitrides. In this section, we review the major challenges encountered and the conventional ways for mitigating them.

### 2.3.1. Gallium Meltback Etching and Unintentional Nitridation of Silicon

The direct epitaxial growth of InGaN (or any Ga-containing III-nitrides) on Si by MOCVD is challenging for two reasons. First, a strong chemical reaction between Ga and Si occurs at MOCVD temperatures of ~ 800°C or more, leading to roughening or degradation of the surface. This is a eutectic reaction often known as Ga meltback etching of Si in MOCVD [88, 89]. Surface pits and Ga droplets may be observed in such a scenario. Even if InGaN deposition were achieved through low growth temperatures (< 800°C), subsequent rise in temperature above ~ 800°C will result in a similar reaction. Second, even at lower growth temperatures, surface nitridation of Si can occur in the $NH_3$ environment used in MOCVD. The consequent formation of amorphous or polycrystalline $SiN_y$ will lead to subsequent disordered growth and poor growth quality [90, 91]. A suitable buffer layer that prevents these reactions is thus warranted. While a multilayer of AlN/AlGaN/GaN is often employed to overcome the aforementioned problems and to reduce lattice mismatch [92, 93], such a buffer possesses relatively high electrical resistance, making it unsuitable for vertically integrated monolithic InGaN/Si tandem solar cells. Hence, a thin AlN protective layer has been used and shown to allow a low resistance contact to be achieved between the epilayer and Si [23-26, 94]. However, this comes at the expense of greater lattice mismatch which degrades structural quality.

### 2.3.2. Thermal Expansion and Lattice Mismatch

III-nitrides are typically grown heteroepitaxially due to a lack of native substrates as discussed in Section 1.2.2. In heteroepitaxy, the epilayers and substrate are of different materials and thus possess dissimilar coefficients of thermal expansion (CTE). Upon growth completion and cooling down from the elevated growth temperatures, residual stress will build up due to a difference in contraction rate or mismatch in CTE. The CTE residual stress depends on the temperature difference, epilayer thickness, CTE mismatch and other mechanical properties of the materials and can modify the electronic properties of the epilayer. The CTE of the binary III-nitrides and Si are tabulated in Table 2-2. Due to the smaller CTE of Si, the CTE residual stress in the III-nitride layer grown on Si is tensile. When the layer thickness reaches a critical value, cracking occurs to lower the total strain energy of the system. This value is known as the critical thickness for steady state propagation by cracks parallel to the interface. For instance, a GaN layer with thickness more than 1μm grown over a AlN buffer layer on Si are susceptible to cracking [95]. A more in-depth treatment of cracking in brittle films is presented in ref. [96, 97].

**Table 2-2** Lattice constants and mechanical properties of the III-nitrides and Si(111) [98].

| **Parameters** | | **InN** | **GaN** | **AlN** | **Si(111)** |
|---|---|---|---|---|---|
| **Lattice constants** | ***a* (Å)** | 3.538 | 3.189 | 3.112 | 3.8403 |
| | ***c* (Å)** | 5.703 | 5.185 | 4.979-4.982 | - |
| **Coefficient of thermal expansion** | **$\Delta a/a$ ($K^{-1}$)** | ~$2.85 \times 10^{-6}$ | $5.59 \times 10^{-6}$ | $4.2 \times 10^{-6}$ | $2.616 \times 10^{-6}$ |
| | **$\Delta c/c$ ($K^{-1}$)** | ~$3.75 \times 10^{-6}$ | $3.17 \times 10^{-6}$ | $5.3 \times 10^{-6}$ | |
| **Poisson's ratio ν** | | 0.272 [99] | 0.23 | 0.18-0.21 | 0.218 |
| **Young's modulus *E* (GPa)** | | 145 [100] | 150 | 374 | 165.6 |

Strain engineering and other growth strategies are thus essential to mitigate residual stress. For GaN-on-Si, strain engineering typically involves the insertion of low-

temperature AlN (LT-AlN) interlayers within a buffer stack [101, 102]. As the LT-AlN interlayer is (partially) relaxed, it disrupts the coherence between the underlying buffer layer and the subsequent layers. Due to the smaller lattice constant of AlN, AlGaN or GaN layers grown over LT-AlN are initially compressively stressed. Depending on the LT-AlN deposition temperature, its relaxation extent can be tuned to offset the intrinsic and thermal stress associated with GaN growth on Si. 8" crack-free GaN-on-Si wafers with (0002) $\omega$-rocking curve FWHM of 220 arcsec rivaling that of conventional GaN-on-sapphire has since been achieved for LED applications [103]. However, for applications where thick buffer and transition layers need to be avoided, other growth strategies may be needed to reduce the residual thermal strain.

In addition to a difference in CTE, the III-nitride epilayer and Si substrate also possess different lattice constants. The mismatch $f$ in the lattice constants is expressed in Equation (2-3), where $a_s$ and $a_f$ are the bulk in-plane lattice constant of the substrate and the film respectively.

$$f = \frac{a_s - a_f}{a_s} \tag{2-3}$$

In the early stage of heteroepitaxy, the lattice of the epilayer is elastically strained to match the lattice constant of the substrate. If $a_f < a_s$, the epilayer is under in-plane tensile strain. Conversely, if $a_f > a_s$, the epilayer is under in-plane compression. The in-plane distortion is accompanied by distortion in the out-of-plane lattice parameter in accordance to Poisson's ratio $\nu$. This coherently strained epilayer is described as pseudomorphic. When the epilayer thickness is increased, strain accumulates. Above the critical layer thickness $h_c$, the strain energy becomes sufficiently large to cause plastic deformation in the epilayer and the material relaxes through the generation of misfit dislocations at the heteroepitaxial interface. A dislocation that threads into the epilayer is termed a threading dislocation (TD). There are three types of TDs as

defined by the direction of the Burgers vector **b** relative to the propagation vector **u** or dislocation line: (i) edge dislocation (type a) with **b** perpendicular to **u**, (ii) screw dislocation (type c) with **b** parallel to **u**, and (iii) mixed dislocation with both edge and screw character. Edge and screw dislocations are structural accommodations of lattice twist and tilt respectively. Due to the possession of both edge and screw components, mixed dislocations accommodate both twist and tilt. See Figure 2.4.

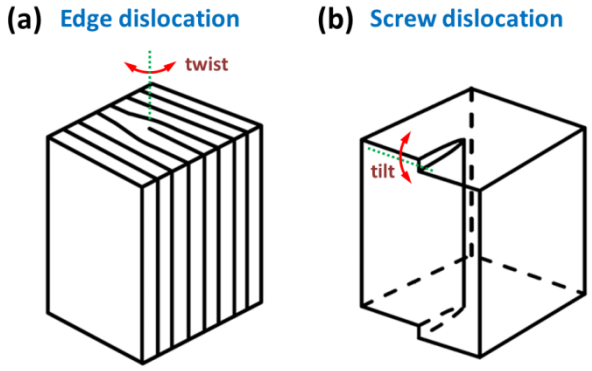


**Figure 2.4** Schematic showing edge and screw dislocation and their correlation with lattice twist and tilt respectively. (Adapted from ref. [104])

In epitaxial [0001]-oriented III-nitride wurtzite films, TDs typically have a line direction of [0001]. Here, edge, screw and mixed dislocations have Burgers vector of 1/3[11$\underline{2}$0], [0001] and 1/3[11$\underline{2}$3]. High TD densities are common in III-nitride heteroepitaxy due to the extreme difference in lattice constants as seen in Table 2-2. TD densities in the range of $10^8$ to $10^{10}$ $cm^{-2}$ are typically encountered and pose challenges to efficient and high performance III-nitride device realization. The dislocations and defects present non-radiative recombination centres that lower carrier lifetime and reduce the quantum efficiency of photovoltaic devices. They may also function as undesirable scattering centres that limit carrier mobility. Further, nitrogen vacancies ($V_N$) associated with dislocations have been proposed as possible donors that contribute to the high background electron density in InGaN [105, 106]. This compounds the pre-existing challenges associated with *p*-type doping by Mg

acceptors for device fabrication. Moreover, as TDs traverse the epilayer from the substrate to the top, shunt current flow along TDs can reduce device performance and lifetime [107, 108]. Hence, in view of the myriad of adverse effects associated with dislocation formed in heteroepitaxy, there is significant impetus to reduce the TD density and improve the quality of the grown III-nitride layers. Various dislocation reduction techniques involving selective area growth and epitaxial lateral overgrowth have since been developed which is discussed in Section 2.4.

### 2.3.3. Composition Inhomogeneity and Phase Separation

Due to the large difference in lattice parameters between GaN and InN a solid phase miscibility gap exists in InGaN [65, 66]. The extreme lattice mismatch of ~ 11% is a strong driving force for GaN and InN to "unmix" in InGaN. Depending on the In content $x$ in $In_xGa_{1-x}N$ and the strain state of the film [109, 110], minor compositional fluctuation or complete phase separation by spinodal decomposition can occur.

Compositional fluctuation within InGaN or non-random distribution of In atoms within the alloy has been postulated to arise from a few mechanisms, all of which act to reduce the energy of the system. These include (i) composition pulling effect in InGaN grown on GaN where $x$ is low near the InGaN/GaN interface but increases with InGaN thickness to reduce deformation energy arising from lattice mismatch with GaN [111, 112], (ii) strain induced island formation in which islands with a larger misfit component preferentially nucleate because the nucleation barrier is lower [113], (iii) surface segregation and [0001] chemical ordering of the Group III sublattice to minimize the number of In-N bonds since the bond strength of In-N bonds is notably weaker than that of the Ga-N bond [114, 115], and (iv) binodal and spinodal decomposition [65, 116]. It is likely that some or all of these mechanisms play a role in the formation of nanoscale In-rich clusters embedded within InGaN.

These structures manifest as localized bandgap minima, favoring radiative recombination and function as luminescent centers. Hence, despite high TD densities, InGaN/GaN MQW devices still exhibit strong emission due to carrier localization [117, 118]. While compositional fluctuation likely affects photovoltaic performance, the effect is unlikely to be large, provided major phase separation is absent.

Unfortunately, phase separation by spinodal decomposition can occur in InGaN, especially at mid-In compositions [16, 67]. In spinodal decomposition, spontaneous up-hill diffusion of In atoms leads to the formation of two phases with high and low In content to reduce the system's free energy. Using a modified valence force field model, Ho et al. has calculated the binodal and spinodal curves in the InN-GaN phase diagram [65] as seen in Figure 2.5(a). The binodal curve defines a region of composition and temperature for a solution across which a transition occurs from miscibility of the components (region above the curve) to metastability or instability (region below it). For a typical growth temperature of 800°C, the equilibrium solubility of In in GaN is less than 6%. The spinodal curve defines the limit of stability of a solution. Within the curve, equilibrium occurs via phase separation by spinodal decomposition. By encouraging non-equilibrium growth conditions, phase separation can be suppressed to obtain higher In content single phase InGaN [68, 119]. However, obtaining high quality InGaN remains a challenge. Phase separation is highly undesired because the much lower $E_g$ regions can greatly limit photovoltaic performance of solar cells by acting as recombination centers that decrease the short-circuit current, and by pinning down the open-circuit voltage of the device [120].

By incorporating the effect of strain in the calculation of the InN-GaN phase diagram, Karpov et al. showed that phase separation can be suppressed by elastic strain [110]. This accounts for the ability to produce InGaN/GaN MQWs without phase separation

for $x > 0.2$. Tessarek et al. employed a more consistent set of elastic constants [121] to calculate the phase diagram under varying strain as given by Figure 2.5(b). This shows that increasing strain reduces the critical temperature (maximum of the spinodal line), decreases the binodal and spinodal regions, and shifts them towards higher $x$ and lower temperature. InGaN with low to mid $x$ can thus be grown without phase separation. While the case for InGaN/GaN MQWs in LEDs or laser diodes is fully justified, its case in PV is tenuous. This is because a combined InGaN layer thickness of a few hundred nanometers is required for effective optical absorption but implementation of InGaN/GaN MQWs or superlattices (SL) to increase the total absorption thickness eventually degrades crystal quality [46].

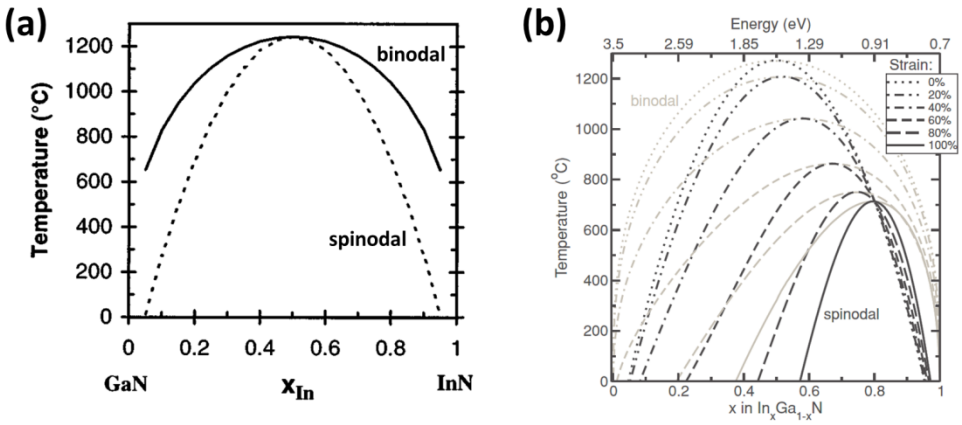


**Figure 2.5** Theoretical phase diagram for the InN-GaN system for (a) the bulk unstrained case [65], and (b) varying extent of strain [121].

### 2.3.4. Temperature Tradeoff Between Good Structural Quality and High Indium Content

The phase diagrams in Figure 2.5 indicate that phase separation in InGaN could theoretically be overcome by using temperatures higher than the maximum of the spinodal line. However, a conflict arises due to the high equilibrium vapour pressure of $N_2$ over InN even at normal growth temperatures [72]. This is much higher than that of AlN and GaN as seen in Figure 2.6(a). High temperatures would result in the

rapid dissociation of InN due to the weak In-N bond, and a sizable reduction of the In content in InGaN. An analysis of the main reaction pathways following the adsorption of In atoms on the growth surface is illustrated in Figure 2.6(b).

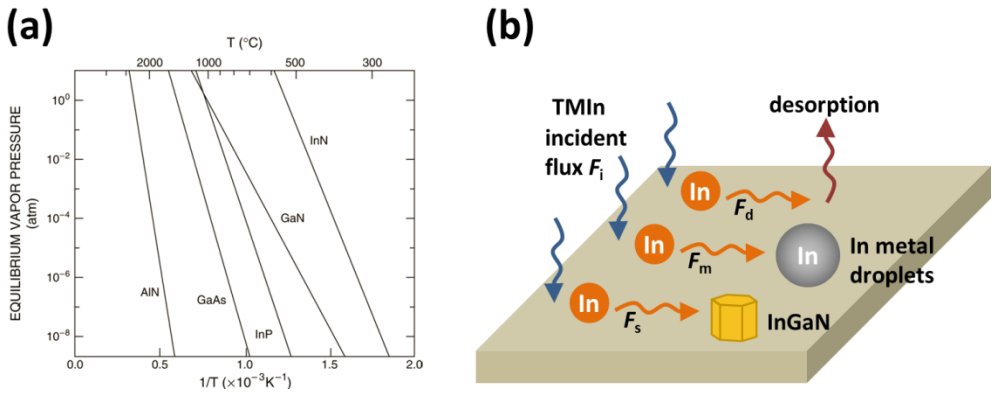


**Figure 2.6** (a) Equilibrium vapour pressure of $N_2$ over AlN, GaN, and InN (reprinted from ref. [122]); (b) Reaction pathways of adsorbed In during InGaN growth (adapted from ref. [123]).

The processes involved are (i) In incorporation into the solid ternary InGaN alloy, (ii) In incorporation into In metal droplets, and (iii) In desorption from the growth surface due to non-incorporation of In or breaking of existing In-N bonds [123]. The respective flux associated with each process in atoms/cm$^2$/s is $F_s$, $F_m$ and $F_d$. For an incident flux of trimethylindium (TMIn) $F_{in}$, the mass balance equation below applies

$$F_{\text{in}} = F_{\text{s}} + F_{\text{m}} + F_{\text{d}} \tag{2-4}$$

The residence lifetime $\tau$ of In on the growth surface can be expressed as

$$\tau = \tau_0 \exp\left(\frac{E_{\text{d}}}{k_{\text{B}}T}\right) \tag{2-5}$$

where $\tau_0$ is fixed for a given set of conditions, $E_d$ is the activation energy for In desorption, and $k$ is the Boltzmann constant . Since $F_d$ is inversely proportional to $\tau$,

$$F_d \propto \exp\left(-\frac{E_d}{k_{\text{B}}T}\right) \tag{2-6}$$

Due to the exponential temperature dependence, In desorption is significant at high growth temperatures. Further, the relative stability of Ga atoms compared to In atoms

on the nitride surface (or weaker bond strength of In-N compared to Ga-N) implies that TMIn flow rates much higher than trimethylgallium (TMGa) flow rates are necessary to increase the chances of In incorporation into the growing lattice.

From the above analysis, higher In content InGaN is favored with high TMIn flow rates and low growth temperatures. However, selection for low temperatures is opposed by other considerations which advocate otherwise [124]. First, as mentioned earlier, phase separation could theoretically be overcome or reduced by employing temperatures greater than that of the binodal and spinodal curves in the phase diagram. Second, structural quality would likely be improved with higher temperatures due to the reduction of carbon-related impurities, nitrogen vacancies, and other structural defects [125-127]. Third, and perhaps most critical in MOCVD of III-nitrides, is the necessity for higher temperatures (> ~ 800°C) to increase $NH_3$ decomposition efficiency due to the strong N-H bonds [98]. The dissociation of $NH_3$ is needed to provide the N atoms for bonding in III-nitrides. A deficiency of N atoms in a situation where there is an abundance of In atoms adsorbed onto the growth surface can lead to the formation of small In metal droplets. When the droplets reaches a critical size and become thermodynamically stable, they can getter In atoms on the surface and compete with In incorporation in the solid InGaN phase [123]. This possibly explains reports of In droplets in the growth of high In content InGaN at low temperatures [128-130]. Fourth, higher temperatures are associated with greater surface mobility of adatoms which promote better surface coverage and two-dimensional film growth.

To summarize, the conflicting requirement on growth temperature is a major consideration in the growth of InGaN. Typically, a compromise has to be made between good structural quality and high In content. Growth strategies that mitigate such a conundrum would greatly advance progress in the growth of InGaN. In

particular, techniques that improve or maintain In incorporation with the use of higher temperatures is highly desired in view of the advantages of high-temperature growth.

## 2.4. Novel Growth Strategies

### 2.4.1. Development of New Growth Methods

New growth methods of InGaN are typically based on modified MBE techniques and employ non-equilibrium conditions to achieve single phase high In content InGaN within the miscibility gap. One such method called energetic neutral atom-beam lithography and epitaxy (ENABLE) has recently been reported [24, 27, 131]. The growth process occurs in a standard MBE ultra-high vacuum (UHV) environment with conventional Knudsen cells as the metal sources but employs a high-intensity energetic beam of neutral nitrogen atoms as the nitrogen source. By exposing a heated substrate to the reactive N atom beam flux and co-evaporated Ga and/or In metal fluxes, InGaN films can be grown. The energetic N atoms activate film growth even at low temperatures (450 - 700°C). This reduces In desorption and dissociation of InN. Due to the large N atom kinetic energy and flux, $In_xGa_{1-x}N$ can be grown at high rates (~ 2 μm/h). These favor non-equilibrium conditions allowing high In content single phase $In_xGa_{1-x}N$ ($x$ up to ~ 0.35) on Si(111) to be grown. The results are promising but high $n$-type carrier concentration of ~ $9 \times 10^{20}$ $cm^{-2}$ greatly impedes $p$-type doping [132]. Structural quality improvement is also warranted.

Metal-modulated epitaxy (MME) is a III-nitride growth technique based on MBE. In MME, the metal and dopant cell shutters are open and closed at regular intervals while the active nitrogen flux supplied by plasma remains constant. Highly metal-rich fluxes are used to exploit the enhanced adatom diffusion facilitated by an excess metal layer [133] to achieve abrupt interfaces. While excess metal would rapidly form droplets in conventional MBE, this is consumed into the film due to periodic closing

of the metal and dopant cells. Low growth temperature reduce adatom desorption and favor non-equilibrium conditions allowing thin (< 60 nm) $In_xGa_{1-x}N$ films throughout the miscibility gap to be grown [133]. In addition, very high hole concentrations in the order of ~ $10^{19}$ $cm^{-3}$ has been achieved in $In_xGa_{1-x}N$ for $x$ = 0 to 0.22 [134]. This is more than an order greater than the highest reported value [135]. However, as the growths were performed on GaN templates or AlN/sapphire wafers, the results may differ for growth on Si. The latter is expected to be more challenging due to unintentional nitridation of the Si surface and Ga meltback etching of Si [132].

The above non-equilibrium growth methods are highly promising means to grow single phase $In_xGa_{1-x}N$ with $x$ within the solid phase miscibility gap. However, they do not address the fundamental problem of high dislocation and defect densities associated with heteroepitaxy of InGaN on Si substrates.

### 2.4.2. In-situ Silicon Nitride Masking

In-situ silicon nitride ($SiN_y$) masking is a threading dislocation (TD) reduction technique first reported by Vennegues et al. for GaN growth on sapphire [136]. Here, the growth is interrupted by a short-duration deposition of a thin, discontinuous $SiN_y$ mask layer (a few nanometers thick). The growth is then resumed. Due to the lower sticking coefficient of the Ga precursor on $SiN_y$, growth occurs only on the unmasked regions of the surface. This forms GaN islands which overgrow over the mask and eventually coalescence to form a continuous layer. A transition from two-dimensional growth mode to three-dimensional growth mode is thus effected. With this method, TD densities (TDDs) as low as mid $10^7$ $cm^{-2}$ has been achieved [137]. In-situ $SiN_y$ masking has also been combined with AlN/AlGaN buffer stacks for GaN growth on Si(111) substrates [138]. This mechanism of TDD reduction is similar to epitaxial lateral overgrowth (ELO). The $SiN_y$ mask blocks TDs from propagating into the

overgrown layer. TDs that emerge from the unmasked regions tend to bend in the (0001) plane where TDs of opposite Burgers vector annihilate each other.

In addition to TDD reduction, the method is also found to reduce tensile stress since it favours the growth of larger size crystallites which have less grain boundaries, the latter being a source of intrinsic tensile stress [139]. In-situ $SiN_y$ masking is a simple non-lithographic method that has been used almost exclusively for GaN growth. Its use for InGaN films has yet to be demonstrated but may function similarly.

### 2.4.3. Selective Area Growth

Selective area growth (SAG) involves the localization of material growth to specific regions of the substrate by the use of a growth mask. Growth selectivity is achieved by the destabilization of the solid phase (nucleation) on the mask surface while permitting growth on the unmasked region. The mask material is usually a dielectric e.g. $SiO_2$ or $SiN_y$, although metal masks have also been used. SAG of the III-nitrides by MOCVD was first reported by Kato et al. for GaN on GaN/sapphire substrates using a stripe-patterned $SiO_2$ mask [140]. Hiramatsu et al. [141] and Zheleva et al. [60] have found that the morphology of the SAG structure depends on the shape of the mask opening, its orientation with respect to the crystallographic orientation of the underlying layer, and growth conditions. For stripe mask openings patterned along the <1$\underline{1}$00> direction of the underlying GaN, an increase in growth temperature *T* or a decrease in reactor pressure *P* leads to a change in morphology of the overgrown GaN from a triangular shape with {11$\underline{2}$2} sidewalls to a rectangular shape with {11$\underline{2}$0} sidewalls as seen in Figure 2.7. However, for stripes along the <11$\underline{2}$0> direction, the shapes remain triangular with {1$\underline{1}$01} sidewalls regardless of *T* and *P*. The phenomenon may be explained as follows.

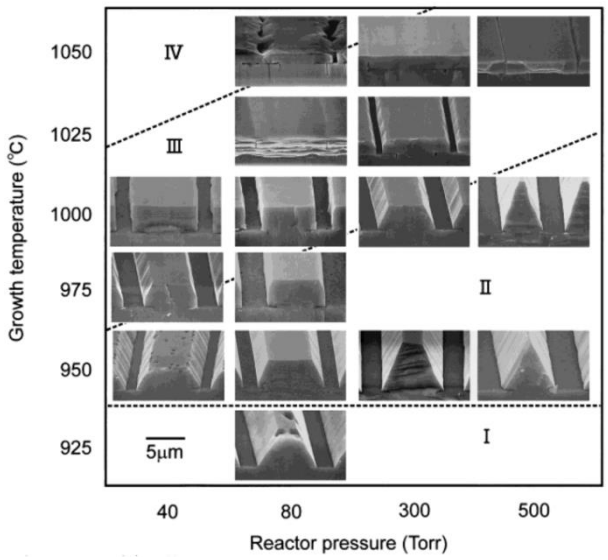


**Figure 2.7** Morphological changes in SAG of GaN using <1$\underline{1}$00> mask stripe openings under different reactor pressures and growth temperatures. (Reprinted from ref. [141])

The shape of the SAG structure is governed by the slowest growing crystallographic plane according to Wulff's theory [142]. This is in turn determined by the plane stability which depends on the termination of the planes (either N-terminated or Ga-terminated) and the dangling bond density (DB) of the plane [141] as seen in Figure 2.8. In general, N-terminated planes are stable under MOCVD conditions of high V/III ratio, especially with high *P* or low *T*, and present the slowest growth rate. This has been attributed to H-passivation of the N-terminated planes [143-146]. Thus, for Ga-polar growth, the H-passivated, N-terminated planes of {1$\underline{1}$01} and {11$\underline{2}$2} are observed under high *P* or low *T*. When passivation of these planes is not effected in the reverse growth conditions, the planes with the lowest DB density, and thus the greatest stability, will determine the crystal morphology.

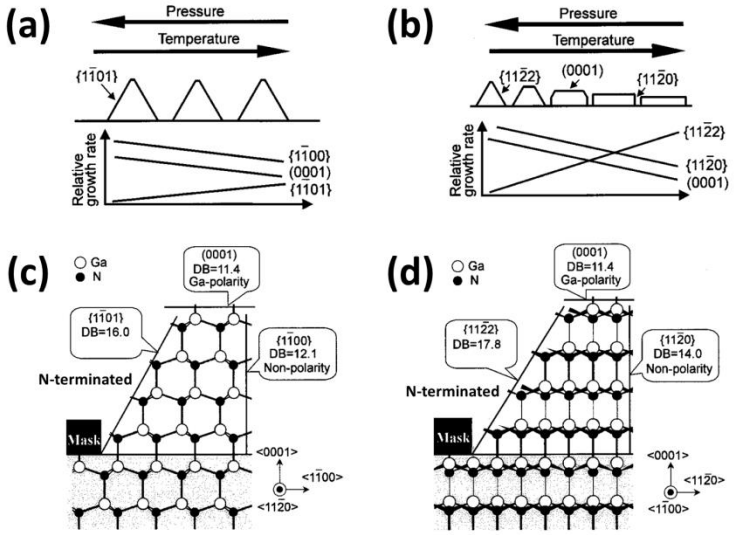


**Figure 2.8** Morphological changes and relative plane growth rates in SAG of GaN as a function of growth pressure and temperature for mask stripe openings along the (a) <11$\underline{2}$0>, and (b) <1$\underline{1}$00> directions. Respective atomic configurations are shown in (c) and (d). (Adapted from ref. [141])

In addition to elongated stripes, SAG of hexagonal GaN pyramids bound by {1$\underline{1}$01} facets has also been realized using hexagonal [147] and circular [60] mask openings. A major benefit of SAG is associated with the three-dimensional morphology of the structures. Not only is the active device area increased, the exposure of semipolar or non-polar facets allows the fabrication of devices with reduced undesired polarization effects [148, 149]. Further, instead of confining growth to within the mask openings, some form of epitaxial lateral overgrowth (ELO) is typically allowed. In such a case, the mask effectively prevents the propagation of TDs into the overgrown region. Moreover, for triangular or trapezoidal SAG structures (pyramids or stripes), many of the TDs originally propagating along the *c*-axis in the openings are observed to bend towards the lateral facets [59, 60, 150]. The top part of the structure is thus of improved quality. In all, TDD reduction is achieved as seen in Figure 2.9.

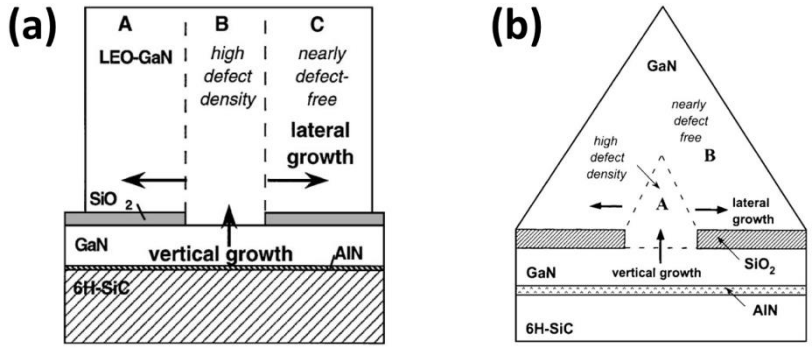


**Figure 2.9** Distribution of defects in SAG of (a) GaN stripe and (b) GaN pyramid. LEO, synonymous with ELO, refers to lateral epitaxial overgrowth (Reprinted from ref. [60])

We note that III-nitride SAG is performed mainly with GaN due to its role in device applications and as a growth template. However, it may be applicable to InGaN too. It has been shown that among the common wurtzite planes, the semipolar planes of {1101} and {1122} exhibit the highest indium incorporation $x$ in $In_xGa_{1-x}N$ [151, 152]. This has been associated with the favorable energetics of the planes for accommodating In atoms [115, 153]. The higher $x$ may help to alleviate the constraints associated with the temperature budget in InGaN growth. Further, the segmentation of the SAG structures may also relieve thermal residual stress.

### 2.4.4. Epitaxial Lateral Overgrowth (ELO)

Epitaxial lateral overgrowth (ELO) may be performed after SAG with the aim of coalescing the SAG structures to obtain low TDD continuous films. This combinatory approach is known as two-step ELO or facet-controlled epitaxial overgrowth (FACELO) [59, 64]. In III-nitrides, ELO is performed almost exclusively with GaN due to its use as a growth template. Variants of ELO includes pendeo-epitaxy (PE) which involves lateral suspended growth from elevated GaN pillars to produce GaN with low and uniform dislocation density [154, 155], maskless pendeo-epitaxy where the mask in PE is removed to reduce crystallographic tilt, thermal stress and impurity incorporation [156, 157], and maskless ELO [158, 159] as illustrated in Figure 2.10.

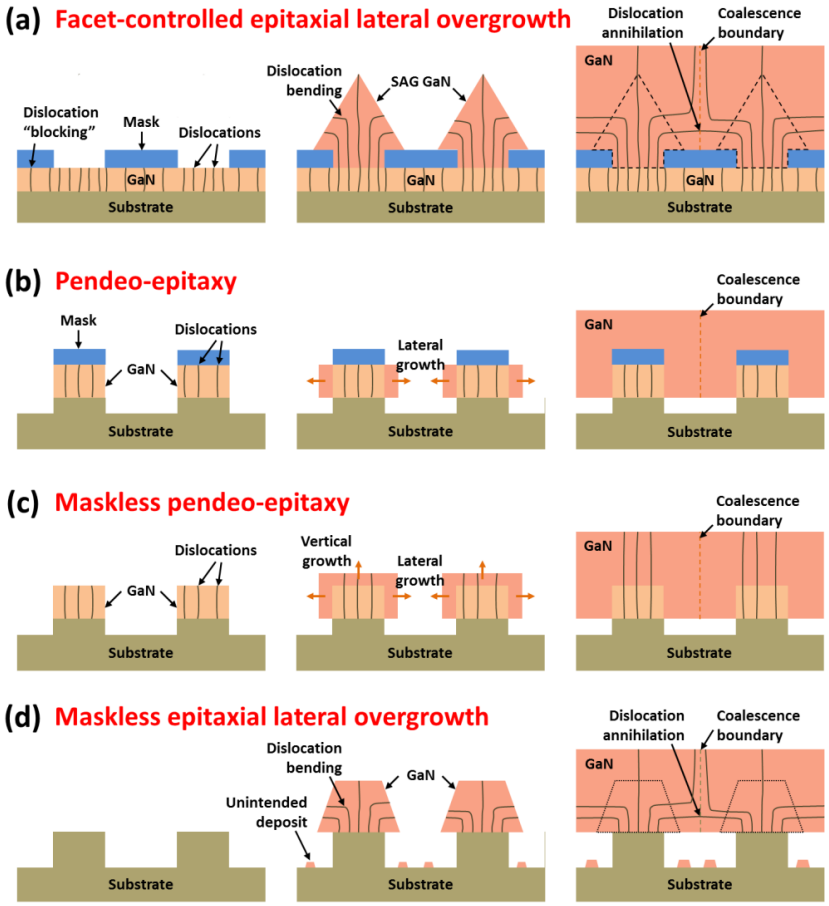


**Figure 2.10** Schematic showing some common TDD reduction techniques. (a) Facet-controlled epitaxial lateral overgrowth, (b) pendeo-epitaxy, (c) maskless pendeo-epitaxy, and (d) maskless epitaxial lateral overgrowth.

However, while ELO and its variants are effective in reducing TDD, it does not address the issue of phase separation and the temperature tradeoff between crystal quality and In content in the growth of InGaN. In contrast, SAG structures which expose the semipolar planes show not only reduced TDDs and increased active device area, but also exhibit reduced polarization effects and increased In content.

### 2.4.5. Nanostructured Growth

In Sections 2.3 to 2.4, we reviewed the challenges associated with InGaN growth, the conventional mitigation approaches, as well as other novel methods. However, the

techniques, with the exception of SAG, are unable to tackle all the issues concurrently. Conversely, we have shown in Section 1.2.4 the benefits and potential of nanostructuring in overcoming all the challenges. In this section, we review the bottom-up growth of III-nitride nanostructures. These may be broadly classified into non-templated (e.g. self-assembly) and templated (e.g. lithography) approaches.

#### 2.4.5.1. Non-templated Nanostructure Growth

In the non-templated growth of nanostructures, no prior patterning step is performed. The formation of nanostructures relies on statistical formation of nucleation centres on the substrate. A vapour-liquid-solid (VLS) mechanism is typically involved in which the nucleation sites may be defined by the self-assembly of foreign catalysts (e.g. Au droplets), or by droplets of the Group III metal formed by specific growth conditions. We note that foreign catalysts can lead to contamination of nanostructures.

MBE is commonly used for the non-templated growth of III-nitride nanostructures [160]. Through this, good crystalline quality AlN [161], GaN [162-164] and nearly intrinsic InN [165, 166] nanowires (NWs) relatively free of extended defects have been obtained on Si and sapphire via VLS mechanisms. MBE has also been used for growing InGaN nanostructures and may be well-suited to access the entire composition range due to its relatively low growth temperatures. Single phase, single crystalline faceted InGaN nanopillars well-oriented along the *c*-axis with blue and green PL have been grown on *p*-type Si(111) in RF-MBE [167]. Wu et al. further observed that InGaN RF-MBE grown on *c*-plane sapphire NWs are dislocation-free and exhibit further strain relaxation with growth duration as indicated by the red-shift in band edge PL from 559 to 582 nm [168]. However, as MBE growth of III-nitride nanostructures on Si is not exactly epitaxial due to formation of amorphous $SiN_y$ at the Si interface, NW disorientation, merging and formation of grain boundary

dislocations can result [169]. Basal stacking faults (SFs) and nanoscale In content variation have also been detected. By reducing the growth temperature, In incorporation of InGaN nanocolumns grown on Si(111) by PA-MBE can be increased [170]. Indium is most easily incorporated into NW tops due to top-to-bottom diffusion of In atoms [169, 171]. Non-uniform interwire and intrawire In distribution were also reported for InGaN NWs [172]. While, the high SF densities in the NWs is reduced with higher growth temperatures [173], reduction in In content ensues.

Using X-ray fluorescence and energy-dispersive X-ray spectroscopy, it was found that InGaN NWs may comprise a Ga-rich shell and an In-rich core [174]. The natural non-polar NW core-shell structure can benefit PV applications. Very high In content $In_xGa_{1-x}N$ (x~0.86 to 1) NWs with PL emission from 1500 to 1920 nm have also been grown by PA-MBE on Si(111) [175]. Further, $In_{0.86}Ga_{0.14}N/In_{0.79}Ga_{0.21}N$ multiple quantum disks (MQDs) have been grown on $In_{0.79}Ga_{0.21}N$ NWs with PL emission tunable by well thickness. However, heterostructures are more commonly fabricated upon GaN NWs and invariably for LED applications. p-i-n heterostructures [176], InGaN/GaN MQDs (or MQWs) [177-179] and insertions [180-182] have also been fabricated on GaN nanostructure arrays for variable color light emission.

In addition to PA-MBE, chemical vapour deposition (CVD) has been employed to grow III-nitride NWs. Using evaporated Au as a catalyst on *p*-type Si(100) substrates, InN NWs have been grown via the VLS reaction [183]. Also, helical InGaN NWs consisting both hexagonal and cubic phases have been grown via Au-catalyzed CVD on Si substrates by Cai et al. [184-186]. However, unlike nanostructures grown in MBE which bear a pseudo-epitaxial relationship with the Si substrate, CVD NWs are randomly oriented in a mesh-like network. Despite this, complete compositional

tunability of InGaN NWs has been achieved using catalyst-free low temperature halide CVD by Kuykendall et al. [70] as discussed in Section 1.2.4.3.

HVPE has been used to grow *c*-axis oriented, single-crystalline GaN nanorods with high spatial density on sapphire and Si substrates [187-190], as well as, *c*-axis oriented $In_xGa_{1-x}N$ nanowires on Si(111) [191] and *c*-plane sapphire substrates with $x$ up to 0.2 [192]. $x$ was limited to 0.2 due to the consumption of the $InCl_3$ precursor by $H_2$ in the reactor. Nanowires are so termed due to their much higher aspect ratios than nanocolumns. By introducing TMIn as the In precursor in metal-organic HVPE (MO-HVPE), dislocation-free $In_{0.25}Ga_{0.75}N$/GaN MQW nanorod arrays (NRAs) were grown [193] and fabricated into high efficiency and brightness blue LEDs [194]. Separately, $In_xGa_{1-x}N$ nanocolumns with varying $x$ (0 to 0.57) have been grown via plasma-enhanced evaporation on amorphous $SiO_2$ substrates[195] . While the nanocolumns are hexagonal and approximately normal to the substrate surface at low $x$, the order, dimensional uniformity and crystallinity degrades as $x$ increases.

Metal-catalyzed [196, 197] and catalyst-free MOCVD [198, 199] have been used to grow GaN NWs. For the latter, an in-situ deposited $SiN_y$ layer is found to contribute to GaN seed formation for NW growth. VLS growth of InN by In self-catalysis in MOCVD has also been performed [200]. While metal-catalyzed MOCVD synthesis of GaN and InN NWs has been achieved, growth of InGaN NWs by the same approach is difficult [201]. This is because when In and Ga are present in the VLS metal droplet, In metal is preferentially reabsorbed back into the droplet. As such only $In_xGa_{1-x}N$ with low $x$ ( $\leq 0.05$) is formed. The MOCVD growth of III-nitride nanostructures by a templated approach is thus more frequently employed. This also allows better dimensionality control in contrast to non-templated approaches where the nanostructures are highly disordered and exhibit a broad range of sizes.

### 2.4.5.2. Templated Nanostructure Growth

While non-templated approaches allow nanostructures to be easily grown, such that their characteristics can be studied, control over their arrangement and dimensions is desired. This is because these directly influence the structural [54], optical [179, 202] and electronic properties [203]. A templated approach which provides size-, shape- and site-control, would thus allow these properties to be tuned. Templated epitaxial growth of nanostructure may be broadly classified under two schemes, (A) nano-SAG from recessed regions of the substrate as delineated by a nano-featured SAG mask, and (B) nanoheteroepitaxy from elevated regions of a nanopillar substrate. These are termed Schemes A and B respectively and were discussed in Sections 1.2.4.1 and 1.2.4.2. Nano-SAG is typically combined with MBE or MOCVD.

#### 2.4.5.2.1. Nano Selective Area Growth (Nano-SAG or Scheme A)

Nano-SAG in RF-MBE has largely focused on the growth of GaN nanocolumns and InGaN/GaN heterostructures. This was first achieved by Sekiguchi et al. using a focused ion beam (FIB) patterned nanohole Ti mask to fabricate InGaN/GaN MQW nanocolumn arrays [204]. The nanocolumns were single crystalline and bears a hexagonal cross-section with vertical (1$\underline{1}$00) side facets. A high growth temperature ~ 900°C was critical for SAG. This is facilitated by low $N_2$ flow rate which enhances desorption and diffusion of Ga from/on the nitridated Ti mask, and effectively suppress nucleation on it [205]. The GaN nanocolumns appeared free of TDs. While GaN on sapphire substrates are typically used in the MBE nano-SAG of GaN, nano-SAG of GaN on AlN buffered Si substrates using $SiN_y$ masks has also been achieved with essentially perfect selectivity [206]. Pores with diameters < 500 nm produced single nanowires with symmetrically faceted tips but larger openings yielded material appearing to comprise of coalesced nanostructures. The effect of temperature, III/V

flux ratio, mask geometry have also been examined [207, 208]. Sekiguchi et al. further showed that by increasing the diameter of InGaN/GaN MQW nanocolumn within a fixed period array, a change in beam shadow effect results [209]. This was utilized for increasing In composition and hence elongating the emission wavelength. Further, by tuning the growth condition, quantum dots can be fabricated at the pyramidal apex of the InGaN/GaN nanocolumns [210]. Emission shifts likewise with nanocolumn diameter and was found to exhibit high PL internal quantum efficiency (~ 48 to 62%). This was attributed to the high quality of the GaN nanocolumn since TDs in the lower sections bend towards the sidewalls and do not propagate to the upper active layer.

Work on nano-SAG in MOCVD is more extensive and has been performed with GaN, InN and InGaN. Selective area epitaxy of InGaN nanorings and nanodots on GaN/sapphire substrate using a nanoporous $SiO_2$ mask was first reported by Chen et al. [211]. The mask (~ 80 nm diameter pores) was patterned by anodization of aluminum oxide (AAO). During MOCVD, the edges of the $SiO_2$ mask serve as heterogeneous nucleation centers where the free energy of the nucleus is lower than that of a flat surface, leading to the formation of InGaN nanorings which follow the contours of the $SiO_2$ pores. The noncapped InGaN nanorings exhibited strong PL at ~ 420 nm at room temperature due to strong confinement of excitons. By tuning the AAO process, the $SiO_2$ mask feature size can be correspondingly changed, allowing InGaN nanostructure diameters to be varied from 35 to 250 nm [212]. Further, by controlling the growth duration, high density arrays of nanorings, faceted nanodots and nanoarrows can be obtained. AAO-patterned $SiO_2$ masks was also applied to the nano-SAG of GaN nanorod arrays [58, 213-215] and to realize InGaN/GaN heterostructures [216, 217]. MQW PL intensity higher than planar structures was obtained and attributed to improved light extraction and improved crystal quality.

Further, increased In incorporation was achieved due to strain relaxation. The reports, along with that discussed in Section 2.4.3 for SAG support the validity of the proposed approach in this work. Likewise, AAO-patterned $SiO_2$ masks has been applied for nanoscale lateral epitaxial growth of GaN films on Si(111) [61] and sapphire substrates [218] leading to low TDD ~ $10^7$ $cm^{-2}$.

Other lithography methods have been employed in nano-SAG. Ultra-high density InGaN-based quantum dots (diameter ~ 22 – 25 nm) have been achieved with diblock copolymer lithography [219]. Electron beam lithography (EBL) has also been used for $SiO_2$ mask patterning to form highly uniform and periodic line and hole arrays with sizes down to 52 nm and pattern size deviation < 4% [220, 221]. Nano-SAG of horizontal InGaN nanowires and nanodots/nanorings thus fabricated on GaN/sapphire possess high optical quality and PL peak emission from 450 – 500 nm. Compared to random nanodots, size-homogeneous nanodot arrays (Figure 2.11(a)) produce narrower PL emission [221, 222]. Patterning in SAG is discussed in ref. [223].

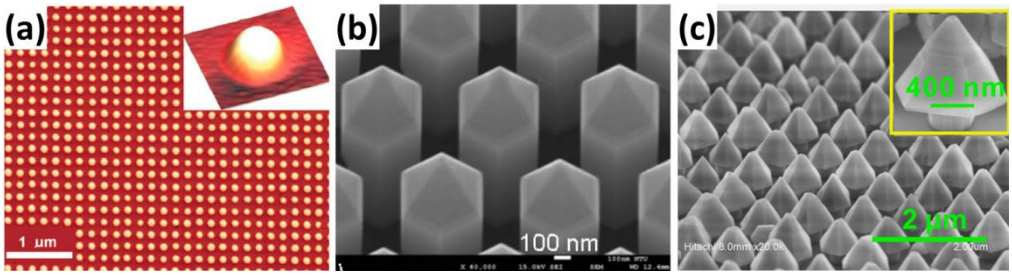


**Figure 2.11** SEM images of nanostructures grown via nano-SAG. (a) InGaN nanodot array [221], (b) InGaN/GaN MQW LED nanorod array [224], and (c) InGaN/GaN MQW LED nanopyramidal array [225].

On a separate front, highly uniform, high aspect ratio, vertical GaN nanowire arrays with excellent long range order have been grown by *pulsed* MOCVD using a $SiN_y$ mask patterned by interferometric lithography [49]. Alternate introduction of the Group III and V precursors presents a low V/III ratio and leads to a VLS mechanism

that significantly increases the vertical-to-lateral growth rate ratio. Despite the presence of TDs beneath the growth mask, none were observed in the NWs. This presents a scalable method for the fabrication of high quality GaN NW arrays. Alternatively, pulsing of just the $NH_3$ precursor can be performed [226]. Pulsed MOCVD has also been attempted for nano-SAG of InGaN via AAO-patterned $SiO_2$ masks on sapphire, and *a*-plane GaN/sapphire [227]. The Ga precursor was introduced intermittently to avoid nucleation on the mask due to the low growth temperatures. However, only low aspect ratio nanostructures were obtained.

Pulsed MOCVD has been combined with nanoimprint lithography (NIL) patterned $SiO_2$ SAG mask to form GaN nanocolumn arrays [228, 229]. When coalescence overgrowth is facilitated, it was showed that nanoporous masks with the smallest hole/spacing ratio have the lowest TDD. InGaN/GaN QWs have been grown on the sides and tops of pulsed deposited GaN nanorods to form *m*-plane core-shell and *c*-plane disc structures [230, 231]. Here, QWs are narrower and In content higher at the *m*-plane sidewalls than the *c*-plane tops. Further, nanorods with shorter height, greater cross-sectional size, or larger pitch have longer emission wavelengths. LEDs based on these InGaN/GaN QW nanorod arrays ( Figure 2.11(b)) have been fabricated and show a smaller blue shift with increasing injection current than planar devices due to reduced quantum-confined Stark effect (QCSE) in the non-polar *m*-plane QWs [224]. LED core-shell nanorod arrays have also been demonstrated [232, 233].

Nano-SAG of high aspect ratio vertical GaN nanorod arrays can also be achieved under *continuous* flux conditions in MOCVD. Bergbauer et al. obtained N-polar GaN nanorods on patterned sapphire substrate using such an approach [234, 235]. The high aspect ratio was enabled by low V/III ratio and high $H_2/N_2$ ratio. Higher temperatures also helped [236]. Further, silane injection was reported to dramatically enhance

vertical growth rate of Ga-polar GaN nanorods [237, 238]. Choi et al. found that the anisotropy in growth rate is increased with low $NH_3$ and Ga precursor flow rates and that SAG efficiency hinges on pattern fill factor [239]. Increased $NH_3$ flux was accompanied by greater lateral growth and dominance of the {11$\underline{2}$02} and {11$\underline{0}$1} facets. Ga-polar GaN nanowires with diameter as small as 50 nm were achieved.

Surface polarity plays a crucial role on the morphology of nanostructures [143]. For Ga-polar GaN, the inclined {11$\underline{0}$1} planes are terminated by N atoms. Under high V/III ratios, these are passivated by H, which leads to a stable surface with low growth rates, and hence pyramidal structures bound by them. The reduced temperature growth of InN and InGaN requires high $NH_3$ flow rates or high V/III ratios to compensate for the low $NH_3$ dissociation efficiency to avoid In droplet formation. This explains the nanopyramidal morphology obtained in nano-SAG of InN and InGaN on Ga-polar growth surfaces [203, 212, 240]. For GaN nanostructure growth (of both polarities), the H-passivation effect is relieved under Ga-rich, low V/III ratio conditions, thus aiding vertical growth. Here, the {11$\underline{0}$1} planes are modified by $H_2$ etching, leading to the more stable vertical (11$\underline{0}$0) *m*-planes. InGaN/GaN MQW structures have been grown on Ga-polar GaN nanorod arrays [237], and on the {11$\underline{0}$1} facets of GaN nanopyramid arrays [225, 241] by continuous-flux MOCVD to form core-shell LED structures. In fact, quantum dot formation on the apex of GaN nanopyramids has been reported [242].

#### 2.4.5.2.2. Nanoheteroepitaxy on Nanopillar Substrates (Scheme B)

The theory of nanoheteroepitaxy (NHE) on patterned substrate was originally developed by Luryi and Suhir [53] and extended by Zubia et al. to include effects of substrate compliance [55]. This was demonstrated in the MOCVD of GaN structures on Si nanoscale islands (diameter 80 – 300 nm) patterned by interferometric

lithography from <111>-oriented silicon-on-insulator substrates [243]. As predicted, the defect concentration decays rapidly away from the heterointerface. Interfacial defects were unavoidable due to the large GaN/Si misfit of ~ 20% but formation and propagation of threading defect were notably reduced in the highly coalesced films [244]. NHE of GaN on patterned Si(111) substrates has also been performed. Film relaxation and improvement in optical properties were reported for MBE-grown highly coalesced GaN on AAO patterned nanoporous Si(111) [245]. Dense arrays of Si(111) nanopillars similarly derived from AAO patterning has been used in NHE of GaN by MOCVD [246]. Grain boundary defects can heal leading to single crystal GaN layers. Mismatch defects were mainly in-plane stacking faults and TDD was < $10^8$ $cm^{-2}$ at the interface and reduces away from it as seen in Figure 2.12(a). Facet voids present at the GaN/Si interface were believed to reduce strain energy. The excellent prospects of nanoheteroepitaxy on nanopillar substrates have been shown via the industrially implemented growth of GaN on nanopatterned sapphire substrates [247-249].

Besides aiming for coalesced films, III-nitride heteroepitaxy has also been performed on pillar-patterned Si(111) substrates for fabricating GaN truncated pyramids and GaN-based nanoLEDs. To achieve deep-etched Si patterns, Fündling et al. developed a low temperature inductive coupled plasma etching process [250]. GaN pyramidal structures possessing InGaN/GaN MQWs have been successfully grown on top of Si pillars [50, 63, 250, 251]. Crystal quality is improved due to the small lateral size of the structures which lowers mismatch strain energy, and reduction of defect densities (especially towards the top) because of dislocation bending towards the lateral free surface as seen in Figure 2.12(b). Some GaN crystallites grew on the Si pillar sidewalls and at the bottom of the etched substrate. The growth mode was found to depend on pillar geometry (size, pitch). A smaller pitch results in higher growth rate

on top of the pillars and smaller growth at the bottom [250]. Lower growth rates on the {11$\underline{0}$1} sidewalls relative to that of the (0001) top was found to result in thinner InGaN QWs and a blue-shift in luminescence [50, 63]. A study of GaN growth on the sidewalls of high aspect ratio Si micro-pillars patterned from substrates of various orientation has also been performed [252]. Depending on the orientation and growth conditions, various symmetrical growth patterns were achieved. To suppress spurious GaN growth on the sidewalls and bottom surface, patterned AlN templates on Si substrate with in-situ nitridation have been used with good results [251].

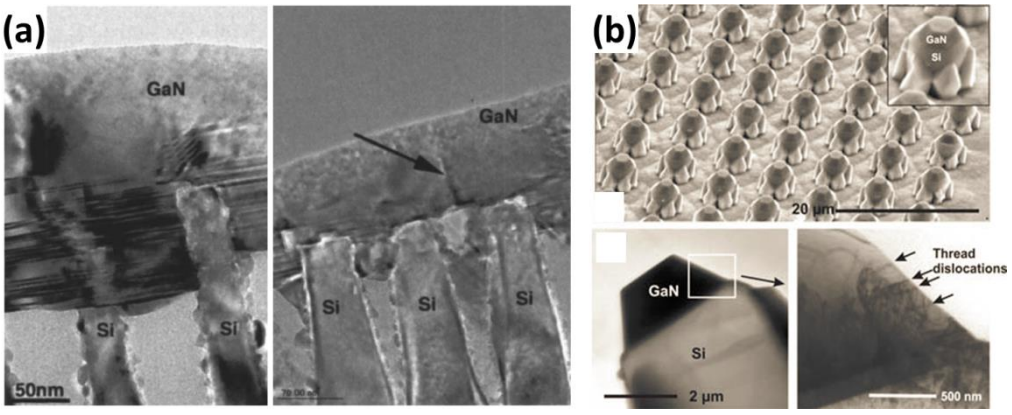


**Figure 2.12** Heteroepitaxy of GaN on patterned Si substrate. (a) TEM images of GaN films grown on Si nanopillars [246]. The main defect type is stacking fault (left). A arrow marks a coalescence defect (right). (b) GaN structures grown on Si pillar array [251]. SEM image (top). TEM images showing threading dislocations bending towards the sidewall (bottom).

## 2.5. Chapter Summary

In this Chapter, an introduction to InGaN was provided. The challenges associated with InGaN growth, namely, (i) Ga-meltback etching and unintentional nitridation of Si, (ii) thermal and lattice mismatch, (iii) compositional non-uniformity and phase separation, and (iv) temperature tradeoff between structural quality and In content, were discussed along with traditional mitigation methods. For (i), the deposition of a thin AlN buffer in MOCVD may be a viable solution. For the other challenges, novel growth strategies are needed. This includes variants of MBE, in-situ $SiN_y$ masking , ELO, SAG, and nanostructuring schemes. While MBE and its variants improve In

composition range by providing low temperature N-rich non-equilibrium conditions, it is likely that mismatch strain, defects, and TDs associated with (ii) are not reduced. Further, unintentional nitridation of Si in MBE is inevitable. In-situ $SiN_y$ masking and ELO in MOCVD, typically performed in GaN growth, reduces heteroepitaxy-related TDDs, but do not address compositional issues (iii) and (iv). In contrast, SAG of 3D structures not only reduces TDDs and increases active device area, but also reduces polarization effects and increases In content on non-polar or semipolar planes.

The merits of nanostructuring stem from strain relaxation and dislocation reduction, and show the potential to mitigate all the aforesaid growth issues. See Section 1.2.4.3. A review of non-templated and templated III-nitride nanostructuring methods was presented in this Chapter. For good size and hence property control in nanostructures, a templated approach is preferred. Two types are identified, namely, (A) nano-SAG from recessed regions (nanopores) of a mask fabricated on a substrate, and (B) nanoheteroepitaxy from elevated regions of a nanopillar substrate. In particular, nano-SAG of InGaN, though promising, has yet to be performed on AlN-buffered Si substrates for PV applications. Such a work will have direct implications in the development of InGaN/Si tandem solar cells.

# Chapter 3 Experimental Methods: Patterning, Growth & Characterization

## 3.1. Introduction

In this Chapter, the experimental methods employed in this work are described. For nanopatterning, Step and Flash™ Imprint Lithography (S-FIL™), a form of nanoimprint lithography (NIL), is employed. For growth of III-nitrides, metalorganic chemical vapour deposition (MOCVD) is used. Morphology characterization involves scanning electron microscopy (SEM) and atomic force microscopy (AFM). For structure and composition characterization, X-ray diffraction (XRD) and transmission electron microscopy (TEM) are used. Lastly, optoelectronic and optical properties are measured by photoluminescence (PL) and reflectance spectroscopy. A good understanding of these techniques is desired for correct equipment operation, setting proper precautions in place, and interpretation of results. The equipment described are personally operated by me except for TEM for which an advanced user was involved.

## 3.2. Nanoimprint Lithography

### 3.2.1. Background

In order to fabricate the templated substrates bearing nanoscale features (in the size range of < 100 nm to 300nm) for InGaN growth, a form of nano-scale lithography is required. While deep-UV projection lithography and UV interference lithography enable higher resolution patterning, they remain constrained by the UV diffraction limit. Electron beam lithography (EBL) overcomes the optical diffraction limit and allows realization of customizable features down to a few nanometers. However, it is too slow to achieve large area patterning. Self-assembly methods such as colloidal lithography [253, 254], anodization of aluminum oxide (AAO) [215], and diblock-

copolymer lithography [219, 255] are simple, cost-effective means of nano-scale patterning over larger areas. However, ordering is restricted to domains with little pattern versatility. The aforementioned restrictions may be circumvented by NIL in which the mould pattern can be defined by EBL or other high-resolution nano-scale patterning techniques and thus possess excellent pattern versatility and resolution. As NIL depends on direct mechanical deformation of the resist material, its resolution is not limited by diffraction or beam scattering during the imprinting process. Large area, high-throughput nano-scale imprinting can subsequently be realized at low cost by parallel printing or through a stepper. NIL was originally reported by Chou et al. [256, 257] in the scientific literature and has since undergone significant development [258].When heat is employed for resin curing, the technique is known as thermal NIL. Conversely, when the technique utilizes UV for curing, it is termed UV-NIL. A pre-requisite in UV-NIL is that either the substrate and/or mould be UV transparent. Other variations of NIL, e.g. soft lithography, are also possible [259, 260].

### 3.2.2. Step and Flash™ Imprint Lithography (S-FIL™)

The Step and Flash™ Imprint Lithography (S-FIL™) process is a variation of UV-NIL and was originally developed by Wilson et al. at the University of Texas at Austin. Essentially, it is a step and repeat nano-replication technique based on UV-curable low viscosity liquids. Molecular Imprints, Inc. develops the commercial tools for the technology [259, 261, 262]. Through the stepper mechanism, S-FIL™ enables wafer-scale patterning of nano-scale features. As the process is performed at room temperature, it is very attractive for IC semiconductor device manufacturing. Hence, this method is adopted as the central technique for patterning growth substrates in this work. This is carried out in a Molecular Imprints, Inc. Imprio 100 machine placed in a Class 100 cleanroom. The S-FIL™ process is detailed in Figure 3.1. The numbers in the figure follow the numerals in the following text.

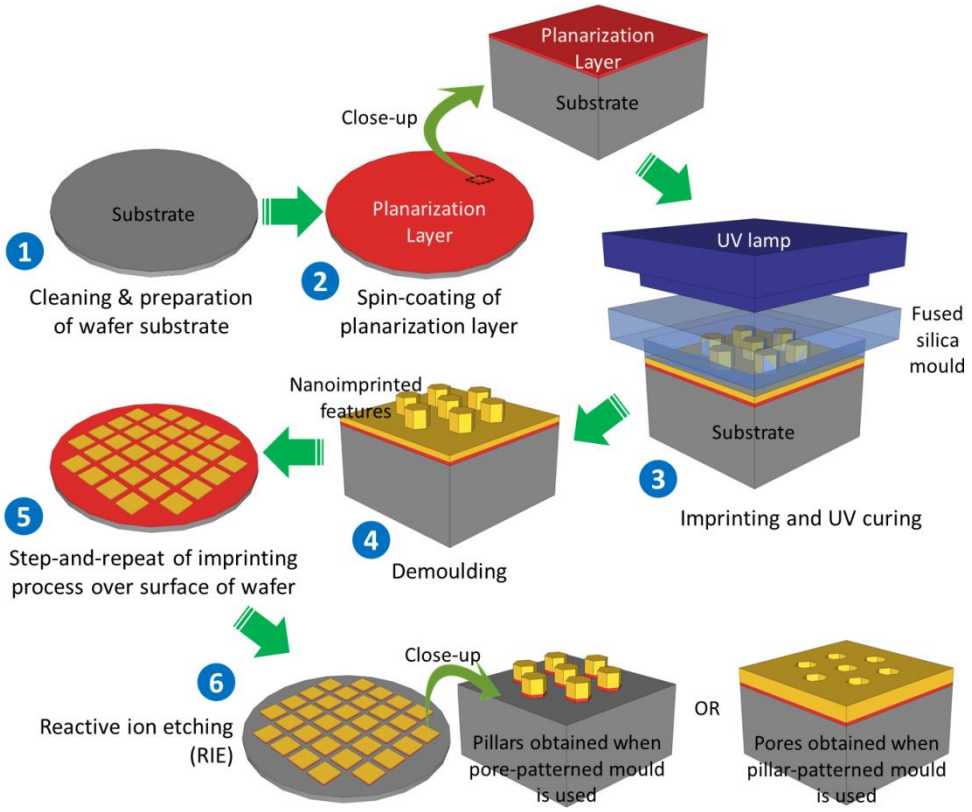


**Figure 3.1** Schematic illustrating the steps involved in Step and Flash™ Imprint Lithography (S-FIL™) to produce pillar- or pore-patterned nanoimprinted wafers.

The substrate to be patterned is (1) thoroughly cleaned in boiling piranha solution and (2) spin-coated with an organic planarization layer (Transpin from Molecular Imprints, Inc.). (3) It is then loaded into the Imprio 100, oriented and leveled against a patterned fused silica mould. For each imprint area, nanolitre droplets of UV-curable, low-viscosity acrylate resist (MonoMat from Molecular Imprints, Inc.) are dispensed onto it and the mould is brought into close proximity with the substrate, thus displacing the resist. This induces the resist to spread across the imprint field and fill up the mould relief via capillary action. A short exposure to UV light causes the polymerization of the monomers in the resist, after which (4) the mould is separated from the substrate, leaving behind an inverse replica of the mould pattern. This nanoimprint process is optimized for full pattern transfer while minimizing the residual material at the base of the recessed features and maintaining its uniformity

across the field. (5) The process is step-and-repeated over the wafer to achieve wafer-scale nanopatterning. (6) The residual layer and underlying planarization layer are removed by $O_2$ RIE, thus exposing the substrate in these regions. The remaining features form the high-resolution pattern for later pattern transfers.

The key concerns in S-FIL™, as well as other methods of NIL are cleanliness, substrate flatness and levelness, and residual layer removal. Due to the use of mechanical contact to shape the resin or resist, it is essential that the contact regions be free of particles. Particles can cause poor pattern transfer, defects, or may even damage the surface-relief features on the mould. Further, it is critical that the substrate surface be flat and properly levelled against the mould to avoid non-uniformity in residual layer thickness in the imprinted patterns. Thus, wafer warp, bow and surface curvature and irregularities must be minimized. While the residual layer in the imprint support alignment and buffer against direct impact between the substrate and mould, its removal during RIE can significantly impact the critical dimension achievable in NIL. This is due to the inevitable lateral etching which occurs during RIE. Thus, the residual layer thickness must be minimized uniformly across the imprinted area to ensure spatially uniform, accurate pattern transfer.

## 3.3. Metalorganic Chemical Vapour Deposition (MOCVD)

### 3.3.1. Background

Metalorganic chemical vapour deposition (MOCVD) is the key method for the epitaxial growth of III-nitrides or InGaN in this work. It is commonly referred to as organometallic vapour phase epitaxy (OMVPE) or other permutations of the same words e.g. MOVPE and OMCVD. In this thesis, the more generic and historical name of MOCVD is used. MOCVD is a method for the deposition of a condensed matter phase on a heated substrate via a chemical reaction utilizing metalorganic (MO)

precursors in the vapour phase. MOCVD was first reported in the scientific literature in 1968 by H. M. Manasevit [263], however, patents describing earlier variants of MOCVD clearly predates his report [264, 265]. MOCVD is capable of producing high purity, high quality material with atomically abrupt interfaces for device applications. It is a versatile technique and is suitable for large-scale production. Favorable economics in terms of high growth rates and high yield (uniformity and reproducibility) further enhance its attractiveness. Today, MOCVD is undoubtedly the preferred technique for the production of nearly all III-V and II-VI semiconductor compounds and devices, displacing other epitaxial growth techniques such as molecular beam epitaxy (MBE) and chemical beam epitaxy (CBE).

### 3.3.2. EMCORE/Veeco D125 MOCVD System

InGaN epitaxy was conducted in an EMCORE/Veeco D125 MOCVD system. Figure 3.2 shows a schematic diagram of the equipment. The layout may be divided into four main sections, namely, (1) the growth chamber/reactor where deposition takes place, and to which a loadlock is connected; (2) the gas handling system comprising the precursor, other gases sources, pipelines and manifolds; (3) the vacuum and exhaust system; and (4) the electronic/process control system.

**(1) The growth chamber** is a vertical geometry rotating disk reactor (RDR). Basically, this comprises a vertical tube into which the precursor gases are introduced from the top flange and directed perpendicularly down onto the sample placed on a horizontal, rapidly spinning circular susceptor. The top flow flange contains separate inlets for the alkyls and hydrides, each having several concentric input zones. The flow can be ratio-ed between the zones for tuning of uniformity over the deposition surface. Reactant gases are entrained in a shroud flow to facilitate laminar flow at the top of the growth chamber. This averts mixing of reactants prior to reaching the

growth surface and thus circumvents parasitic pre-reactions. The top flange, sidewalls and base regions are water-cooled to prevent overheating and parasitic reactions.

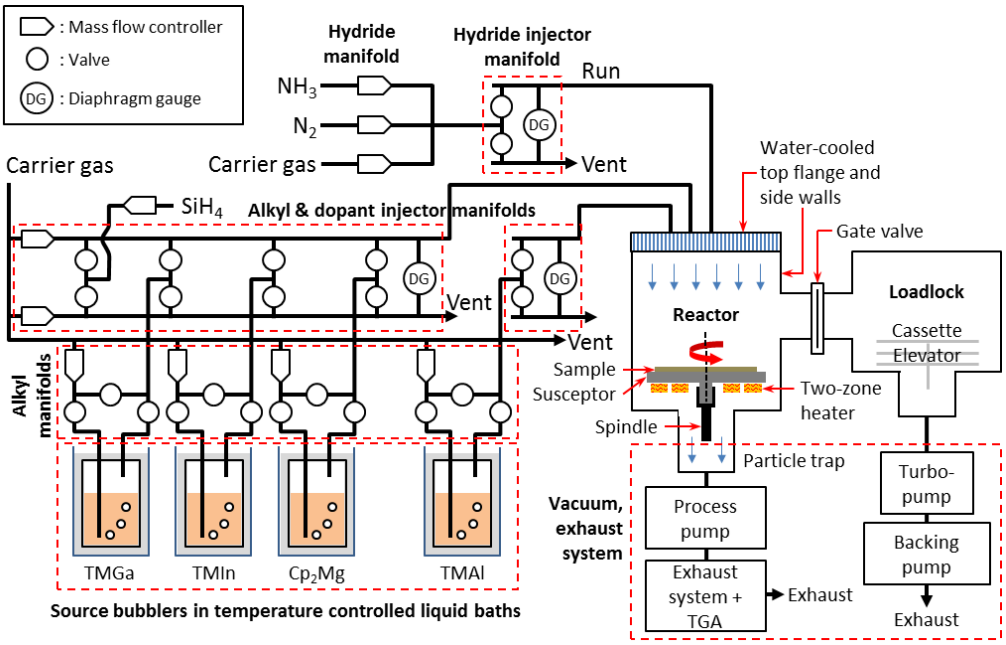


**Figure 3.2** Schematic diagram of the EMCORE/Veeco D125 MOCVD system.

The susceptor rests on a spindle which is driven to rotate by a toothed belt connected to a high speed motor. During growth, the rapidly rotating susceptor (up to 1000 rpm or more) create a pumping action that pulls the gases down and across the substrate. This assures a uniform boundary layer over a wide range of injection conditions. Along with the flow flange design, this leads to more uniform mass transport rate and reactant concentration, and hence more uniform composition, thickness and doping across the deposition area. The susceptor is heated by a two-zone resistive heating system, comprising an inner and outer zone heater. The temperature at each zone is measured by a thermocouple. This provides the reference signal to the proportional-integral-differential (PID) controlled DC low voltage power supply for controlling the heater temperature. Two pyrometers at the top of the growth chamber measure the surface temperatures of the inner and outer parts of the sample-susceptor ensemble since the thermocouples do not measure the temperature of the ensemble directly. A

loadlock, maintained at high vacuum by a turbopump, is used as an intermediary for transferring samples in/out of the reactor by a mechanical arm. This minimizes exposure of the reactor to the ambient. Contamination to the reactor by atmospheric oxygen and water vapour, and leakage of gases to the ambient is thus avoided.

**(2) The gas handling system** distributes, maintains, and controls the Group III, Group V and dopant precursors, and carrier/purge gases for growth. It comprises their sources, the respective source manifolds, the injector manifolds, and other pipelines, pressure gauges, valves, mass flow controllers (MFCs) for delivering the gases to the reactor. The Group III precursors employed in MOCVD growth of III-nitrides are the Group III alkyls or metalorganics (MO). Trimethylgallium (TMGa), trimethylindium (TMIn), and trimethylaluminum (TMAl) are used as the Group III sources of Ga, In, and Al respectively. The Group V precursor or hydride used is highly purified $NH_3$ (99.99994% purity). Bis-cyclopentadienyl-magnesium ($Cp_2Mg$) and silane (46.50 ppm $SiH_4$ in 99.9954% $H_2$) are used as the *p*-type and *n*-type dopant precursors, respectively. $H_2$ (99.999% purity and further purified by a palladium cell) and $N_2$ (99.9995% purity) are available as the carrier gases. For InGaN epitaxy, $N_2$ is typically used since $H_2$ causes InGaN etching. The carrier gases and hydride precursor are stored in pressurized gas cylinders and MFCs precisely control the flow rates (specified as standard cubic centimeters per min or sccm).

The MO sources (SAFC Hitech$^{TM}$) including $Cp_2Mg$ are stored in 3" diameter stainless steel cylinders called bubblers placed in temperature controlled liquid baths. Adduct grade sources are used to ensure that they are free of metallic impurities. The high reactivity of Al further requires TMAl to be of low oxygen grade. At the set temperatures of -10°C, 20°C, 30°C and 40°C, for TMGa, TMAl, TMIn and $Cp_2Mg$, respectively, TMGa (-15.8°C, 55.7°C) and TMAl (15.4°C, 127°C) are liquids, while

TMIn (88.4°C, 133.8°C) and $Cp_2Mg$ (176°C, 290°C) are solids. The temperatures in parentheses are the melting and boiling points respectively. The precursors are transported by flowing carrier gas into the inlet of the bubbler as seen in Figure 3.2. As the gas "bubbles" through the precursor reservoir it "carries" the precursor in vapour phase and exits the bubbler into the MOCVD gas lines. By controlling the flow rate of the carrier gas and the bubbler pressure $P_b$, through the system of mass flow controllers and valves, the molar flow rate may be controlled. It is important to note $P_b$ must be higher than the chamber growth pressure $P$ to avoid backflow. Relationships between the different quantities are as follows. The equilibrium vapour pressure of the precursor $P_{MO}$ is a function of the bubbler temperature $T_b$ and given by

$$\log_{10} P_{\mathrm{MO}}(\mathrm{Torr}) = A - \frac{B}{T_{\mathrm{b}}(\mathrm{K})} \tag{3-1}$$

where A and B are constants specified by the manufacturer and taken from Ref [266]. $P_{MO}$ may be converted to units of Pa by

$$P_{\mathrm{MO}}(\mathrm{Pa}) = P_{\mathrm{MO}}(\mathrm{Torr}) \times \frac{101325}{760} \tag{3-2}$$

The molar flow rate of the precursor $F_{MO}$ can be calculated by

$$F_{\mathrm{MO}}(\mathrm{mol/min}) = \frac{P_{\mathrm{std}} Q_{\mathrm{b}}}{10^6 \times R T_{\mathrm{std}}} \times \frac{P_{\mathrm{MO}}}{P_{\mathrm{b}} - P_{\mathrm{MO}}} \tag{3-3}$$

where $P_{std}$ and $T_{std}$ are the pressure and temperature at standard conditions taken as 101325 Pa and 273.15 K respectively, $R$ is the molar gas constant (= 8.314 J $mol^{-1}$ $K^{-1}$), $Q_b$ is the volume flow rate of the carrier gas into the bubbler in sccm, and $P_b$ is in Pa. Taking a set of TMIn growth conditions used in this work, where A = 10.52, B = 3014, and $T_b$ = 303.15 K, then $P_{TMIn}$ = 3.782 Torr or 504.2 Pa. For $Q_b$ = 120 sccm and $P_b$ = 400 Torr or 53329 Pa, $F_{MO}$ = 51.1 × $10^{-6}$ mol/min or 0.0511 mmol/min. Each source has an individual manifold for control. Further, there are three injector manifolds, one for the hydride and carrier gases, one for the alkyls and the dopants,

and one solely for TMAl to avoid parasitic reactions. The injector manifolds are integrated valve blocks (multiples of 2 port configurations) that provide switching of gases between the run mode (for delivery of gases to the reactor) and vent mode. By balancing the pressure (measured by a diaphragm gauge) between the run line and vent line, the injector manifold enables rapid switching of gases at stable flow rates.

**(3) The vacuum and exhaust system** is responsible for controlling the process chamber pressure, evacuation of the loadlock, and treatment of the exhaust before safe release to the environment. For the reactor, the main components are the vacuum system, the exhaust system, and the toxic gas adsorber (TGA). In the vacuum system, the reactor pressure is controlled by adjustment of a throttle valve via a closed loop with feedback from a Baratron pressure sensor. The rotary vane pump provides the necessary suction for continuous gas flow through the chamber. The role of the exhaust system is to trap all particles in the exhaust before it goes to the TGA. This is accomplished by filters and a particle trap situated under the reactor base. Within the TGA system, special activated charcoal granules adsorb all hydrides and metal-organics. In this way, the treated exhaust may be safely released to the environment.

**(4) System control** is executed by a real time programmable controller that controls all MFC flows, valves, heater power supplies, pressures and spindle rotation. The controller is interfaced with a computer for recipe input or entry of other parameters. The computer enables supervisory control of the system and also monitors all the safety systems. Recipes are entered in a spreadsheet format that specifies the reactants, pressures, growth temperature, duration, and flow rates.

Chemical reactions in MOCVD involve the decomposition of the input compounds using thermal energy. This is termed pyrolysis and may involve many intermediate

reactions. The actual reactions are influenced by reactor and growth conditions, such as reactor chamber geometry, temperature of susceptor and reactor wall, pressure, flow rates of precursors and carrier gases. They may be classified into homogeneous gas-phase reactions occurring between the same phases, and heterogeneous surface reactions occurring at the interface between different phases (e.g on solid surfaces). Reactions that limit the growth efficiency or form unwanted by-products (mainly in homogeneous reactions) are termed parasitic reactions. The growth process may be analyzed in terms of thermodynamics, kinetics and hydrodynamics.

### 3.3.3. Thermodynamics Consideration

In MOCVD, thermodynamics may be employed to predict whether a solid will form from the vapour phase, or the energetic feasibility of a proposed chemical reaction, under a given set of conditions by considering the reaction "driving force". Hence, for *a given set of conditions*, the *equilibrium* phase composition may be predicted. We consider the thermodynamic analysis by Koukitu et al. [267, 268] for the growth of InGaN which is the subject of this work. Near the vapour-solid interface, the MO precursors ($R_3In$ and $R_3Ga$, where R is an alkyl group, such as $CH_3$ or $C_2H_5$) are decomposed irreversibly according to the following homogeneous reactions.

$$R_3In\ (g) + 3/2\ H_2\ (g) \rightarrow In\ (g) + 3\ RH\ (g) \tag{3-4}$$

$$R_3Ga\ (g) + 3/2\ H_2\ (g) \rightarrow Ga\ (g) + 3\ RH\ (g) \tag{3-5}$$

The chemical reactions which proceed at the substrate surface to form $In_xGa_{1-x}N$ are

$$In\ (g) + NH_3\ (g) \rightleftharpoons InN\ (alloy) + 3/2\ H_2\ (g) \tag{3-6}$$

$$Ga\ (g) + NH_3\ (g) \rightleftharpoons GaN\ (alloy) + 3/2\ H_2\ (g) \tag{3-7}$$

where InN(alloy) and GaN(alloy) stand for the binary compounds in the ternary $In_xGa_{1-x}N$ alloy. Under complete *equilibrium* conditions, most of the $NH_3$ is expected to decompose into $N_2$ and $H_2$ at temperatures > 300°C. However, the decomposition

rate is slow without a catalyst, such that only a fraction  is decomposed even for the higher temperatures (~ 650°C to 800°C) used in this work. The equilibrium partial pressure and vapour-solid distribution relationship for different conditions in $In_xGa_{1-x}N$ growth have been calculated [267, 268]. It is found that three deposition modes exist: the growth regime, In droplet formation regime, and the etching regime. The results indicate high V/III ratios are required to obtain suitable deposition of InGaN and avoid In droplet formation. Thus, high V/III ratios (~ 9200) are typically used in this work to obtain InGaN growth.

### 3.3.4. Kinetics Considerations

Thermodynamic equilibrium concepts dictate the state of a system given very long times. However, MOCVD is not exactly an equilibrium process. An understanding of the kinetics is needed to elucidate the actual steps involved and describe the rates of the intermediate steps occurring between the initial and final equilibrium state. Even if a thermodynamic driving force for a reaction exists, the energy barrier of the overall reaction (which is linked to the intermediate states) needs to be overcome for it to actually happen. The rate constant $k$ is related to the energy barrier or activation free energy $\Delta G^*$, temperature $T$, and molar gas constant $R$ by

$$k = \exp(-\frac{\Delta G^*}{RT}) \tag{3-8}$$

MOCVD can be kinetically modeled with rate-limiting steps. The rates of these are functions of temperature, flow dynamics, pressure and substrate orientation. The typical rate-limiting steps during growth at various substrate temperatures $T$ are shown in Figure 3.3. At low T, the surface reaction is slow. The growth rate $R_g$ increases with increasing temperature and is influenced by substrate orientation. That is, it is surface-reaction limited. At higher $T$, $R_g$ becomes limited by the mass transfer of precursors through the boundary layer, with relative insensitivity to $T$ and substrate

orientation. When the surface reaction is fast enough, the vapour pressure on the surface approaches the equilibrium value and $R_g$ is determined by the partial pressure of precursors in the input gas stream near the boundary layer. Further increase in $T$ reduces the growth rate due to "parasitic" homogeneous reactions, increased reactor wall deposition, and desorption of atoms from the growth surface. That is, at high $T$, MOCVD is thermodynamically limited.

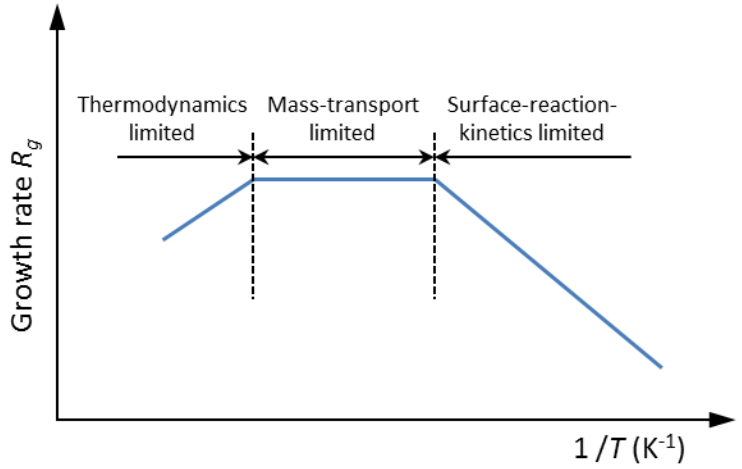


**Figure 3.3** Graphical representation showing the rate-limiting steps as a function of reciprocal temperature 1/$T$ during MOCVD.

### 3.3.5. Hydrodynamics and Mass Transport

Hydrodynamics and mass transport are closely related, and influence the transport of material to the growing solid-vapour interface. In an open-flow system for MOCVD, the following steps occur: (1) mass *transport* of input precursors by the flowing gas stream; (2) mass *transfer* (also called diffusion or mass "*transport*" type II) of precursors through the boundary layer near the substrate surface; (3) surface processes including adsorption of precursors and/or pyrolyzed precursors; (4) chemical reactions resulting in material growth; and (5) desorption of by-products from the surface. It is important to note that in some literature, the mass "*transfer*" step is also referred to as a mass "*transport*" step. There, "diffusion-limited" and

"mass-transport-limited" are used synonymously to describe the mass transfer step. However, this does not refer to mass transport by a flowing gas stream.

Hydrodynamics depend strongly on the reactor configuration and total system pressure $P$. At very low $P$ (< 7.5 Torr), $R_g$ is entirely kinetically controlled, even at relatively high $T$, such that $R_g$ is virtually independent of $P$. In fact, at lower $P$ (< 0.075 Torr), molecules can travel from the source to the substrate without interacting with other molecules. This is known as the molecular flow regime. For $P$ > 7.5 Torr (in most MOCVD systems, such as that used in this work) the growth process is in a viscous-flow regime and $R_g$ is influenced by mass transfer.

## 3.4. Characterization Techniques

### 3.4.1. Scanning Electron Microscopy (SEM)

The small size of the nanostructures (down to a few nm) fabricated in this work necessitates the use of a scanning electron microscope (SEM) for rapid topography measurement. Light microscopes utilizing visible light (wavelength 400 - 700 nm) are unable to resolve feature sizes less than ~ 200 nm due to the diffraction limit. SEM provides improved depth of field, higher magnification, analytical capabilities and image processing benefits. Lateral resolutions of 1 – 5 nm (with a field emission source) and depth resolutions of 1 – 10 nm (using secondary electrons signals) are achievable. The two main components of an SEM are the electron column and the control console. The electron column comprises an electron gun, electron lenses, apertures, and scan coils which affect the electron path down the evacuated column (pressures ~ $10^{-4}$ Pa), specimen stage and detector. The control console consists of displays, electronics, and computers that control the electron beam and are involved in image/data acquisition [269]. See Figure 3.4 for a schematic drawing of a SEM.

The electron gun provides a stable source of electrons and accelerates them to an adjustable energy range of 0.1 – 30 keV. The electron lenses focuses the electron beam to a small spot size (< 10 nm) on the specimen, thus enabling the generation of a sharp image. A deflection system, consisting of a scan generator and two pairs of electromagnetic scan coils, sweeps the electron beam over the specimen surface in a raster scan pattern. As the electron beam interacts with the specimen, signals are collected for image formation. Contrast in an image arises from spatial variation in the signal collected from beam-specimen interaction. The electronics of the detector system converts the signals to point-by-point intensity changes for image formation.

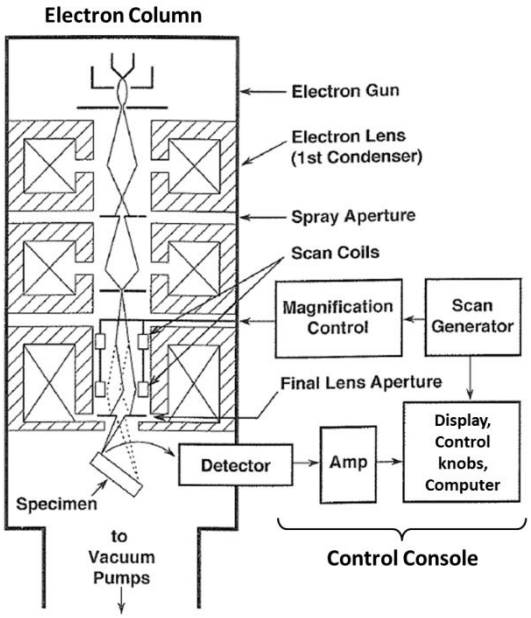


**Figure 3.4** Schematic showing the components of a scanning electron microscope [269].

The most common signal used to produce SEM topographic images is that formed by secondary electrons (SE). SE are principally liberated due to the interaction of the energetic beam electrons and weakly bound conduction band electrons in metals or outer shell valence electrons in insulators and semiconductors. One of their defining characteristics is the very low kinetic energies (peaking in the range of 2 – 5 eV) which dictate a shallow escape depth. SE generated directly by the incoming beam of

electrons constitutes a high-resolution signal since the lateral spatial resolution of the focused beam and the shallow sampling depth of the SE are preserved.

Electrostatic charging arises when electrons injected into a specimen are not effectively conducted to ground and accumulate, thus developing a highly negative electrical charge. This is a common problem when imaging insulating or poorly conducting specimens (e.g. the $SiN_y$ templates fabricated in this work) and manifests as unexpected brightening/darkening or distortion in images generated from SE. SE are vulnerable due to their low kinetic energies. Deposition of a thin layer of conductive material, e.g. ~ 10 nm of gold, on the specimen with good mounting and grounding can alleviate the problem.

Machining errors, non-uniformities or asymmetry in the electron lenses, and unclean apertures may lead to astigmatic or non-perfectly cylindrical lenses. The astigmatism blurs the image. This may be corrected by a stigmator which applies a weak supplement magnetic field to make the lens appear "symmetric" to the electron beam. The *x*- and *y*-stigmator controls and the focus control are adjusted alternately at high magnification to achieve the sharpest image allowable at which point the beam cross-section is at its minimum. In this work, images are acquired by either a JOEL JSM 6700F or a Nova NanoSEM 230. Both employ field emission type electron guns (specifically, a cold field emitter and a Schottky field emitter respectively), thus, the term, field emission SEM (FESEM). These offer higher brightness, longer lifetime and lower energy spread than older electron sources. Excellent lateral resolutions of 1 – 5 nm are achievable compared to 10 – 50 nm for conventional electron sources.

### 3.4.2. Atomic Force Microscopy (AFM)

Atomic force microscopy (AFM) is a technique that allows visualization and measurement of the surface topography in three-dimensional (3D) detail down to the nanometer scale. Unlike conventional methods of imaging which utilize a wave (e.g. light or electrons) and perceive the surface morphology by line-of-sight reflections and shadows, AFM measures surface height at each point on a surface by "feeling" with a sharp solid probe or tip (attached to the end of a cantilever) that is raster scanned over the surface. Excellent height resolution (sub-nm range) and lateral resolution (~ 1 nm) or better is achievable. As the image is constructed from spatial height values, various metrics of topography can be derived, such as standard deviation of height, root-mean-square (RMS) roughness, and slopes. The latter is used for the identification of crystal facets of InGaN nanostructures in this work. An AFM consists of several key components, namely, a *x*-*y*-*z* scanner, a piezo stack, a cantilever with a tip at one end, a laser beam directed at this end, a photo-diode detector which picks up the reflected signal from the cantilever, a specimen stage, detector electronics, controller electronics and computer as illustrated in Figure 3.5.

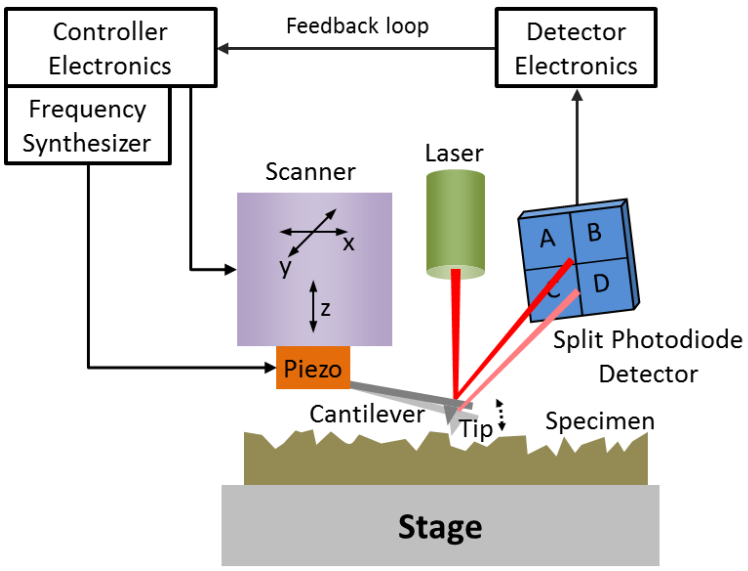


**Figure 3.5** Schematic drawing of an atomic force microscope showing its general operation.

AFM can be operated in one of three ways, namely, contact mode, non-contact mode and tapping mode. As contact occurs only gently and briefly in tapping mode, tip and specimen damage is minimized. Hence, it is employed in this work, in a Bruker Dimension Icon® Atomic Force Microscope. Topography is measured by monitoring the cantilever's oscillation amplitude as the tip is scanned across the specimen surface. The piezo stack excites the cantilever to vibrate vertically with a constant sinusoidal "free" amplitude at or below its fundamental resonant frequency. When the tip interacts with the surface, the amplitude decreases and is detected by the split photodiode detector via the laser beam reflected off the cantilever. The feedback loop (encompassing the detector electronics and controller electronics) maintains a constant damped oscillation amplitude (typically 20 – 100 nm) by vertically moving the scanner at each (x, y) data point to maintain a constant "setpoint" amplitude. By keeping a constant oscillation amplitude, a constant tip-sample interaction is maintained [270]. The motion information is then utilized for image construction.

While AFM can provide detailed high-resolution 3D information of a surface's topography without an evacuated environment, and the capability for data processing and analysis, AFM image acquisition is slow. Typically, a few minutes to a few tens of minutes is required depending on the scan area and rate. The measurement range is typically limited to several micrometers vertically and several tens of micrometers laterally [271].Unlike SEM, where the probing electron beam can be rapidly deflected and raster scanned over relatively large areas of the specimen surface, the raster scan speed of the AFM tip is kept low to ensure accurate surface tracking with minimal loss of topography information. Hence, AFM is best suited for characterizing small areas where detailed topography information is needed. In this work, 1 μm × 1 μm scan areas with a scan rate of 0.80 Hz is employed for reliable surface measurement. Due to the physical contact that inevitably occurs between the tip and surface during

scans, blunting or contamination of the tip with debris may occur. This may lead to a loss of resolution, distorted imaging or generation of artefacts in the acquired image. A replacement of tip is indicated in such cases. Secure sample mounting and vibration isolation stages are also necessary to avoid external or environmental noise introduction. Ultimately, resolution and accuracy is limited by the tip sharpness.

### 3.4.3. Transmission Electron Microscopy (TEM)

Transmission electron microscopy (TEM), like SEM, employs an electron beam to produce magnified images of a specimen. However, it differs from SEM in that TEM images are constructed from transmitted electrons, rather than secondary or backscattered electrons. A pre-requisite for the transmission of electrons is that the specimen has to be made extremely thin or "electron-transparent" such that electrons can be transmitted through rather than scattered or absorbed by the specimen. The nature of specimen preparation and imaging thus allows the ultrastructure of the specimen to be observed. In fact, modern TEMs which possess resolution ~ 0.2 nm or better are able to image individual atomic planes or columns of atoms. The technique can also be used to produce electron diffraction patterns for analyzing the properties of crystalline specimens, such as epitaxial relationships and crystal structure. In addition, defects may also be imaged in TEM. These capabilities are particularly suited for characterizing epitaxially grown III-nitride structures in this work.

A transmission electron microscope may be divided into three sections, namely the illumination system, the specimen stage and the imaging system as illustrated in Figure 3.6. The illumination system consists of an electron gun, two or more condenser lenses and apertures that focus the electrons onto the specimen. The specimen stage secures the specimen, allows it to be moved, inserted or withdrawn. The imaging system comprises at least three lenses and various apertures that allow

diffraction patterns (DP) or highly magnified images of the specimen to be produced on a fluorescent screen or detector of an electronic camera system [272].

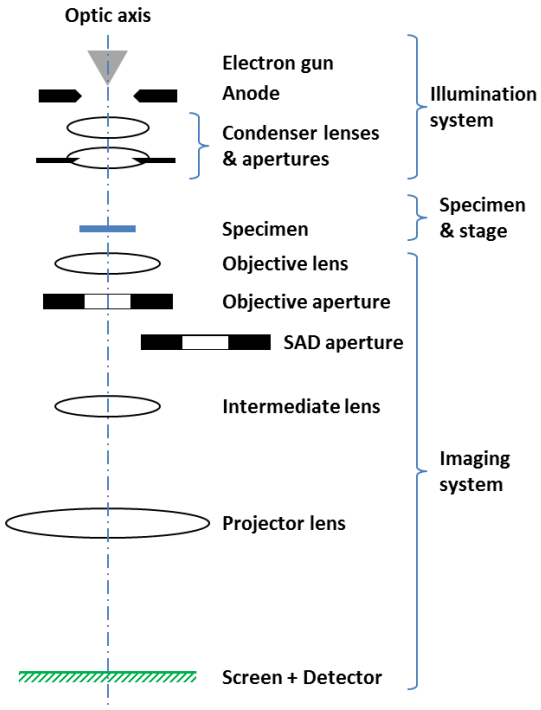


**Figure 3.6** Schematic drawing of a transmission electron microscope in which the objective aperture is inserted and SAD aperture is withdrawn for imaging.

In the diffraction mode, the objective aperture is removed while the selective area diffraction (SAD) aperture is inserted. The different positions of these apertures relative to the TEM optics enable their respective modes and functions to be fulfilled. The DP provides information on the crystallinity (crystalline or amorphous, monocrystalline or polycrystalline), crystallographic characteristics (lattice parameter, symmetry), phase and orientation of the specimen. The SAD pattern of an InGaN film is given in Figure 5.11(c). The well-defined diffraction spots indicate that it is monocrystalline and the pattern indicates its hexagonal close packed lattice structure. In the imaging mode, the objective aperture is inserted while the SAD aperture is withdrawn. Two types of imaging can be achieved, bright field (BF) imaging and dark field (DF) imaging. In BF imaging, the objective aperture is centered on the

direct beam and is the standard imaging mode of TEM. Here, weakly diffracting regions appear bright while strongly diffracting regions appear dark. In dark field imaging, the objective aperture is centered on a diffracted beam such that weakly diffracting regions appear dark and regions strongly diffracting into the selected diffracted beam appear bright [273].

"Weak-beam (WB) microscopy" is a technique in TEM which allows formation of diffraction-contrast images in BF and DF for imaging defects. The WBDF approach is commonly used as it gives stronger contrast (white lines on a dark gray background). The specimen is tilted to a so-called two-beam condition, in which the intensity of the selected diffracted beam is enhanced (but remains weaker than the direct beam). If a defect is present, this allows the diffracting planes to be bent locally back into the Bragg-diffracting orientation and provide stronger contrast in the image. When the corresponding diffraction pattern is viewed on the screen, the vector from the direct beam spot to the diffracted beam spot is known as the **g** vector. For contrast of a defect with Burgers vector **b** to be detectable, $\mathbf{g} \cdot \mathbf{b}$ should be greater than 1/3. This criterion is useful for imaging TDs in cross-sectional TEM specimens [274]. Screw and mixed TDs in III-nitrides have **b** = [0001] and **b** = 1/3<11$\underline{2}$3> respectively, and can be imaged in the two-beam condition with **g** = 0002 under the [2$\underline{11}$0] or [01$\underline{1}$0] zone axis. Figure 5.11(a) and (b) respectively show the BF and WBDF images of an InGaN film allowing TDs with screw character to be visualized. For the two-beam condition with **g** = 01$\underline{1}$0 (under the [2$\underline{11}$0] zone axis) or **g** = $\underline{2}$110 (under the [01$\underline{1}$0] zone axis), edge TDs (with **b** = 1/3[11$\underline{2}$0]) and mixed TDs (with **b** = 1/3<11$\underline{2}$3>) can be imaged. In this work, a JEOL JEM-2100 transmission electron microscope operated at an accelerating voltage of 200 keV was used.

### 3.4.4. X-ray Diffraction (XRD)

X-ray diffraction (XRD) is a characterization technique used to find the thickness, lattice parameters, strain, composition and defect densities or quality of crystalline layers. Its non-destructive nature and fast analysis have endeared it to III-nitrides characterization. XRD employs X-rays to probe a crystalline sample. For epitaxially grown single crystalline III-nitrides, a high-resolution XRD setup using a four-circle diffractometer is typically employed. X-rays generated by bombarding a Cu target (Cu $K_{\alpha 1}$, $\lambda$ = 1.540598Å) with electrons in an evacuated tube is passed through a monochromator to select for monochromatic X-rays and directed at the specimen. The specimen is mounted on a stage at the center of the diffractometer. The configuration permits relative rotation of the sample and detector such that a large number of (*hkl*) or reflections can be individually accessed. Detection of the reflections is based on constructive interference and elegantly described by Bragg's law as shown in Equation (3-9).

$$n\lambda = 2d \sin \theta \tag{3-9}$$

Equation (3-9) relates the spacing *d* between the atomic planes from which diffraction is occurring with $\theta$ as the angle between the incident X-ray and atomic planes. $\lambda$ is the wavelength of the X-ray and *n* is an integer taken as unity in XRD. In a double-axis setup, "reflected" X-rays are screened just by a slit as seen in Figure 3.7. This setup is usually used due to its higher intensity, simpler and faster operation [275].

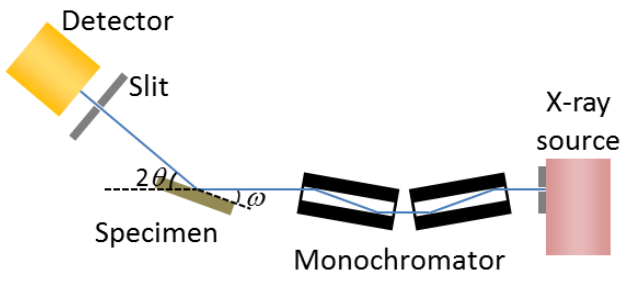


**Figure 3.7** Schematic drawing of a double-axis high-resolution X-ray diffractometer.

When the "reflected" X-rays are collimated by an optical element (analyzer crystal), finer features and details can be resolved, and the configuration is termed triple-axis. While crystal planes exist in *real* space, each set of crystal planes produces a diffraction spot corresponding to a *reciprocal lattice point* (RLP) in *reciprocal* space. The reciprocal space concept aids in the analysis and interpretation of results. Directions remain the same in both real and reciprocal space but distances are inverted. It is helpful to visualize the reciprocal lattice as being 'stuck' to the crystal, such that the when the crystal moves relative to the incident X-ray beam, so does the reciprocal lattice. A section through the reciprocal space for a [0001]-oriented III-nitride crystal is shown in Figure 3.8. The definition of angles ($\omega$, $\chi$, $\phi$, $2\theta$) in a four-circle diffractometer is shown in Figure 3.9.

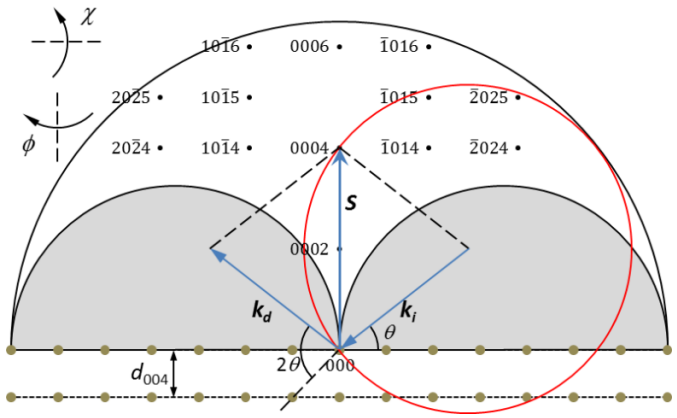


**Figure 3.8** Section through reciprocal space for a [0001]-oriented III-nitride layer.

$\boldsymbol{k_i}$ and $\boldsymbol{k_d}$ are the incident and diffracted beam vectors respectively. The scattering vector $\boldsymbol{S}$ is given by $\boldsymbol{k_d}$ - $\boldsymbol{k_i}$. The magnitude of $\boldsymbol{k_d} = \boldsymbol{k_i} = 1/\lambda$. The Ewald sphere is shown in Figure 3.8 as the red full circle intersecting the origin and the RLP of 0004. Diffraction occurs when the sphere intersects a RLP. The outer limit of the reciprocal lattice space that can be accessed by $\boldsymbol{S}$ for a given X-ray wavelength in the symmetric ($\theta = \omega$) and asymmetric configuration ($\theta \neq \omega$) is outlined by the large semicircle.

Regions blocked by the incoming or outgoing beams are inaccessible and are shaded. However, these may still be accessed in a skew symmetric configuration by rotating the specimen 90° about $\phi$ and tilting the sample about $\chi$ (Figure 3.9) since the shaded semicircular regions remain fixed in the plane containing $\boldsymbol{k_i}$ and $\boldsymbol{k_d}$. This configuration is used to access RLPs blocked in the asymmetric configuration such as that associated with the (20.1) and (10.2) set of planes mentioned in Section 6.5.2.2.

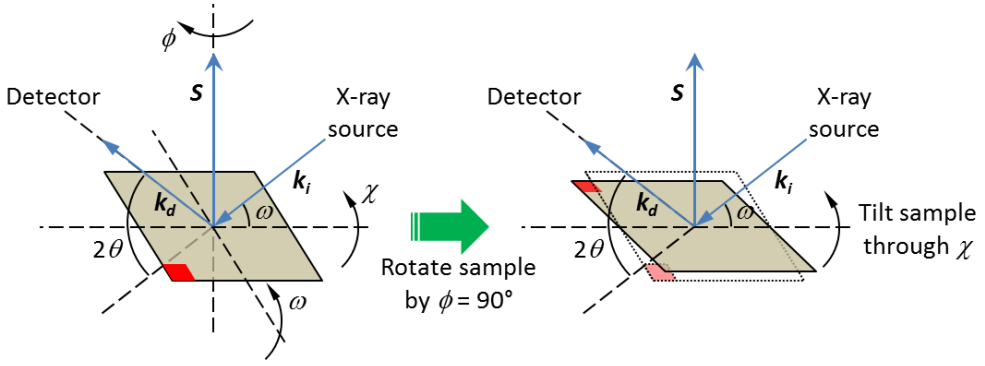


**Figure 3.9** Schematic showing a sample in a symmetric configuration in a four-circle XRD diffractometer along with the four axes of rotation ($\omega$, $\chi$, $\phi$, $2\theta$) (left). To access the reciprocal space in the forbidden region, a skew symmetric configuration may be used and is achieved by rotating the sample by 90° about the $\phi$-axis and tilting the sample about the $\chi$-axis (right).

For a hexagonal system, the interplanar spacing $d_{hkl}$ for the ($hkl$) or corresponding ($hkil$) set of planes is related to the $a$ and $c$ lattice parameters by:

$$\frac{1}{d_{hkl}^2} = \frac{4}{3}\frac{h^2 + k^2 + hk}{a^2} + \frac{l^2}{c^2} \tag{3-10}$$

To determine the lattice parameters of an epilayer, at least two $d_{hkl}$ measurements are required. Usually, one symmetric reflection (giving $d_{0002}$ or $d_{0004}$) to find $c$, and one off-axis (asymmetric or skew symmetric) reflection (typically $d_{10\underline{1}5}$) are used. As an example, from the (0002) $2\theta$-$\omega$ spectrum of the InGaN film grown at 795°C in Figure 5.3, $2\theta_{002}$ = 34.452°. Using Equation (3-9) gives $d_{002}$ = 2.6011 Å. Further, using Equation (3-10) gives $c$ = 5.2022 Å. Similarly, for $2\theta_{105}$ = 104.499°, $d_{105}$ = 0.97422 Å. This gives $a$ = 3.2042 Å. In this work, InGaN is directly grown on AlN/Si(111)

substrates. Due to the large mismatch in thermal expansion and lattice constants between InGaN and the substrate, the InGaN layer is likely in a partially strained state. Estimation of the In content $x$ in $In_xGa_{1-x}N$ thus requires the prior determination of both $a$ and $c$ lattice parameters as described above. The strain and composition are then determined together, iteratively, in accordance to ref. [104], by taking into account that in a hexagonal system under simple biaxial strain, the out-of-plane strain is related to the in-plane strain by:

$$\frac{c - c_0}{c_0} = -\frac{2\upsilon}{1 - \upsilon}\left(\frac{a - a_0}{a_0}\right) \tag{3-11}$$

where $\nu$ is the composition-dependent Poisson's ratio, and $a_0$ and $c_0$ are the fully relaxed lattice parameters. An initial estimate of $x$ is first made, and $\nu$, $a_0$ and $c_0$ are obtained by linear interpolation and Vegard's Law calculations from GaN and InN reference values obtained from ref [276-278]. The values are inserted into the left-hand-side (LHS) and right-hand-side (RHS) of Equation (3-11). The computed LHS and RHS values are compared and adjustment to $x$ is made (with updates to $\nu$, $a_0$ and $c_0$) to reduce the difference between the LHS and RHS values. The process continues iteratively until the difference is acceptably small (< 0.01%). For the prior example with $c$ = 5.2022 Å and $a$ = 3.2042 Å, an In content $x$ = 0.037 is calculated.

The XRD characterization of III-nitrides frequently employs $\omega$-scans, $2\theta$-$\omega$ scans, and $\phi$-scans. In $\omega$-scans (or rocking curve scans) both the X-ray source and detector remain stationary as the sample is "rocked" or rotated about the $\omega$-axis. This corresponds to the scattering vector $\boldsymbol{S}$ shown in Figure 3.8 tracing out an arc centered on the origin in reciprocal space. The length of $\boldsymbol{S}$ remains constant but its direction changes. The scan probes the broadening of diffraction spots in reciprocal space which may arise from microstructural defects. This manifests as a broadening of the full-width-at-half-maximum (FWHM) of the rocking curve. For instance, the FWHM

of 000*l* $\omega$-scans provides an indication of lattice tilt. Figure 3.10 shows a typical (0002) $\omega$-scan of an InGaN film grown on AlN(0001)/Si(111). In simple thin films, as tilt is associated with screw and mixed TDs, it is possible to estimate the densities of these TDs [279-281]. Pure edge dislocations have **b** within the (000*l*) planes, and hence do not distort these planes and contribute to tilt. Indication of lattice twist may be provided by the FWHM of skew symmetric $\omega$-scans with high inclination angles $\chi$ (e.g. the (20.1) reflection). In simple thin films, since twist is associated with edge and mixed TDs, the densities of these TDs may similarly be estimated from the FWHM values [279-281].

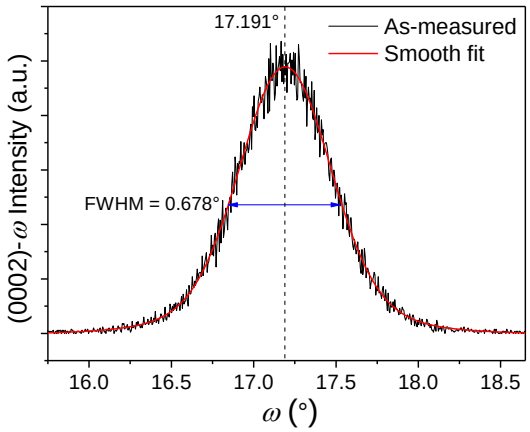


**Figure 3.10** (0002) $\omega$-scan of an InGaN film grown on AlN(0001)/Si(111) at 795°C and 300 Torr. The FWHM is an indication of lattice tilt.

Higher tilt may be measured for material grown with TD reduction techniques such as two-step epitaxial lateral overgrowth (ELO) [282], pendeoepitaxy [154], and deliberate island formation. Hence, caution should be employed in the analysis of TD densities obtained from tilt measurements in these cases. This is due to the bending of edge TDs away from the [0001] direction. The tilt appears higher while the twist remains the same. Mathematically, the invisibility criterion $\mathbf{g} \cdot (\mathbf{b} \times \mathbf{u})$ is used to ascertain the influence of inclined or bent TDs. Here, **g** is the 000*l* reflection, **b** is the Burgers vector and **u** is the TD line direction. If $\mathbf{g} \cdot (\mathbf{b} \times \mathbf{u}) \neq 0$, then the TD will

affect the 000*l* $\omega$-scan, as is the case for edge TD with **b** = 1/3[11$\underline{2}$0] inclined away from the [0001] direction. Hence, comparison of structural characteristics between InGaN thin films and nanopyramids grown in this work (see Figure 6.4) is based on FWHM values of $\omega$-scans rather than TD densities estimated from $\omega$-scans.

In $2\theta$-$\omega$ scans, the sample is rotated about the $\omega$-axis and the detector is rotated about the $2\theta$-axis with an angular ratio of 1:2. The length of ***S*** changes but its direction stays constant. As the III-nitrides grown in this work are [0001]- or *c*-oriented, $2\theta$-$\omega$ scans may be used in phase composition analysis. This is because different III-nitride members have different lattice constants and hence manifest as peaks occupying different $2\theta$ positions. For InGaN, peaks broadening may arise from alloying and inhomogeneous strain [283]. Further, the presence of a few InGaN peaks may indicate phase separation. In droplet peaks may also be present as seen in Figure 6.2.

Azimuthal $\phi$-scan of either the skew symmetric and asymmetric reflections over 360° may be used to establish the epitaxial relationships between the III-nitrides and the underlying substrates. For instance, the six-fold in-plane symmetry of the III-nitrides presents six periodic peaks in the (10.5)-$\phi$-scan while the three-fold in-plane symmetry of on-axis Si(111) substrates presents three periodic peaks in the (11$\underline{1}$)-$\phi$-scan. The relative positions of the periodic peaks between the two scans may be used to rapidly determine the epitaxial relationship of the two layers non-destructively. For example, the coincidence of the III-nitride peaks and Si peaks in the skew symmetric scans as seen in Figure 5.14 allow an epitaxial relationship of InGaN(0001) [2$\underline{1}\underline{1}$0] || AlN(0001) [2$\underline{1}\underline{1}$0] || Si(111) [01$\underline{1}$] to be established in accordance to Figure 2.3(a).

In this work, high-resolution X-ray diffraction (HR-XRD) was performed in PANalytical X'Pert Pro-MRD X-ray diffractometers utilizing the Cu $K_{\alpha 1}$ line with a wavelength of 1.540598Å in double-axis or triple-axis configuration.

### 3.4.5. Photoluminescence (PL) Spectroscopy

Photoluminescence (PL) spectroscopy is a non-destructive optical characterization technique that may be used to study the quality of semiconductor materials and elucidate the physics accompanying radiative recombination. It may be used to characterize band edge luminescence, optically active impurities and defects which give rise to radiative transitions in semiconductors. PL refers to the emission of light or photons when a semiconductor material is optically excited by an external light source. The excitation leads to a non-equilibrium distribution of electrons and holes, or excitons which may recombine radiatively. Figure 3.11 shows several possible radiative recombination mechanisms.

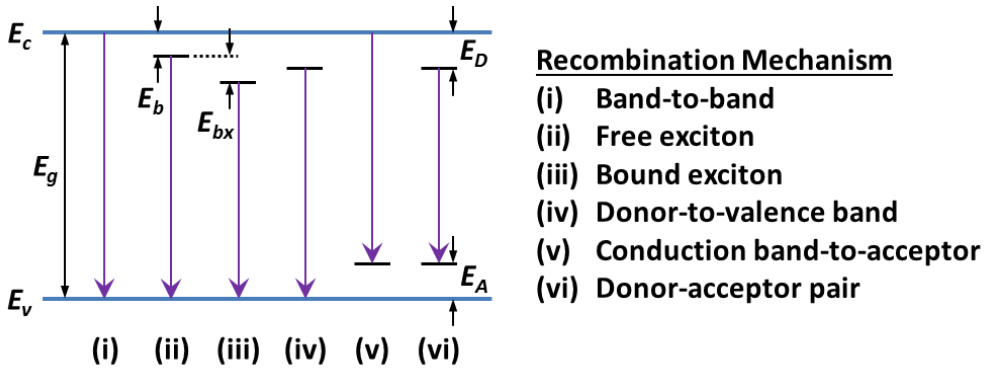


**Figure 3.11** Illustration of some possible radiative recombination routes in photoluminescence.

The above recombination pathways give rise to various features in the PL spectra such as peaks and shoulders. Their identification typically involves the use of complementary information obtained from other characterization techniques such as deep-level transient spectroscopy, Hall measurement and secondary ion mass

spectroscopy to characterize and quantify optically active defects or dopants in the semiconductor. Non-radiative recombination centers arising from structural defects such as dislocations, or impurity incorporation will also affect the PL line shape by competing with radiative recombination routes. Further, a PL spectrum may also be complicated by Fabry-Perot interference effects and phonon replicas which manifests as periodic peaks. Thus, prior information on the layer structure and background of the material is warranted. For $In_xGa_{1-x}N$, because the ternary alloy continuously spans a range of compositions (from $x = 1$ to $x = 0$), and hence bandgaps (from 0.7 eV to 3.4 eV), identification of the optically active defects and impurity states for all compositions is difficult, and information remains rare. Moreover, identification may be obscured by phase inhomogeneities which give rise to additional secondary peaks or In clustering which cause a red-shift in the emission. Thus, analysis of InGaN PL lineshapes is challenging.

More comprehensive spectroscopic information can be obtained by performing PL spectroscopy at low temperatures. This minimizes thermally activated non-radiative recombination processes and thermal line broadening. A microscopic defect such as that due to dislocations or impurity can induce a deformation of the band structure such as that illustrated in Figure 3.12. The deformations may be due to local trapped charges, local strain or composition fluctuations and generate a barrier of height $E_A$ around the recombination center. Only carriers with sufficient energy to overcome the barrier can recombine thus explaining the thermal activation of non-radiative transitions [284].

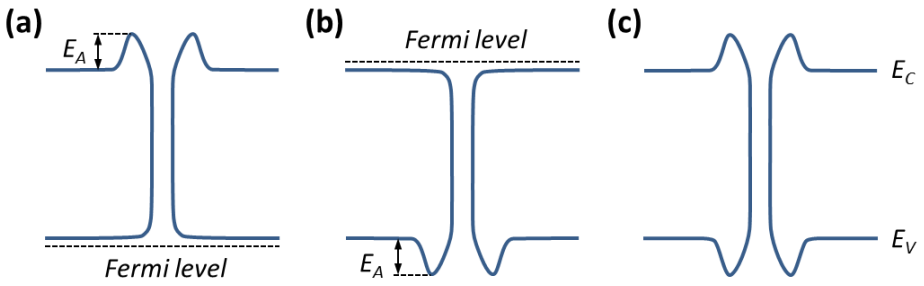


**Figure 3.12** Band structure of thermally activated non-radiative recombination centers showing the energetic barrier surrounding it. Band deformations of (a) and (b) may be due to local trapped charges, while that of (c) may arise from local strains.

The thermal quenching of PL intensity $I$ can be modeled by the following Arrhenius equation with a variable number of thermally activated non-radiative recombination channels, each associated with an activation energy $E_A$ [285-288].

$$I = \frac{I_0}{1 + \sum_i C_i \exp\left(\frac{-E_{Ai}}{k_B T}\right)} \tag{3-12}$$

where $I_0$ is the PL intensity at low temperature, $C_i$ is the constant relating to the strength of the $i^{th}$ non-radiative recombination channel, $E_{Ai}$ is the corresponding activation energy, $k_B$ is the Boltzmann's constant and $T$ is the temperature.

In this work, μ-PL measurements were carried out in a Renishaw Ramascope 2000 setup using a Kimmon 325 nm He-Cd laser tube (101 mW continuous wave) as the excitation source. The setup is integrated with a microscope (see Figure 3.13) for measurement of micron-scale areas, hence the term μ-PL. Raman spectroscopy may also be performed on the same equipment. The beam from the laser tube is first attenuated with neutral density filters if needed, after which it is passed through a plasma filter (to remove the background plasma and secondary emissions), conditioned and directed onto the sample in the microscope. The latter also allows viewing and selection of the area to be characterized. Emission from the sample is directed and conditioned via a series of optical components (which also filters off the

laser source emission) into a monochromator. The monochromator employs a diffraction grating and prism mirror to scan through the wavelength components of the emission which is detected by a CCD camera. A laser spot with diameter ~ 40 μm is used, with a probe depth ~ 100 nm (for an absorption coefficient of $10^5$ $cm^{-1}$). Low-temperature measurements from 20 to 300K, when performed, employs a cryostat operating on a CTI-Cryogenics closed cycle He refrigeration setup.

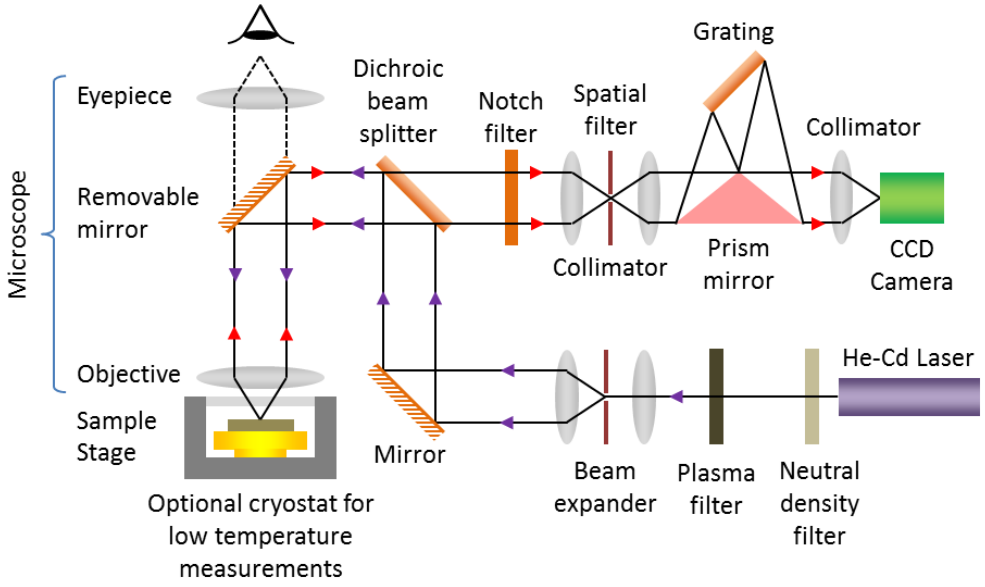


**Figure 3.13** Schematic drawing of the setup used for micro-photoluminescence spectroscopy. A cryostat may be used to cool the sample for low temperature μ-PL measurement.

### 3.4.6. Reflectance Spectroscopy

Incident light arriving at a surface of a medium may be reflected from or transmitted into it. Of the transmitted light, some of it may be absorbed, or scattered (e.g. through Raman scattering, Brillouin scattering, etc.) while the rest passes through the medium. Part of the absorbed electromagnetic waves may be dissipated as heat or re-emitted at a different frequency as photoluminescence. Reflectance spectroscopy is the investigation of the spectral intensity and composition of radiation reflected from a surface with respect to that of the incident radiation and their angular dependences [289]. In optical surface engineering and surface texturing schemes to reduce

reflection losses and promote light coupling into a material (e.g. semiconductor for photovoltaic applications), reflectance spectroscopy provides a quantitative measure of the anti-reflection and light admission capabilities of the surface. In this work, normal reflectance measurements were made in a CRAIC QDI 2010 UV-Visible-NIR range micro-spectrophotometer. The setup is illustrated in Figure 3.14.

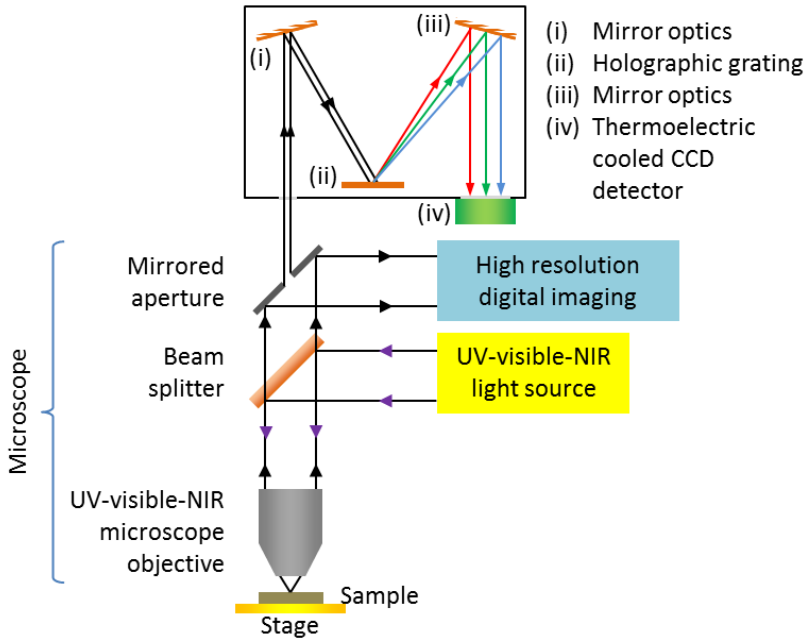


**Figure 3.14** Schematic drawing of the setup used for normal reflectance measurement.

White light from a UV-visible-NIR illumination source (Xe lamp) is directed via a series of optical components in the microscope and focused onto the sample via the microscope objective. Depending on the material properties and structure, the sample absorbs or reflects some wavelengths of light better than others. Reflected light is collected by the objective and focused onto the mirrored entrance aperture of the spectrophotometer. Since the aperture is mirrored, majority of the light is reflected into a digital imaging system. This allows the observation of the aperture being overlain on the sample such that the sampling area can be easily selected via movement of the sample stage. Light that passes through the aperture enters the

spectrophotometer and is dispersed into its component wavelengths by an optical grating. The intensity as a function of wavelength is measured by a thermoelectric (TE) cooled charge coupled device (CCD) detector and processed by the computer into a reflectance spectrum. The setup may also be configured for measurement of absorbance, transmittance and emission (such as fluoresence) spectra of sub-micron sized samples.

Operation of the equipment for reflectance measurement is straightforward. A dark scan is first performed to measure the dark counts of the system. Then, the spectrum from a reference material (in this case, an aluminum standard mirror) is acquired. The reference spectrum contains the spectral characteristics of the reference material, the light source, the optics and the CCD. The spectrum from the sample of interest is then collected and an algorithm applied to calculate the reflectance spectrum taking the illumination conditions into consideration.

## 3.5. Chapter Summary

In this Chapter, the main experimental methods employed in this thesis have been discussed. For nanopatterning, S-FIL$^{TM}$ was employed, while for III-nitride growth, MOCVD was used. Sample characterization involved SEM, AFM, XRD, TEM, reflectance and photoluminescence spectroscopy. The basic theory, operating principles and precautions taken for these methods were presented. This will facilitate good understanding of the techniques so that results can be reliably obtained and correctly interpreted.

# Chapter 4 Nanopatterning Techniques on Si Substrates

## 4.1. Introduction

This Chapter describes some nanopatterning techniques developed to realize the nano-scale selective area growth mask for Scheme A and the nanopillar substrates for Scheme B as introduced in Sections 1.2.4.1 and 1.2.4.2 respectively. The techniques combine wafer-scale Step and Flash Nanoimprint Lithography (S-FIL) with some pattern transfer methods to alleviate certain shortcomings of S-FIL and provide greater flexibility to the nanopatterning process. The imprinted features for Scheme A are nanopores while that of Scheme B are nanopillars/nanostuds. Examples of these are shown in Figure 4.1(a) and (b) respectively.

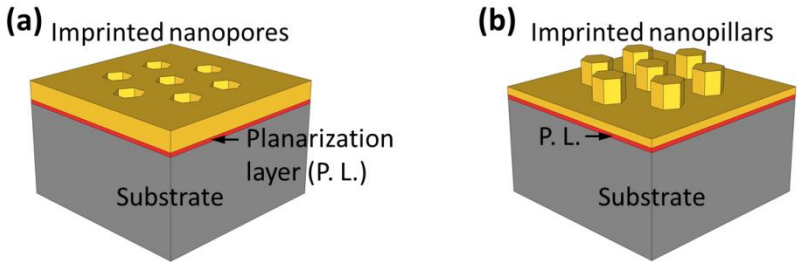


**Figure 4.1** Schematic showing the two categories of patterns formed in S-FIL, namely (a) nanopores which are used in Scheme A, and (b) nanopillars which are used in Scheme B.

## 4.2. Fabrication of Nano-SAG Masks on Si Substrates (Scheme A)

The basic fabrication process of nano-SAG dielectric masks on Si substrates for Type A templates using S-FIL is shown in Figure 4.2. Essentially, the Si substrate (with the buffer and/or device structure) is deposited with a dielectric layer, e.g. $SiN_y$ or $SiO_2$. S-FIL is then performed as described in Section 3.2.2 to form S-FIL patterns. These are transferred to the underlying dielectric via $CHF_3$ or $CF_4$ based reactive ion etching (RIE). The S-FIL resist is then removed to reveal the patterned dielectric mask.

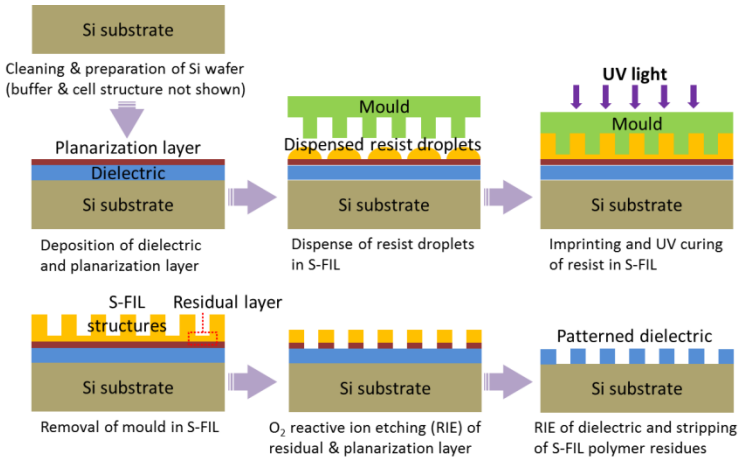


**Figure 4.2** Schematic showing the fabrication of nano-SAG dielectric mask on Si substrate (Type A) using S-FIL and RIE. Buffer and device structure in Si substrate are not shown.

### 4.2.1. Challenges to Uniform and Deep Pattern Transfer in S-FIL

S-FIL is a wafer-scale, low pressure imprint process in which the resist pattern is defined by the space between the surface relief features of the mould and the topography of the substrate when they are brought into close proximity. The low imprint pressure, and rigidity of the mould implies that the latter does not readily conform to the general topography of the substrate. Particles, surface undulations and non-parallel alignment of the mould and substrate surfaces can lead to incomplete pattern transfer and non-uniform residual layer thickness (RLT) during S-FIL. Thus, substrate attributes such as cleanliness, low wafer bow and warp, flat and smooth topography, and proper mould-substrate leveling in S-FIL are desired. However, RLT variation is inevitable as it is impossible to have an ideal flat surface that is perfectly leveled relative to the mould and free of particles. Further, non-uniform capillary action and inhomogeneous resist spreading associated with puncturing the resist with high aspect ratio, pillar-patterned moulds during S-FIL exacerbate RLT variation. For the 300nm-period hexagonal array of pores (~ 140 nm diameter, ~ 300 nm depth) replicated by a pillar-patterned S-FIL mould employed in this section, the impact of RLT variation and RIE duration on the imprinted profile is shown in Figure 4.3.

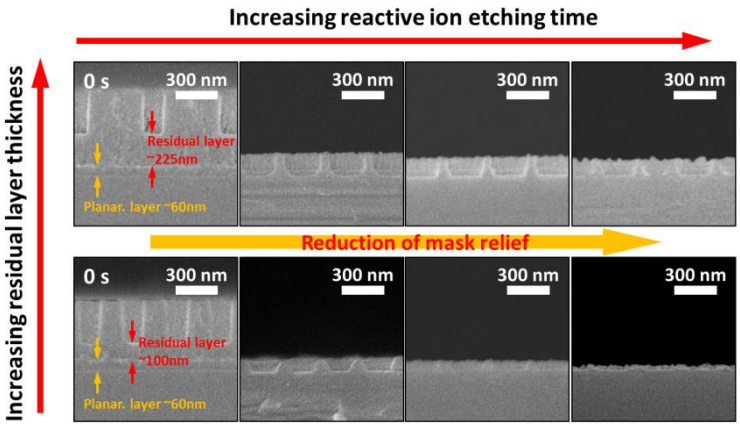


**Figure 4.3** Evolution of S-FIL imprinted profile (cross-section) with duration of $O_2$ RIE for different initial residual layer thickness.

Using extended RIE duration to clear off the thick residual layer in one region of the imprinted area will unavoidably result in over-etching in regions with thinner residual layer. In cases where the RLT variation is greater than the maximum imprint depth, destruction of the imprinted pattern in these regions may result as seen in Figure 4.4. Even if the imprinted patterns are not destroyed, widening of pore sizes can occur. This will eventually be transferred to the underlying layer. Figure 4.5 shows the case where uneven substrate topography leads to RLT variation and non-uniform widening of pores in the underlying dielectric layer following pattern transfer. It is important to note that RLT variation is shown to be caused by substrate topography in Figure 4.5 and subsequent Figures. This has been greatly exaggerated for illustration purposes. Typically, the RLT variation is on the order of a few hundred nm's per cm and will not be visible in a high magnification SEM image. Also, RLT variation may also be caused by non-uniform capillary action and inhomogeneous resist spreading in S-FIL. These effects are related to mould design and not explicitly shown in the Figures.

Further, due to the inadequate etch resistance of the S-FIL pattern, the maximum depth of pattern transfer to the dielectric layer is limited (a few tens of nm for ~ 300

nm of S-FIL mould relief). Hence, a technique to reduce the impact of RLT variation and S-FIL pattern etch resistance is desired to improve the yield, controllability and depth of the S-FIL pattern transfer process.

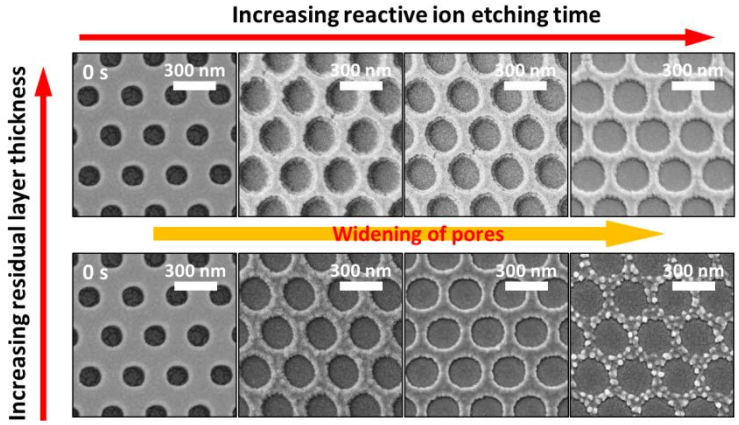


**Figure 4.4** Evolution of S-FIL imprinted profile (plan view) with duration of $O_2$ RIE for different initial residual layer thickness.

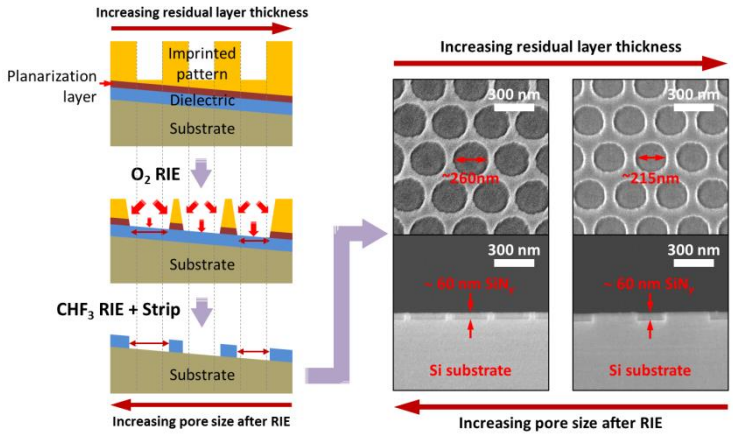


**Figure 4.5** Variation of $SiN_y$ dielectric pore size after pattern transfer. This is due to variation in residual layer thickness which causes variation in pore widening during $O_2$ RIE.

### 4.2.2. Uniform and Deeper Pattern Transfer in S-FIL using an Angled Deposited Metal Mask

To reduce the dependency on mould, resist and substrate attributes, and leveling in S-FIL, an additional step to the basic process flow is proposed. Summarily, a thin layer of Ti metal (~ 20 nm) is deposited over the top of the S-FIL resist pattern. This is

achieved by positioning the S-FIL patterned substrate at an angle to the incoming Ti flux during deposition and rotating it about its normal such that Ti uniformly coats the top and rim of the pores as seen in Figure 4.6. The deposited Ti mask effectively protects the S-FIL imprinted features during prolonged $O_2$ RIE for complete residual layer removal and significantly improves the uniformity and yield of pattern transfer.

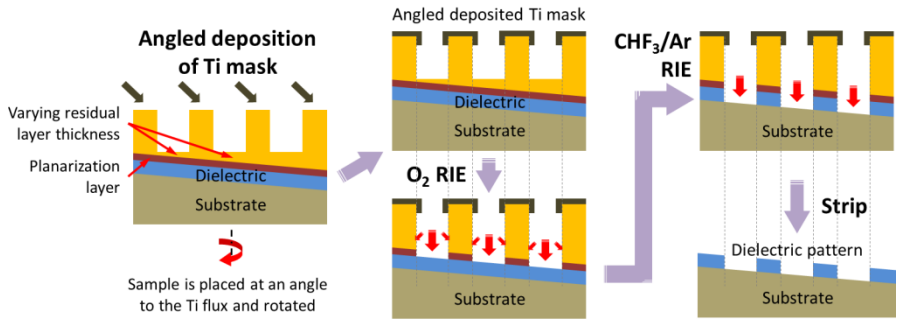


**Figure 4.6** Schematic of the modified nano-SAG mask fabrication process involving angled deposition of a Ti mask to achieve uniform pattern transfer despite RLT variation.

Moreover, the Ti/S-FIL mask is more resistant to subsequent RIE for pattern transfer to the underlying dielectric layer. Previously, $SiN_y$ dielectric layers could be etched to a depth 60 nm but with significant variation in pore diameters over the imprinted area using just the S-FIL mask. With the Ti/S-FIL mask and an optimized dry etching chemistry of $CHF_3$ and Ar, the etched depth in $SiN_y$ can be extended up to ~ 430 nm over the entire imprint area for pores ~ 200 nm in diameter. The same etch chemistry may also be used to etch $SiO_2$. FESEM images of a $SiN_y$ dielectric pattern fabricated by this method showing the deep etch and vertical sidewall profiles are given in Figure 4.7. The bottom of the pores is concave as the etch stop with the Si substrate is not reached. The modified dielectric nano-SAG mask fabrication process is repeatable and greatly reduces the sensitivity of the process to mould, resist and wafer attributes, S-FIL mould-substrate leveling and RIE conditions.

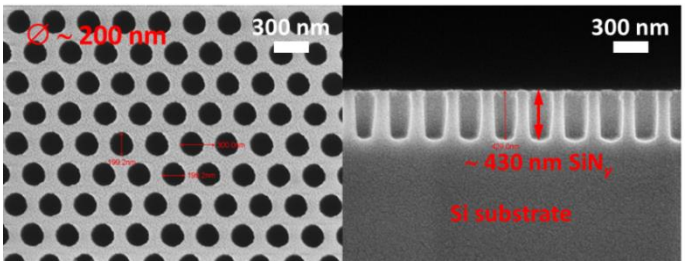


**Figure 4.7** FESEM images of a 300nm-period hexagonal array of 200nm-diameter pores fabricated in a $SiN_y$ layer by S-FIL and Ti masking. Plan view (left) and cross-section (right).

In fact, preliminary results show that the pore diameter in the $SiN_y$ dielectric can be tuned to a certain extent by adjusting the conditions of the $O_2$ RIE process. Increasing process pressure in $O_2$ RIE is found to increase the level of undercut in the Ti/S-FIL pattern. This in turn leads to an increase in $SiN_y$ pore diameter upon $CHF_3$/Ar-based RIE pattern transfer as illustrated in Figure 4.8. Such a method to control the pore diameter is plausible provided that RLT variation and hence spatial variation in pore size is small. Over the range of $O_2$ RIE process pressures from 5 to 40 mTorr, $SiN_y$ pore diameters can be tuned from ~ 130 to 200 nm as seen in Figure 4.9.

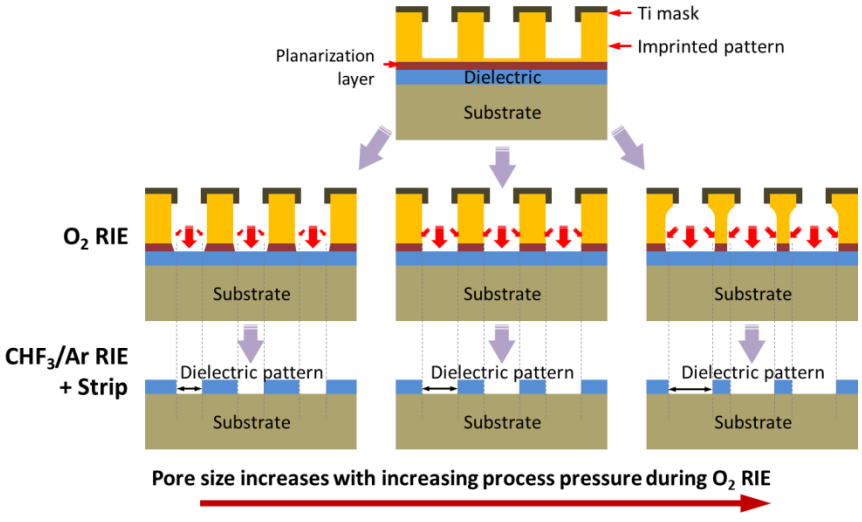


**Figure 4.8** Schematic showing the mechanism by which pore size in the transferred dielectric pattern may be tuned in the combinatory approach of S-FIL and Ti masking. Increase in process pressure during $O_2$ RIE, increases the undercut of the Ti/S-FIL mask resulting in an increase in the diameter of the pores etched in the dielectric layer.

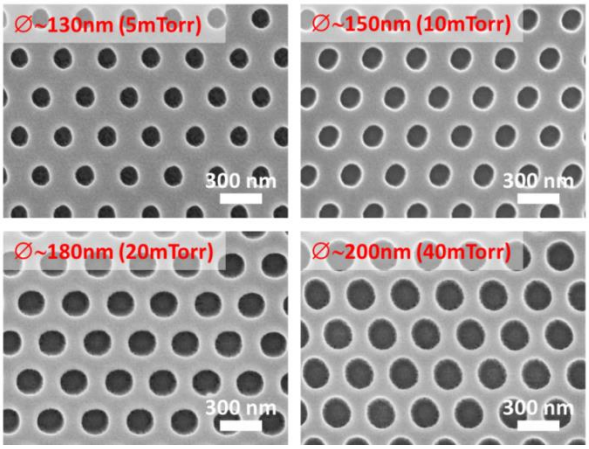


**Figure 4.9** FESEM images showing variable pore diameters (~ 130 to ~ 200 nm) etched in $SiN_y$ dielectric on Si substrates by varying the process pressure from 5 to 40 mTorr in the initial $O_2$ RIE step in the combinatory approach of S-FIL and Ti masking.

### 4.2.3. High Aspect Ratio Patterning using a Combinatory Approach of S-FIL and AAO

While a combinatory approach of S-FIL and Ti masking enables deeper dielectric pattern transfers, the depth is limited to a few hundred nanometers. For even deeper pattern transfers, an even more etch-resistant mask is required. Anodization of aluminum oxide (AAO) has been used extensively for nano-SAG mask patterning. See review in Section 2.4.5.2.1. An advantage of the AAO process is the ability to generate very high aspect ratio pores in thick AAO layers. However, the self-ordering process during anodization only allows the formation of pores with short range order. By combining the ability of AAO to form high aspect ratio pores and the ability of S-FIL to perform large-area highly ordered nanopatterning, high aspect ratio nano-sized pores in a regular lattice pattern on a large area can be generated in AAO. The etch-resistant nanoporous AAO may then act as a mask for high aspect ratio dielectric pattern transfers. The process flow of this combinatory approach is shown in Figure 4.10. Briefly, a layer of Al (~1μm) is first deposited onto the dielectric coated substrate. Depending on the thickness of the AAO mask required, a thinner or thicker layer of the metal can be deposited. S-FIL is then performed to form the polymeric

mask. Angled deposition of a Ti mask may be carried out if required. Removal of the residual layer by $O_2$ RIE and subsequent nano-indentation of the Al layer using dry/wet etch to predefined the pore positions are subsequently performed. The Ti/S-FIL mask layer is then stripped, after which anodization is carried out to generate high aspect ratio, highly regular AAO pores over the imprint area. A further pore widening step allows tunability of the pore diameter. The AAO mask can then be used to pattern the underlying dielectric layer to generate high aspect ratio nano-SAG masks for controlled nanostructured growth of InGaN. FESEM images corresponding to the anodization and pore widening processes are also shown in Figure 4.10.

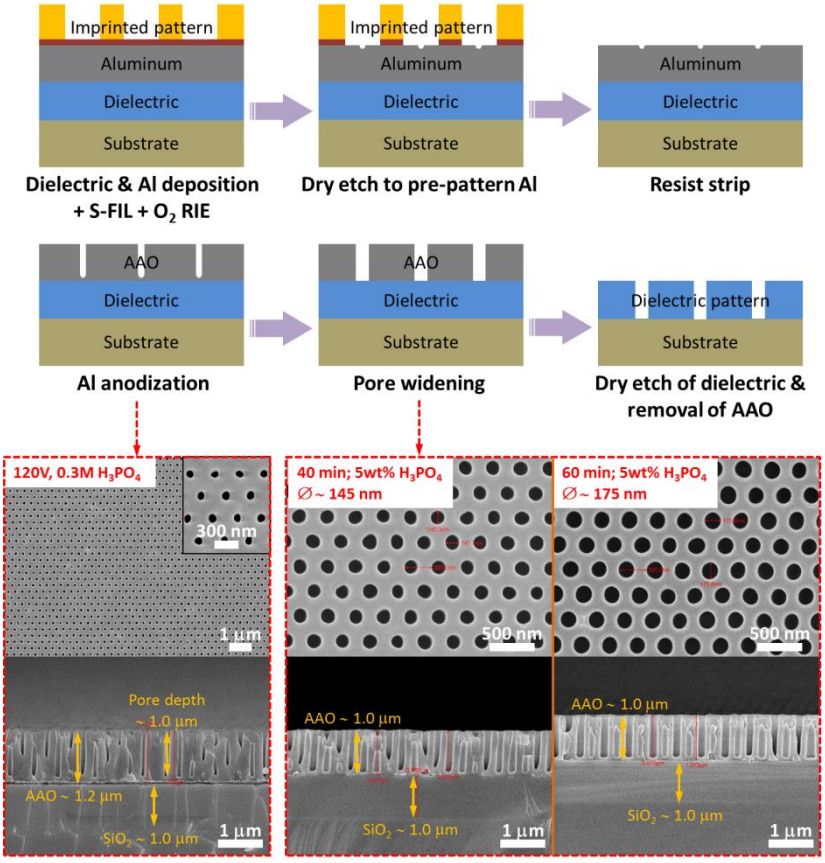


**Figure 4.10** Fabrication of high aspect ratio, long range order AAO pores and subsequent pattern transfer to an underlying dielectric layer using a combinatory approach of S-FIL and anodization of aluminium oxide. FESEM images of the plan and cross-sectional views of samples after Al anodization and pore widening at 40 and 60 min are also shown.

### 4.2.4. Summary on Fabrication of Type A Templates

In the preceding sections, three routes for the fabrication of nano-SAG masks on Si substrates (Type A templates) were examined: (i) the basic S-FIL process, (ii) a combinatory approach of S-FIL and Ti masking, and (iii) a combinatory approach of S-FIL and AAO. While the basic S-FIL process is simple, its sensitivity to mould, resist and substrate attributes, and leveling reduces the uniformity and repeatability of pattern transfers especially with high aspect ratio, pore-patterned moulds. The issues are mitigated by the combination of S-FIL with Ti-masking which also allows deeper dielectric pattern transfers. The depth may be further extended by combining S-FIL with AAO. However, the process is complex and should be judiciously employed.

## 4.3. Nanopatterning of Si Substrates for Nanoheteroepitaxy (Scheme B)

### 4.3.1. Overview

Type B template fabrication involves the direct patterning of the Si substrate to form Si nanopillars for nanoheteroepitaxy. Nanopillars may be defined by wafer-scale S-FIL as with Type A templates, but with the difference that pore-patterned moulds are used. While similar S-FIL challenges apply, the use of bare Si wafers for S-FIL with no prior layer deposition or other process steps correlates to lower RLT variation. This is because the absence of process steps prior to S-FIL prevents the introduction of additional topography or particles to the surface that would contribute to RLT variation. Further, as the lateral dimensions of features (pillars and pores) are relatively small compared to their spacing in this work, greater surface area-to-volume ratios exist for the *cavities* in pore-patterned moulds compared to pillar-patterned moulds. This is expected to facilitate more uniform capillary action. It is important to point out that the “surface area-to-volume ratio” pertains to the cavity which is being filled by resist in the mould to form the nanoimprinted pattern. For similar feature sizes and which are less than their spacing, it can be deduced that the

surface area-to-volume ratio is greater for the nanopillar pattern (imprinted by pore-patterned mould) than the imprinted nanoporous layer (imprinted by pillar-patterned mould). This is because the surface area is similar but the volume is smaller in the former than the latter. Also, the greater "contact" area of the pore-patterned mould with the substrate is expected to promote more homogeneous resist spreading. These effects lead to lower RLT variation in S-FIL of nanopillar patterns on Si substrates compared to S-FIL of nanoporous patterns on dielectric-coated substrates. Hence, use of Ti masking to improve pattern uniformity is not absolutely necessary.

As the S-FIL mask is susceptible to RIE, metal-catalyzed electroless etching (MCEE) which specifically etches Si may alternatively be employed for pattern transfer into the Si substrate. Also known as metal-assisted chemical etching (MACE), MCEE is a simple technique first demonstrated by Peng et al. and used to generate high aspect ratio Si nanostructures [290, 291]. Sidewall inclination common in RIE [292] and scalloping effects typical of deep RIE (DRIE) [293] are avoided in MCEE. Further, the process does not need expensive equipment like inductive coupled plasma-RIE or DRIE. Also, due to the anisotropic nature of MCEE, deep Si etching is possible.

### 4.3.2. High Aspect Ratio Patterning of Si Substrate by S-FIL and Metal-Catalyzed Electroless Etching (MCEE)

Wee at al have fabricated Si nanostructures by MCEE for GaN deposition [294]. However, the nanostructures are disordered, and lack good size and morphology control. In this section, we describe a simple two-stage procedure combining S-FIL and MCEE to fabricate wafer-scale, near perfectly ordered Si nanostructures with controlled feature sizes down to sub-50nm from the Si substrate. The results of this have been published in ref. [295, 296]. Using this method, circular, hexagonal and rectangular cross-section Si nanostructures in hexagonal or square array

configurations with 150nm or 300nm periods (corresponding to array packing densities up to $5.13\times10^7$ structures $mm^{-2}$) and aspect ratio as high as 20:1 or more have been produced. The results clearly illustrate the high-resolution potential of S-FIL and deep etching capabilities of MCEE. This offers a simple and fast route towards semiconductor nanostructure production.

The process steps are summarized as follows. First, the cleaned Si substrate is patterned in S-FIL as described in Section 3.2.2. For this section, three different pore-patterned quartz moulds were employed allowing the corresponding inverse nanopillar patterns to be defined. The replicated patterns consist of: (i) 300 nm-period hexagonal array of 180 nm (facet-to-facet dimension) hexagonal pillars/studs, (ii) 300 nm-period square array of 200 nm by 100 nm rectangular pillars, and (iii) 150 nm-period hexagonal array of 50 nm diameter circular studs. By incorporating some degree of lateral etching in the RIE of the residual layer, S-FIL pillars/studs can be narrowed, thereby providing some tunability in the dimensions of the S-FIL features. The patterns are shown in Figure 4.11(a)-(c).

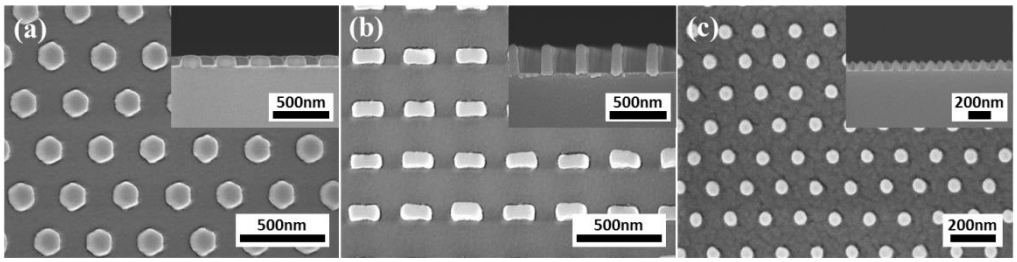


**Figure 4.11** FESEM images of S-FIL nanoimprinted samples after $O_2$ RIE. Inset shows the respective cross-sections. (a) 300 nm-period hexagonal array of 180 nm (facet-to-facet) hexagonal pillars/studs, (b) 300 nm-period square array of 200 nm by 100 nm rectangular pillars, and (c) 150 nm-period hexagonal array of 50 nm diameter circular studs.

The patterned area in each 300 nm-period mould is 10 mm × 10 mm while that for the 150 nm-period mould is 5 mm × 5 mm, enabling equal sized imprints to be replicated over a wafer surface. A wafer nanoimprinted by S-FIL is shown in Figure 4.12. In

this case, 32 nanoimprinted fields were generated over the surface of a 4" Si wafer. The street size between fields can be varied to accommodate more or less fields. Furthermore, by virtue of the step-and-repeat mechanism, the NIL process can be extended for up to 8" wafers.

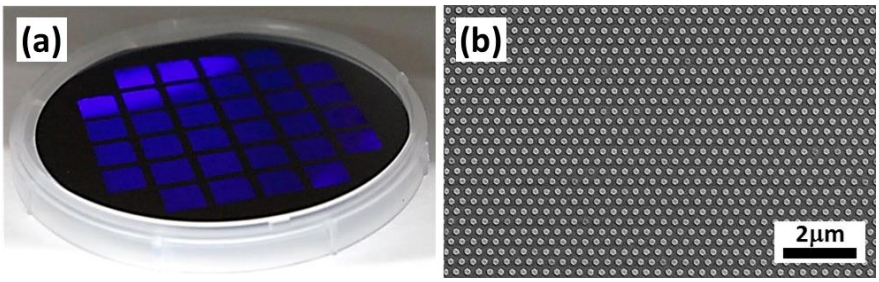


**Figure 4.12** (a) Photograph of a S-FIL nanoimprinted 4" Si wafer, and (b) FESEM image showing the long range order of the corresponding nanostructures of 300 nm periodicity. The wafer in (a) is deliberately tilted at an angle to bring out the violet blue tinge arising from the optical diffraction caused by the highly ordered nanoimprinted hexagonal studs.

The mechanism of MCEE is well discussed in literature and will not be described at length here [297]. Briefly, in a solution of HF and an oxidative agent, e.g. $H_2O_2$, of appropriate concentrations, regions of Si that are in contact with a noble metal, such as Au or Ag, are etched much faster than those regions without metal coverage. This phenomenon arises because the noble metal acts as a catalyst facilitating the local injection of holes into Si resulting in its oxidation and subsequent removal by HF. The reaction is redox in nature and the metal "sinks" into Si creating an etched path. Therefore, by pre-patterning a noble metal layer on Si prior to immersion in $HF/H_2O_2$, patterned etched structures can be generated. The steps leading up to MCEE for the S-FIL studs-patterned wafers are described as follows and schematically shown in Figure 4.13. After removal of the residual material at the recessed regions between the studs by RIE, a thin layer of Au (~ 20 nm thick) acting as the catalyst is deposited by electron beam evaporation at a pressure of ~ $10^{-6}$ Torr. The wafer is then immersed in a solution of 4.6M HF and 0.44M $H_2O_2$ for the required time, after which the reaction is halted by rapid removal of the wafer from the solution and subsequent

immersion in deionized water. Next, the Au layer is removed in aqua regia at 70°C and the NIL mask stripped in boiling piranha solution to reveal the Si nanopillars.

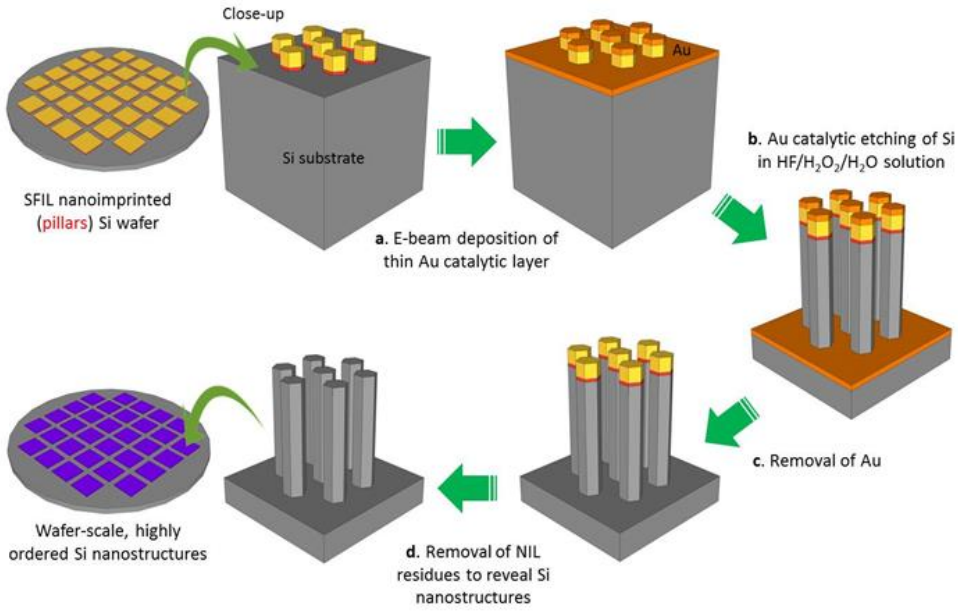


**Figure 4.13** Schematic illustrating the generation of wafer-scale, highly-ordered Si nanostructures by MCEE from a S-FIL nanoimprinted Si wafer.

Figure 4.14(a) shows a 4" Si wafer bearing 32 fields of hexagonal Si nanopillars in a hexagonal arrangement generated by the prior approach. The near perfect ordering of the Si nanopillars can be deduced from the optically diffracted violet-blue light when the wafer is tilted at an angle against a diffused white light source. The near-perfect long range ordering is also observed in the FESEM image of Figure 4.14(b). Figure 4.14(c) shows the closed-up FESEM plan view of the hexagonal Si nano-pillars. The period of the nanopillars is 300 nm (area density of $1.28 \times 10^7$ pillars $mm^{-2}$) as defined by the S-FIL mould while the lateral dimensions (between opposite sides of a nanorod) is ~ 160 nm, a reduction from the ~ 180 nm pores in the S-FIL mould. The S-FIL mask which forms a cap over each nanopillar is visible in the FESEM images demonstrating the resistance of the material to attack by the $HF/H_2O_2$ etching solution. The inset of Figure 4.14(b) shows the FESEM cross-section of the Si nanopillars,

revealing the etched profiles, straight sidewalls and S-FIL mask caps. The height of the etched hexagonal Si nanopillars is approximately proportional to the etching duration indicating a near constant etch rate (~ 320 nm/min). By varying the time of etching, the height of the structures can be adjusted, thus tuning the aspect ratio.

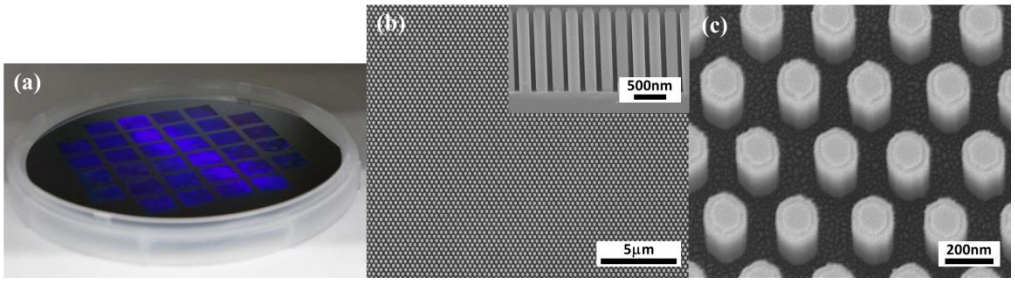


**Figure 4.14** Wafer-scale Si nanopillars formed by the combined approach of S-FIL and MCEE. (a) Photograph of a 4" Si wafer consisting of 32 arrays of hexagonally ordered hexagonal Si nanopillars. (b)FESEM image showing the hexagonal long range order of the Si nanopillars. Inset shows the cross-sectional FESEM image of the Si nanopillars showing the relatively straight sidewalls and S-FIL mask caps. (c) FESEM close-up plan view of the Si nanopillars showing the NIL mask cap on the top surface of each structure.

Molar concentrations of HF and $H_2O_2$, abbreviated as [HF] and [$H_2O_2$] respectively, other than that reported in this work (4.6M HF and 0.44M $H_2O_2$) have been used in our experiments. However, it is found that 4.6M HF and 0.44M $H_2O_2$ are optimal for rapidly generating high aspect ratio Si nanostructures with sidewalls of low porosity. Similar concentrations have also been used by other works reported in literature [298-302]. The influence of [HF] and [$H_2O_2$] in fabricating Si nanostructures in MCEE has been discussed by Lianto et al. [298, 303].

Unlike other reported Si nanostructures produced by MCEE which sports a highly roughened top surface due to chemical attack, with greater roughening with etch duration [297, 299, 300, 302, 304, 305], our technique produces Si nanostructures with considerably smoother top surface. As shown in Figure 4.15, the top surface of the Si nanostructure remains well-defined and flat after MCEE and S-FIL mask removal. While maintaining relatively low doping levels in the Si wafers (resistivity

10-20 Ω.cm) play a contributory role in slowing the progress of porosity attack, the preservation of the smooth top surface is more likely linked to the use of the S-FIL mask. The latter is formed by the UV-polymerization of a silicon-containing acrylate resist, the adhesion of which is strongly enhanced by the use of a planarization/primer layer. This is found to be highly resistant to chemical attack by both acids and bases with complete removal being effected by immersion in boiling piranha solution only. The S-FIL mask caps remain after MCEE and are shown in Figure 4.14(b)-(c). The observations show that under our conditions of etching, the mask offers good protection to the Si surface against chemical attack by the $HF/H_2O_2$ etching solution.

However, a slight narrowing of the hexagonal Si nanopillars (from ~ 180 nm to ~ 160 nm) occurs with increased etch duration (from 30 s to 180 s) as seen in Figure 4.15. This should be taken into consideration when fabricating Si nanostructures with low tolerance for dimensional deviations. While this lateral component of etching is much slower than the vertical component occurring at the regions of Si covered by the Au catalyst, thus conferring a high degree of anisotropy to the MCEE process, it will nonetheless impose a limit to the maximum achievable aspect ratio. Aspect ratios as high as 20:1 have been obtained by us, with values up to 220:1 being reported [306]. However, this will ultimately be limited by dissolution of the Si nanowires [299].

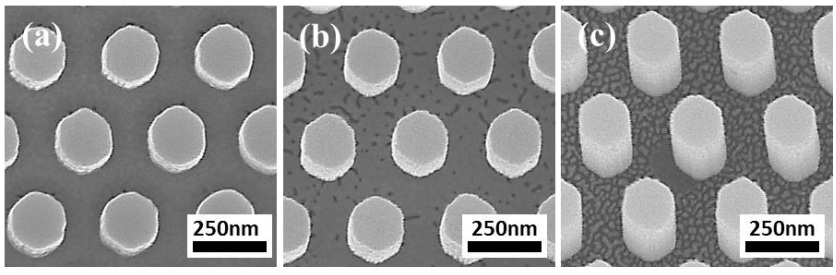


**Figure 4.15** Plan view FESEM images of Si nanostructures after different etch durations with the S-FIL masks removed. (a) 30 s, (b) 60 s, and (c) 180 s etch durations. The top surfaces of the nanostructures remain smooth after the process due to a good degree of protection offered by the S-FIL masking layer. This contrasts with the rougher sidewalls.

Other S-FIL patterns may similarly be transferred into the underlying Si substrate by MCEE. Figure 4.16 shows the Si nanostructures ( ~ 190 nm by 95 nm rectangular cross-section and ~ 46 nm diameter circular cross-section nanopillars) generated from the patterns in Figure 4.11(b) and Figure 4.11(c). The results demonstrate that the array configurations are not restricted to hexagonal arrangement alone and may be extended to square arrays too. In addition, the Si nanostructures may take on other cross-sectional shapes such as rectangular or circular profiles with feature dimensions down to sub-50 nm. Aspect ratios up to 20:1 or more have been achieved but the compliant Si nanowires have a tendency to adhere to each other due to surface tension forces exerted during processing resulting in partial loss of ordered arrangement. In all, we believe that these patterns are sufficient to demonstrate the versatility in nano-scale Si pattern generation of our approach for nanoheteroepitaxy.

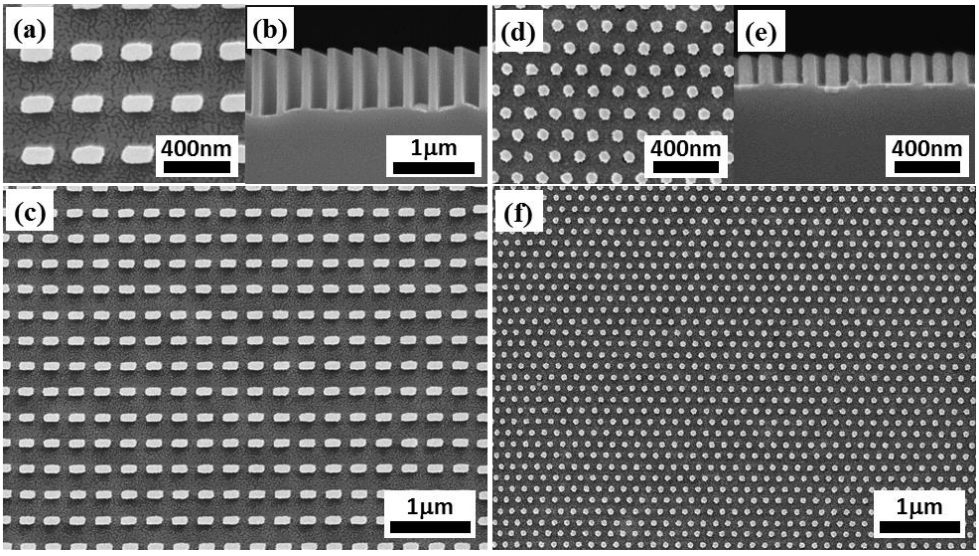


**Figure 4.16** FESEM images of Si nanostructures fabricated by S-FIL and MCEE. (a), (b), and (c) show the close-up, cross-section, and overview of a 300 nm-period square array of ~ 190 nm by 95 nm rectangular cross-section Si nanopillars. (d), (e), and (f) show the close-up, cross-section, and overview of a 150 nm-period hexagonal array of sub-50 nm diameter cylindrical Si nanopillars.

### 4.3.3. Summary on Fabrication of Type B Templates

In Section 4.3.2, nanopatterning of Si substrates using a combinatory approach of S-

FIL and MCEE for the fabrication of Type B growth templates was described. The approach combines the merits of the constituent methods enabling the wafer-scale fabrication of high aspect ratio Si nanostructures with controlled dimensions (down to sub-50 nm) and arrangement. The dimensional and pattern control can permit control over the properties of III-nitrides subsequently grown. Further, preservation of the smooth top surface morphology of the Si nanostructures is expected to be conducive for material growth. In all, these attributes make the combinatory approach of S-FIL and MCEE very attractive for producing Type B templates for nanoheteroepitaxy, considering the dearth of methods with these capabilities.

## 4.4. Chapter Summary

In this Chapter, nanopatterning techniques that have been developed for fabrication of Type A (nanopore arrays) and B (nanopillars arrays) growth templates were described. By combining S-FIL with Ti and/or AAO masking for RIE, ordered nanoporous dielectric of tunable pore size and depths on Si substrates can be fabricated for Type A templates. Further, by combining S-FIL with MCEE, Si nanostructure arrays of variable patterns and adjustable aspect ratio on Si substrates may be fabricated for Type B templates. The combination of S-FIL with various pattern transfer methods helps to overcome the shortcomings of S-FIL and provide greater flexibility to the nanopatterning process. However, to ensure a manageable scope, this work will focus on the use of Type A nanostructured templates which are suitable for InGaN nano selective area growth (nano-SAG). Nonetheless, the combinatory approach of S-FIL and MCEE developed for the fabrication of Type B templates remains highly promising for production of Si nanostructured templates in future work on nanoheteroepitaxy.

# Chapter 5 Scaling InGaN Thin Films into Three-Dimensional Nanostructures on AlN/Si(111) Substrates

## 5.1. Introduction

A suitable substrate for InGaN growth in this work is AlN-buffered Si(111) substrate. Si(111) is favored due to its trigonal symmetry which favors epitaxial growth of the (0001) plane in III-nitrides, as discussed in Section 2.2. The thin AlN buffer layer is required to prevent Ga-meltback etching and unintentional nitridation of Si during InGaN growth as discussed in Section 2.3.1. While the ultimate goal is to develop InGaN/Si tandem solar cells, where the Si substrate forms a subcell, for the purpose of this material study, no device architecture is incorporated in the Si substrate.

In this Chapter, the scaling of InGaN thin films into three-dimensional nanostructures on AlN/Si(111) substrate is presented. The results of a growth study of InGaN thin films on the unpatterned substrates are first shown. Pre-requisite growth conditions and effect of growth pressure and temperature on InGaN properties are discussed. These results were used for templated InGaN nanostructured growth on AlN/Si(111)-based Type A template. Characteristics of the InGaN nanostructure array grown via nano-SAG for a set of growth conditions is then presented and discussed in comparison with the control InGaN film grown on unpatterned AlN/Si(111) substrate.

## 5.2. Growth of InGaN Films on AlN/Si(111) Substrates

### 5.2.1. Experimental Procedure

Si(111) wafers with a thin layer of separately MOCVD-grown, high-temperature AlN(0001) buffer layer were used as the starting substrates. These were diced into 17 mm × 17 mm square samples and cleaned ex-situ by successive ultra-sonication in

acetone, isopropanol, deionized (DI) water, HCl, and DI water prior to growth. The growth of $In_xGa_{1-x}N$ was conducted in an Emcore/Veeco D125 vertical geometry rotating disk MOCVD reactor utilizing TMGa and TMIn as the Group III precursors, and $NH_3$ as the Group V precursor. The samples were first annealed at 1000°C in $H_2$ after which the temperature was ramped down to the growth temperature *T* (655-795°C). The chamber pressure *P* was varied in the range of 100-300 Torr. For all growths, the flow rates of TMIn, TMGa and $NH_3$ were kept constant at 120 sccm, 5 sccm, and 18 slm respectively, corresponding to a V/III ratio of 9200 and a high TMIn/(TMIn+TMGa) molar flow ratio $r_m$ of 0.80. During $In_xGa_{1-x}N$ growth, $N_2$ was used as the carrier gas and ambient while $H_2$ was turned off. The duration of InGaN growth was kept at 12 min unless otherwise stated. The first set of $In_xGa_{1-x}N$ growth was performed at a relatively low *T* of 655°C to improve In incorporation *x* and at *P* of 100, 200 and 300 Torr. It was found that the use of an elevated *P* (300 Torr) dramatically improves morphological and compositional uniformity of the alloy on AlN/Si(111) substrates. The results and details will be discussed later. The second part of the experiment involved growth at higher *T* but at a constant *P* of 300 Torr. The InGaN growth conditions are tabulated in Table 5-1.

**Table 5-1** Summary of growth conditions used in the MOCVD of InGaN *film* on AlN/Si(111).

| | ***T*** **(°C)** | ***P*** **(Torr)** | **Duration (min)** | **Flow Rate (sccm)** | | | | |
|---|---|---|---|---|---|---|---|---|
| | | | | **TMIn** | **TMGa** | **$H_2$** | **$N_2$** | **$NH_3$** |
| **Pressure series** | 655 | 100 | 12 | 120 | 5 | 0 | 6000 | 18000 |
| | 655 | 200 | 12 | 120 | 5 | 0 | 6000 | 18000 |
| | 655 | 300 | 12 | 120 | 5 | 0 | 6000 | 18000 |
| **Temperature series** | 685 | 300 | 12 | 120 | 5 | 0 | 6000 | 18000 |
| | 705 | 300 | 12 | 120 | 5 | 0 | 6000 | 18000 |
| | 735 | 300 | 12 | 120 | 5 | 0 | 6000 | 18000 |
| | 765 | 300 | 12 | 120 | 5 | 0 | 6000 | 18000 |
| | 795 | 300 | 12 | 120 | 5 | 0 | 6000 | 18000 |

The morphology of the samples was examined by FESEM and tapping mode AFM while the crystal quality was analyzed by HR-XRD. Lastly, μ-PL measurement was performed at room temperature with a He-Cd 325nm laser as the excitation source. The results are published in ref. [130] and are discussed in the following sections.

### 5.2.2. Substrate Pretreatment

Prior to the growth of $In_xGa_{1-x}N$, the AlN/Si(111) substrate was annealed in-situ in the MOCVD reactor in $H_2$ at 1000°C for 5 min. This substrate pretreatment was found to be critical for achieving InGaN epitaxial growth. Annealing of the substrate in $N_2$ or $NH_3$ for the same duration was inadequate and resulted mainly in In droplet formation during subsequent growth. It is likely that a thin layer of oxide exists on the AlN surface. This is supported by reports of the presence of oxygen bonded to Al in both $O^{2-}$ and $OH^-$ chemical states in air-exposed or water-exposed AlN surfaces [307-309]. Despite the cleaning of the substrates in dilute HCl prior to loading into the growth chamber, oxidation to some extent would inevitably occur during the subsequent rinse in DI water or transfer into the chamber. The oxidized surface would have interfered with epitaxial growth thus contributing to In droplet formation and polycrystalline deposits. The high temperature in-situ annealing process in a reducing $H_2$ environment at 1000°C removes the oxidized layer, thermally cleans and prepares the surface for epitaxy.

### 5.2.3. Influence of Reactor Pressure

#### 5.2.3.1. Composition

Figure 5.1 shows the (0002) $2\theta$-$\omega$ XRD scans for the $In_xGa_{1-x}N$ samples grown at 655°C and at reactor pressures of 100, 200 and 300 Torr.

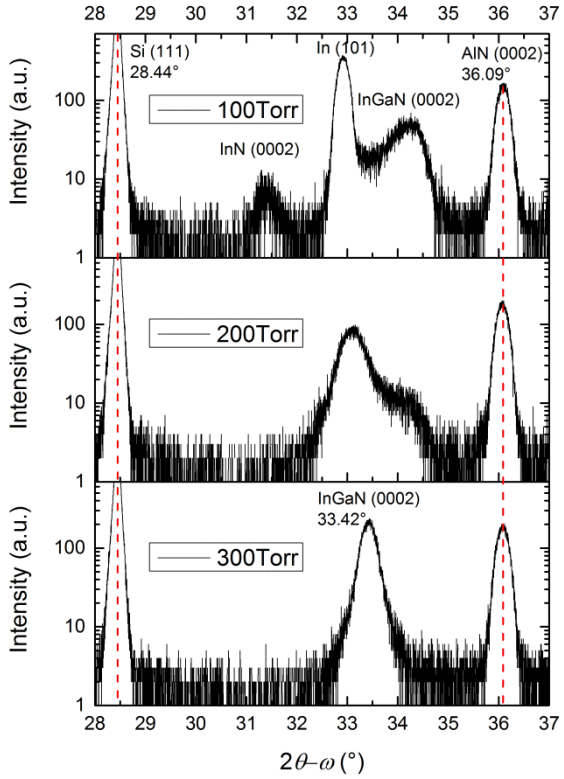


**Figure 5.1** XRD (0002) $2\theta$-$\omega$ scans of InGaN films grown on AlN/Si(111) substrates at 655°C with pressures of 100, 200, 300 Torr. An increase of growth pressure is correlated with the suppression of phase separation and In droplet formation.

For all samples, the Si(111) substrate peak is clearly observed at 28.44° together with the AlN(0002) peak located at 36.09°. At a low growth pressure of 100 Torr, the InGaN film produced is compositionally non-uniform in two aspects. First, a substantial amount of In droplets exists, giving rise to the strong In(101) peak at about 32.90°. Second, considerable InGaN phase inhomogeneity is present. This exists in the form of InN, detected as a weaker InN(0002) peak at 31.40°, and wide InGaN compositional fluctuation manifested as a broad asymmetric InGaN(0002) peak. Increase of the growth pressure to 200 Torr, results in the significant suppression of the InN(0002) peak, while the In(101) peak appears to merge with the low In content InGaN peak and is converted into a broad but mid-indium content, shouldered InGaN(0002) peak. At an elevated pressure of 300 Torr, a solitary

InGaN(0002) peak is achieved ($2\theta$ = 33.42°), indicating single phase InGaN is realized with suppression of InGaN phase separation and In droplet formation.

### 5.2.3.2. Morphology

FESEM observations corroborate with the XRD results. For the sample grown at 100 Torr, growth appears to occur in a highly uncontrolled manner. The surface is riddled with In droplets of various sizes which account for the strong In(101) peak in the $2\theta$-$\omega$ XRD spectrum, and areas that are relatively much less covered during deposition. These features occur amidst an ensemble of interconnected tapered islands of various sizes and result in a highly disordered and rough morphology as seen in Figure 5.2(a)-(b). As the growth pressure is increased to 200 Torr, the morphology smoothens and becomes more homogeneous as shown in Figure 5.2(c). There is a marked decrease in the size and density of In droplets, though a few are still discernible. At an elevated pressure of 300 Torr, In droplets are not observed. A dense ensemble of fine islands that is homogeneous over the sample surface is obtained as seen in Figure 5.2(d). Improved surface homogeneity arises because the overpressure facilitates uniform, dense nucleation over the highly lattice mismatched surface [310]. However, the shallow structures are indicative of a slower growth rate and may be a consequence of increased parasitic reactions occurring in the ambient at higher growth pressures. The improved InGaN compositional uniformity may be explained as follows. Consider the vapour-solid interface, where the input metal-organic precursors of TMIn and TMGa, are decomposed irreversibly according to the homogeneous reactions given by Equations (3-4) and (3-5) in Section 3.3.3 [268]. These are repeated here as

$$(CH_3)_3In\ (g) + 3/2\ H_2\ (g) \rightarrow In\ (g) + 3\ CH_4\ (g) \qquad (5\text{-}1)$$

$$(CH_3)_3Ga\ (g) + 3/2\ H_2\ (g) \rightarrow Ga\ (g) + 3\ CH_4\ (g) \qquad (5\text{-}2)$$

The equilibrium chemical reactions which proceed at the substrate surface to form $In_xGa_{1-x}N$ are given by Equations (3-6) and (3-7). These are reiterated here as

$$In\ (g) + NH_3\ (g) \rightleftharpoons InN\ (alloy) + 3/2\ H_2\ (g) \quad (5\text{-}3)$$

$$Ga\ (g) + NH_3\ (g) \rightleftharpoons GaN\ (alloy) + 3/2\ H_2\ (g) \quad (5\text{-}4)$$

A rise in the growth pressure, while maintaining the same flow rates, correspondingly increases the partial pressures of the various vapour species (TMIn, TMGa, $NH_3$, $N_2$, etc.) within the reactor. While the rise of TMIn partial pressure is likely to increase the driving force for the formation of In droplets on the surface, an increase in In(101) intensity is not observed in the XRD spectrum at 200 Torr. On the contrary, it is greatly suppressed. We postulate that the increase in growth pressure exerted a greater effect by favouring the forward equilibrium reaction (5-3) to convert In and $NH_3$ into InN and $H_2$, thus suppressing In droplet formation. Further, the nanoscale 3D island growth morphology allows the strain energy to be partially released through elastic relaxation [311]. This improves InN incorporation within the InGaN alloy, and reduces InGaN phase separation or compositional fluctuation. [70]. These can account for the disappearance of the InN(0002) peak and the generation of a solitary InGaN(0002) peak indicating that single phase InGaN is achieved. Future work employing a more detailed thermodynamic approach at the nanoscale would be useful in providing greater insight into the observed phenomenon [267, 268, 312]. However, the relatively low temperature grown, finely textured island morphology is likely to be defective and contain a significant amount of surface states.

The In composition $x$ of the single phase film was estimated by assuming it to be partially strained to the underlying AlN layer. The asymmetric (10.5) XRD reflection was obtained in addition to the symmetric (0002) XRD reflection. Using the iterative method described in Section 3.4.4, an In composition of $x \sim 0.40$ was estimated.

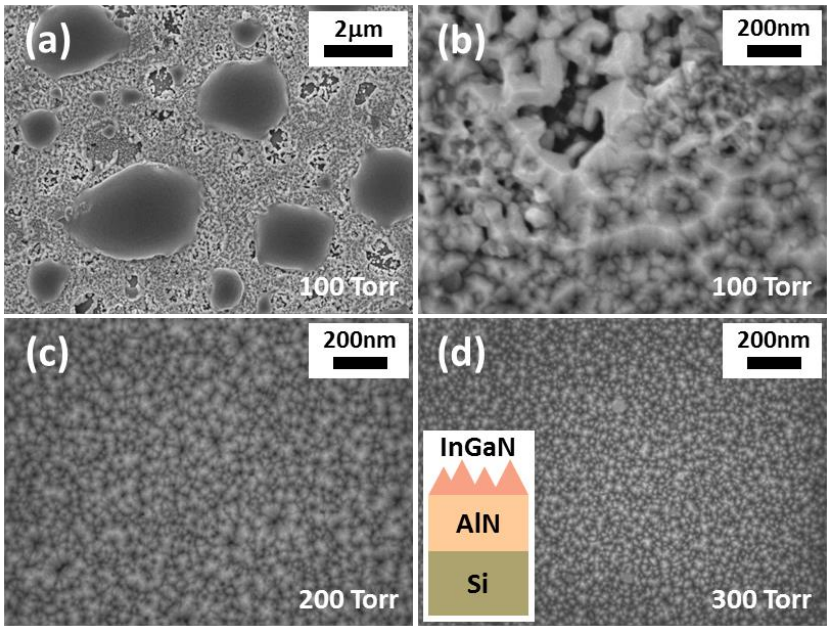


**Figure 5.2** FESEM images of InGaN films grown for 12 min on AlN/Si(111) substrates at 655°C with pressures of (a)-(b) 100 Torr, (c) 200 Torr, and (d) 300 Torr. Inset shows a schematic of the cross-sectional profile of (d).

### 5.2.4. Influence of Growth Temperature

#### 5.2.4.1. Structural Characteristics and Composition

In subsequent growths, the growth pressure was maintained at 300 Torr, while the growth temperature was varied upwards to a maximum of 795°C, other conditions remaining constant. The corresponding (0002) $2\theta$-$\omega$ XRD scans at various temperatures are given in Figure 5.3. In each case, a solitary InGaN(0002) peak is observed, indicating single phase InGaN was achieved. However, the In composition $x$ decreases with rise in temperature as depicted in the shift of the $2\theta$ angular position towards higher values. $x$ were calculated as before and plotted against the temperature in Figure 5.4. The general monotonic decrease in $x$ with increasing temperatures is attributable to the increasing equilibrium vapour pressure of $N_2$ over InN within the InGaN alloy [72] as discussed in Section 2.3.4.

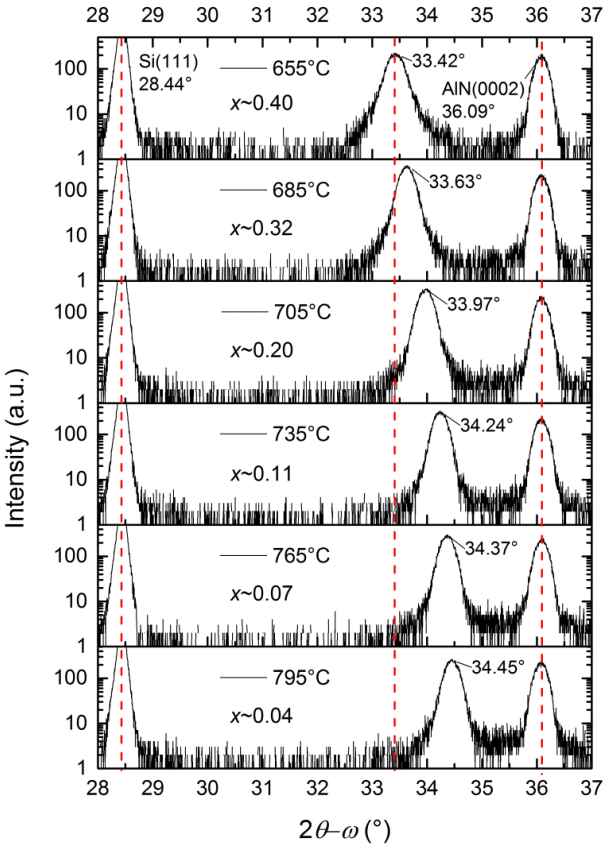


**Figure 5.3** XRD (0002) $2\theta$-$\omega$ scans of InGaN films grown on AlN/Si(111) substrates at 300 Torr with temperatures of 655°C, 685°C, 705°C, 735°C, 765°C, and 795°C. Single phase InGaN was achieved at all temperatures, with the $2\theta$ angular position increasing (or In content decreasing) with increasing temperature.

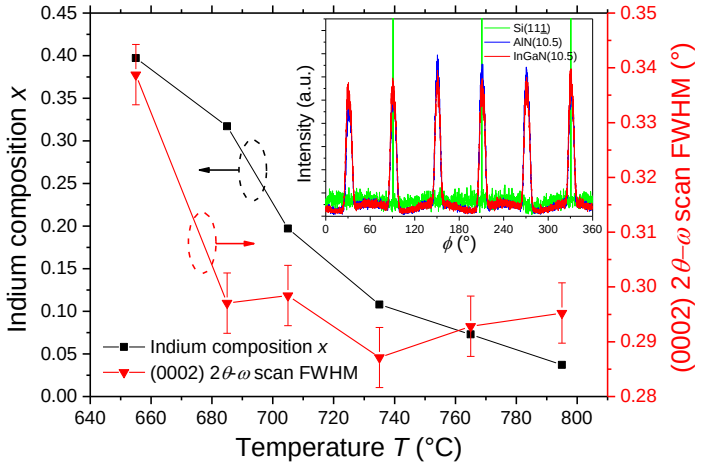


**Figure 5.4** Plot of the dependence of In content $x$ and XRD (0002) $2\theta$-$\omega$ FWHM in $In_xGa_{1-x}N$ with growth temperature. A decrease in $x$ and FWHM with temperature increase are observed. Inset: (10.5) $\phi$-scans of an InGaN film grown at 765°C and the AlN buffer showing the six-fold in-plane symmetry relative to the three-fold in-plane symmetry of the Si(111) substrate.

The (10.5)-$\phi$ azimuthal scan of the InGaN film (grown at 765°C) relative to the AlN/Si(111) substrate is presented in the inset of Figure 5.4. The coincident six-fold in-plane symmetry of the (0002)-oriented InGaN and AlN layers relative to the three-fold in-plane symmetry of the Si(111) substrate is apparent. Taken together, the XRD results revealed that the as-grown InGaN film can best be described as textured epitaxial [313] and oriented in the *c*-direction with a wurtzite crystal structure with the following epitaxial relationship with AlN on Si: InGaN(0001) [2$\underline{1}\underline{1}$0] || AlN(0001) [2$\underline{1}\underline{1}$0] || Si(111) [01$\underline{1}$]. This epitaxial relationship remains the same in other single phase samples and corresponds to that depicted in Figure 2.3. The azimuthal width of the InGaN peaks follows that of the underlying AlN layer and indicates that the latter exerts a strong influence on the growth quality of the former. An average azimuthal width of $\Delta\phi \sim 7.5°$ is measured for both layers. The full-width-at-half-maximum's (FWHMs) of the InGaN (0002) $2\theta$-$\omega$ curves at each growth temperature *T* are also plotted in Figure 5.4 and shows a sharp drop as *T* is raised from 655°C to ~ 685–705°C. The comparatively large FWHM at ~ 655°C suggests that significant alloying, compositional non-uniformity and inhomogeneous strain are present [283]. Noting that the estimated experimental uncertainty in FWHM is ~ 0.011°, the FWHM (and aforementioned effects) may be considered to level off at *T* higher than ~ 685-705°C. The levelling off is contributed in part by the composition of the ternary $In_xGa_{1-x}N$ alloy tending towards the binary GaN compound (reduced *x*). Increase in *T* up to 685-705°C exerts a strong influence in improving InGaN compositional and strain homogeneity as growth quality is in the regime limited by *T* [125]. Beyond this *T* range, improvement is possibly limited by other factors, e.g. the structural quality of the underlying AlN layer, etc. The structural qualities of the epitaxial layers are next investigated by measuring the FWHM of their (0002)-$\omega$ rocking curves. The results are plotted in Figure 5.5.

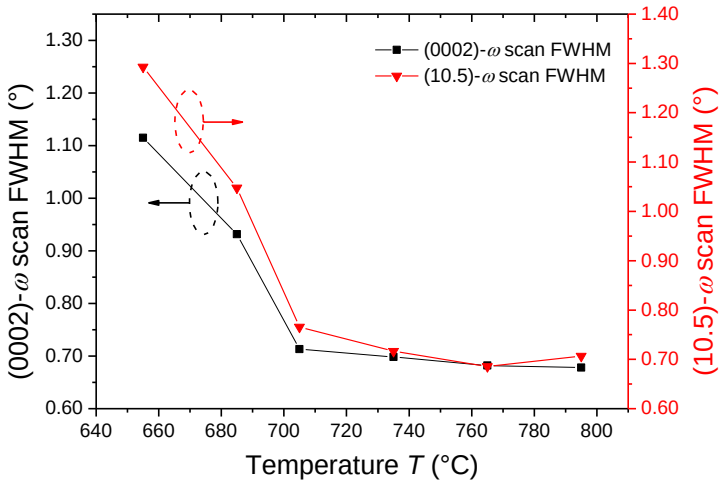


**Figure 5.5** Plot of the dependence of the FWHM of the (0002)-$\omega$ and (10.5)-$\omega$ XRD rocking curve with temperature $T$ for $P$ = 300 Torr. For both cases, an appreciable reduction in FWHM is observed when $T$ is reduced to 705°C but the decrease plateaus off at higher $T$.

The FWHM of the (0002)-$\omega$ rocking curve is an indicator of the extent of lattice tilt or density of TDs with screw component in the textured film. The observed general reduction of FWHM is consistent with improvements in crystal quality with higher growth temperature as reported in literature [72]. Increase in temperature to 705°C results in a notable reduction in the FWHM (from ~ 1.11° to ~ 0.71°), denoting an appreciable improvement in the crystal quality. Increase in temperature from 705°C to 795°C continues to decrease the (0002)-$\omega$ FWHM but the marginal reduction (or gain in crystal quality) diminishes with increasing temperature. A value of ~ 0.68° is attained at 795°C. A similar dependence of the FWHM of the asymmetric (10.5)-$\omega$ rocking curves with temperature is observed (Figure 5.5), this quantity being a measure of lattice tilt as well since the XRD inclination angle is low. The appreciable increase in crystal quality at ~ 705°C correlates to changes in morphology and photoluminescence measurements which are examined later. Improvement in properties of MOCVD-grown InGaN in the vicinity of 700°C has similarly been reported on GaN/sapphire [125].

The range of levelled-off FWHM values (0.68° to 0.71°) of the InGaN (0002)-$\omega$ rocking curves lies in the locale of the AlN (0002)-$\omega$ rocking curve FWHM at 0.69°. Hence, we posit that at temperatures beyond ~ 705°C, for the relatively thin InGaN layers (~ 29 to 45 nm), the crystal quality is in the regime limited by the buffer quality and lattice mismatch, such that higher temperatures are unlikely to bring about appreciable improvement as $x$ approaches 0. Lower FWHMs may be afforded by increasing the layer thickness which improves the structural quality to a limited extent by coalescence and dislocation annihilation. For instance, prolonging the duration of growth at 765°C from 12 min to 48 min reduces the (0002)-$\omega$ FWHM further from 0.68° to ~ 0.65°. The general inadequate structural quality is a consequence of the highly mismatched and defective thin AlN buffer being used but which cannot be avoided due to two reasons. First, to prevent Ga meltback etching and unintentional nitridation of the Si substrate when subjected to MOCVD growth temperatures. And, second, to facilitate a low-resistance InGaN/Si interface.

#### 5.2.4.2. Morphology

The evolution in morphology of the InGaN samples with growth temperature was examined using FESEM and shown in Figure 5.6. The average thickness of the films grown at 655°C, 685°C, 705°C, 735°C , 765°C and 795°C are 48 nm, 47 nm, 45 nm, 41 nm, 35 nm and 29 nm respectively. These values and the respective RMS surface roughness obtained by AFM are also included in Figure 5.6. At low temperatures (< 705°C), the InGaN film is composed of a densely packed layer of fine InGaN islands in intimate contact with each other. Such a morphology seems to suggest a polycrystalline structure. However, due to the existence of an epitaxial relation of the film with the underlying AlN/Si template as described earlier, it may be more apt to describe the structure as highly textured epitaxial.

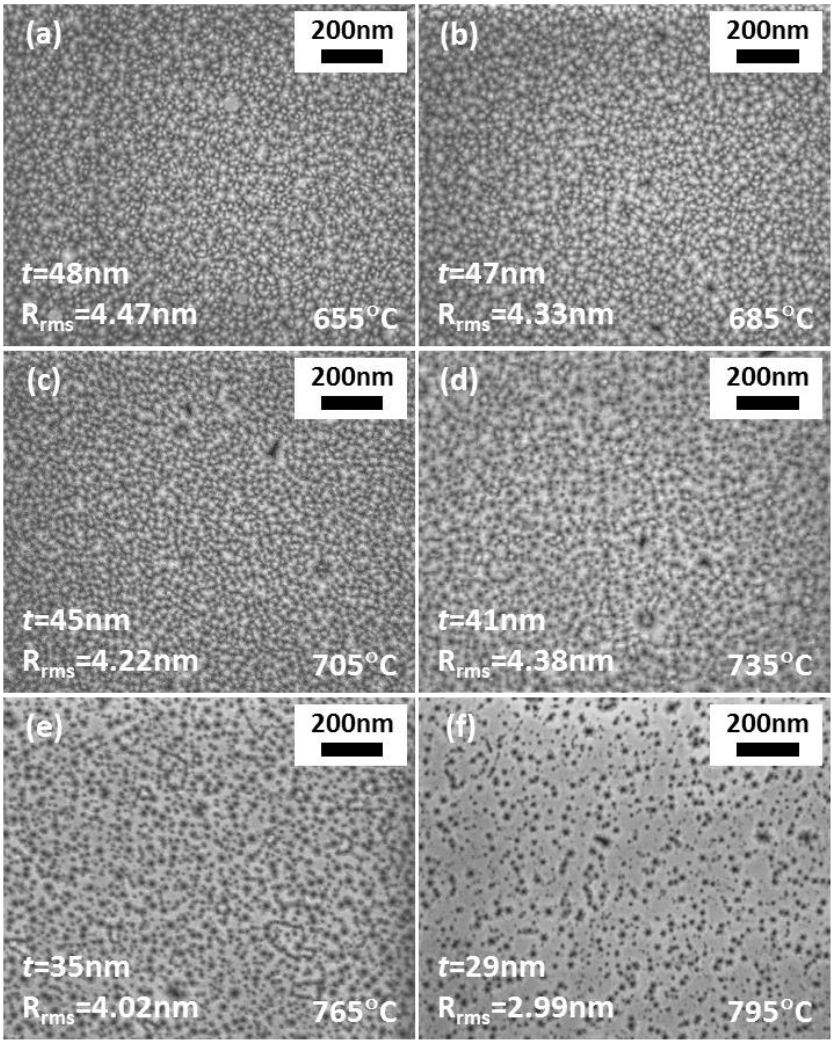


**Figure 5.6** FESEM images of InGaN films grown on AlN/Si(111) substrates at 300 Torr with temperatures of (a) 655°C, (b) 685°C, (c) 705°C, (d) 735°C, (e) 765°C, and (f) 795°C. The morphology evolves from a fine granular structure to a more planarized surface dotted with pits as temperature increases.

Increase in temperature to ~ 705°C and above causes a notable change in morphology. Island density is reduced while island size is increased within a more interconnected morphology. The island boundaries and V-pits (recessed regions) are correspondingly reduced. Despite the changes in morphology, widespread coverage of the surface is maintained. The rough surfaces are indicative of three-dimensional growth. Samples grown at 765°C and 795°C register notably lower roughnesses as explained later. Despite the tensile stress exerted by the Si(111) substrate on the AlN buffer, a large lattice mismatch (~ 1.7% to 6.6%) still exists between the small lattice constant AlN

and the InGaN epilayer. This leads to substiantial compressive strain experienced by the latter. A Stranski-Krastanov growth mode is hence probable [310] where the stress field tends to force adatoms to coalesce and the formation of islands can partially relax the strain energy through elastic relaxation [311]. A change in temperature influences several physical processes during MOCVD. In this work, we posit that the key temperature-dependent parameters that bear a significant impact on the observed InGaN film morphology are adatom surface mobility and In species adsorption/desorption. The following describes the effects of these parameters on the morphology as temperature changes.

Under lower deposition temperatures, reduced adatom mobility and diffusion length contribute to higher island nucleation density and smaller island sizes [311]. Further, a higher concentration of adsorbed In species exists at lower temperatures facilitating In incorporation to form higher In content InGaN. The latter presents a larger lattice mismatch with the underlying AlN layer which also tends to favour smaller island sizes for strain relaxation. The small-island growth mode and widespread coverage contribute to the formation of the densely packed, fine island appearance of InGaN under low deposition temperatures as seen in Figure 5.6(a)-(b).

Increase in temperature improves the surface mobility of species, reducing island density but increasing island size. Desorption of In species from the surface also increases such that the amount of In incorporated decreases. The lower In content InGaN has a smaller lattice mismatch with the underlying AlN layer which permits larger/broader island sizes for strain relaxation. This has the effect of reducing the network of island boundaries and V-pits, or recessed regions where coalescence is incomplete. In addition, the higher evaporation of In species on the surface can cause a reduced growth rate. This will account for the reduction in film thickness observed.

We further suggest that the strain energy of lower In content and smaller lattice mismatched InGaN is likely reduced with the effect of delaying the onset of 3D growth. Hence, a slower growth rate may allow the smoother morphology prior to 3D growth in the Stranski-Krastanov growth mode to be observed as shown in Figure 5.6(e)-(f) for InGaN samples grown at 765°C and 795°C. Increased surface mobility will also contribute to the reduced surface roughness. V-pits orginate from incomplete coalescene of neighbouring islands, TDs and from the underlying AlN layer. The net effect of an increase in temperature would be the formation of broader InGaN islands of lower spatial density, island boundaries and V-pits, and show a tendency towards coalescence.

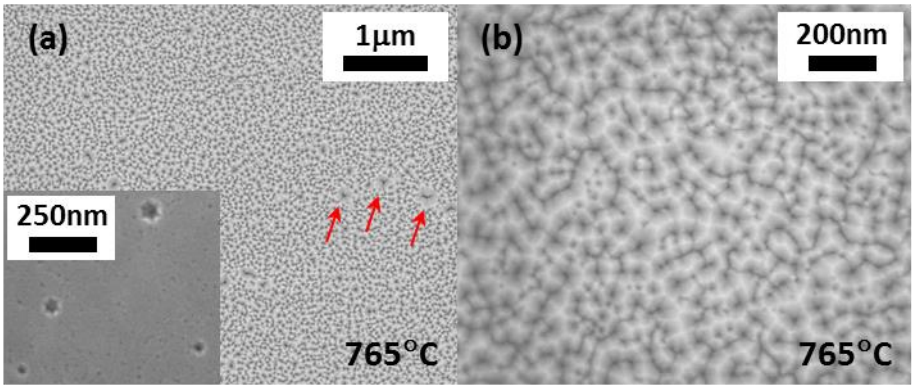


**Figure 5.7** FESEM images of InGaN films grown on AlN/Si(111) substrates at 300 Torr and 765°C for a prolonged growth of 48min. (a) Low magnification, and (b) high magnification. Inset of (a) shows the pre-existing V-pits in the underlying AlN/Si(111) substrate.

Prolonging the growth duration increases the layer thickness and maintains the single phase nature of the epitaxial InGaN layers. Figure 5.7 shows the FESEM images of the morphology of an InGaN sample grown at 765°C at 300 Torr for 48 min under low and high magnification. The more planarized morphology of the sample grown at the same conditions for 12 min as shown in Figure 5.6(e) has given way to 3D growth. However, the surface remains homogeneous without gross defects or In droplets. The island size is larger due to coalescence such that island boundaries are reduced. Strain

relaxation afforded by the coarser 3D morphology may also explain an increase in *x* from ~ 0.073 to ~ 0.087 measured in the sample grown for 48 min. Large pits indicated by red arrows in Figure 5.7(a) arise from pre-existing large V-pits in the underlying AlN layer as seen in the inset of Figure 5.7(a). However, a faceted island morphology remains.

### 5.2.4.3. Photoluminescence (PL)

μ-PL measurements were performed at room temperature using a 325 nm He-Cd laser as the excitation source on the single phase samples. The PL spectra are plotted in Figure 5.8. While the XRD plots in Figure 5.3 all show single InGaN $2\theta$-$\omega$ (002) diffraction peaks and each can be fitted by a simple Gaussian function, the PL emission spectra are more complex. InGaN samples grown at temperatures less than 705°C do not emit any detectable PL and are not shown. The lack of PL at growth temperatures lower than 705°C (or samples with In content above 20%) correlates with the high FWHMs of the $\omega$-rocking curves (Figure 5.5), indicative of large lattice tilt, and a morphology consisting of fine islands with extensive island boundaries in the samples as seen in Figure 5.6(a)-(b). Low temperature growth (< 700°C) is often associated with formation of C-related impurities, N- and Ga- vacancies, and structural defects [125, 126]. The inadequate crystal quality and low growth temperatures result in a high concentration of non-radiative recombination centers and is responsible for the absence of detectable PL. The onset of PL occurs at ~ 705°C and is characterized by broad band emission at wavelengths of about 470 nm to 620 nm characteristic of radiative recombination involving defects. This relates to the drop in the FWHMs of the $\omega$-curves, and is consistent with a change in morphology towards larger island sizes. The improvement in crystal quality reduces the concentration of non-radiative recombination centers, thus permitting PL emission. Further increase in temperature beyond 705°C results in near-band-edge

(NBE) emission as indicated by the emergence of narrow and high intensity PL peaks. At 735°C, a secondary peak at 487nm is observed in addition to the primary peak at 436 nm. The primary peak corresponds to NBE emission as confirmed by calculation from XRD measurement, while the secondary peak likely arises from defect-related emission. As temperature rises, the PL spectra are characterized by a prominently solitary peak that narrows in FWHM and shifts towards shorter wavelengths, consistent with improvement in crystal quality or reduction in defect states, and reduction in *x* respectively. A maximum intensity is observed at 765°C. The PL peak for 795°C is diminished due to reduced InGaN thickness.

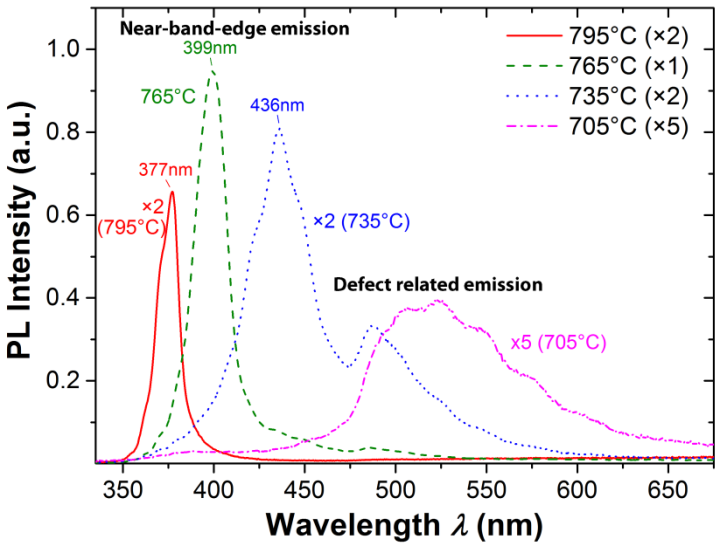


**Figure 5.8** Room-temperature PL of the InGaN films grown at 300 Torr with temperatures from 705°C to 795°C. No PL was detectable for samples grown at 655°C and 685°C.

### 5.2.5. Conclusion

In this work, we demonstrate the growth of single phase, textured epitaxial $In_xGa_{1-x}N$ (for *x* up to 0.40) directly on AlN/Si(111) substrates through the use of elevated growth pressures. Growth at 300 Torr promotes dense and uniform nucleation of InGaN islands, suppresses InGaN phase separation and In droplet formation. Low growth temperatures permitted higher In incorporation but do so at the expense of

crystal quality. Samples grown at temperatures lower than 705°C are characterized by densely packed fine islands, appreciably higher lattice tilt as indicated by a substantial increase in the (0002)-$\omega$ FWHM (from ~ 0.71° to ~ 1.11°), and absence of detectable room temperature PL. Increase in temperature to 705°C and above resulted in a notable improvement in crystal quality as shown by a change in morphology towards larger island sizes, drop in lattice tilt and increase in room temperature PL intensity. However, In content was reduced. Further increase in temperature does not improve the crystal quality significantly as this is now limited by the lattice mismatch with the underlying AlN layer. Innovative growth strategies are thus needed to overcome this limitation. One such strategy is nano-SAG which forms the focus of this thesis.

## 5.3. Three-Dimensional InGaN Nanostructures on AlN/Si(111) Substrate

### 5.3.1. Experimental Procedure

In Section 5.2, pre-requisite conditions and influence of growth parameters in the epitaxy of single phase InGaN films on AlN/Si(111) substrates were examined. Taking into consideration the optimum conditions for film growth, nano selective area growth (nano-SAG) of three-dimensional InGaN nanostructures was performed on AlN/Si(111)-based Type A template. Substrate pre-annealing in $H_2$ at 1000°C was employed with subsequent nano-SAG at 780°C and 300 Torr. Continuous flux MOCVD was still employed with other growth parameters similar to that described in Section 5.2.1. However, growth duration was prolonged to 48 min (instead of 12 min). As described in Section 4.2.2, Type A template consists of a nanoporous $SiN_y$ mask fabricated by S-FIL, Ti masking and RIE on AlN/Si(111) substrate. The nanoporous pattern comprises a highly-ordered hexagonal array of holes with diameters of ~ 210 nm and a period of 300 nm. The close-packed axis of the array was oriented parallel to the [$\underline{11}$2] direction of the Si(111) substrate.

The objective of nanostructuring is to achieve single phase InGaN with higher In content and improved crystal quality. The qualities of the InGaN nanostructures are compared against a control InGaN thin film grown on AlN/Si(111) substrate in the same run. This directly tests the postulation regarding the benefits of InGaN nanostructuring discussed in Section 1.2.4.3.

### 5.3.2. Morphology

Figure 5.9(a)-(b) show the morphology of the hexagonal array of nano-SAG InGaN nanostructures after 48 min of MOCVD. Each nanostructure is shaped as a hexagonal nanopyramid that has emerged from a pore of the $SiN_y$ template. Good growth selectivity was obtained using the $SiN_y$ template with InGaN nucleation and growth confined within the template openings in the early growth stage. Truncated hexagonal nanopyramids totally confined within the pores were first observed as seen in Figure 5.9(c). Each bears six inclined side facets and is topped by a V-pitted horizontal (0001) facet. With further growth, each truncated nanopyramid developed into a more complete hexagonal nanopyramid with six smooth side facets which overgrew onto the $SiN_y$ mask. After 48 min of growth, an average base dimension ~ 270 nm was achieved. The facet inclination angle was measured in TEM and AFM to be ~ 62° indicating that they are {11$\underline{1}$01} planes. These slow-growing, energetically stable planes, frequently encountered in III-nitrides growth [59, 143, 147, 203, 314], govern the growth morphology in accordance to Wulff's theory [142]. A growth model is proposed later to account for the growth progression and other structures observed in TEM.

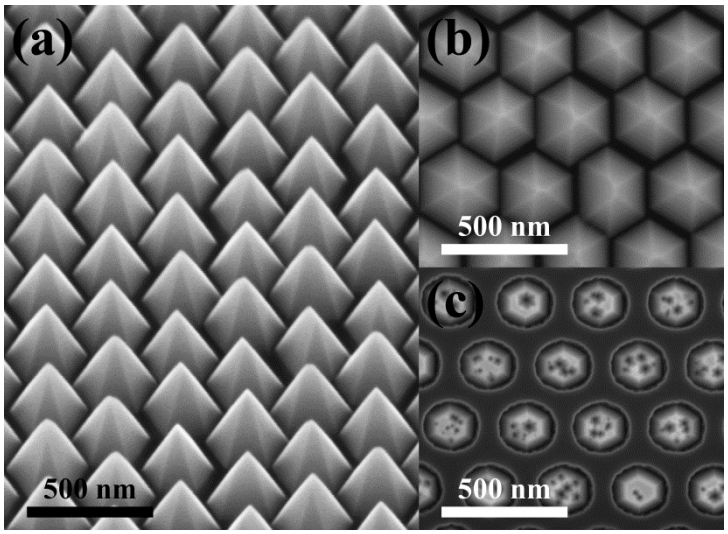


**Figure 5.9** FESEM images of InGaN nanostructures grown via nano-SAG through a $SiN_y$ template on AlN/Si(111) substrates. (a) and (b) Hexagonal array of hexagonal nanopyramids grown for 48 min when viewed at an angle of 40° and at plan view respectively. (c) Hexagonal array of truncated hexagonal nanopyramids in the early growth stage of nano-SAG, each confined within a pore of the $SiN_y$ template and possessing a pitted horizontal top surface.

Drawing upon reports on the SAG of GaN by MOCVD (see Section 2.4.3), the slow growth rate of the {1$\underline{1}$01} planes is related to their termination in N atoms arising from high V/III ratio growth conditions and Ga-polarity growth. The {1$\underline{1}$01} planes of the Ga-polar structures are passivated by H and thus lead to stable surfaces with low growth rates. The atomic configuration of Ga-polar structures is shown in Figure 2.8. However, for MOCVD of GaN, the H-passivated surface can be destabilized under Ga-rich, low V/III ratio conditions as discussed in Section 2.4.5.2.1. The unstable surface is then susceptible to etching by $H_2$ via Ga-H and N-H formation, thus aiding growth of GaN micro- or nanorods with vertical sidewalls. However, for the MOCVD of InN and InGaN, high V/III ratios are required to avoid In droplet formation. This explains the lack of reports on high aspect ratio InN and InGaN nanostructures grown by MOCVD. Hence, reported InN and InGaN nanostructures predominantly bear hexagonal pyramidal shapes [203, 212, 240] as seen in this work. As discussed in Section 2.4.5.2.1, reports in literature has focused on the SAG of GaN nanostructures "homoepitaxially" over GaN seed layers to achieve nearly

defect-free quality [49, 58, 61, 232, 237] and “heteroepitaxially” on AlN buffer layers [206]. While InGaN nanostructures have been achieved in MOCVD via SAG [219, 221], these methods invariably involve GaN as a seed layer. To our knowledge, SAG of InGaN nanostructures directly on AlN/Si(111) has yet to be demonstrated. We posit that instead of growing InGaN into rough planar films with high defect densities on highly mismatched and defective AlN films, it may be more meaningful to look into the growth of spatially ordered, epitaxial 3D InGaN nanostructures where a nano-SAG approach may improve structure quality. This forms the focus of this work which we believe will fill a void that has yet to be addressed in the community and has direct implications in the development of InGaN/Si tandem solar cell applications.

The morphology of the control InGaN film is shown in Figure 5.10(a)-(b) and is similar to that observed in Section 5.2.4.2. A regular morphology like that in SAG is not observed due to the absence of control over the sites for nucleation and growth. In the early growth stage, the InGaN film is populated with a high density of nano-scale pits as seen in Figure 5.10(c). The pits likely arose from pre-existing V-pits and dislocations in the highly defective AlN buffer layer, and the generation of new dislocations from the highly lattice mismatched InGaN growth. As growth proceeded, partial coalescence resulted in a reduction in pit density and the formation of an interconnected 3D faceted island morphology. The 3D growth mode, resembling the later stage of Stranski-Krastanov growth, allows relaxation of the strain within the InGaN layer. This generates a rough, undulating surface consisting of ridges and troughs (pits), with the undulations becoming more pronounced with growth duration.

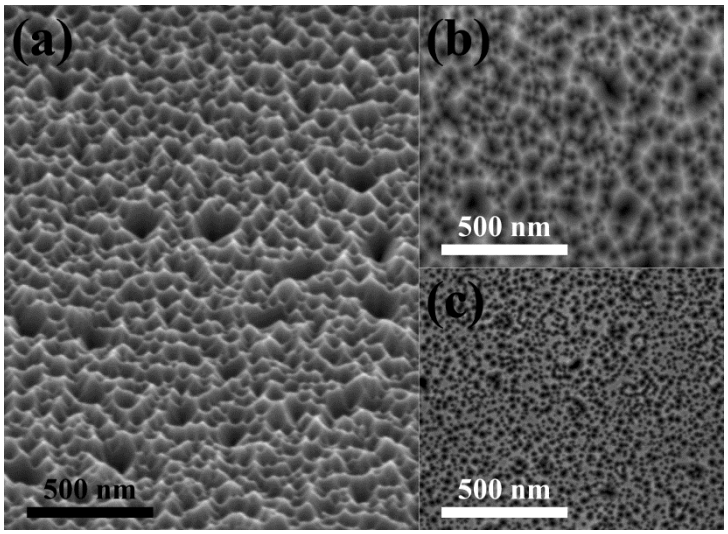


**Figure 5.10** FESEM images of the InGaN control film grown on AlN/Si(111) substrates. (a)-(b) Rough undulating morphology after 48 min of growth when viewed at an angle of 40° and at plan view respectively. (c) High density of nano-scale pits in the early growth stage.

### 5.3.3. Structural Characteristics

#### 5.3.3.1. Cross-Sectional TEM

The structural characteristics of the InGaN samples were examined by cross-sectional TEM. Diffraction contrast imaging under two-beam condition in bright field (BF) and weak beam dark field (WBDF) was performed along the [1$\underline{1}$00] zone axis for **g** = 0002 for viewing threading dislocations (TDs) with screw character. In both samples, the AlN buffer layer, ~ 150 nm thick, is riddled with TDs. These arise during growth from the mismatch in lattice parameters between AlN and Si (~ 19%). For the control sample, TDs from the underlying AlN buffer layer propagate directly into the InGaN layer with a line direction of [0001], without bending and typically terminate in a V-pit as seen in Figure 5.11(a)-(b) and as reported by Northrup et al. [115]. The calculated inclination angles (~ 62°) of the pit sidewalls with respect to the *c*-plane indicate that they are {1$\underline{1}$01} planes as observed by Liliental-Weber et al. for InGaN grown on GaN [69]. The high density and close proximity of pits to each other, and competing facet growth lead to a complex undulating surface consisting of ridges formed by the meeting of pit sidewalls, and troughs formed by the pits. The rough

morphology is also energetically favoured for strain relaxation in InGaN. TDs are also formed at the InGaN/AlN interface since the InGaN layer thickness (~ 140 nm) exceeds the critical thickness [54]. The selected area electron diffraction (SAED) pattern along the [2$\underline{1}\underline{1}$0] zone axis and the corresponding high-resolution TEM (HR-TEM) image of the InGaN/AlN interface are shown in Figure 5.11(c) & (d) respectively. The later reveals the defects formed at the InGaN interface due to lattice mismatch growth.

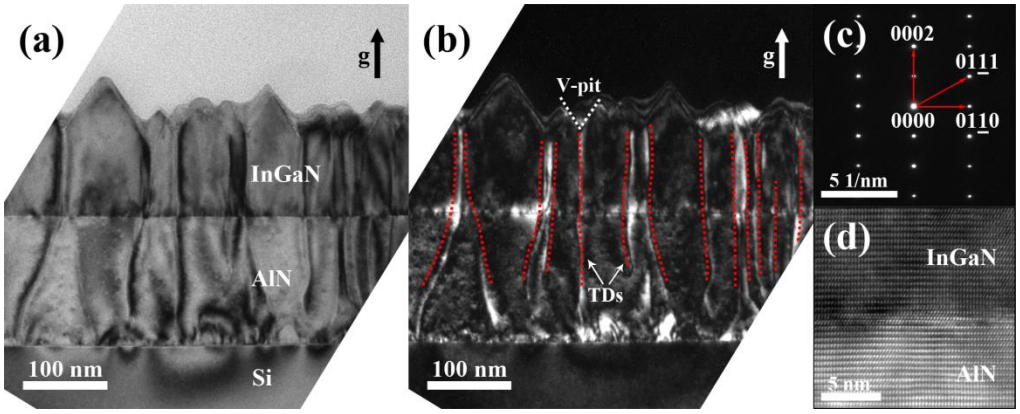


**Figure 5.11** Cross-sectional TEM images of the InGaN control film. (a) Bright field, and (b) weak beam dark field images along the [1$\underline{1}$00] zone axis with **g** = 0002. The dotted red lines in (b) delineate the threading dislocations (TDs) propagating from the underlying AlN layer into the InGaN film. The TDs traverse the film along the [0001] line direction and each typically terminates in a V-pit. (c) SAED pattern of the InGaN layer along the [2$\underline{1}\underline{1}$0] zone axis, and (d) corresponding high-resolution TEM image of the InGaN/AlN interface showing interfacial defects due to lattice mismatch InGaN film growth.

The BF and WBDF TEM images of a nano-SAG nanopyramid are shown in Figure 5.12(a) and (b) respectively. While TDs similarly exist due to dislocations threading from the defective AlN layer and generation of new TDs at the InGaN/AlN interface, the dislocation behavior is notably different. Three main observations can be made and are labelled as (1), (2) and (3) in Figure 5.12(b). First, some TDs, labelled as (1), in the AlN layer are "blocked" by the $SiN_y$ template and prevented from propagating into lateral *overgrown* regions of the InGaN nanostructure. In extension, for a completely coalesced film, ~ 56% of the TDs would be "blocked" by the $SiN_y$

template, based on the area fraction occupied by the template which bears a hexagonal array of circular pores. See Equation (1-1). Second, most TDs, labelled as (2), in a nanostructure bend towards and/or remain in the axial region, such that TDs are increasingly confined within the axial region as growth proceeds. The persistence of an axial TD to continue propagating axially has been theoretically calculated by Eshelby [62] and modeled by Colby et al. [58] When the TD is maintained in the center of a nanorod, a state of metastable equilibrium can be achieved. Active bending of TDs towards the central core may also be linked to the formation of an embedded central void within the nanopyramid which presents a free surface for TD termination during growth. Void formation has been observed by Cao et al. [241] in selective area grown GaN nanopyramids and is discussed in Section 5.3.3.2.

The TD bending mechanism in the second observation is similar to that described in our third observation denoted as (3) in Figure 5.12. Here, TD bending towards the free {1$\underline{1}$01} surface of the nanopyramid occurs, albeit to a smaller extent compared to bending of TDs towards the axial region. This arises for TDs located approximately more than halfway radially outwards from the axis of the nanopyramid. The phenomenon is similar to that reported by Eshelby [62] and Colby et al. [58], and can be explained by the action of image forces which tend to pull TDs located at such distances out of the nanostructure. In all, the net effect of nano-SAG of InGaN nanopyramid on the dislocation behavior is that the regions near the six bounding {1$\underline{1}$01} facets away from the axial region are visibly less defective.

Some of the TDs present in InGaN in the nano-SAG and control samples which are visible under **g** = 0002 retain their contrast under **g** = 1$\underline{1}$00 (not shown here). This indicates that they are of mixed character containing both screw and edge components. The SAED pattern along the [2$\underline{1}\underline{1}$0] zone axis and the corresponding

HR-TEM images of the nanopyramid tip, epitaxial lateral overgrown (ELO) region and InGaN/AlN interface are shown in Figure 5.12(c), (d), (e), and (f) respectively.

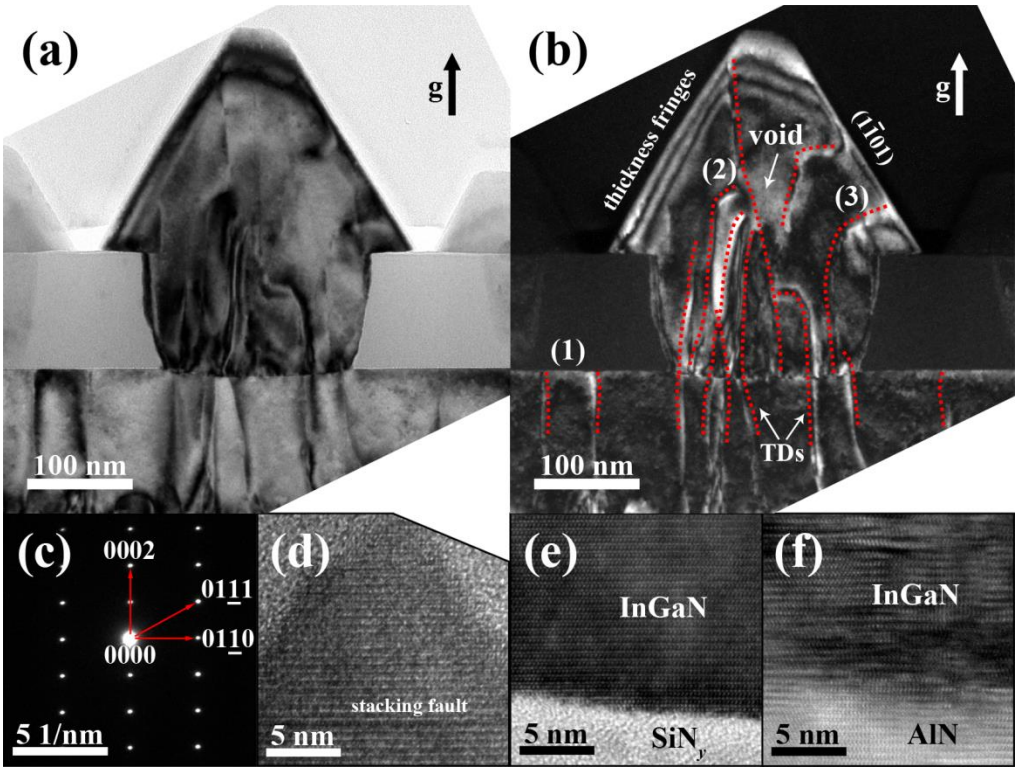


**Figure 5.12** Cross-sectional TEM images of InGaN nanopyramids grown via nano-SAG through a nanoporous $SiN_y$ template on AlN/Si(111) substrate. (a) Bright field (BF), and (b) weak beam dark field (WBDF) images along the [11$\underline{0}$0] zone axis with **g** = 0002 of a heavily dislocation-laced InGaN nanopyramid. Dotted red lines delineate the approximate positions of threading dislocations (TDs). Dislocation termination at the $SiN_y$ mask (1), dislocation congregation within the nanopyramid central core (2), and dislocation bending to the {11$\underline{0}$1} free surfaces of the nanopyramid can be observed (3). Thickness fringes are observed at the inclined sides of the nanopyramid due to significant thickness variation present at the intersection of the {11$\underline{0}$1} facets in this cross-section. A small void is also observed due to imperfect coalescence. (c) Selected area electron diffraction (SAED) pattern of the InGaN layer along the [2$\underline{1}\underline{1}$0] zone axis, and corresponding high-resolution TEM images of (d) the nanopyramid tip showing a stacking fault, (e) the epitaxial lateral overgrown (ELO) region showing the improved growth quality, and (f) the InGaN/AlN interface showing a high density of stacking faults and coalescing dislocations.

Within a distance of ~ 20 nm from the InGaN/AlN interface, a high density of stacking faults and coalescing dislocations is observed. (Figure 5.12(f)) These arise from the highly mismatched heteroepitaxy and possibly etch damage of the AlN layer sustained during $SiN_y$ template fabrication. The observations contrast with that of the control sample which exhibit an apparently less defective interfacial region (Figure

5.11(d)) due to a smaller lattice mismatch (arising from a lower In content in InGaN as shown later) and the absence of etch damage. Despite this, crystal quality in the nano-SAG sample improves markedly away from the interface due to dislocation annihilation, relaxed growth and dislocation bending as mentioned earlier. The ELO or the nanopyramid {11$\underline{0}$1} facet regions are of visibly improved quality as seen in Figure 5.12(e). However, at the nanopyramid tip, stacking faults can be observed along with the congregation of TDs. (Figure 5.12(d)).

#### 5.3.3.2. Growth Model

Considering the morphology observations in Section 5.3.2, we propose a growth model, as illustrated in Figure 5.13, to account for void formation. During growth, the incoming precursor flux impinges all over the sample surface. (Figure 5.13(a)) However, nucleation on the $SiN_y$ mask is destabilized such that InGaN nucleates and grows selectively in the unmasked regions within the pores. The destabilized adatoms on the mask migrates to the pores and presents an additional supply of reactant flux. Initially, the deposited InGaN is densely pitted like the control. But confinement of growth within a pore promotes the filling up of pits to form a truncated nanopyramid bound by six smooth slow-growing {11$\underline{0}$1} inclined sidewalls with a pitted (0001)-top. (Figure 5.13(b)) The structure has a hexagonal base which does not follow the circular contour of the pore due to growth selectivity. (Figure 5.9(c)) As growth proceeds, the structure enlarges with an increase of {11$\underline{0}$1} sidewall area and a corresponding decrease in (0001) top area due to the slower growth rate in the <11$\underline{0}$1> direction relative to the [0001] direction. (Figure 5.13(c)) This is in accordance to Wulff's theory where crystal facets with the slowest growth rate governs the morphology. [142] Due to the increasing sidewall area that must be traversed by the migrating adatoms from the $SiN_y$ mask arriving at the pore periphery to reach the nanopyramid center, the reactant flux and hence growth rate at the center is less than

that at the periphery, forming a cratered hexagonal nanopyramid. (Figure 5.13(d))

Over time, the crater rim coalesces but traps an embedded void. (Figure 5.13(e))

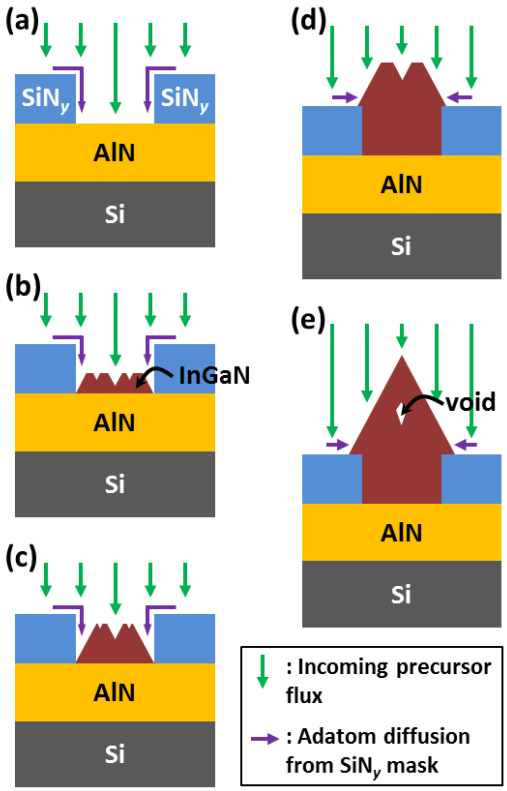


**Figure 5.13** Schematic showing growth model of InGaN nano-SAG through a nanoporous $SiN_y$ mask on AlN/Si(111) substrate. In addition to vapour phase mass transport of reactants (vertical green arrows), adatom surface migration from the $SiN_y$ mask presents an additional supply of reactants (purple arrows). (a) Starting substrate. (b) Formation of pitted truncated nanopyramid. (c) Truncated nanopyramid grows with an increase in sidewall area and narrowing of top. (d) Formation of central crater due to smaller reactant flux and hence growth rate at the center relative to the periphery. (e) Crater rim coalesces and cuts off crater to form an embedded void.

### 5.3.3.3. High-Resolution XRD

Figure 5.14 shows the (0002) $2\theta$-$\omega$ high-resolution X-ray diffraction (HR-XRD) scans obtained in a triple axis configuration for both samples. In each case, three peaks are observed, namely, the Si(111) substrate peak at 28.44°, the AlN(0002) peak at 36.11°, and the InGaN(0002) located between them. No phase separation or In droplets are observed. While the InGaN(0002) peak of the control has a smaller spread (FWHM ~ 0.105°), the calculated In content is notably low at ~ 6.1%. In

contrast, the InGaN nanopyramids grown by nano-SAG showed a ~ 74% relative increase in In content to ~ 10.6%. However, greater compositional variation is present as indicated by a broader InGaN(0002) peak (FWHM ~ 0.155°).

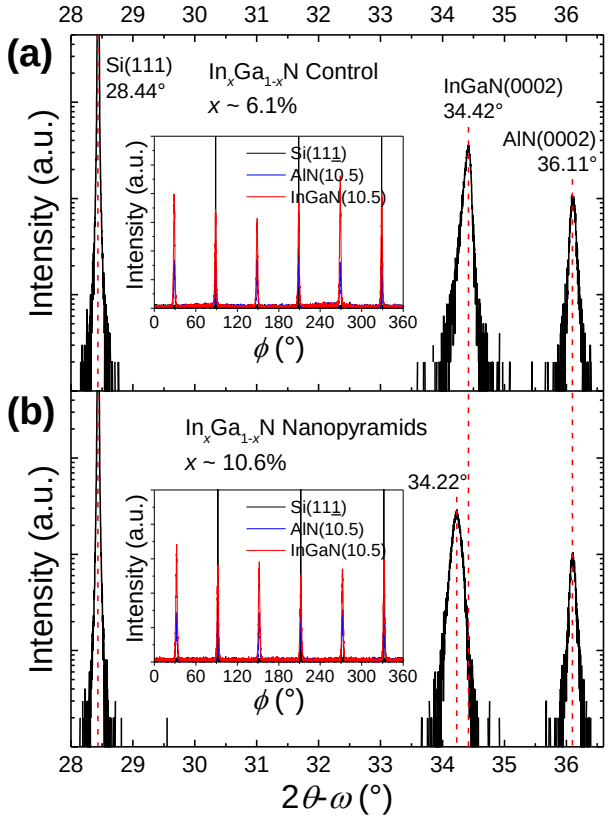


**Figure 5.14** XRD (0002) 2$\theta$-$\omega$ scans of (a) InGaN control grown on unpatterned AlN/Si(111) substrate, and (b) InGaN nanopyramid array grown via nano-SAG on AlN/Si(111). The insets show the respective skew symmetric (10.5)-$\phi$ azimuthal scans of InGaN and AlN showing the coincident six-fold in-plane symmetry. An epitaxial relationship of InGaN(0001) [2$\underline{1}$10] || AlN(0001) [2$\underline{1}$10] || Si(111) [01$\underline{1}$] can be established.

The skew symmetric (10.5)-$\phi$ azimuthal scans, included in the inset of each (0002) 2$\theta$-$\omega$ spectrum in Figure 5.14, show the coincident six-fold in-plane symmetry of the (0002)-oriented InGaN and AlN layers, indicating that the InGaN grown on both samples follow the same epitaxial relationship as the underlying AlN layer. Taking into account, the skew symmetric (11$\underline{1}$)-$\phi$ azimuthal scan of the Si(111) showing the coincident three-fold in-plane symmetry, the following epitaxial relationship can be established: InGaN(0001) [2$\underline{1}$10] || AlN(0001) [2$\underline{1}$10] || Si(111) [01$\underline{1}$]. The results

were verified with the TEM SAED patterns. Since the base edges of the nanopyramids are along the <2$\underline{11}$0> directions of the hexagonal wurtzite structure, the orientation of the close-packed axis of the hexagonal array of pores parallel to the [$\underline{11}$2] direction of the Si(111) substrate (or the [1$\underline{1}$00] direction of the AlN(0001) buffer) allows the dense edge-to-edge packing arrangement of the nanopyramids to be realized as seen in Figure 5.9. This maximizes the InGaN coverage of the surface for light absorption. Refer to Figure 2.3 for the typical epitaxial relationship of the III-nitrides and Si(111) substrate.

### 5.3.4. Photoluminescence

#### 5.3.4.1. Temperature Dependent Photoluminescence

The temperature dependent photoluminescence (PL) spectra of the control sample are shown in Figure 5.15. Two pronounced peaks $I_1$ and $I_2$ can be identified and suggest the presence of two major luminescence centers. The positions of the peaks and their dominance with temperature are plotted in the inset. While the lower energy peak $I_1$ red-shifts monotonically with temperature increase, $I_2$ exhibits a red-blue-red shift. $I_1$ is likely associated with In-richer regions and the red-shift may be explained by the temperature dependence of the bandgap according to Varshni's law [86]. On the other hand, the behavior of $I_2$ closely resembles the S-shaped emission shift reported in InGaN films and has been explained by the localized character of electron-hole radiative recombination [285, 315, 316]. For temperatures up to 30K, $I_2$ is the dominant peak. However, as temperature increases to 40K, the dominant peak switches from $I_2$ to $I_1$ and remains so until about 210K. The double-peak temperature dependence, similarly reported by Moon et al. [316], indicates a carrier transfer from the luminescent center of $I_2$ to the more thermally stable center of $I_1$. However, the dominant peak returns back to $I_2$ at 240K, possibly due to thermal activation of non-radiative recombination centers.

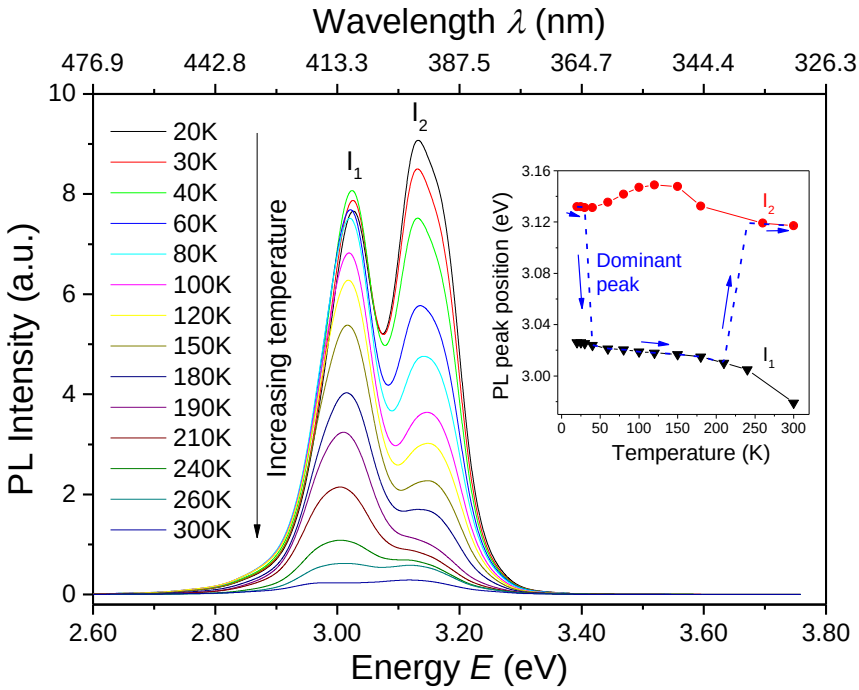


**Figure 5.15** Temperature-dependent photoluminescence (PL) spectra of the InGaN control from 20K to 300K. Two pronounced peaks $I_1$ and $I_2$ can be discerned. The inset plots the peak positions and their relative dominance (dash blue lines) with temperature. $I_1$ exhibits a Varshni-like red-shift, while $I_2$ undergoes a red-blue-red shift.

As discussed earlier, the InGaN control film has an undulating surface consisting of ridges and troughs. The former are sites of elastic relaxation [316]. Segregation of In to ridges is energetically favored due to a reduction of the number of compressively strained In-N bonds. Further, In segregation from bulk to surface may also occur due to favorable energetics [114, 115]. Hence, as growth proceeds, In-rich regions can be formed which can act as luminescent centers. It is plausible that the $I_1$ peak is related to In-richer regions while the $I_2$ peak is associated with regions of lower In content. The temperature dependent PL spectra of the nano-SAG sample are shown in Figure 5.16. Peaks attributed to Fabry-Perot interference have been removed by a Fourier filtering technique for easier comparison [221]. However, as reference, the original as-acquired Fabry-Perot spectra at a few temperatures are superimposed as dash lines against the processed spectra.

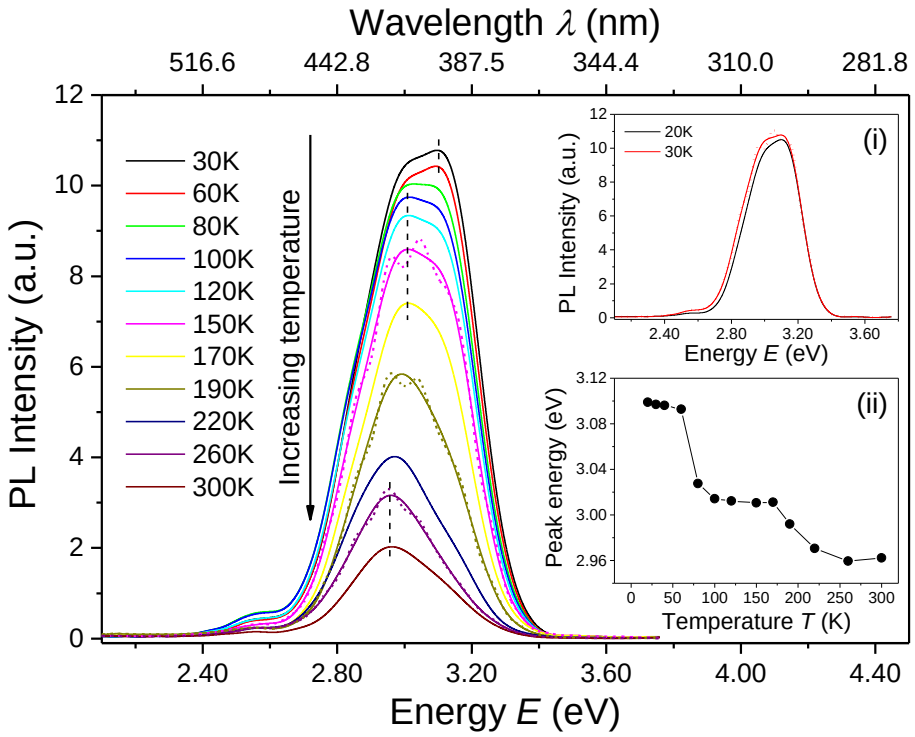


**Figure 5.16** Temperature-dependent photoluminescence (PL) spectra of the ordered InGaN nanopyramid array from 20K to 300K. Fringes caused by optical interference have been removed by a Fourier filtering technique for a more straightforward comparison. The oscillatory as-acquired spectra (short dash lines) at 30K (inset (i)), 150K, 190K and 260K are included as reference. Inset (i) compares the PL spectra at 20K and 30K showing a red-shift and intensity increase of the low energy edge. Inset (ii) plots the peak position with temperature, showing a double step shift.

Except for a slight increase in the PL intensity of the nano-SAG sample at low temperatures from 20K to 30K (inset (i)), the PL intensity generally decreases with temperature increase due to thermal quenching [284]. The initial increase in PL intensity might have origins in the thermal activation of carriers to spatially localized bandgap minima which are more efficient radiative recombination regions. This accounts for the red-shift in the lower energy PL edge and its increase in intensity while the high energy edge remains relatively unchanged.

In addition, the PL emission of the nano-SAG sample is relatively broad with photon energies spanning ~ 2.6 eV to ~ 3.4 eV. Interestingly, the PL peak position shifts to

lower photon energies in a double step manner with temperature increase as seen in Figure 5.16 inset (ii). Single step shift of the dominant PL peak between two peaks has been reported by Moon et al. [316] in compositionally non-uniform InGaN films. Similarly, spatial variation of In content generated during nano-SAG may account for the observation and may arise as follows. In incorporation efficiency is higher on {11$\underline{1}$01} facets than (0001) facets [115, 317]. Prior to the formation of complete hexagonal nanopyramids bounded by {11$\underline{1}$01} facets, the nanopyramids are truncated with the (0001) facet forming the top plane. In compositional variation may inevitably be introduced during growth due to facet-dependent In incorporation efficiency. Further, lower In incorporation *x* is expected in the bottom part of the nanostructure near the InGaN/AlN interface due to greater compressive strain. As growth proceeds, strain relaxation afforded by the availability of free surfaces in the nanopyramids would likely result in an increase in *x* [70, 318]. The increase of *x* with nano-SAG duration is directly observed in Section 6.5.2.1. Further, a spatial difference in growth rate, indicated by incomplete coalescence or void formation in some nanopyramids, during nano-SAG may also lead to non-uniform *x* [240].

The higher In incorporation *x* of $In_xGa_{1-x}N$ on the semipolar {11$\underline{1}$01} planes [151, 152], has been associated with the favorable energetics of the planes for accommodating In atoms [115, 153] as discussed in Section 2.4.3. As the complete InGaN nanopyramids are bound exclusively by {11$\underline{1}$01} facets and grow via successive deposition on the {11$\underline{1}$01} planes, this will contribute to greater *x* compared to growth on other planes. While the rough surface of the thin film control also contains {11$\underline{1}$01} planes, the area of it is considerably less than the 3D nanopyramid array. Strain relaxation of the highly 3D nanostructures is also expected to increase *x* further. This also explains the higher *x* relative to the control and accounts for the generally lower PL emission energies. As the mechanisms for increase in *x* and non-uniform In incorporation are

inextricably linked, the higher average *x* has a more gradual and broader composition spread, giving rise to the broader PL emission. Luminscent centers may be present but their emission energies are close and overlap such that multiple PL peaks are not observed. Carrier transfer between three major luminescent centers may account for the double step shift of the PL peak position with temperature increase.

The normalized PL spectra of both samples at room temperature are plotted in Figure 5.17 for direct comparison. The higher In content of the nanopyramid sample is apparent from the lower energy of the PL peak (at 2.962 eV) compared to that of the double-peaked control (at 3.117eV and 2.979eV). A broader spread of composition accompanies the increase as indicated by the larger FWHM of the PL peak at 0.325eV compared to 0.278eV in the control. The results are in-line with high-resolution XRD observations. The increase in In content with nano-SAG to form 3D nanostructures compared to film growth under the same MOCVD growth conditions affirms the benefits of such an approach.

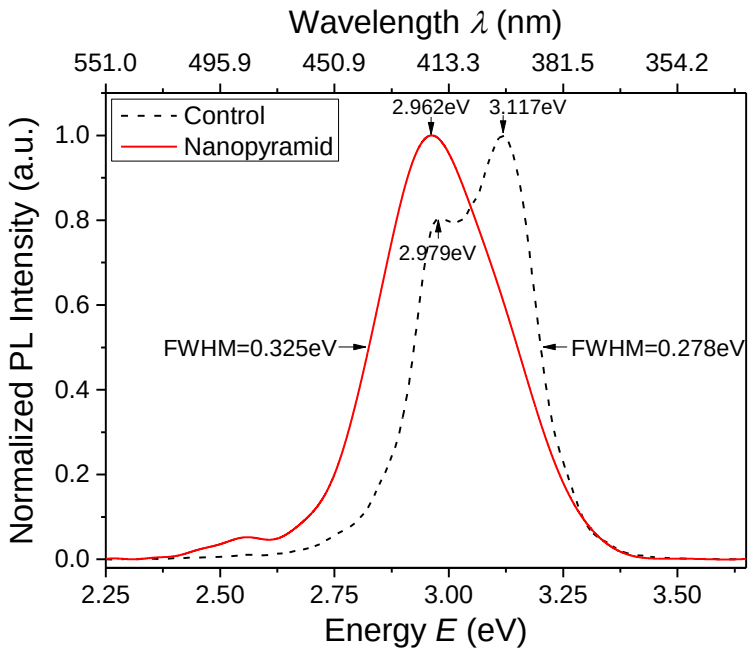


**Figure 5.17** Normalized room-temperature PL spectra of the InGaN control (black dash line) and InGaN nanopyramid array (solid red line). The higher In content InGaN nanopyramid array emits at lower energies over a broader range compared to the control.

### 5.3.4.2. Arrhenius Plot

The normalized integrated PL intensities of the control and nanopyramid samples as a function of reciprocal temperature are plotted in Figure 5.18. As discussed in Section 3.4.5, the observed thermal quenching of integrated PL intensity $I$ can be modeled by the Arrhenius equation (Equation (3-12)) with a variable number of thermally activated non-radiative recombination channels, each associated with an activation energy $E_A$ [285-288]. In the control sample, a good Arrhenius fit over the measured temperature range required two channels with $E_A$'s of 14 meV and 131 meV, while in the nanopyramid sample, a single $E_A$ of 72 meV sufficed. The value of $E_A$ in the nanopyramid sample is similar to that obtained in InGaN films with similar In composition grown on GaN [316]. This was postulated to be associated with localization of carriers in In-rich regions and would have been generated in our nanopyramid samples by the mechanisms discussed earlier. In the control sample, the notably high $E_A$ of 131 meV may be linked to deep localization states as reported for

InGaN structures emitting over a comparable photon energy range [288, 319]. The smaller $E_A$ of 14 meV may arise from smaller potential fluctuations. Further, the single $E_A$ of the nanopyramid sample is situated close to the mean $E_A$ of the control sample. This suggests that the magnitude of local potential fluctuations occurring in the nanopyramid structure is relatively constant and lies between the deep and shallow localizations occurring in the control. The internal quantum efficiency η at room temperature (300K), expressed as the ratio of the integrated PL intensity at 300K to that at 20K, for the control sample is ~ 4.4%, while that of the nanopyramids sample is almost four times as high at ~ 17.5%. The high η of the nanopyramids is indicative of its improved crystalline quality achieved by dislocation confinement to the axial region, dislocation bending and filtering during nano-SAG.

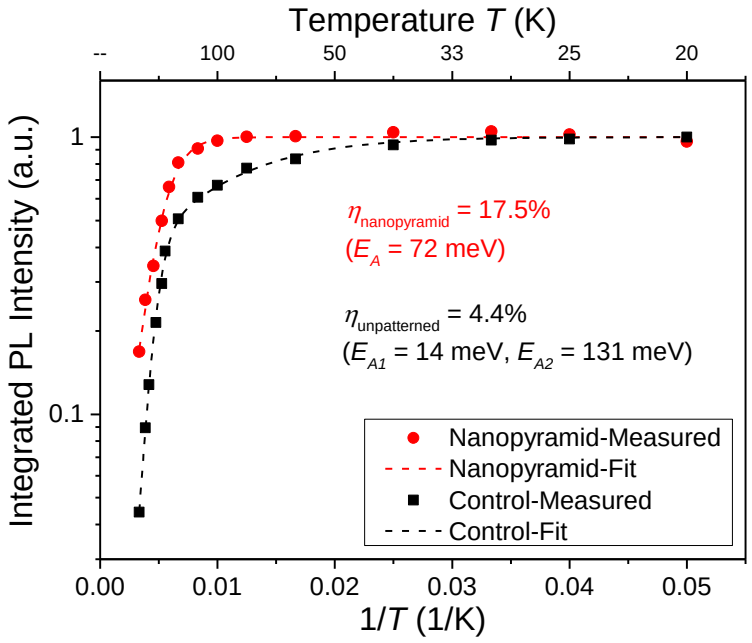


**Figure 5.18** Arrhenius plot of the integrated PL intensities of the InGaN control and InGaN nanopyramid array. Internal quantum efficiency $\eta$ of the latter is ~ four times as high.

### 5.3.5. Reflectance

The dense hexagonal array of hexagonal InGaN nanopyramids exhibits excellent antireflection and light-trapping properties compared to the unpatterned control

sample. Unabsorbed light rays reflected off one facet of a nanopyramid will likely land onto the facet of a neighboring nanopyramid and have another chance at absorption. Considering the high refractive index of $In_xGa_{1-x}N$ (~ 2.2 to 3.0 depending on $x$) [320], reflection losses can be significant for a bare untextured InGaN surface not bearing any anti-reflection coating (ARC). The 3D sculpting of InGaN can greatly reduce reflection lossess even without application of an ARC. The reflectance $R$ at normal incidence for the samples in this work is plotted in Figure 5.19.

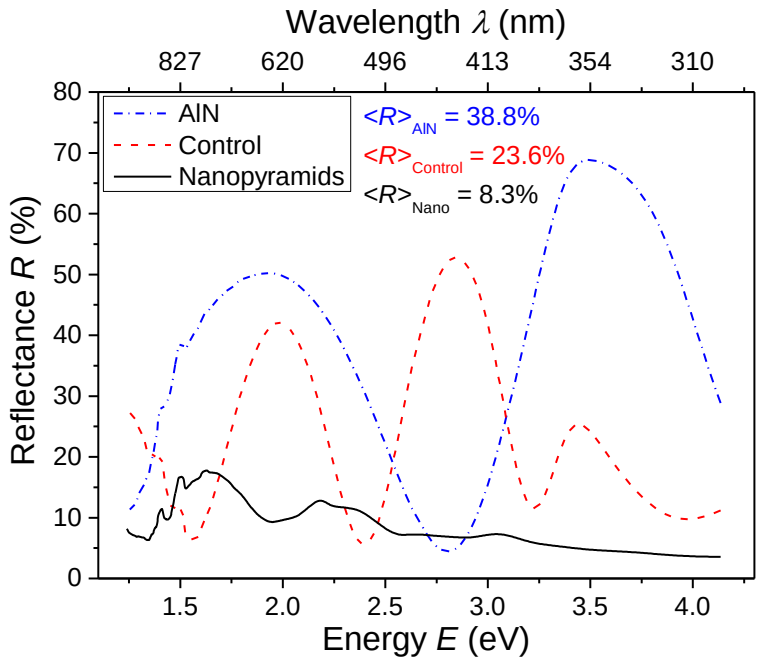


**Figure 5.19** Reflectance $R$ at normal incidence of the bare AlN/Si(111) substrate (blue dash-dot line), InGaN control (red dash line) and InGaN nanopyramid array (black continuous line). The anti-reflection nanopyramid array has $R < 7.3\%$ over the absorption region ($E > 2.6$ eV) and $\langle R \rangle = 8.3\%$. This is significantly lower than the control with $\langle R \rangle = 23.6\%$.

Over the absorption region (photon energy $E > 2.6$ eV) of the InGaN nanopyramids, $R$ is less than 7.3% while average reflectance $\langle R \rangle$ remains low at 8.3% over the range of $E$ corresponding to wavelength $\lambda$ from 300 nm to 1000 nm. For the control sample, as well as the AlN/Si(111) substrate, $R$ is comparatively higher and more oscillatory. This is characteristic of reflectance due to thin-film interference and has been verified by a reflectance modeling software from Filmetrics (a thin-film metrology company).

The phenomenon arises from the relatively smooth interlayers and large refractive index contrast between the optical media. <*R*> of the control sample, at 23.6%, is almost three times as high as the nanopyramid array. As reference, the AlN/Si(111) substrate has an even higher <*R*> of 38.8% due to its much smoother surface, as seen in the inset of Figure 5.7(a), and wide bandgap of AlN which, at 6.2 eV, means that much of the incident light is not absorbed. Pyramidal texturing is a widely used technique for reflection control in Si solar cells [77] and the nanopyramidal texture obtained during nano-SAG of InGaN may similarly be adapted for InGaN photovoltaic applications.

### 5.3.6. Discussion

For the same growth time and conditions as the unpatterned control, nano-SAG results in an arrangement of InGaN in the form of 3D nanostructures with improved characteristics such as increased In content, improved crystal quality, and reduced reflectance. While the initial mask deposition, patterning and etching prior to nano-SAG presents additional process steps compared to planar film growth, these steps will need to be introduced if texturing or nanostructuring need to be employed at a later stage in the case of thin film growth. Even so, post-growth top-down etching to form nanostructures cannot offer the same benefits associated with strain relaxation and defect reduction achieved in nanostructured growth. Further, top-down etching of the grown material implies a waste of resources and the need for etch damage removal. This also signifies an initial redundant expenditure of growth time which is avoided in nano-SAG. In the case of the latter, following template fabrication over the seed layer, nano-SAG to form 3D nanostructures can be performed for deposition of all subsequent layers till completion of the device architecture [224, 231].

The qualities of nanopyramid arrays grown by nano-SAG make such an approach appealing. However, admittedly, the In content reported in this work ($x \sim 0.11$) is considerably less than that optimal for InGaN/Si tandem solar cell application ($x \sim 0.46$). In the next Chapter, it will be shown that $x$ may be increased by changing the growth conditions. The InGaN nanopyramids typically contain TDs in the axial region although regions near the facets are much less defective. The TDs are due to heteroepitaxy and the highly defective AlN buffer layers. Axial TDs cannot be totally eliminated due to the metastability associated with the axial region [58, 62] but may be terminated at embedded voids. Nonetheless, the reported approach of nano-SAG using ~ 210 nm diameter nanoporous template has shown the potential of improving the quality of InGaN grown on AlN and increasing its In content.

### 5.3.7. Conclusion

Nano-SAG was used to grow InGaN nanostructures via MOCVD on AlN/Si(111)-based Type A template. A dense, highly ordered, hexagonal array of InGaN hexagonal nanopyramids was achieved. Each nanopyramid, bound by six {1$\underline{1}$01} facets, have an average base dimension of ~ 270 nm and a periodicity of 300 nm. The volume of high crystalline quality InGaN is substantially increased through dislocation confinement to the core region of the nanopyramid, dislocation bending to the free surface, and dislocation filtering by the template. This contrasts with the control, where dislocations thread into the InGaN layer without bending resulting in a defective, pitted and undulating film. The InGaN nanopyramids possess a higher In content of ~ 10.6% (versus ~ 6.1% in the control) and a broader In compositional spread due to strain relaxation effects, facet-dependent In incorporation efficiency, and non-uniform growth rates. This correlates with PL emission at lower energies and with a broader spread than the control sample. Temperature dependent PL measurements indicate the presence of luminescent centers arising from In-rich

regions for both samples. The higher quality of the InGaN nanopyramids is evidenced by its internal quantum efficiency which, at 17.5%, is almost four times as high as that of the control at 4.4%. Average reflectance over the 300 – 1000 nm wavelength range is also reduced to 8.3% from 23.6% due to light trapping effects.

## 5.4. Chapter Summary

In this Chapter, the growth of InGaN thin films on AlN/Si(111) substrates was first examined to establish the pre-requisite conditions and influence of growth parameters for obtaining single phase epitaxial InGaN. High temperature in-situ annealing of the AlN/Si(111) substrate in $H_2$ at 1000°C was found to be critical to obtaining epitaxial growth. Further, elevated pressures (~ 300 Torr) aid in obtaining single phase InGaN especially at low growth temperatures, while relatively high temperatures (> 765°C) improves crystal quality albeit at the expense of In content. Taking these factors into consideration, nano selective area growth (nano-SAG) of three-dimensional InGaN nanostructures was performed at 780°C and 300 Torr on AlN/Si(111)-based Type A templates with substrate pre-annealing. Three-dimensional InGaN hexagonal nanopyramids in a dense hexagonal array were successfully grown. Strain relaxation, dislocation confinement and filtering result in improved InGaN crystalline quality. Compared to the thin film control, the nanopyramid array has higher In content (~ 10.6% vs ~ 6.1%), higher internal quantum efficiency (17.5% vs 4.4%) and substantially lower reflectance (8.3% vs 23.6%). The results indicate that nano-SAG is a promising approach to grow low reflectance, improved crystalline quality InGaN nanostructures with enhanced In content on AlN-buffered Si for the development of high efficiency InGaN/Si hybrid tandem solar cells. This affirms the initial proposition on the benefits of InGaN nanostructuring discussed in Section 1.2.4.3.

# Chapter 6 Nano Selective Area Growth of InGaN Nanostructure Arrays

## 6.1. Introduction

In 0, the scaling of InGaN into three-dimensional nanopyramid arrays on AlN/Si(111)-based Type A templates using nano-SAG was demonstrated. In this Chapter, a more detailed study on the influence of MOCVD growth conditions in the nano-SAG of InGaN nanopyramid arrays on the same type of templates is presented. The In content, morphological, structural and PL qualities of the nanopyramid arrays are reported. This will form a guide to obtaining InGaN nanopyramids of the desired properties. Lastly, results on the growth of multiple quantum wells on the inclined planes of the nanopyramids are reported. This demonstrates the possibility of fabricating core-shell nanopyramid structures for device applications.

## 6.2. Experimental Procedures

As with Section 5.3, AlN/Si(111)-based Type A templates were used for nano-SAG of InGaN with bare AlN/Si(111) substrates as the growth control. Investigation of the influence of growth conditions on nano-SAG of InGaN is divided into four series. In the first series, the effect of growth temperature over 700°C to 800°C is examined with the reactor pressure maintained at 300 Torr. In the second series, the influence of reactor pressure in the range of 70 Torr to 300 Torr is studied at a relatively high growth temperature of 775°C to maintain growth quality. In the third series, the effect of growth duration is examined. For these three growth series, the flow rates of precursors and gases are the same as in Sections 5.2.1 and 5.3.1, and correspond to a V/III ratio of 9200 and a TMIn/(TMIn+TMGa) molar flow ratio $r_m$ of 0.80. In the fourth series, the effect of gas flow ratio is examined. For all growths, the total gas

flow rate of $H_2$, $N_2$, and $NH_3$ is kept at 24000 sccm, while that of TMIn and TMGa are kept at 120 sccm and 5 sccm respectively. Lastly, MQWs are grown on the inclined facets of InGaN nanopyramids to demonstrate the possibility of achieving core-shell device structures. Grown structures are examined by FESEM, AFM, XRD, μ-PL, reflectance spectroscopy, and/or TEM. The heights of the nanopyramid section in nano-SAG are at least 220 nm while the thickness of the control films is > 130 nm.

**Table 6-1** Summary of growth conditions used in the nano-SAG of InGaN nanostructures on AlN/Si(111)-based Type A templates. Four growth series, (1) to (4), are performed.

| | ***T*** **(°C)** | ***P*** **(Torr)** | **Duration (min)** | **Flow Rate (sccm)** | | | | |
|---|---|---|---|---|---|---|---|---|
| | | | | **TMIn** | **TMGa** | **$H_2$** | **$N_2$** | **$NH_3$** |
| **(1) Temperature series** | 700 | 300 | 40 | 120 | 5 | 0 | 6000 | 18000 |
| | 725 | 300 | 40 | 120 | 5 | 0 | 6000 | 18000 |
| | 750 | 300 | 40 | 120 | 5 | 0 | 6000 | 18000 |
| | ***775*** | ***300*** | ***40*** | ***120*** | ***5*** | ***0*** | ***6000*** | ***18000*** |
| | 800 | 300 | 40 | 120 | 5 | 0 | 6000 | 18000 |
| **(2) Pressure series** | 775 | 70 | 40 | 120 | 5 | 0 | 6000 | 18000 |
| | 775 | 100 | 40 | 120 | 5 | 0 | 6000 | 18000 |
| | 775 | 200 | 40 | 120 | 5 | 0 | 6000 | 18000 |
| **(3) Duration series** | 825 | 300 | 12 | 120 | 5 | 0 | 6000 | 18000 |
| | 825 | 300 | 72 | 120 | 5 | 0 | 6000 | 18000 |
| **(4) Gas flow rate series** | 775 | 300 | 40 | 120 | 5 | 1000 | 5000 | 18000 |
| | 775 | 300 | 40 | 120 | 5 | 0 | 12000 | 12000 |

## 6.3. Influence of Growth Temperature

### 6.3.1. Morphology

For the range of growth temperatures of 700°C – 800°C, good site control for nucleation and growth was obtained with the nanoporous $SiN_y$ template. Nano-SAG at each pore resulted in the formation of an InGaN hexagonal nanopyramid bound by six facets. Figure 6.1 shows the FESEM images of these nanopyramids.

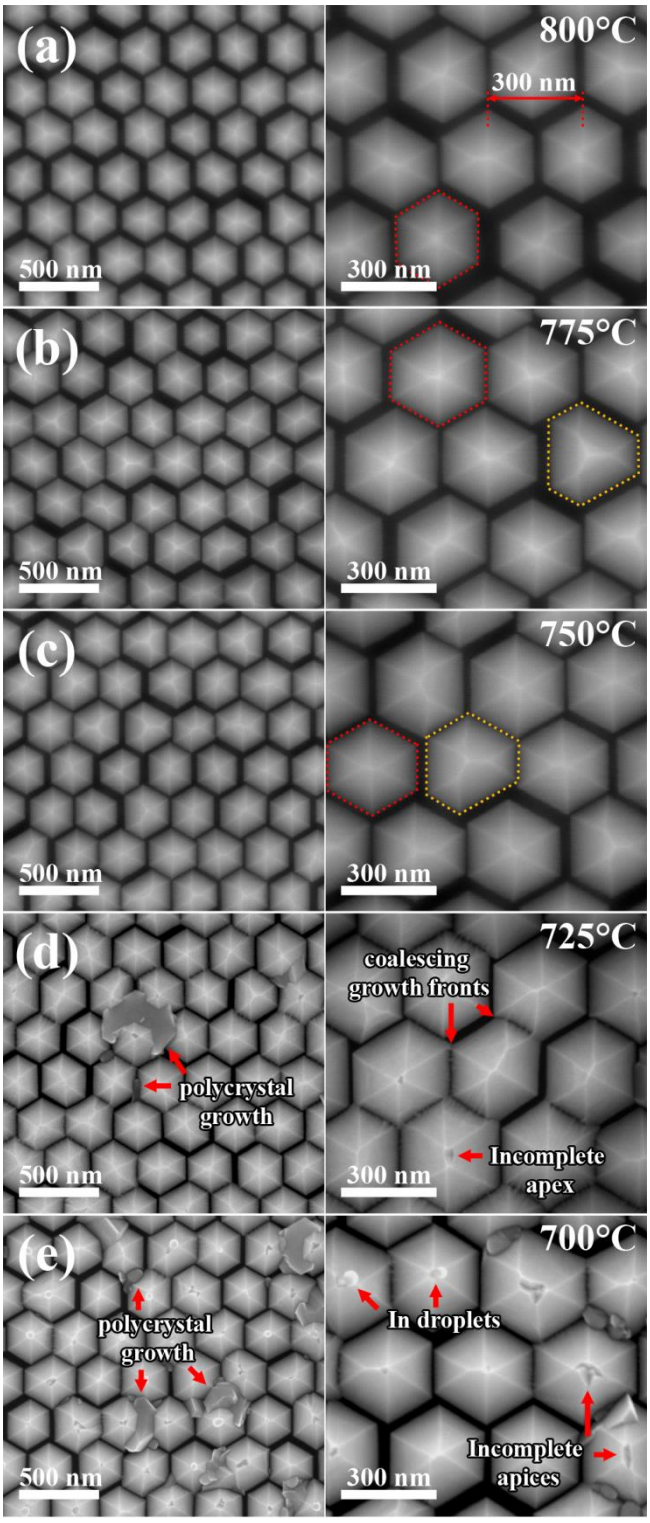


**Figure 6.1** FESEM images of InGaN hexagonal nanopyramids grown on AlN/Si(111) substrates for 40 min at temperatures of (a) 800°C, (b) 775°C, (c) 750°C, (d) 725°C, and (e) 700°C with a reactor pressure of 300 Torr. A few hexagonally symmetric and asymmetric nanopyramids are outlined in red and yellow dotted lines respectively. Temperature reduction is correlated to a slight increase in nanopyramid size. Incidence of incomplete apices, polycrystalline deposits and In droplets are increased at temperatures less than ~ 750°C.

The inclination of each nanopyramid facet from the basal plane is determined by AFM measurement to be ~ 62°, confirming that these are {11$\underline{1}$01} planes. The formation of these facets in SAG of InGaN has been discussed in Section 5.3.2.

#### 6.3.1.1. Size uniformity

In general, while all nanopyramids grown under 300 Torr over the temperature range of 700°C to 800°C possess six sidewalls, not all sidewalls have the same size. Further, a slight variation in nanopyramid size is also observed. The size non-uniformity was investigated by examining the morphology of InGaN nanopyramids grown under reduced reactor pressure *P*. It is known that a reduction in *P* increases the mass transport of reactants through the boundary layer in MOCVD growth [321]. According to Lundskog et al., the increased arrival rate of adatoms will favor growth in the adsorption regime which will degrade uniformity [322]. On the contrary, we found that the size uniformity of InGaN nanopyramids is notably improved as seen in Figure 6.7. In another work by Miao et al., asymmetry of GaN nanopyramids of a size similar to our InGaN nanopyramids has been correlated to stacking fault formation although the reason for this is still under study [241]. While stacking faults are observed in our work, these are present in both asymmetric and symmetric InGaN nanostructures as observed in cross-section TEM. Hence, the size non-uniformity in our case may not be due to growth in the adsorption regime or simply stacking faults.

However, the non-uniformity most definitely arises from a difference in growth rate among the sidewalls. Although each sidewall is composed of a slow growing {11$\underline{1}$01} plane with, theoretically, the same growth rate, the growth rate may be altered by certain sidewall features. For instance, TDs in *c*- and *m*-plane GaN create spiral mounts when they terminate at the surface [323, 324]. These provide a source of atomic steps which increases the growth rate [325]. In analogy, TD exits on the

nanopyramid {11$\underline{1}$01} sidewalls due to TD bending can have similar effects. The non-equal distribution of TD exits among sidewalls can result in non-uniform sidewall and nanopyramid growth rates. Observations of a thicker InGaN/GaN MQW structure grown on a nanopyramid sidewall with TD exit in Section 6.7.3 support this premise.

Noting that the diffusion coefficient $D$ is inversely proportional to the pressure $P$ [265], the improvement in uniformity when $P$ is reduced suggests that factors relating to gas phase diffusion or mass transport of precursors are at work. A reduction in $P$ enhances mass transport of precursors to the growing surface. The consequent rise in growth rate (discussed in Section 6.4.1.1) occurs over all sidewalls and may dominate and mitigate the effects of non-uniform defect exits on sidewall growth rates.

#### 6.3.1.2. Growth Rate

A reduction in growth temperature $T$ from 800°C to 700°C has several effects. From Figure 6.1, it is noticed that the average diameter of the nanopyramids is slightly increased. The increase in growth rate may be attributed to reduced In desorption as $T$ decreases. As the nanopyramids enlarge and overgrow onto the mask, neighboring base edges approach each other and when in sufficient proximity start to coalesce. This manifest as a transition from straight base edges to rough coalescing growth fronts. See Figure 6.1(d)-(e).

#### 6.3.1.3. Growth Artefacts

Nanopyramid arrays grown at $T$ above ~ 750°C are generally clear of growth artefacts. However, reduction in $T$ below ~ 750°C, results in the growth of polycrystals at the valleys between the nanopyramids, the incidence of which increases with lower $T$. See Figure 6.1. Such deposits are generally absent on the control samples (not shown). We posit that a combination of factors is responsible for the observation. First, the

energetic stability of the {11$\underline{1}$01} facets implies that adatoms are not easily incorporated into these slow growing planes. Second, the suppression of adatom desorption at low *T* suggests a higher concentration of adatoms but which are not easily incorporated into the stable {11$\underline{1}$01} planes. Third, the sharply recessed valleys framed by the steep {11$\underline{1}$01} slopes of adjacent nanopyramids are possible trapping sites of adatoms. Fourth, due to reduced surface mobility at low *T* [98], adatoms that have diffused from energetically stable {11$\underline{1}$01} facets or vapour phase diffused and adsorbed at the valleys are less likely to escape. Fifth, the driving force for nucleation is increased at lower *T* [326]. Consequently, the chance for adatoms at the valleys to nucleate, grow and form polycrystalline deposits is increased with reduced *T*.

In addition, while incompletely coalesced apices are hardly observed for nanopyramids grown above ~ 750°C, these are observed at *T* below ~ 750°C, the incidence of which increases with lower *T*. Apical pits are inextricably correlated with TDs terminating at the apices of the nanopyramids. In cross-sectional TEM observations, apical TDs are found in almost all nanopyramids. However, the actual manifestation of apical pits depends on growth conditions. The latter affects adatom mobility, growth rate, In content *x*, lattice mismatch and structural quality. InGaN with higher *x* has greater lattice mismatch and poorer structural quality which tends to exacerbate the size of the pits. However, higher adatom mobility and faster growth rate promote filling up of the pits. TDs have been observed to terminate at the apices of nanopyramids for $T > 750$°C but without apical pit formation. Hence, we posit that the formation of apical pits at lower *T* is a consequence of the lower adatom surface mobility and higher *x* when *T* is reduced resulting in incomplete apical coalescence. Furthermore, at the lowest *T* used, In droplets are also observed at the apex of the nanopyramids. These likely arise from the lower cracking efficiency of $NH_3$ at the low *T* resulting in less nitrogen or nitrogen radicals available for bonding [122, 268].

### 6.3.2. Structural Characteristics

#### 6.3.2.1. Indium Content and Phase Composition

The composition and structure of the MOCVD grown InGaN samples are analyzed with HR-XRD. Figure 6.2 shows the (0002) $2\theta$-$\omega$ XRD scans for both nanopyramid array and control samples grown over $T$ from 700°C to 800°C at a $P$ of 300 Torr.

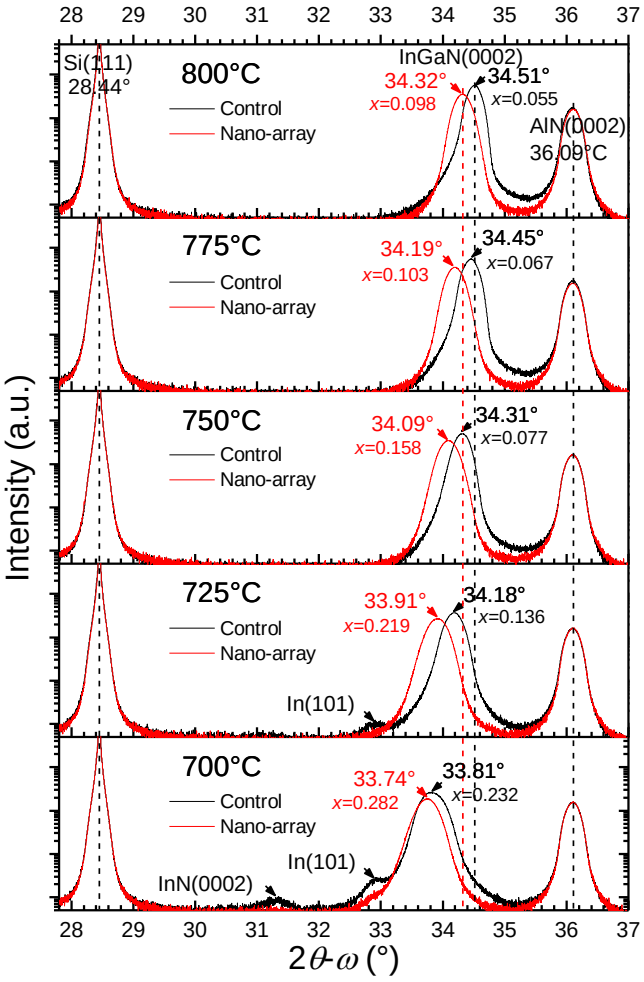


**Figure 6.2** HR-XRD (0002) $2\theta$-$\omega$ scans of InGaN nanopyramid array (red line) and corresponding control (black line) samples grown on AlN/Si(111) substrate over the temperature range of 700°C to 800°C at a reactor pressure of 300 Torr.

As expected, the InGaN(0002) peak shifts towards lower $2\theta$ values for both InGaN sample types as $T$ is reduced from 800°C to 700°C, indicating an increase in $x$. This is

due to reduced In desorption which facilitates greater In incorporation into the lattice. Moreover, at each *T*, the nanopyramid array invariably possesses a higher *x* than the corresponding control. This is in line with our early nano-SAG results in Section 5.3 and provides further support for a nano-SAG approach to increase *x* in InGaN even on non-conventional highly mismatched AlN buffer layers. As discussed earlier, the nanostructures afford strain relaxation within the wurtzite structure such that the larger In atoms can be more easily accommodated alongside the smaller Ga atoms within the lattice [57, 69-71]. Further, the more favorable energetics for In incorporation relative to Ga on the {1$\underline{1}$01} planes [115, 151, 152] widely exposed in nano-SAG of InGaN is also likely to increase *x*. Figure 6.3 show the variation of *x* with *T* for both the nanopyramid arrays and control samples. *x* is estimated by assuming that the structures are partially strained, with the *c* and *a* lattice parameters calculated from the (0002) and (10.5) XRD reflections [104].

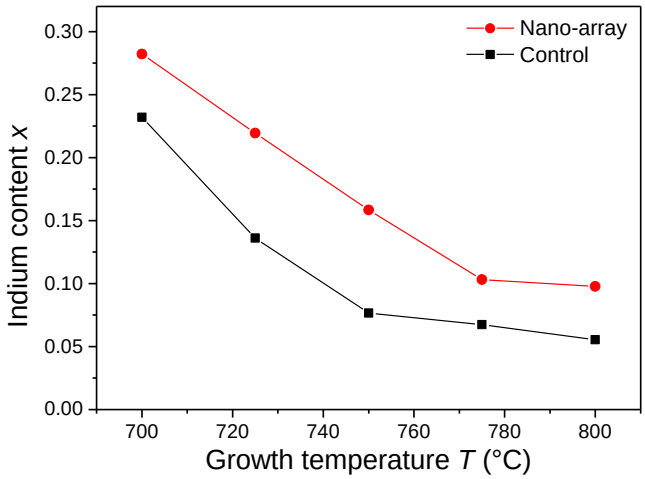


**Figure 6.3** Variation of HR-XRD estimated In content *x* with growth temperature *T* for InGaN nanopyramid array (red line) and corresponding control (black line) samples grown at a reactor pressure of 300 Torr.

From the $2\theta$-$\omega$ XRD scans in Figure 6.2, InGaN nanopyramid arrays grown over the temperature range of 700°C to 800°C are generally single phase, except for the formation of In droplets at ~ 700°C. The latter manifest as an In(101) minor peak at

$2\theta$ ~ 32.9° in the scans and is consistent with the FESEM images of Figure 6.1(e). For the thin film control series, the onset of In droplets occurs at a higher temperature of ~ 725°C, and becomes more pronounced at ~ 700°C. In fact, InN is also detected at ~ 700°C as an InN(0002) peak at $2\theta$ ~ 31.40°. The observations suggest that a nano-SAG approach may aid in reducing phase inhomogeneity and In droplet formation. The smaller amount of In droplets present in the nanopyramid sample compared to the corresponding control film, as indicated by the lower In(101) intensity in the XRD, may be due to more of the In being incorporated into the lattice but may also partially be due to the formation of polycrystalline deposits which are not observed in the control film. See Figure 6.1(d)-(e). The reason for this is still under investigation.

The absence of InN or improved phase homogeneity in the nanopyramid arrays may be related to the faceted nanopyramid morphology where exposed surfaces are invariably {11$\underline{1}$01} planes with low surface energy. The In droplets which are confined to the apices of the nanopyramids can act as sinks for excess In adatoms [124] that are not incorporated into the surrounding uniformly stable {11$\underline{1}$01} surfaces. While this may actually compete with the incorporation of In into the grown structures, such a phenomenon may also help in maintaining some degree of phase homogeneity. Metal droplets, albeit of Ga content, have also been observed at the truncated pyramidal tips of GaN nanorods during pulsed MOCVD growth by Liao et al. [231]. In our case, while continuous flux MOCVD growth is employed, the similar location of metal droplets at the tips of the nanostructures suggest that these sites are preferential areas for their formation during MOCVD.

#### 6.3.2.2. Lattice Tilt and Twist

The full-width-at-half-maximum (FWHM) of the X-ray $\omega$-rocking curve for the on-axis symmetric (0002) and off-axis skew symmetric (20.1) reflections at each growth

temperature *T* are plotted in Figure 6.4. Due to the use of an open detector configuration in these XRD measurements to increase signal intensity, the FWHM's may be overly broadened. Nonetheless, the parameters remain valid indicators for relative lattice tilt and twist respectively [104].

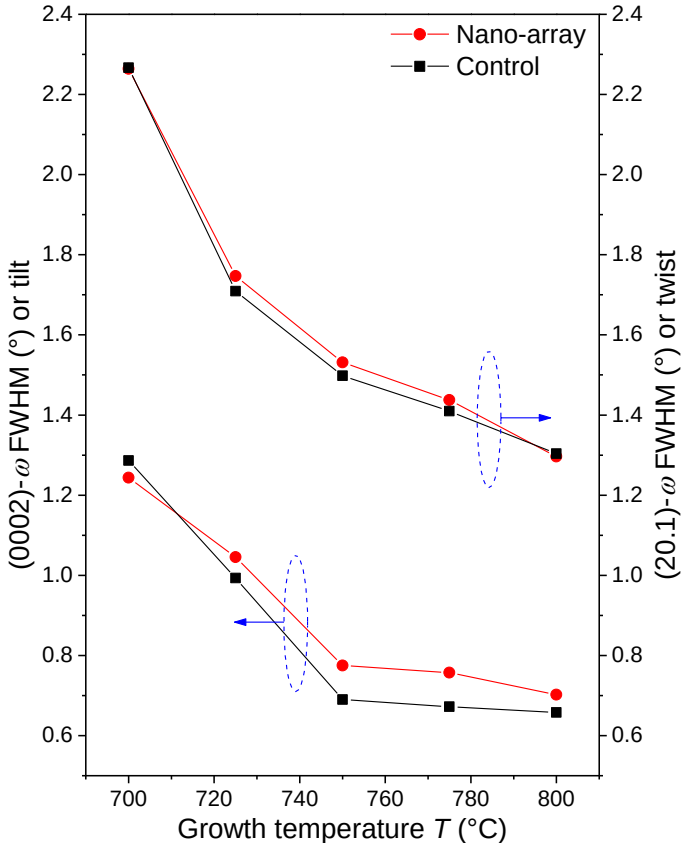


**Figure 6.4** Variation of the FWHM of the X-ray $\omega$-rocking curve for the symmetric (0002) and skew symmetric (20.1) reflections over 700°C to 800°C at a reactor pressure of 300 Torr. The FWHMs are indicative of relative lattice tilt and twist respectively.

From Figure 6.4, both parameters are observed to decrease with increase in *T* for the nanopyramid and control samples, indicating an improvement in crystal quality [72]. However, the rate of decrease becomes less at higher *T*. That is, crystal quality is gradually being limited by factors other than *T* in this regime. In particular, it is observed that the levelling-off values for the (0002)-$\omega$ rocking curve FWHM, taken as the 800°C FWHM values (at ~ 0.70° and ~ 0.66° for the nanopyramid and control series, respectively), lie close to that of the AlN buffer at ~ 0.68°. Since screw

threading dislocations are a source of lattice tilt and that it propagates directly from the AlN buffer into the InGaN layer, the former plays a major role in limiting the quality of the latter. Tilt and twist are related to and have been used in formulas to estimate screw and edge dislocation densities respectively in GaN epitaxial thin films [279-281]. However, the formulas may not be directly applicable to nanostructures in SAG. Therefore, we restrict comparison between the films and nanostructures to the use of tilt and twist instead of dislocation densities. It is noted that the lowest (20.1)-$\omega$ rocking curve FWHM values (twist) for both at ~ 1.30° (for 800°C) remain notably higher than that for the AlN buffer layer at ~ 1.07°. This is attributable to the generation of new edge dislocations at the highly mismatched InGaN/AlN interface.

The effect of growth temperature *T* on crystal quality is multi-pronged. Generally, higher *T* improve crystal quality due to increased adatom mobility into lattice sites, reduced interstitials and vacancies, reduced carbon contamination, and reduced defect densities [72, 125, 126]. In the growth of InGaN, *T* exerts an additional effect, due to the temperature sensitivity of In incorporation. Lower *T* increase the In content but also increase the dislocation densities generated at the InGaN/AlN interface due to the larger lattice mismatch of higher In content InGaN. The myriad of factors are responsible for the increase of the $\omega$ rocking curve FWHM's with *T* reduction. Of special note is that while tilt values of the nanopyramid series are higher than the control series in the mid-to-high temperature range, the twist values are more similar. Such a phenomenon has been attributed to dislocation bending effects by Moram et al. [104] and observed in cross-sectional TEM in Section 5.3.3.1.

### 6.3.3. Photoluminescence

The room temperature μ-PL spectra of both nanopyramid array and control samples excited by a 325 nm He-Cd laser are shown in Figure 6.5. A few observations can be

made. First, the PL spectra for both nanopyramid array and control samples are not composed of a single smooth Gaussian profile. While Fabry-Perot interference and optical phonon effects may be responsible for the more periodic features, the PL line shape is also a consequence of other factors affecting near band edge (NBE) emission. We note that both sample types are not defect-free due to the propagation of TDs from the underlying AlN buffer layer, generation of new TDs due to heteroepitaxial growth beyond the critical thickness, and presence of other defect states. These and other microstructural non-uniformities [118] are likely to influence NBE emission.

Second, the PL emission intensity of the nanopyramid array at each growth temperature is substantially stronger than that of the corresponding control sample. The integrated PL intensities of the nanopyramid samples are at least 3.8 times as strong as that of the control samples. This is a consequence of the improved in-coupling of excitation light into the material, and out-coupling of photoluminescence related to the pyramidal texture. The increased PL intensity is also likely a result of an increase in volume of better crystal quality InGaN relative to the control samples due to dislocation filtering by the $SiN_y$ mask, dislocation confinement to the core region of the nanopyramid and bending/exit of dislocations to the nanopyramid sides as observed in cross-sectional TEM analysis in Section 5.3.3.1. Third, for each growth temperature, the PL emission peak of the nanopyramid arrays invariably occurs at lower photon energies than the control sample. This is consistent with HR-XRD measurement that nanopyramid arrays contain higher In content than the control.

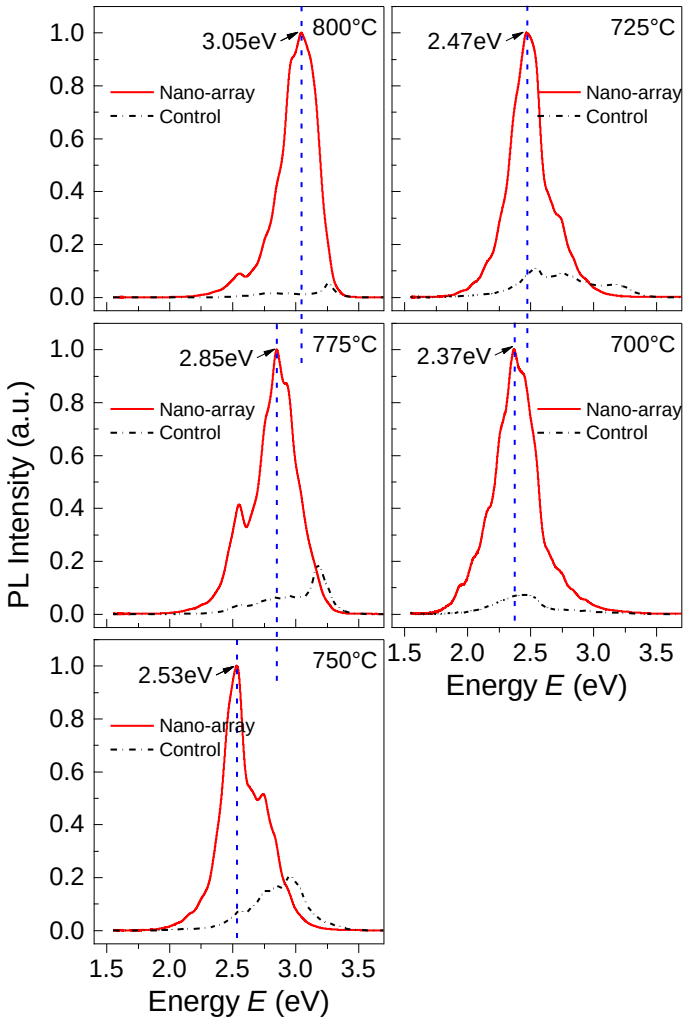


**Figure 6.5** Room temperature micro-photoluminescence (μ-PL) spectra of nanopyramid array (solid red line) and corresponding control (dash-dot black line) samples over the growth temperature range of 700°C to 800°C at a reactor pressure of 300 Torr.

### 6.3.4. Reflectance

The reflectance spectra at normal incidence of the samples are presented in Figure 6.6. As expected, not only are the spectra of the nanopyramid arrays much less oscillatory than that of the control films, the average reflectance <*R*> at ~ 7.4% to 8.6% are low, being less than a third of that in the control samples at ~ 25.3% to 28.9% over $\lambda$ of 300 nm to 1000 nm. The strong anti-reflection properties of the nanopyramidal texture have been discussed in Section 5.3.5.

The properties of the InGaN nanopyramid arrays and the corresponding control films for the temperature series are summarized in Table 6-2. Low *T* (down to 700°C), allow *x* up to 0.28 to be achieved in nano-SAG. However, this comes at the expense of reduced structural quality, polycrystalline growth and In droplet formation. This indicates that other growth conditions may need to be employed in order to overcome the tradeoff. For each *T*, the nanopyramid array invariably possesses higher *x*, more intense PL emission (almost fourfold or more) which indicate better material quality, and lower reflectance (by a least a factor of three) than the control sample. These are similarly obtained in Section 5.3. The results show that these properties remain for nanopyramids grown under different *T*.

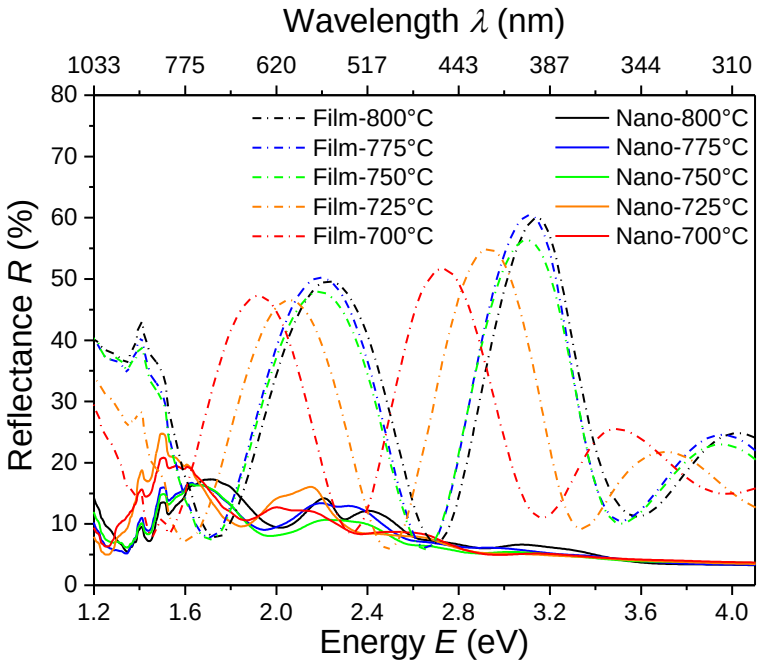


**Figure 6.6** Reflectance spectra at normal incidence of nanopyramid arrays (solid lines) and corresponding control (dash-dot lines) samples grown over the temperature range of 700°C to 800°C at a reactor pressure of 300 Torr. The nanopyramid arrays exhibit substantially lower reflectance which is also less oscillatory than the thin film control samples.

**Table 6-2** Properties of InGaN nanopyramid array and corresponding control thin film samples grown on AlN/Si(111) at a reactor pressure *P* of 300 Torr and growth temperature *T* between 700° to 800°C.

| ***T*** **(°C)** | **In content *x*** | | **PL peak (eV)** | | **Int. PL intensity ratio ($I_{nano}/I_{con}$)** | **Reflectance <*R*> (%)** | | **$\langle R\rangle_{control}/\langle R\rangle_{nano}$** |
|---|---|---|---|---|---|---|---|---|
| | Control | Nano | Control | Nano | | Control | Nano | |
| **700** | 0.232 | 0.282 | 2.46 | 2.37 | 11.5 | 25.3 | 8.4 | 3.0 |
| **725** | 0.136 | 0.219 | 2.54 | 2.47 | 5.3 | 25.6 | 8.6 | 3.0 |
| **750** | 0.077 | 0.158 | 2.96 | 2.53 | 3.8 | 27.7 | 7.4 | 3.7 |
| **775** | 0.067 | 0.103 | 3.18 | 2.85 | 6.8 | 28.9 | 7.9 | 3.6 |
| **800** | 0.055 | 0.098 | 3.26 | 3.05 | 26.7 | 28.9 | 8.2 | 3.5 |

## 6.4. Influence of Reactor Pressure

As discussed in Section 5.2.3, elevated reactor pressure *P* (300 Torr) has been found to suppress phase separation and In droplet formation in the MOCVD of InGaN *films* on AlN/Si(111) substrates at low *T* ~ 655°C. Hence, *P* = 300 Torr has been adopted in subsequent growth runs for *T* up to ~ 800°C). However, the influence of lower *P* at higher *T* has yet to be examined (for both nano-SAG and film growth). In fact, lower *P* may aid mass transport which improves In incorporation [321]. Thus, such an approach is warranted. In Section 6.3, it is noted that higher *T* leads to better morphology and structural quality but excessively high *T* depletes the In content. Bearing these considerations in mind, the subsequent set of growth runs investigating the influence of *P* on nano-SAG was performed at 775°C which is below the highest *T* (800°C) previously examined.

### 6.4.1. Morphology

#### 6.4.1.1. Growth Uniformity, Growth Rate and Mass Transport

Figure 6.7 shows the FESEM images of nanopyramid arrays grown over the range of *P* from 70 to 300 Torr at 775°C.

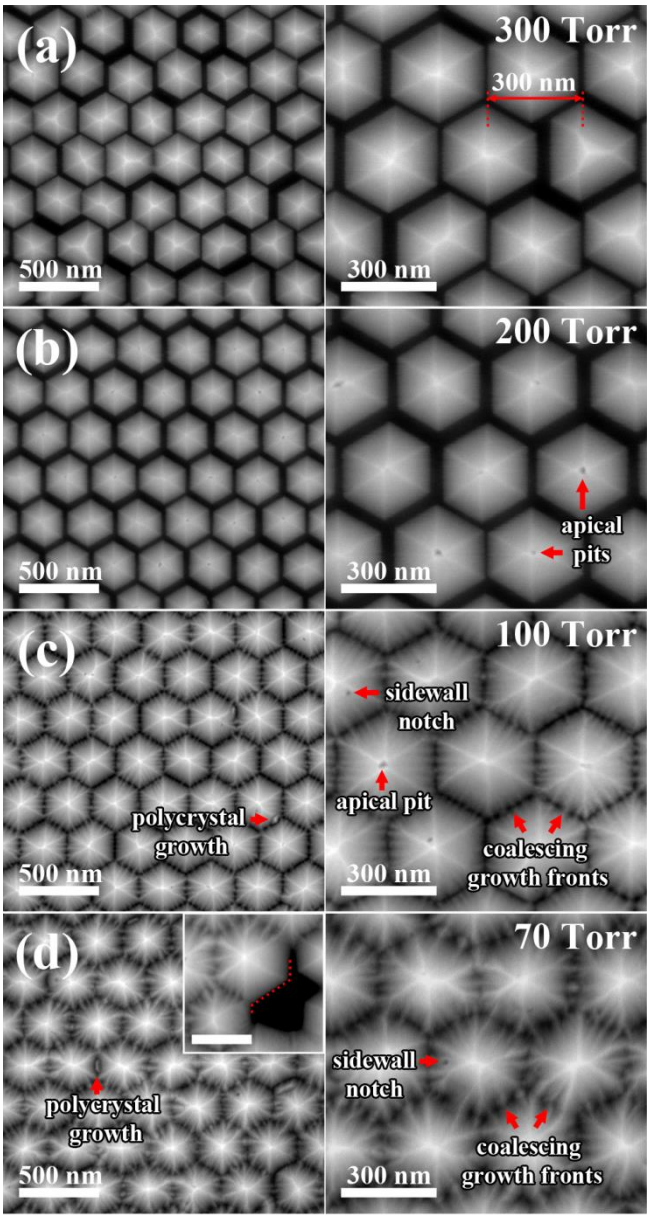


**Figure 6.7** FESEM images of InGaN hexagonal nanopyramids grown on AlN/Si(111) substrates for 40 min at reactor pressures of (a) 300 Torr, (b) 200 Torr, (c) 100 Torr, and (d) 70 Torr with a growth temperature of 775°C. Pressure reduction from 300 Torr is correlated to an improvement in homogeneity and increase in nanopyramid size (or growth rate). Some apical pits arising from incomplete coalescence are observed at 200 Torr and are filled out with further reduction in pressure or increased growth. Growing {11$\underline{0}$1} facets from neighboring nanopyramids that become sufficiently close start to coalesce by forming multiple ridges bridging the facets. Otherwise the facets remain smooth. See inset of (d). Inset scale bar corresponds to 300 nm. Dark contrast features or notches are observed at the sidewalls of some nanopyramids grown at 70 Torr and l00 Torr.

From AFM, the bounding facets of the nanopyramids remain inclined at ~ 62°, indicating that they are still composed of {11$\underline{0}$1} planes. The three dimensional AFM reconstruction of the nanopyramid morphology is shown in Figure 6.8. A reduction in

*P* has a number of effects. First, as discussed in Section 6.3.1.1, the size uniformity of the nanopyramids is improved. Second, the growth rate is generally increased. This is evident by the shrinking gaps between nanopyramids, and the coalescence behavior at 100 Torr and 70 Torr.

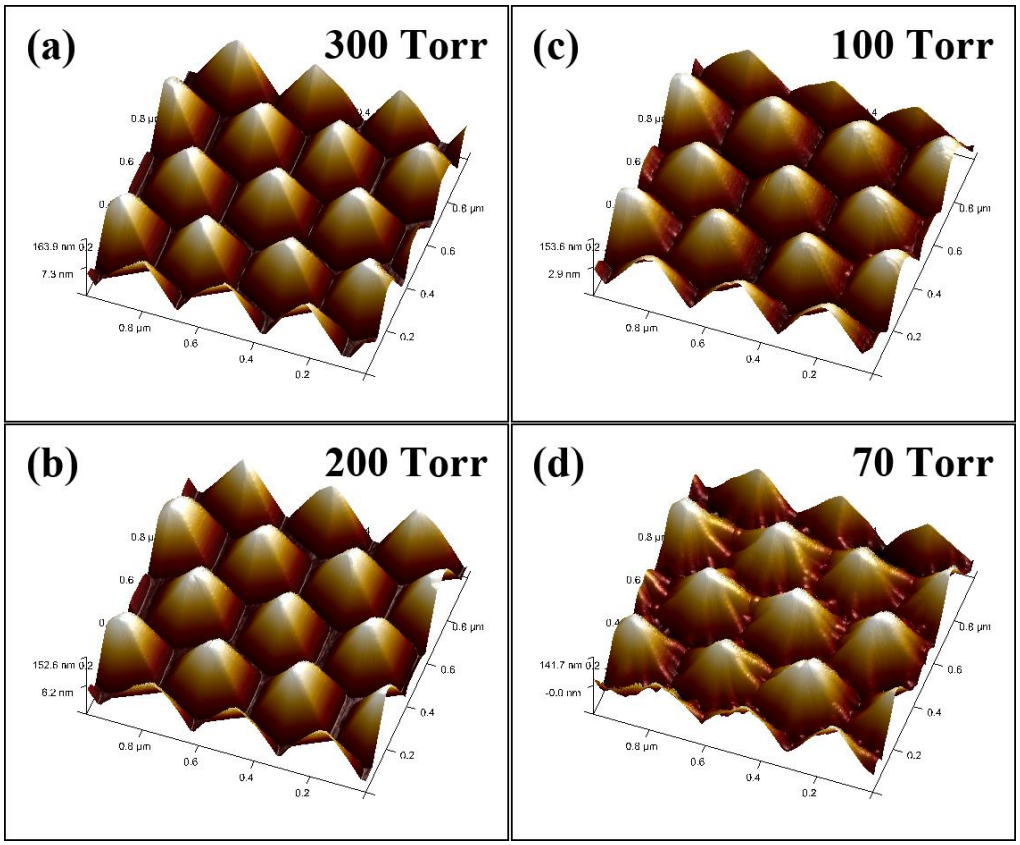


**Figure 6.8** AFM reconstruction of the three-dimensional morphology of the InGaN nanopyramid arrays grown on AlN/Si(111) substrates for 40 min at reactor pressures of (a) 300 Torr, (b) 200 Torr, (c) 100 Torr, and (d) 70 Torr with a growth temperature of 775°C. AFM profile measurements of the uncoalesced nanopyramids show that the bounding facets are inclined at ~ 62°to the basal plane, indicating that they are {11$\underline{0}$1} planes. Coalescence behavior results in the formation of ridges bridging the facets and is especially obvious in (d) due to the higher growth rate. At abrupt, sharp edges and tips, AFM tracking of the surface is less accurate, and susceptible to noise introduction. This results in apparent blunting (e.g. at the apex of each nanopyramid) or roughening of the surface at some locations.

The effect of *P* on mass transport in the Rotating Disc Reactor (RDR) used in this work can be understood as follows. For flow near a rotating disk, the velocity boundary-layer thickness $\delta_0$ is given by

$$\delta_0 \cong 4\left(\frac{\eta}{\rho\Omega}\right)^{1/2} \quad (6\text{-}1)$$

where $\eta$ is the dynamic viscosity, $\rho$ is the density and $\Omega$ is the disk's angular rotation rate [265]. Since the mass density $\rho$ is proportional to the reactor pressure $P$, $\delta_0$ can be expressed as $\delta_0 \propto P^{-1/2}$. For diffusion through a mass transport boundary layer, the mass flux $J$ of the precursor of interest is proportional to $D/\delta_0$ where $D$ is the diffusion coefficient and is inversely proportional to $P$. Considering these relationships, the mass flux J can be expressed as $J \propto P^{-1/2}$. That is, even though the boundary layer thickness $\delta_0$ is increased, this is more than offset by the increase in $D$ since the mean time between gas phase collisions is increased as $P$ is reduced [265]. Hence, the mass transport of precursors through a boundary layer becomes more rapid with a reduction in $P$. The increase in mass transport directly increases the growth rate as the growth conditions pertain to the viscous flow regime and is mass transport limited as discussed in Section 3.3.5. The dependence of the growth rate on $T$ is comparatively weaker (although a slight increase with $T$ reduction is observed as discussed in 6.3.1.2) and may be represented as the middle plateau segment of the graph in Figure 3.3 which shows the rate-limiting steps as a function of $T$.

### 6.4.1.2. Coalescence Behavior

Coalescence between the {11$\underline{0}$1} facets of adjacent nanopyramids begins when they are sufficiently close and manifests as ridges bridging the facets. These ridges enlarge with growth and roughen the nanopyramid sidewalls as seen in Figure 6.7(d) and Figure 6.8(d). The ridges are absent and the sidewalls remain smooth when there are no facets from neighboring nanopyramids that are sufficiently close as seen in Figure 6.7(d) inset. Ridges are also observed during coalescence at longer growth durations (see Section 6.5.1) indicating that they are not features associated with low $P$. By adopting a nano-SAG pattern with a longer period, coalescence can be delayed to

allow the growth of larger nanopyramids with a greater volume of high quality overgrown regions. However, this will inevitably prolong the time required to achieve coalescence. Nonetheless, the size controllability of nano-SAG InGaN nanopyramids can be harnessed in the design for specific light-trapping or light-extraction properties.

#### 6.4.1.3. Growth Artefacts

Nanopyramids grown at reactor pressure *P* less than 300 Torr exhibit apical pits and/or sidewall notches. Here, "apical pit" refers to the pit that is observed at the apex of some nanopyramids, while "sidewall notch" refers to the small dark contrast feature observed at some nanopyramid sidewalls. Some apical pits and sidewall notches are labelled in Figure 6.7. As discussed in Section 6.3.1.3, apical pits are related to the termination of central TDs though their actual manifestation depends on growth conditions. At 200 Torr, mainly apical pits are observed (see Figure 6.7(b)) similar to that observed at low growth temperatures in Figure 6.1(d)-(e). The occurrence of apical pits with lower *P*, and hence higher *x* (as will be explained in Section 6.4.2.1), supports the proposition that higher *x* (greater lattice mismatch and poorer structural quality) may contribute to apical pit formation. The smaller size of the apical pits in Figure 6.7(b) may be due to the higher adatom mobility afforded by the higher *T* and increased growth rate at lower *P*. With further reduction in *P* to 100 Torr, the incidence of apical pits decreases as these fill up with increased growth rate. However, sidewall notches emerge as seen in Figure 6.7(c). By 70 Torr, mainly sidewall notches remain while apical pits are hardly observed.

Features similar to the sidewall notches observed here have been reported by Winden et al. for InN hexagonal nanopyramids [203]. These have been attributed to slow coalescence and are expected to fill up with growth duration. However, we do not think that prolonged growth duration would lead to the eradication of the sidewall

features, at least under the growth conditions examined in our work. This is because the sidewall features are found under conditions that already promote fast growth rate (at low reactor pressures *P* albeit at higher temperature), but are ironically absent with slow growth rate (at higher *P* over the temperature range investigated). Further, considering that the sidewall features occur on the normally energetically stable and slow growing {11$\underline{1}$01} surface, normal irregularities would have been smoothened out during the initial stages of growth according to Wulff's theory [142]. In other words, the sidewall features may not be a simple collection of uncoalesced planes but are structural features brought out by low pressure growth.

The sidewall notches are also observed on smooth, uncoalesced nanopyramid sidewalls grown at 70 Torr. This rules out that they are features of coalescence. On the other hand, it is well known that TDs bend and emerge at the {11$\underline{1}$01} facets of GaN pyramids.[327] The existence of TDs inclined towards the {11$\underline{1}$01} sidewalls, or simply propagating along the *c*-axis near the axial region, is similarly observed in cross-sectional TEM of the InGaN nanopyramids in our work. The emerging points of TDs are discontinuities and have been associated with the formation of various features. These include hillock formation on GaN(11$\underline{1}$01) surface [328], V-pit formation on GaN(0001) surface [115], spiral growth on *c*-plane GaN[325] and *m*-plane GaN [324], and nanopipes formation in GaN nanowires and rods [329]. Therefore, we posit that the sidewall notches might possibly be related to TDs and will be the subject of a future work.

For nanopyramids grown at the higher pressures of 200 Torr and 300 Torr, sidewall notches are generally not observed. The more uniform sidewall surface may be due to a change in growth mechanism. The observation is in line with a work by Wernicke et al. for MOCVD growth on nominally on-axis (11$\underline{1}$01) GaN bulk substrates which

shows that the semipolar (11$\underline{1}$01) surface is planarized by growth at increased pressure [328]. Minor outcrops are also found in a few valleys framed by the nanopyramids grown at 100 and 70 Torr as seen in Figure 6.7(c)-(d). These are not ridges associated with coalescence behavior and are likely polycrystals similar to that in Section 6.3.1.3. However, the size of these is much smaller and their incidence much less due to the higher growth temperature in this growth series which improves adatom mobility.

### 6.4.2. Structural Characteristics

#### 6.4.2.1. Indium Content and Phase Composition

Figure 6.9 shows the (0002) $2\theta$-$\omega$ XRD scans for both nanopyramid array and control samples grown over the pressure range from 70 Torr to 300 Torr at a growth temperature of 775°C. For both sample types, only a single peak attributable to InGaN(0002) is observed in each spectrum. That is, the InGaN grown is generally single phase, with no other major components, like InN or In droplets.

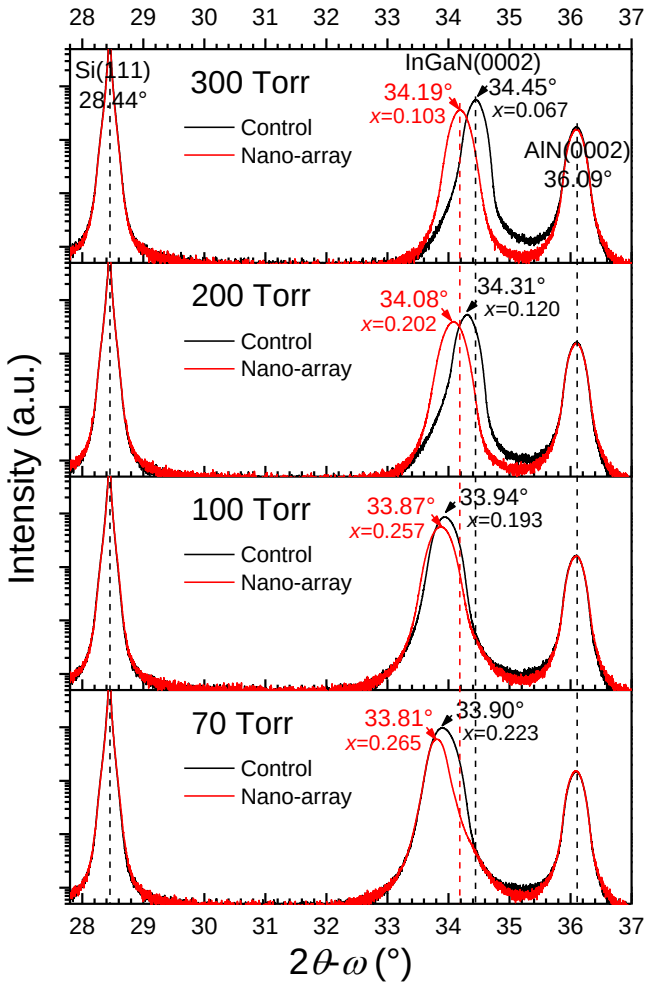


**Figure 6.9** HR-XRD (0002) $2\theta$-$\omega$ scans of InGaN nanopyramid array (red line) and corresponding control (black line) samples grown on AlN/Si(111) substrate over the reactor pressure range of 70 Torr to 300 Torr at a growth temperature of 775°C.

At each growth pressure *P*, the InGaN(0002) peak for the nanopyramid array always occurs at a lower $2\theta$ value than in the control. This is evident of higher In content *x* in the nanopyramids and is attributed to strain relaxation effects and growth on {1$\underline{1}$01} planes, similar to the temperature growth series. With reduction in *P*, the InGaN(0002) peak in both cases shifts towards lower $2\theta$ values, indicative of increasing *x*. The increase in *x* (calculated as before) with decrease in *P* is plotted in Figure 6.10 and may be explained as follows. It was discussed in Section 6.4.1.1 that mass transport of precursors through the boundary layer is enhanced at reduced *P*. Coupled with the high molar ratio of TMIn/TMGa used, the increased mass flux of TMIn greatly

suppresses desorption of In, resulting in an enhancement of In incorporation into the grown structure. While, the TMGa flux is also increased, its influence on In incorporation under such conditions is not significant as shown by Kim et al. [321].

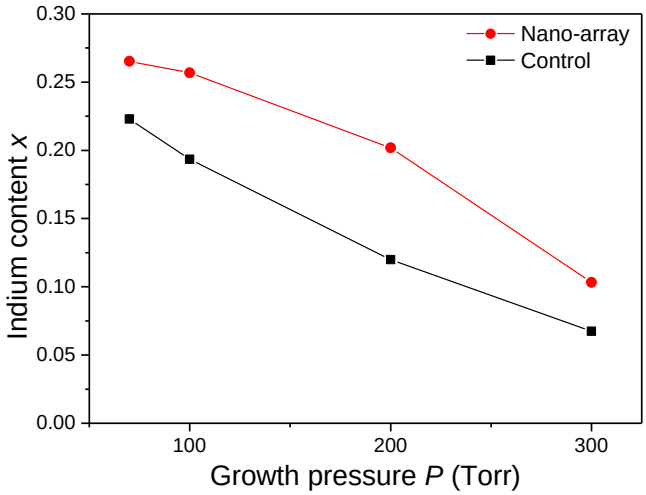


**Figure 6.10** Variation of HR-XRD estimated In content *x* with growth pressure *P* for InGaN nanopyramid array (red line) and corresponding control (black line) samples grown at a temperature of 775°C.

### 6.4.2.2. Lattice Tilt and Twist

The FWHM of the X-ray $\omega$-rocking curve for the on-axis symmetric (0002) and off-axis skew symmetric (20.1) reflections (indicators for relative lattice tilt and twist respectively) at each *P* are plotted in Figure 6.11. Tilt in the control samples remains almost independent of *P* with the (0002)-$\omega$ rocking curve FWHM values remaining approximately constant at ~ 0.67°, very close to that of AlN at 0.68°. Considering that increase in *T* only provides marginal reduction in the tilt and decrease in *T* only serves to increase it, it is evident that the AlN buffer layer exerts a lower bound to the minimum tilt permissible, as discussed in Section 6.3.2.2. For the nanopyramid array series, tilt is higher compared to the thin film control as a consequence of dislocation bending [104]. Further, a slight increase in the (0002)-$\omega$ rocking curve FWHM from ~ 0.78° to ~ 0.83° is observed as *P* is reduced. We note from Figure 6.7 and Figure 6.8 that a greater extent of epitaxial lateral overgrowth (ELO) occurs as a result of the

consequent increased growth rate. It has been reported for selective area ELO that the tilt of the (0001) planes, measured by the (0002) reflection, increases at a rate of ~ 0.6°/μm from the apex [330, 331]. This appears consistent with our observations.

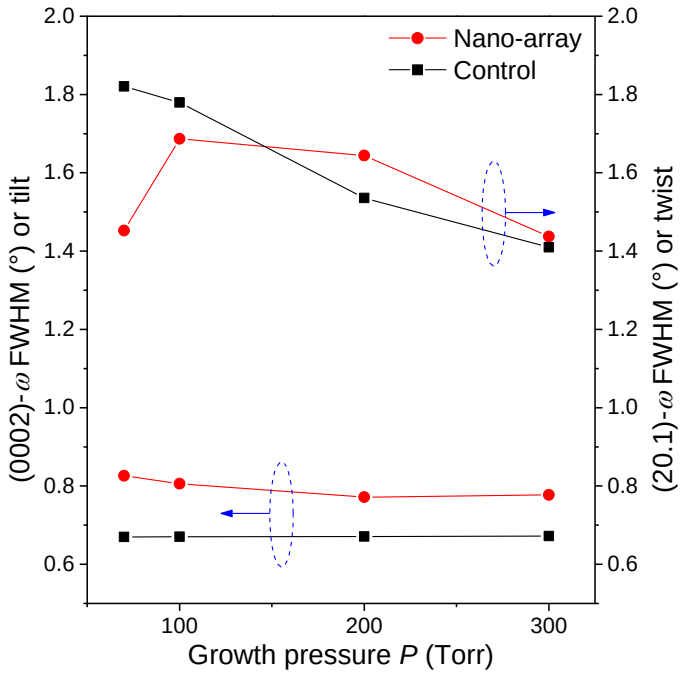


**Figure 6.11** Variation of the FWHM of the X-ray $\omega$-rocking curve for the symmetric (0002) and skew symmetric (20.1) reflections over 70 Torr to 300 Torr at a growth temperature of 775°C. The FWHMs are indicative of relative lattice tilt and twist respectively.

For the control samples, lattice twist, indicated by the (20.1)-$\omega$ rocking curve FWHM, increases as *P* is reduced. This is an indication of a higher density of TDs with edge character generated by the greater lattice mismatch of higher In content InGaN achieved at lower *P*. The TDs propagate through the thin film along the *c*-axis and are generally unaffected by the higher growth rate. For the nanopyramid samples, twist is similar to that of the control sample at ~ 300 Torr, but increases at a decreasing rate with pressure reduction until ~ 150 Torr. Subsequently, it dips below the control values and finally decreases when pressure goes below ~ 100 Torr. The initial increase in twist with a reduction in pressure is due to similar reasons as the control samples. However, the levelling off and decrease in the twist values are consequences

of the more extensive epitaxial lateral overgrowth arising from the higher growth rates at low pressures. The overgrown region grows without the lattice mismatch and edge dislocations associated with growth directly over the AlN opening. The relative volume of improved crystal quality InGaN is thus increased. This mitigates the higher twist associated with increased In content InGaN grown over the opening.

### 6.4.3. Photoluminescence

Figure 6.12 shows the room temperature μ-PL spectra of both nanopyramid array and control samples grown over 70 – 300 Torr at 775°C. The PL spectra share some features with that of the temperature series in Figure 6.5. These likely arise from similar reasons. First, each PL spectrum generally consists of a major peak bearing some minor shoulders and/or secondary peaks, rather than a single smooth Gaussian profile. Second, the PL intensity of the nanopyramid array sample grown at each pressure is substantially stronger than that of the corresponding control. In fact, the integrated PL intensity of each nanopyramid array is at least 4.4 times as strong as that of the corresponding control. This is a consequence of the improved in-coupling of excitation light into the material, and out-coupling of photoluminescence related to the pyramidal texture. The increased PL intensity is also likely contributed in part by the increased volume of improved crystal quality InGaN in the nanopyramid array resulting from the dislocation behavior described in Section 6.3.3. The volume is further increased by the greater epitaxial lateral overgrowth occurring at low *P*.

Additionally, some other observations need to be highlighted. First, the PL peaks of both the nanopyramid array and control samples shift to lower energy values with reduction in *P*. The general shift in PL emission energy is consistent with an increase in *x* due to reasons as discussed earlier in Section 6.4.2.1. Second, the 70 Torr and 100 Torr samples emit at notably lower photon energies (1.93 eV and 2.25 eV) than

would have been obtained in the temperature series or through theoretical estimates (~ 2.41 eV and ~ 2.44 eV) for the HRXRD-estimated In content of $x$ ~ 0.265 and ~ 0.257 [10]. From Figure 1.2, PL emission of 1.93 eV and 2.25 eV corresponds to much higher $x$ of ~ 0.415 and ~ 0.313 respectively. We note that while the nanopyramids in the temperature series are separated from each other in the array due to their slow growth rate (Figure 6.1), the nanopyramids grown at 70 Torr and 100 Torr are partially coalesced and possess numerous ridges bridging the adjacent {1$\underline{1}$01} facets of neighboring nanopyramids. Since In segregation to the ridges of surface undulations reduces the number of compressively strained In-N bonds and is energetically favored [316], we posit that the In rich ridges may be responsible for the low PL emission energies for the 70 Torr and 100 Torr samples.

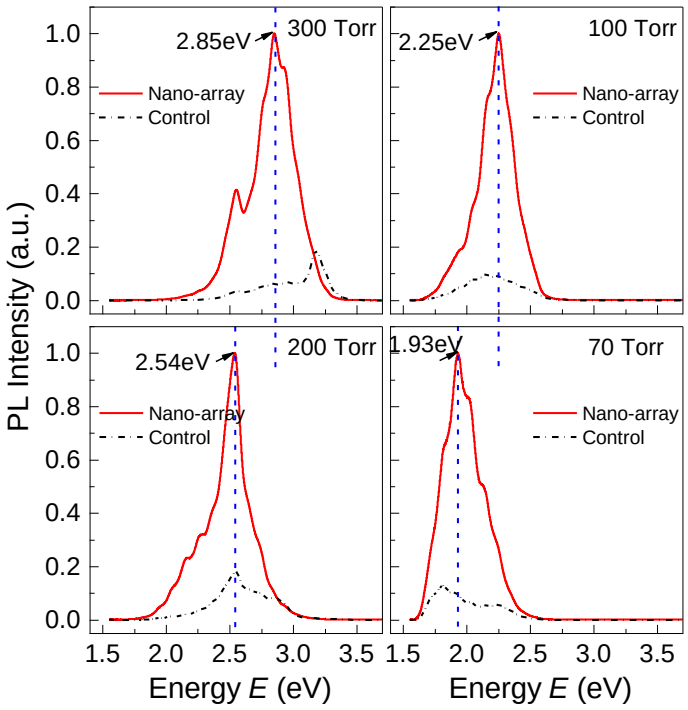


**Figure 6.12** Room temperature micro-photoluminescence (μ-PL) spectra of nanopyramid array (solid red line) and corresponding control (dashed black line) samples over the reactor pressure range of 70 Torr to 300 Torr at a growth temperature of 775°C.

The In rich ridges form only small portions of the nanostructures and hence do not show up as distinct peaks in XRD. However, they contribute to the low-intensity

XRD signals at lower $2\theta$ values (higher $x$) against the main InGaN peak in the (0002) $2\theta$-$\omega$ XRD scans for $P$ = 70 and 100 Torr in Figure 6.9. Third, interestingly, the emission peak of the control samples shifts to lower emission energies at a faster rate than the nanopyramids. Considering the multi-featured, broad PL spectra in the control samples, we posit that the lower energies of their peak emission might be related to In segregation induced by microstructural non-uniformity [316]. This is supported by SEM and AFM observations which reveal the thin film controls to be characterized by rough, undulating surface morphologies. The AFM root mean square roughness $R_{rms}$ values are presented in Table 6-3. While $R_{rms}$ increases only from ~ 8 nm to ~ 11 nm with reduction in $T$, the increase is much greater with reduction in $P$, with $R_{rms}$ increasing from ~ 8 nm to ~ 14 nm. The highly roughened morphology encourages In segregation to a greater extent, accounting for the lower energy PL emission which also occurs over a wide $E$ range.

**Table 6-3** Root mean square roughness $R_{rms}$ of InGaN thin film control samples grown at (a) 300 Torr with various growth temperatures $T$, and (b) 775°C with various reactor pressures $P$.

**(a)**

| **Temperature *T* (°C)** | 700 | 725 | 750 | 775 | 800 |
|---|---|---|---|---|---|
| **Roughness $R_{rms}$ (nm)** | 11.00 | 9.01 | 8.19 | 7.99 | 7.93 |

**(b)**

| **Pressure *P* (Torr)** | 70 | 100 | 200 | 300 |
|---|---|---|---|---|
| **Roughness $R_{rms}$ (nm)** | 14.40 | 12.60 | 8.17 | 7.99 |

### 6.4.4. Reflectance

Figure 6.13 shows the reflectance spectra at normal incidence of the nanopyramid arrays and control thin film samples grown over the pressure range of 70 Torr to 300 Torr at a temperature of 775°C. It is seen that the nanopyramid arrays have much lower and less oscillatory reflectance than the control samples. Over the wavelength range of 300 nm to 1000 nm, average reflectance at normal incidence $\langle R \rangle$ remains

low in the nanopyramid arrays at ~ 7.4% to ~ 9.0%. The highest value of 9.0% is contributed by the partially coalesced sample grown at 70 Torr. This indicates that the coalescence behavior, characterized by the roughening of the otherwise smooth {1101} facets of the nanopyramids, tend to disrupt the light-trapping properties of the array. <*R*> for the control samples grown at 200 Torr and 300 Torr remain high at ~ 28.3% and ~ 28.9% respectively. However, a notable reduction in <*R*> to 22.3% and 21.0% for the 100 Torr and 70 Torr samples, respectively, is observed. This arises from the substantial increase in the surface roughness of the samples observed in AFM and FESEM (not shown) with thickness which promotes light scattering.

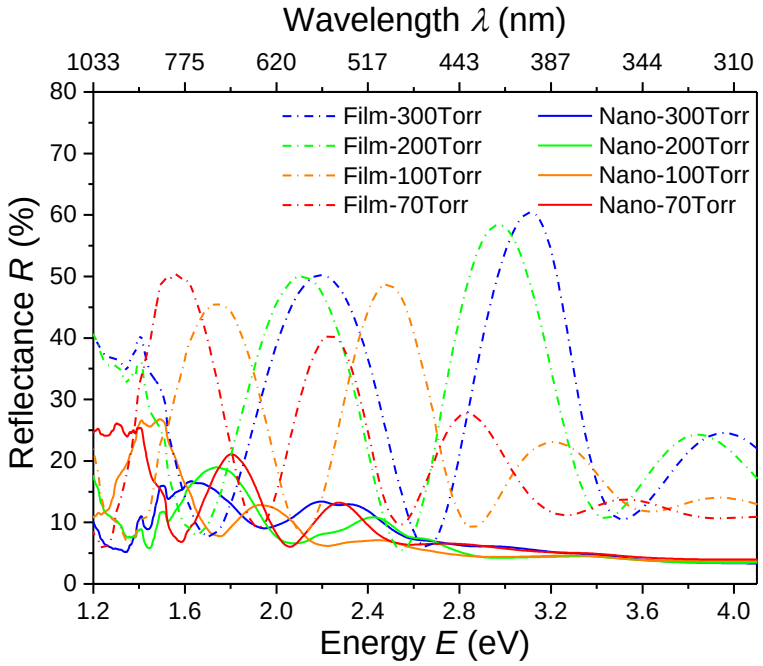


**Figure 6.13** Reflectance spectra at normal incidence of nanopyramid arrays (solid lines) and corresponding control (dash-dot lines) samples grown over the pressure range of 70 Torr to 300 Torr at a growth temperature of 775°C. The nanopyramid arrays exhibit substantially lower reflectance which is also less oscillatory than the thin film control samples.

The general properties of the InGaN nanopyramid arrays and the corresponding thin film control samples for the pressure series are summarized in Table 6-4.

**Table 6-4** Properties of InGaN nanopyramid array and corresponding control thin film samples grown on AlN/Si(111) at a growth temperature *T* of 775°C and reactor pressure *P* between 70 Torr and 300 Torr.

| ***P*** **(Torr)** | **In content *x*** | | **PL peak (eV)** | | **Int. PL intensity ratio ($I_{nano}/I_{con}$)** | **Reflectance <*R*> (%)** | | **$\langle R\rangle_{control}/\langle R\rangle_{nano}$** |
|---|---|---|---|---|---|---|---|---|
| | Control | Nano | Control | Nano | | Control | Nano | |
| **70** | 0.223 | 0.265 | 1.81 | 1.93 | 6.8 | 21.0 | 9.0 | 2.3 |
| **100** | 0.194 | 0.257 | 2.15 | 2.25 | 6.7 | 22.3 | 8.0 | 2.8 |
| **200** | 0.120 | 0.202 | 2.55 | 2.54 | 4.4 | 28.3 | 7.4 | 3.8 |
| **300** | 0.067 | 0.103 | 3.18 | 2.85 | 6.8 | 28.9 | 7.9 | 3.6 |

At each reactor pressure *P*, the nanopyramid array invariably possesses higher In content *x*, more intense PL emission (by at least fourfold) which indicate better material quality, and lower reflectance (by more than a factor of 3 in the uncoalesced nanopyramids) than the control sample. The suitability of the InGaN nanopyramids over thin film structures for photovoltaic applications is thus demonstrated for a range of growth pressures.

## 6.5. Influence of Growth Duration

In the temperature and pressure growth series discussed in Sections 6.3 and 6.4, the duration of nano-SAG was maintained at 40 min to achieve complete InGaN hexagonal nanopyramids while attempting to minimize coalescence. In this Section, the influence of shorter (12 min) and longer (72 min) durations of InGaN nano-SAG on material properties is examined. Similar to the prior growths, the flow rates of TMGa, TMIn, and $NH_3$ were kept at 5 sccm, 120 sccm and 18000 sccm, respectively. The reactor pressure *P* is maintained at 300 Torr while the growth temperature *T* is increased to ~ 825°C (higher than the 700 – 800°C range examined previously) to improve growth quality and minimize the influence of In composition variation which seems to increase with reduced *P* and *T*. The conditions are chosen to allow a more focused examination of the influence of growth duration in nano-SAG.

### 6.5.1. Morphology

The morphology of the InGaN nanostructures grown via nano-SAG through a Type A $SiN_y$ nanoporous template on AlN/Si(111) substrate for 12 min and 72 min is shown in Figure 6.14.

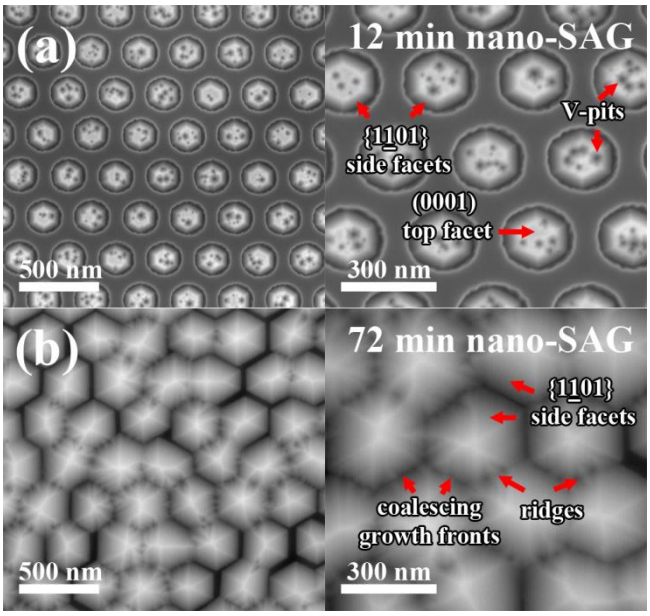


**Figure 6.14** FESEM images of arrays of InGaN nanostructures grown via nano-SAG through a $SiN_y$ Type A template on AlN/Si(111) substrates at 300 Torr and 825°C for (a) 12 min, and (b) 72 min. At 12 min of nano-SAG, truncated hexagonal InGaN nanopyramids each confined within a pore of the $SiN_y$ template and possessing a pitted (0002) top surface are observed. By 72 min of nano-SAG, coalescence of complete InGaN hexagonal nanopyramids occurs by the formation of ridges between the {11$\bar{2}$01} facets.

At 12 min, truncated hexagonal InGaN nanopyramids totally confined within the pores are observed. With longer growth duration these develop into complete 3D hexagonal nanopyramid with six smooth side facets as discussed in Section 5.3.2. By 72 min, coalescence of the InGaN nanopyramids occurs through the formation of ridges which bridge adjacent {11$\bar{2}$01} side facets. The observation also confirms that the ridge formation described in Section 6.4.1.2 is not due to the reduced *P* but due to coalescence behavior.

### 6.5.2. Structural Characteristics

#### 6.5.2.1. Indium Content and Phase Composition

Figure 6.15 shows the (0002) $2\theta$-$\omega$ XRD scans for the nanopyramid arrays after 12 and 72 min of nano-SAG. In each scan, only a single peak attributable to InGaN(0002) is observed. That is, as expected, the InGaN is generally single phase, with no other major components. $x$ increases from ~ 0.026 to ~ 0.051 when nano-SAG is prolonged from 12 to 72 min. We point out that strain relaxation associated with thicker layers and coarser 3D morphologies in nano-SAG can contribute to this phenomenon. This is similarly observed in Section 5.2.4.2 for unpatterned growth. In addition, as mentioned in Section 5.3.4.1 the {11$\underline{1}$01} planes have a higher In incorporation efficiency than the (0001) plane [151, 152]. Hence, as the surface area of (0001) planes in the truncated nanopyramids diminishes with growth duration and the nanostructures become bound only by {11$\underline{1}$01} planes and grow via depositions on these planes, $x$ also increases. The FWHM of the InGaN(0002) $2\theta$-$\omega$ peak at 72 min of nano-SAG (~ 0.273°) is almost unchanged compared to that at 12 min (~ 0.272°), indicating a barely XRD-detectable change in compositional variation with prolonged higher temperature growth. However, minor local fluctuations in In content can still exist amidst the bulk phase due to the aforementioned mechanisms. These will show up in PL spectroscopy.

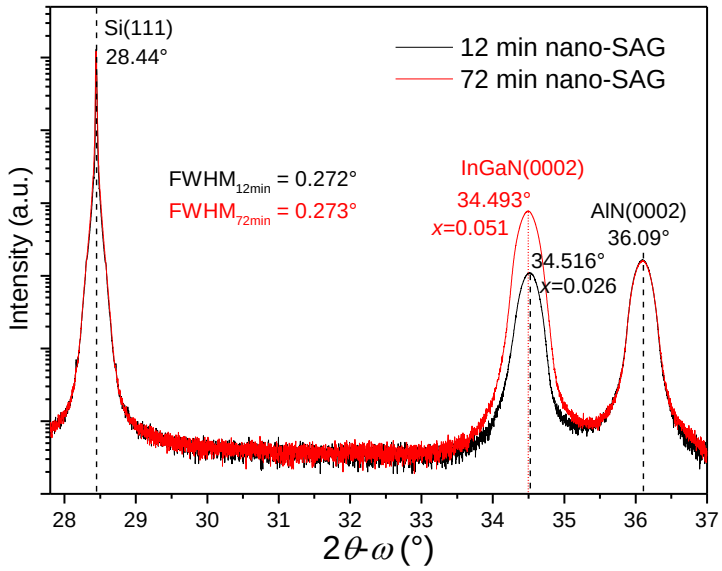


**Figure 6.15** HR-XRD (0002) $2\theta$-$\omega$ scans of InGaN nanopyramid arrays grown on AlN/Si(111) substrate at 300 Torr and 825°C with growth durations of 12 min (black line) and 72 min (red line).

### 6.5.2.2. Lattice Tilt and Twist

Figure 6.16 shows the FWHM of the $\omega$-rocking curves at different inclination angles $\chi$ for the the nanopyramid arrays after 12 and 72 min of nano-SAG. At $\chi = 0°$, the $\omega$-FWHM (of the 0002 reflection) measures lattice tilt only, As $\chi$ is increased, the $\omega$-FWHM measures an increasing component of lattice twist until $\chi = 90°$, where it measures twist only. Measurement of tilt and twist are important because they are indicators of screw and edge dislocation densities, and hence structural quality. However, $\omega$-scans with $\chi = 90°$ would entail probing a plane normal to the sample surface (e.g. the 11$\underline{0}$0 plane for *c*-oriented material) where the probing area is directly determined by the thickness of the grown material  Due to the low thicknesses (few hundred nm's) involved, such a configuration (possible only in skew symmetry to avoid the XRD forbidden regions) will result in an extremely weak, if measurable, reflected XRD intensity. Hence, lower values of $\chi$ (e.g. ~ 75° corresponding to the (20.1) reflection) are typically employed and used to approximate twist measurement.

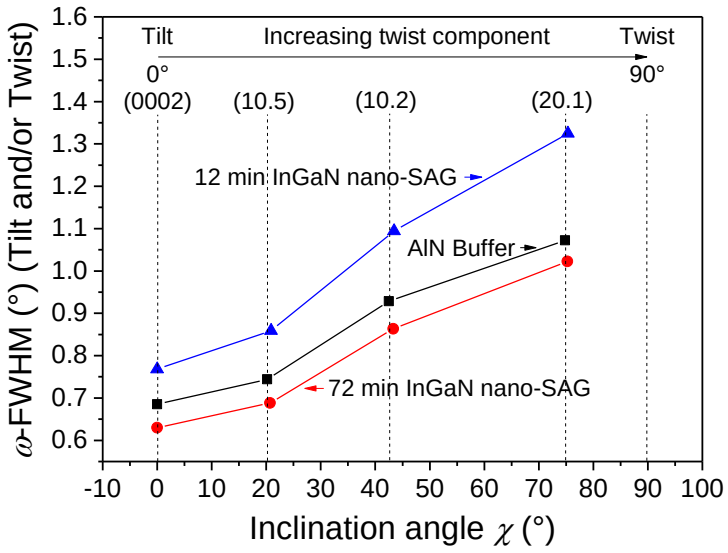


**Figure 6.16** FWHM of the $\omega$-rocking curve of skew symmetric reflections at different inclination angles $\chi$. For $\chi = 0°$, the $\omega$-FWHM measures lattice tilt only. $\omega$-FWHM at increasing $\chi$ measures an increasing component of lattice twist, until $\chi = 90°$ where it measures lattice twist only. Increasing nano-SAG duration reduces both tilt and twist.

The sample with nano-SAG duration of 12 min shows higher $\omega$-FWHM than the AlN buffer at all $\chi$, indicating higher tilt and twist (or higher densities of TDs with screw and edge character). This is due to heteroepitaxy of InGaN on highly mismatched AlN and etch damge of AlN incurred during $SiN_y$ template fabrication such that the material deposited in the early stage is characterized by a high density of coalescing dislocations and stacking faults [332]. This can be seen in the cross-sectional TEM image of the InGaN/AlN interface in Figure 5.12(f).

As growth proceeds, annihilation of coalescing dislocations with opposite Burgers vectors, dislocation bending and ejection partially repairs the crystal structure. For instance, the (0002) $\omega$-FWHM of the *uncoalesced* nanopyramid arrays grown in the temperature growth series for 40 min in Section 6.3.2.2 decreases and approaches that of the AlN buffer at ~ 0.68° (though it still remains higher due to TD bending). In addition to lattice mismatch, the AlN buffer exerts a lower bound to tilt in the InGaN structures, because TDs with screw character from the AlN buffer propagates into the

InGaN nanostructures through the $SiN_y$ mask openings. Twist in the nanopyramid arrays remains greater than the AlN buffer due to the generation of new dislocations with edge character at the mismatched InGaN/AlN interface. Notwithstanding dislocation bending, confinement, and exit mechanisms in the nanostructures which increase the volume of better quality material, the volume of grown material relative to the length of dislocations may be inadequate to present significant reduction to the $\omega$-FWHM values. Hence, these values remain larger than that of the AlN buffer.

By prolonging the growth duration to increase the size of the nanostructures and facilitate coalescence, the $\omega$-FWHM values for both tilt and twist can be reduced to even below that of the AlN buffer as seen in Figure 6.16 for 72 min of nano-SAG. This is in spite of higher *x* and hence lattice mismatch. The findings suggest that longer nano-SAG durations should be suitably employed to improve crystal structure.

### 6.5.3. Photoluminescence

Figure 6.17 shows the normalized μ-PL spectra at room temperature for the nanopyramid arrays after 12 and 72 min of nano-SAG. PL emission of the latter occurs at lower energies (3.279 eV vs 3.299 eV) and over a broader range (FWHM of 0.141 eV vs 0.119 eV) due to higher *x* and a wider spread of *x* than the former, consistent with the discussion on XRD results in Section 6.5.2.1. However, the spread of PL energies for both remain narrower than that grown at lower temperatures in earlier sections. The correlation of purer emission in nano-SAG with higher temperature growth is attributed to improved structural quality and lower *x* which reduce compositional fluctuation within the InGaN alloy. In addition, the integrated PL intensity of the sample at 72 min of nano-SAG is ~ five times that at 12 min of nano-SAG due to the increased volume of material grown.

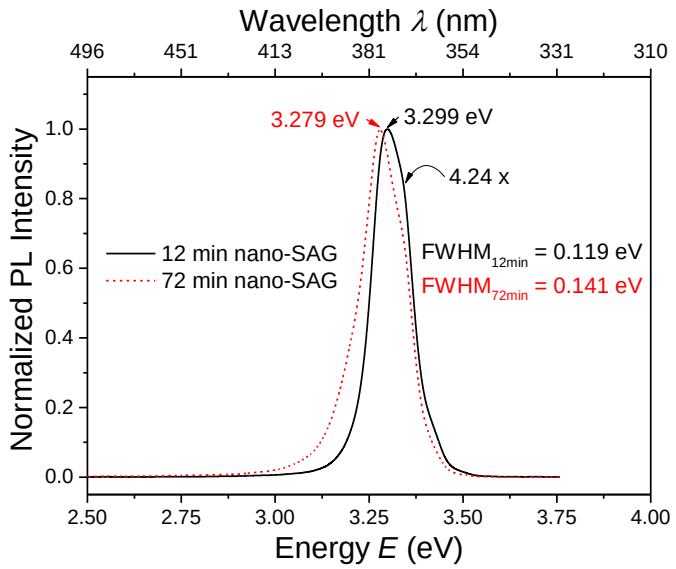


**Figure 6.17** Normalized room-temperature μ-PL spectra of the of InGaN nanopyramid arrays grown on AlN/Si(111) substrate at 300 Torr and 825°C with growth durations of 12 min (black line) and 72 min (red dash line). The latter emits at lower energies over a broader range.

### 6.5.4. Reflectance

Figure 6.18 shows the reflectance spectra at normal incidence of the nanopyramid arrays with different growth durations. The reflectance at 12 min of nano-SAG is oscillatory with a high average reflectance <*R*> of ~ 20.7% because the nanopyramids are small and have yet to emerge from the $SiN_y$ pores. The surface remains relatively smooth with limited light-trapping capabilities. The light-trapping capability of nanopyramid arrays becomes substantial when the nanopyramids emerge from the $SiN_y$ pores and possess larger sizes with complete and distinct inclined sidewalls allowing low <*R*> of less than ~ 8.6% to be achieved as seen in Figure 6.6 and Table 6-2. The roughening of the sidewalls or disruption of the hexagonal nanopyramid structure observed during coalescence in prolonged nano-SAG, e.g. with 72 min of growth duration, causes a slight deterioration of the anti-reflection properties and slight increase in <*R*> to ~ 9.7% as seen in Figure 6.18. This is similarly observed with shorter growth durations but high growth rates at reduced pressures as discussed in Section 6.4.4. The results show that proper design of the array period and growth duration (and hence nanopyramid size) to control coalescence is required to optimize

the light-trapping properties of the nanopyramid array. Table 6-5 summarizes and compares the properties of the samples grown with different nano-SAG durations.

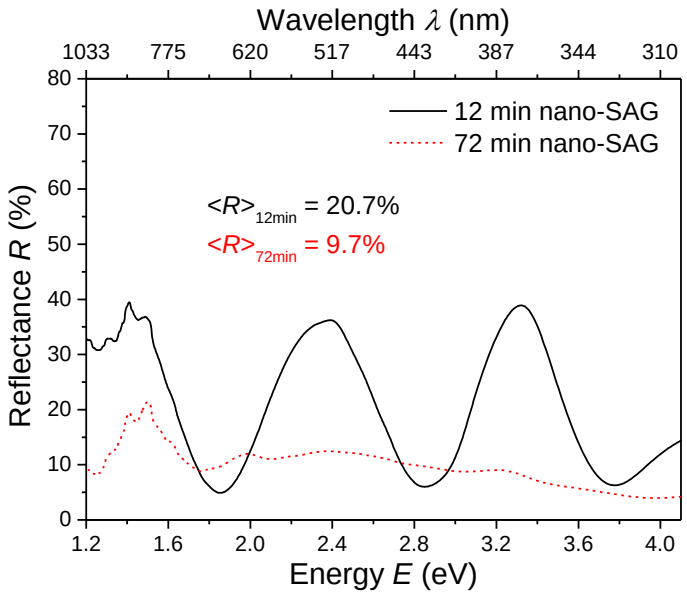


**Figure 6.18** Reflectance spectra at normal incidence of InGaN nanopyramid arrays grown on AlN/Si(111) substrate at 300 Torr and 825°C with growth durations of 12 min (solid black line) and 72 min (dashed red line).

**Table 6-5** Properties of InGaN nanopyramid arrays grown on AlN/Si(111) substrate at 300 Torr and 825°C with growth durations of 12 min and 72 min.

| Duration (min) | In content *x* | HR-XRD FWHM (°) | | | PL peak (eV) | PL FWHM (eV) | Rel. int. PL intensity | <*R*> (%) |
|---|---|---|---|---|---|---|---|---|
| | | (0002) $2\theta$-$\omega$ | (0002) $\omega$ | (20.1) $\omega$ | | | | |
| **12** | 0.026 | 0.272 | 0.768 | 1.325 | 3.299 | 0.119 | 1 | 20.7 |
| **72** | 0.051 | 0.273 | 0.630 | 1.022 | 3.279 | 0.141 | 4.99 | 9.7 |

## 6.6. Influence of Gas Flow Rate

In the preceding Sections of 6.3, 6.4, and 6.5, the influence of growth temperature *T*, reactor pressure *P* and growth duration on nano-SAG have been examined in turn. In this section, the flow rates of the gases $H_2$:$N_2$:$NH_3$ are varied from the prior flow rate of 0:6:18 (in slm) while the flow rates of TMGa and TMIn remain as before (with $r_m$ = 0.80). Two gas flow conditions are examined, namely $H_2$:$N_2$:$NH_3$ of 1:5:18, and 0:12:12. The former examines the effect of $H_2$ on nano-SAG whilst maintaining the

V/III ratio and $r_m$, while the latter examines the effect of a reduced V/III ratio whilst maintaining $r_m$. In all cases, the total gas flow rate is maintained at 24000 sccm, while *T* and *P* are kept at 775°C and 300 Torr. Growth duration is maintained at 40 min.

### 6.6.1. Morphology

The morphology of the InGaN nanostructures grown via nano-SAG through Type A $SiN_y$ nanoporous template on AlN/Si(111) substrate and the corresponding thin film control for $H_2$:$N_2$:$NH_3$ flow rates of 0:6:18, 1:5:18 and 0:12:12 are shown in Figure 6.19, Figure 6.20, and Figure 6.21, respectively.

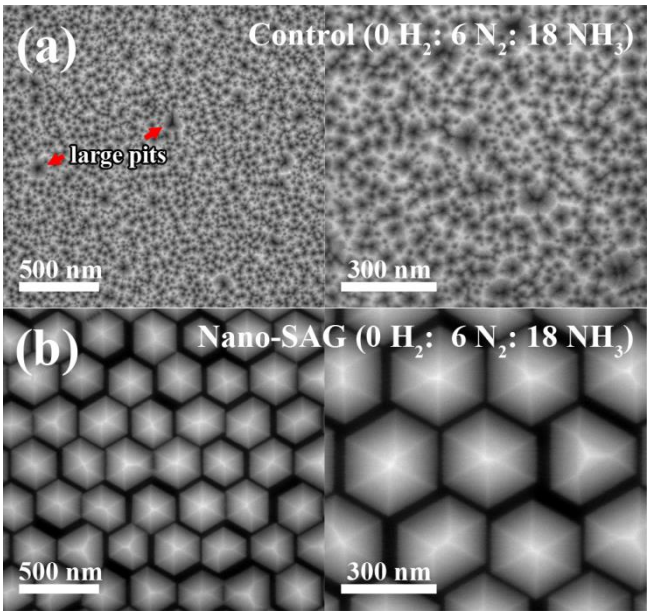


**Figure 6.19** FESEM images of (a) InGaN thin film control grown on unpatterned AlN/Si(111) substrate, and (b) InGaN nanopyramid array grown via nano-SAG on AlN/Si(111) substrate, at the $H_2$:$N_2$:$NH_3$ gas flow rate of 0:6:18, *T* = 775°C, *P* = 300 Torr, and duration of 40 min. The images for (b) are adapted from Figure 6.1(b) and Figure 6.7(a).

The images of the nanopyramid array in Figure 6.19(b) are the same as Figure 6.1(b) and Figure 6.7(a) since these are the same samples. The formation mechanism of the rough, pitted surface of the film control has been described in Section 5.2.4.2 and Section 5.3.3.1. Similar explanations, albeit of InGaN films grown on GaN layers, have also been proposed by Kim et al. [333].

In order to assess the influence of $H_2$ on nano-SAG, 1 slm of $H_2$ was introduced into the MOCVD gas mixture. The flow rate of $N_2$ was correspondingly reduced from 6 slm to 5 slm, to maintain a constant total flow rate. In the film control, pit density was reduced and a more planarized morphology was obtained as seen in Figure 6.20(a).

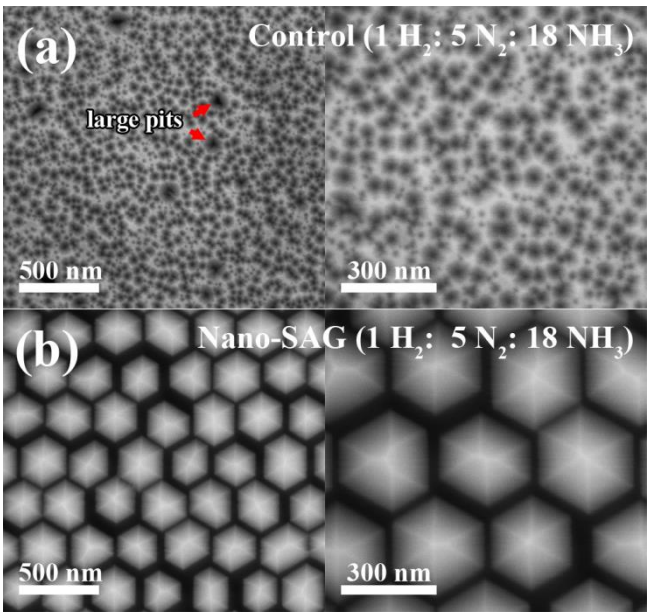


**Figure 6.20** FESEM images of (a) InGaN thin film control grown on unpatterned AlN/Si(111) substrate, and (b) InGaN nanopyramid array grown via nano-SAG on AlN/Si(111) substrate, at the $H_2$:$N_2$:$NH_3$ gas flow rate of 1:5:18, $T$ = 775°C, $P$ = 300 Torr, and duration of 40 min. The introduction of $H_2$ results in a lower pit density and a more planarized morphology in the control. A lower growth rate manifested as a reduction in nanopyramid size is also discerned.

The improvement in morphology with the use of $H_2$ is consistent with reports on GaN growth [334]. Hexagonal nanopyramids are still obtained in nano-SAG as seen in Figure 6.20(b). However, a reduction in size may be discerned. This indicates a lower growth rate since growth duration is kept at 40 min. The $H_2$-induced change in InGaN morphology may be related to a reduction in the lifetime of the reactive In species on the growing surface leading to a decrease in concentration of the reactive In species [335-337]. This will explain the reduction of growth rate. The decrease in In content with $H_2$ introduction observed in XRD in Section 6.6.2.1 also lends support to this

explanation. As discussed earlier in Section 5.2.4.2, InGaN with lower In content will have a smaller lattice mismatch with the AlN buffer such that the strain energy is likely reduced. This has the effect of delaying the onset of 3D growth. Hence, a slower growth rate may allow the smoother morphology prior to 3D growth in the Stranski-Krastanov growth mode to be observed in the film control.

Reducing the flow rate of $NH_3$ from 18 slm to 12 slm, with a corresponding increase of $N_2$ flow rate from 6 slm to 12 slm, (i.e. reducing V/III ratio from ~ 9200 to ~ 6100) results in a degradation of the InGaN morphology in both control and nano-SAG samples. Polycrystal growth is observed in the control as seen in Figure 6.21(a); however, the extent is greater in the nanopyramid array as seen in Figure 6.21(b).

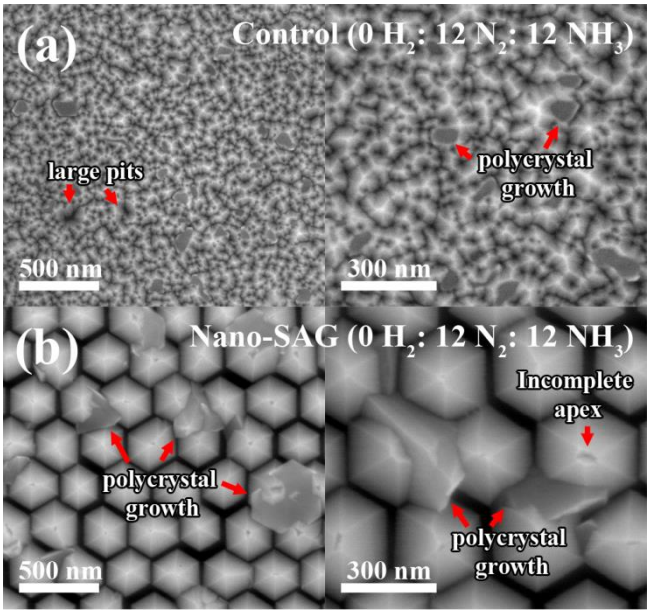


**Figure 6.21** FESEM images of (a) InGaN thin film control grown on unpatterned AlN/Si(111) substrate, and (b) InGaN nanopyramid array grown via nano-SAG on AlN/Si(111) substrate, at the $H_2$:$N_2$:$NH_3$ gas flow rate of 0:12:12, $T$ = 775°C, $P$ = 300 Torr, and duration of 40 min. The reduction of $NH_3$ from 18 to 12 slm gives rise to polycrystal growth in both control and nanopyramid array. Incomplete apices are also observed in the latter.

It was hoped that the greater supply of metallic Group III species relative to N with a reduced V/III ratio will effect a change in nano-SAG morphology from nanopyramids

to nanostructures with vertical sidewalls. However, nanopyramids remained, likely due to an insufficiently high metal flux and/or strong stability of the {11$\underline{1}$01} sidewalls. Polycrystals observed invariably nucleated and grew in the valleys between nanopyramids. Incompletely coalesced apices are also present. The morphology resembles that obtained at lower temperature of 700°C (see Figure 6.1(e)) except that In droplets are not observed. The similarity in effects of low growth temperature and low V/III ratio have been observed in nano-SAG of InN nanopyramids [203]. The absence of In droplets is likely a consequence of the higher temperature (775°C) which promotes their evaporation. The higher temperature also improves the cracking efficiency of $NH_3$ and ensures the availability of N radicals for bonding with In and Ga despite the reduction in $NH_3$ flow rate.

Parasitic nucleation is increased due to the greater supply of metallic Group III species relative to reactive N with a reduced V/III ratio. This in turns increases the incidence of parasitic growth to form polycrystals in both control and nano-SAG samples. Polycrystals are more abundant in the latter and preferentially forms in the valleys between the nanopyramids because the valleys function as sinks for reactive species which are not incorporated into the energetically stable and slow growing {11$\underline{1}$01} sidewalls of the nanopyramids. The abundant supply of reactive species increases the chances of parasitic nuclei in these regions to grow to a suitable size and form polycrystals. Incomplete coalescence of the nanopyramid apices may be a consequence of the competition for reactive species from the polycrystals. This further slows down the coalescence of the apical pits which may be the termination points for axial TDs and is composed of stable {11$\underline{1}$01} facets.

### 6.6.2. Structural Characteristics

#### 6.6.2.1. Indium Content and Phase Composition

Figure 6.22 shows the (0002) $2\theta$-$\omega$ XRD scans for the nanopyramid arrays and the corresponding thin film control samples for $H_2$:$N_2$:$NH_3$ flow rates (in slm) of 0:6:18, 1:5:18 and 0:12:12. For all cases, only a single peak attributable to InGaN(0002) is observed. That is, the InGaN is single phase. Further, higher In content *x* and wider composition range are achieved in the nanopyramid array compared to the control as expected and discussed in prior sections. The values are tabulated in Table 6-6.

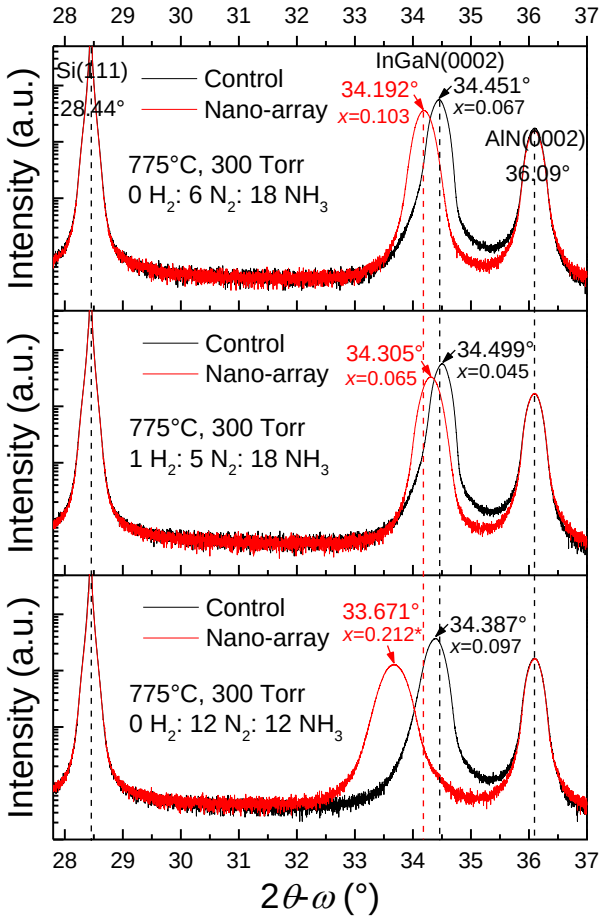


**Figure 6.22** HR-XRD (0002) $2\theta$-$\omega$ scans of InGaN nanopyramid array (red line) and corresponding control (black line) samples grown on AlN/Si(111) substrate with $H_2$:$N_2$:$NH_3$ gas flow rate (in slm) of 0:6:18 (top), 1:5:18 (middle), and 0:12:12 (bottom). For all cases, $T$ = 775°C, $P$ = 300 Torr and growth duration of 40 min were employed.

Introduction of $H_2$ to the reactant gas mixture results in a reduction of *x* from ~ 0.103 to ~ 0.065 in the nanopyramid array, and from ~ 0.067 to ~ 0.045 in the control. This has been similarly observed by Scholz et al. [335] and Piner et al. [336] for the

growth of InGaN films. It has been speculated that $H_2$ may affect the lifetime of the reactive In species on the growing surface due to formation of gaseous $InH_z$ or affect the concentration of contaminates such as C at the surface [336, 337]. These reduce the surface concentration of reactive In species thereby reducing In incorporation.

When the $NH_3$ flow rate is reduced from 18 slm to 12 slm with the $N_2$ flow rate increased correspondingly, an increase in *x*, from ~ 0.103 to ~ 0.212 for the nanopyramid array, and from ~ 0.067 to ~ 0.097 for the thin film control sample is observed. The results are contrary to reports in literature which show a reduction in *x* with lower V/III ratio for $In_xGa_{1-x}N$ films grown on GaN [128, 338, 339]. The exact reason for the deviation is unclear, but this might be related to the extremely rough or 3D morphology of InGaN, in the control sample and nanopyramid array respectively, obtained in this work. A coarser morphology appears to favor increase in *x* with lower V/III ratio as indicated by the much greater increase of *x* in the the 3D nanopyramid array compared to the control. For both sample types, growth occurs via deposition on the inclined {11$\underline{0}$1} planes. Such a growth mode is evident from the MQW structures shown later in Section 6.7.3. A reduction of the $NH_3$ flow rate leads to a lower supply of active $H_2$ derived from $NH_3$ decomposition [203]. This may reduce In desorption and facilitate In incorporation on the inclined {11$\underline{0}$1} facets which already possess a higher In incorporation efficiency. The much broader (0002) $2\theta$-$\omega$ InGaN peak of the nanopyramid array compared to the control might be due to a wider range of In composition arising from the higher *x* and/or greater extent of polycrystals. The latter are misoriented and also broadens the range of *x*.

#### 6.6.2.2. Lattice Tilt and Twist

The FWHM of the (0002) and skew symmetric (20.1) $\omega$-rocking curves which are indicative of lattice tilt and twist of the InGaN samples grown with $H_2$:$N_2$:$NH_3$ gas

flow rate (in slm) of 0:6:18, 1:5:18, and 0:12:12 are shown in Table 6-6 along with other properties. The nanopyramid arrays possess higher tilt than the corresponding film controls while the twist remains approximately the same due to dislocation bending [104]. For the $H_2$:$N_2$:$NH_3$ gas flow rate (in slm) of 1:5:18, a reduction of both tilt and twist values compared to that at 0:6:18 is achieved for both nanopyramid array and control sample types. The improvement in structural quality may be correlated to the use of $H_2$ which is known to improve structural qualities [334], although this comes at the expense of a decrease in *x* which may also improve structural quality due to smaller lattice mismatch with the AlN buffer.

**Table 6-6** Properties of InGaN nanopyramid array and corresponding thin film control samples grown on AlN/Si(111) with $H_2$:$N_2$:$NH_3$ gas flow rate (in slm) of 0:6:18, 1:5:18, and 0:12:12. For all cases, $T$ = 775°C, $P$ = 300 Torr and growth duration of 40 min were employed.

| **Gas flow rate (slm) $H_2$:$N_2$:$NH_3$** | | **In content *x*** | **HR-XRD FWHM (°)** | | | **PL peak (eV)** | **PL FWHM (eV)** | **Int. PL intensity rel. to control** | **<*R*> (%)** |
|---|---|---|---|---|---|---|---|---|---|
| | | | **(0002) $2\theta$-$\omega$** | **(0002) $\omega$** | **(20.1) $\omega$** | | | | |
| **0:6:18** | Contr. | 0.067 | 0.274 | 0.672 | 1.409 | 3.179 | - | 1 | 28.9 |
| | Nano | 0.103 | 0.304 | 0.757 | 1.437 | 2.852 | - | 6.8 | 7.9 |
| **1:5:18** | Contr. | 0.045 | 0.269 | 0.649 | 1.282 | 3.310 | 0.110 | 1 | 27.7 |
| | Nano | 0.065 | 0.316 | 0.734 | 1.267 | 3.048 | 0.389 | 3.5 | 8.7 |
| **0:12:12** | Contr. | 0.097 | 0.316 | 0.847 | 1.330 | 2.945 | - | 1 | 24.5 |
| | Nano | 0.212 | 0.434 | 1.462 | 2.274 | 2.373 | - | 0.7 | 7.9 |

The control sample grown with $H_2$:$N_2$:$NH_3$ gas flow rate (in slm) of 0:12:12 shows notably higher tilt but slightly lower twist than that with 0:6:18. The overall degradation in structure may be related to higher *x* and parasitic polycrystal growth. The nanopyramid array shows significantly higher FWHM of the (0002) and (20.1) $\omega$-rocking curves than the control due to a greater extent of polycrystal growth and a much higher *x*. Misoriented crystals broaden the rocking curves and lead to inaccurate indication of the tilt and twist of the epitaxial material while higher *x* tend to be

correlated with poorer structural quality due to greater lattice mismatch with the underlying buffer layer in heteroepitaxy.

### 6.6.3. Photoluminescence

Figure 6.23 shows the μ-PL spectra at room temperature for the InGaN nanopyramid array and corresponding film control grown at a $H_2$:$N_2$:$NH_3$ gas flow rate (in slm) of 1:5:18. Compared to a gas flow rate of 0:6:12, $H_2$ introduction leads to a shift in PL towards higher energies consistent with XRD measurement of reduced *x*. See Table 6-6. Comparing between the nanopyramid array and control, the former emits at lower energies (3.048 eV vs 3.310 eV) over a broader range (FWHM ~ 0.389 eV vs 0.110 eV) due to higher *x* (0.065 vs 0.045) and larger $2\theta$-$\omega$ FWHM (0.316° vs 0.269°) as measured in XRD. While PL and XRD measurements indicate similar trends with regards to In content and range, it is noticed that the FWHM of the PL peak in the nanopyramid array is more than 3 times that of the control (0.389 eV vs 0.110 eV), while the FWHM of the $2\theta$-$\omega$ peak is only 1.2 times (0.316° vs 0.269°). The PL is also multi-featured. These are due to the sensitivity of PL emission to other factors, e.g. optically active defects and slight composition fluctuations not detected by XRD, Bustein-Mose shift, optical effects such as phonon interactions, and Fabry-Perot interference, and strain etc. These can contribute to multi-featured, broader, and/or shifted PL emission peaks. Thus, while composition variation is a major factor affecting the FWHM of PL and XRD $2\theta$-$\omega$ peaks, the presence of other factors influencing them make direct correlation between them difficult.

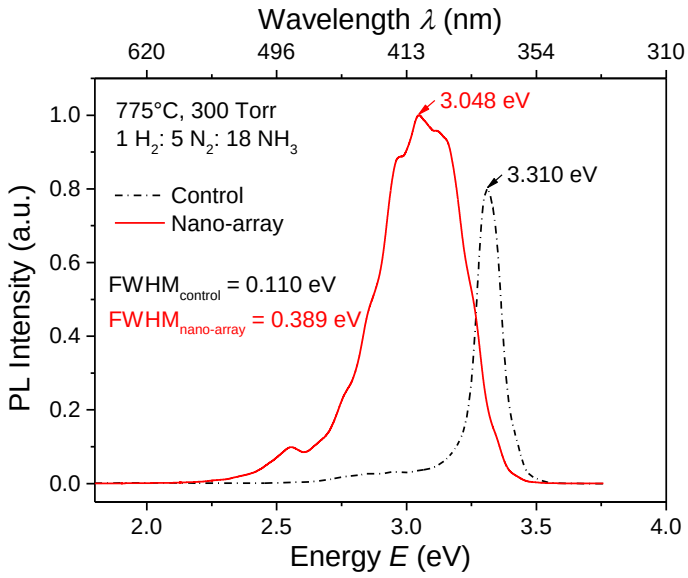


**Figure 6.23** Room-temperature μ-PL spectra of the InGaN nanopyramid array (solid red line) and corresponding thin film control (dash-dot black line) samples grown on AlN/Si(111) with $H_2$:$N_2$:$NH_3$ gas flow rate (in slm) of 1:5:18. The introduction of $H_2$ leads to a considerably narrow PL emission in the control.The InGaN nanopyramid array emits at lower energies despite over a broader range than the control.

Introduction of $H_2$ during MOCVD growth improves InGaN film growth quality. Substantial narrowing of the PL emission peak and increase in peak intensity relative to the nanopyramid array is evident. This is correlated to an improvement in morphology and structural quality as described in Section 6.6.1 and 6.6.2.2 respectively. The improvement in PL emission of the control relative to the nanopyramid array with the introduction of $H_2$ is obvious when comparing the PL emission of the temperature growth series (Figure 6.5) and pressure growth series (Figure 6.12) grown in a pure $N_2$ environment for the same duration. The PL emission of the control samples in the latter two series is broader and much weaker, even at similar PL emission energies. However, as discussed earlier, the introduction of $H_2$ limits In incorporation in InGaN even though nano-SAG alleviates it to some extent.

Figure 6.24 shows the μ-PL spectra at room temperature for the InGaN nanopyramid array and corresponding thin film control sample grown at a $H_2$:$N_2$:$NH_3$ gas flow rate (in slm) of 0:12:12. Compared to a gas flow rate of 0:6:18, the decrease in $NH_3$ flow

rate or decrease in V/III ratio leads to a shift in PL emission towards lower energies in both sample types consistent with XRD measurement of increased *x*. See Table 6-6. Comparing between the nanopyramid array and control, the former emits at lower energies (2.373 eV vs 2.945 eV) due to higher *x* as expected for nano-SAG. However, despite a smaller (0002) $2\theta$-$\omega$ FWHM than the nanopyramid array (0.316° vs 0.434°) the control exhibits broader PL emission. This suggests the presence of luminescent centers with considerable spread of In composition and hence emission energies. In addition, contrary to previous results, the peak PL intensity is comparable to and the integrated PL intensity of the nanopyramid array is less than that of the control. This might be attributed to the much higher In content of the nanopyramid which entails a larger lattice mismatch contributes partly to greater structural defects. This is supported by XRD measurements of higher *x*, greater lattice tilt and twist. See Table 6-6. For similar *x* and PL emission, reduced pressure growth at high V/III ratio produces nanopyramid arrays of better morphology (reduced parasitic growth) and structural quality (lower lattice tilt and twist) as observed in Section 6.4. The results indicate that reduced V/III ratios may not be a suitable route for obtaining InGaN nanostructures with good morphological and structural properties.

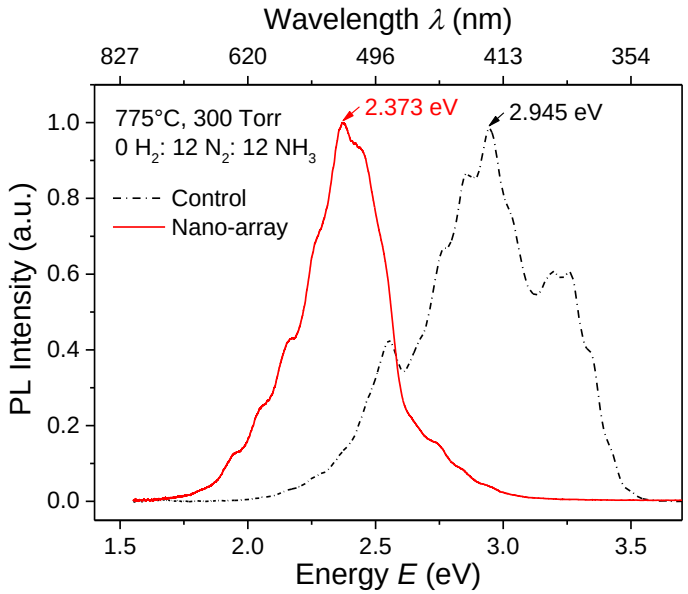


**Figure 6.24** Room-temperature μ-PL spectra of the InGaN nanopyramid array (solid red line) and corresponding thin film control (dash-dot black line) samples grown on AlN/Si(111) with $H_2$:$N_2$:$NH_3$ gas flow rate (in slm) of 0:12:12.

### 6.6.4. Reflectance

Figure 6.25 shows the reflectance spectra at normal incidence of nanopyramid arrays and corresponding control samples grown on AlN/Si(111) with $H_2$:$N_2$:$NH_3$ gas flow rate (in slm) of 1:5:18 and 0:12:12. As expected, the nanopyramid arrays have much lower reflectance *R* which are also less oscillatory compared to the thin film control due to the anti-reflection properties of the array of inclined surfaces (<*R*> ~ 7.9% vs ~ 24.5% for gas flow rate of 0:12:12; and <*R*> ~ 8.7% vs ~ 27.7% for gas flow rate of 1:5:18). Moreover, <*R*> for samples grown at a gas flow rate of 0:12:12 is less than that grown at a gas flow rate of 1:5:18. This may be related to the higher In content of the samples which have lower bandgaps and are hence capable of absorbing a wider range of energies.

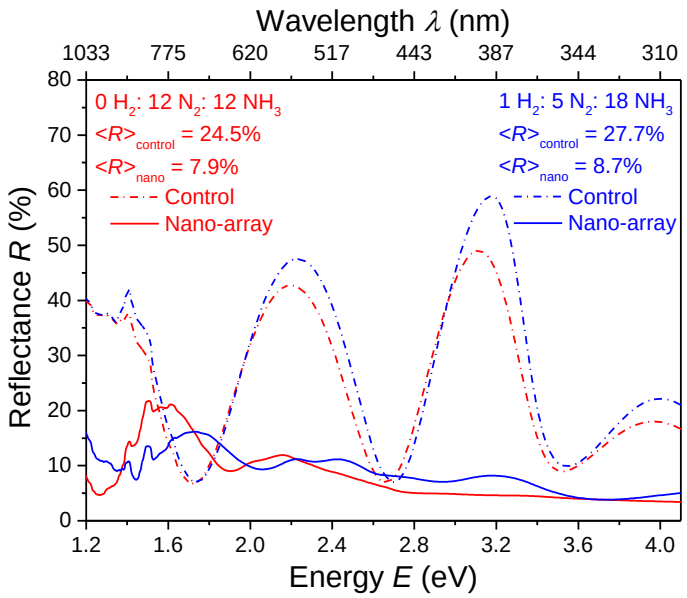


**Figure 6.25** Reflectance spectra at normal incidence of nanopyramid arrays (solid lines) and corresponding control (dash-dot lines) samples grown on AlN/Si(111) with $H_2$:$N_2$:$NH_3$ gas flow rate (in slm) of 1:5:18 (blue lines) and 0:12:12 (red lines). For all cases, $T$ = 775°C, $P$ = 300 Torr and growth duration of 40 min were employed

## 6.7. Growth of InGaN/GaN MQW Core-Shell Nanopyramid Arrays

As discussed in Section 1.2.4.3, core-shell architectures may be employed in nanostructures to enhance charge separation, reduce surface recombination and decouple (at least, partially) requirements for good absorption from charge separation. In this section, we successfully demonstrate the growth of InGaN/GaN MQW core-shell structures on InGaN nanopyramids achieved in nano-SAG. The characteristics of the MQW nanopyramid arrays are examined and discussed.

### 6.7.1. Experimental Procedure

MOCVD growth conditions of $T$ = 775°C, $P$ = 300 Torr, TMGa:TMIn gas flow rate (in slm) of 5:120, $H_2$:$N_2$:$NH_3$ gas flow rate (in slm) of 0:6:18, and growth duration of 35 min were first employed to grow a faceted, uncoalesced InGaN nanopyramid array via nano-SAG on an AlN/Si(111)-based Type A template. This InGaN nanopyramid core is similar to the nanopyramids grown at 775°C in Section 6.3 except for a reduction in growth duration of 5 min. A five-period InGaN/GaN multiple quantum

well (MQW) structure was then grown while maintaining *T* and *P*. The structure was then capped by a GaN layer. As per usual practice, an unpatterned AlN/Si(111) substrate was used as a control substrate. FESEM, cross-sectional TEM, room temperature μ-PL and reflectance were used to characterize the grown structures.

### 6.7.2. Morphology

Figure 6.26(a) and (b) shows the surface morphology of the InGaN/GaN MQW film control and nanopyramid array samples respectively. Similar to the InGaN film samples grown previously, the surface of the MQW control is rough (feature size ~ several tens of nanometers) and undulating, although it remains reflective to the naked eye. Numerous pits populate the surface since these are the termination points of the many TDs. See Figure 6.27. The morphology is coarser than the InGaN film grown without MQWs (see Figure 6.19) due to a longer total growth duration. Despite the low total thickness (~ 210 nm InGaN/GaN layer and ~150 nm AlN), the surface of the film control is lined with cracks. These typically propagate along the family of <$\underline{2}$110> directions or along the {1$\underline{1}$01} planes consistent with reports in literature [96, 340]. As discussed in Section 2.3.2, the cracks are generated upon cooling down from the growth temperatures to relax the high thermal stress associated with the large mismatch of thermal expansion coefficients between the III-nitride layers and Si substrate.

The MQW nanopyramid array remains crack-free even though the total height of the nanopyramid structure (~ 400 nm including the embedded section) exceeds that of the InGaN film in the control. This is due to strain relaxation afforded by segmentation into nanostructures. This clearly demonstrates another advantage of nanostructuring and further supports the validity of the approach to InGaN/Si tandem solar cell applications. While coalescing nanopyramids are observed, this occurs during growth

of the final GaN capping layer or after deposition of the five-period MQW structure is completed on the inclined semipolar {1$\underline{1}$01} facets as seen in Figure 6.28. Similar to prior observations of coalescing InGaN nanopyramids, coalescence of the GaN cap is initiated by ridges bridging adjacent nanopyramid sidewalls which roughen them. Sidewalls remain smooth when there are no sidewalls from neighboring nanopyramids that are sufficiently close as seen in Figure 6.26(b) inset.

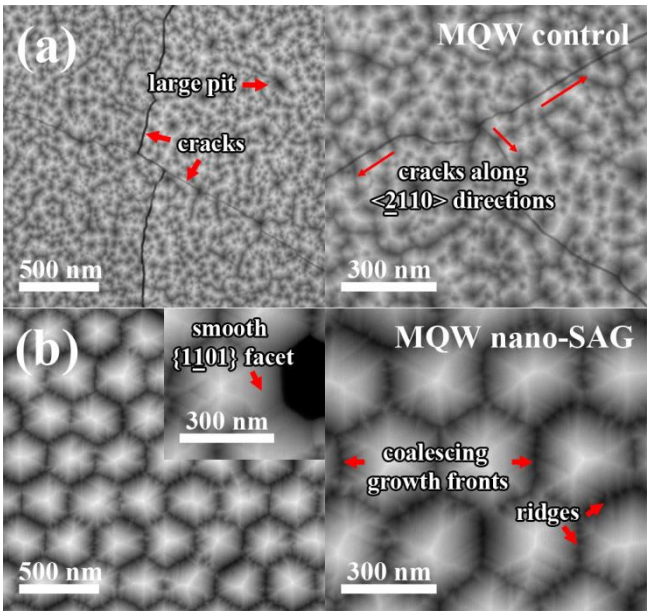


**Figure 6.26** FESEM images showing the surface morphology after MQW growth for (a) InGaN thin film control, and (b) InGaN nanopyramid array grown via nano-SAG. Cracks oriented along the general <2$\underline{1}$10> directions are ubiquitous on the control. Coalescence of nanopyramids occurs during the GaN capping layer growth and manifests as ridges bridging adjacent sidewalls. Non-coalescing sidewalls remain smooth (see (b) inset).

### 6.7.3. Structural Characteristics

Figure 6.27 shows the cross-sectional TEM images of the InGaN/GaN MQW film control viewed along the [2$\underline{1}\underline{1}$0] zone axis. The jagged surface of the film arises from the high density of V-pits which are the termination points of TDs. As discussed in Section 5.3.3.1, many of these TDs originate from the lattice mismatched growth of the AlN buffer on Si, and propagate into the InGaN layer. The sidewalls forming the V-pits are mostly inclined at 62° to the basal plane indicating that they are {1$\underline{1}$01}

planes. Judging from the pitted morphology of Figure 6.26(a), it is probable that much of the surface is composed of {1$\underline{1}$01} planes, and growth of the film occurs through deposition on these inclined planes. Indeed, it is observed in Figure 6.27(c) that the five-period MQW structures, which also serve as markers of growth, are inclined at ~ 62° to the substrate plane and parallel to the V-pits.

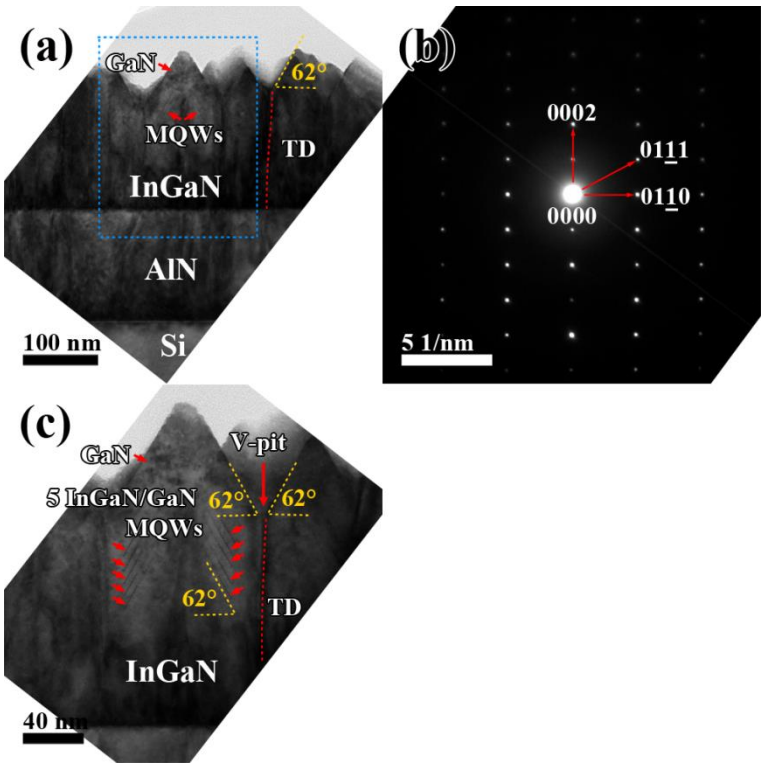


**Figure 6.27** Cross-sectional TEM images of the InGaN/GaN MQW film control. (a) Overview of the structure. The dotted red line delineates a threading dislocation (TD) propagating in the InGaN/GaN film. TDs typically traverse the film along the [0001] line direction and terminate in a V-pit. The sidewalls of the V-pits are inclined at ~ 62° to the substrate plane suggesting that they are {1$\underline{1}$01} planes. (b) Corresponding SAED pattern of the InGaN/GaN layer indicating that TEM imaging was performed along the [2$\underline{1}$1$\underline{1}$0] zone axis. (c) Close-up of the region bounded by the blue dotted box in (a) showing that the five-period MQW structure is deposited on the {1$\underline{1}$01} planes of the V-pits.

Figure 6.28 shows the cross-sectional TEM images of an InGaN/GaN MQW nanopyramid viewed along the [2$\underline{1}$1$\underline{1}$0] zone axis. Inclination of the {1$\underline{1}$01} sidewalls at ~ 62° to the basal planes is clearly observed. In Figure 6.28(a), the left sidewall roughens due to coalescence with an adjacent nanopyramid. This contrasts with the right sidewall which remains smooth. Coalescence can lead to generation of

coalescence dislocations (CD) between nanopyramids as seen in Figure 6.28(c). However, the density of these is less than the density of TDs blocked by the $SiN_y$ mask, such that an overall reduction of TDDs and improvement in structural quality is expected. Bending of TDs through 90° towards the InGaN/$SiN_y$ interface and towards the nanopyramid sidewalls due to the action of image forces is delineated in dotted red lines in Figure 6.28(a) and (c) respectively. That is, the growth temperature of 775°C is already sufficient to mobilize the TDs. TD bending at such a temperature and in InGaN has yet to be observed in literature. Prior work has largely concentrated on TD bending in GaN pyramids.

The five-period InGaN/GaN MQW structure envelopes the nanopyramid on the semipolar {11$\underline{1}$01} sidewalls to form a core-shell nanopyramid structure. However, the thickness of the MQW layers on the left and right sidewalls are markedly different as seen in Figure 6.28(c) and (d) respectively. This indicates a difference in growth rate on the different sidewalls of a nanopyramid, accounting for the asymmetry of the hexagonal nanopyramids and their size distribution. This is similarly observed in the InGaN nanopyramids in Figure 6.1 grown at 300 Torr. As mentioned in Section 6.3.1.1, the non-uniformity in sidewall and hence nanopyramid size may be due to unequal distribution of defect exits among the sidewalls. For instance, the thicker MQW layers (and higher growth rate) on the left sidewall in Figure 6.28(c) appear to be correlated to the exit of the bent TD. In contrast, the MQW layers are noticeably thinner on the right sidewall with no TD exit.

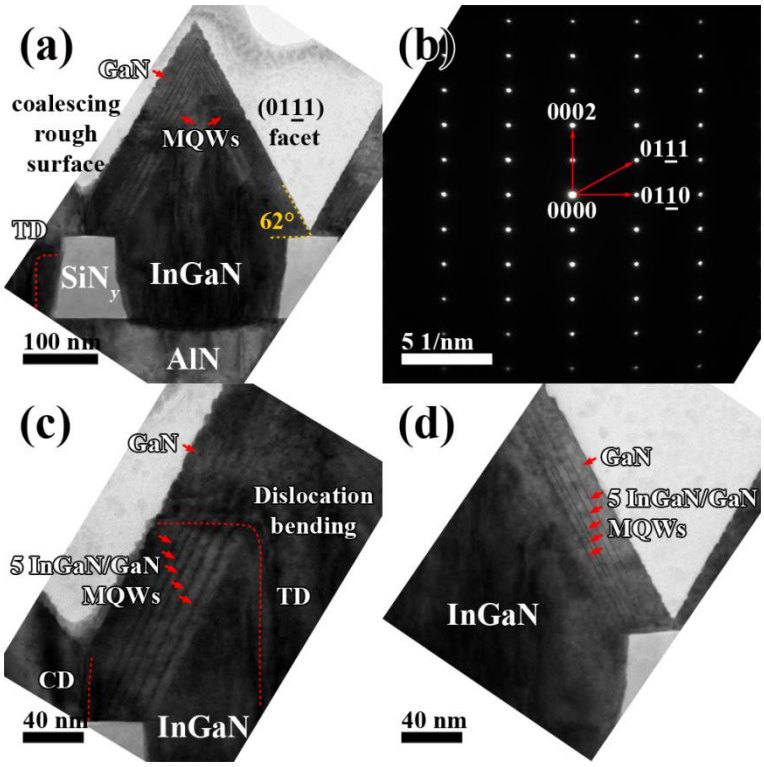


**Figure 6.28** Cross-sectional TEM images of an InGaN/GaN MQW nanopyramid. (a) Overview of the nanostructure. The sidewalls are inclined at ~ 62° to the substrate plane indicating that they are {1$\underline{1}$01} planes. The coalescing sidewall is characterized by a rough surface. The MQWs envelopes the upper surface of the nanopyramid forming a core-shell structure. The dotted red line delineates a threading dislocation (TD) being bent 90° towards the InGaN/SiN$_y$ interface. (b) Corresponding SAED pattern of the InGaN/GaN layer indicating TEM imaging was performed along the [2$\underline{1}\underline{1}$0] zone axis. (c) Close-up of the left sidewall in (a) showing the five-period MQW structure. The bending of a TD by 90° towards the nanopyramid sidewall and its exit from the structure is shown. A coalescence dislocation (CD) is also outlined. (d) Close-up of the right sidewall in (a) showing the five-period MQW structure. The MQW layers are noticeably thinner due to a slower growth rate.

### 6.7.4. Photoluminescence

Figure 6.29 shows the room temperature μ-PL spectra of the InGaN/GaN MQW nanopyramid array and film control. Compared to the InGaN film grown at 775°C in Figure 6.5, the PL intensity of the InGaN/GaN MQW film is noticeably higher, indicating the efficacy of the MQW structure. PL emission of the MQW nanopyramid array remains higher and red-shifted compared to the MQW film control (~ 3.05 eV vs ~ 3.23 eV), due to improved structural quality and increased In incorporation afforded by dislocation reduction and strain relaxation. Further, PL emission from the MQW of the nanopyramid array is blue-shifted compared to that of the pure InGaN

nanopyramid array in Figure 6.5 (~ 3.05 eV vs ~ 2.85 eV). This may be due to quantum confinement effects. The lower intensity shoulder on the high energy edge around ~ 3.42 eV is contributed by GaN emission. The results show that functional core-shell nanopyramid device structures can be generated using a nano-SAG approach in MOCVD. The same concept may be applied to grow nanopyramids consisting of an InGaN core and GaN (or differently doped InGaN) shell in an array structure on Si substrates for InGaN/Si tandem solar cell applications.

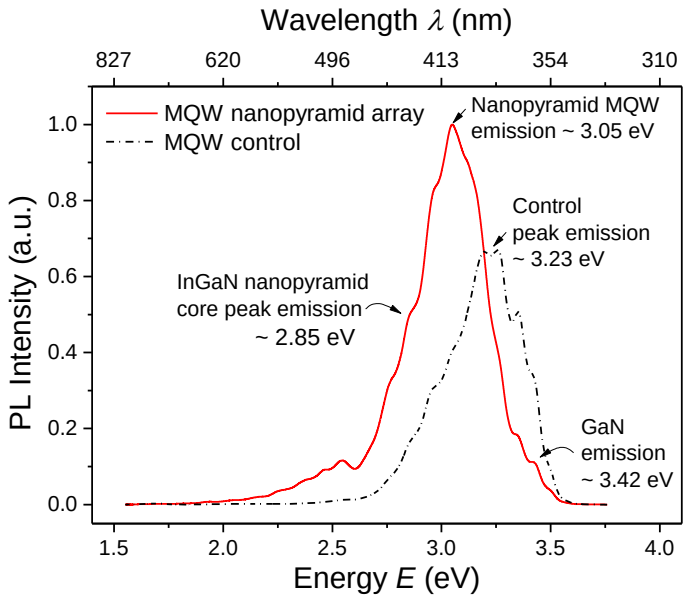


**Figure 6.29** Room-temperature μ-PL spectra of the InGaN/GaN MQW nanopyramid array (solid red line) and thin film control sample (dash-dot black line).

### 6.7.5. Reflectance

Figure 6.30 shows the reflectance at normal incidence of the MQW nanopyramid array and corresponding film control. Consistent with prior reflectance results, lower and much less oscillatory reflectance is obtained in the nanopyramid array compared to the film control due to the light-trapping properties of the nanostructure array. A low average reflectance <*R*> of 9.3%, slightly higher than prior arrays due to partial coalescence, is obtained compared to ~ 24.1% in the control. Further, it can be observed that the absorption edge of the nanopyramid array (onset of low reflectance)

occurs at lower energies than the film control, in line with its higher In content and smaller bandgap, and in accordance to PL measurements.

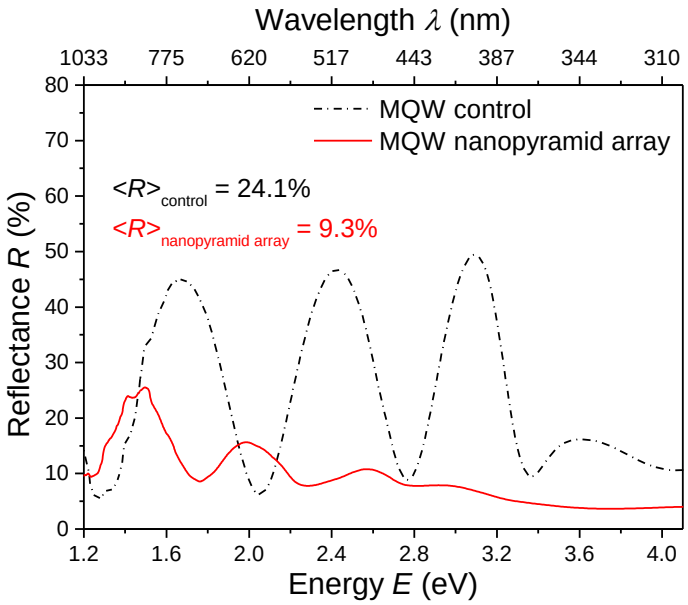


**Figure 6.30** Reflectance spectra at normal incidence of the InGaN/GaN MQW nanopyramid array (solid red line) and corresponding film control (dash-dot black line).

## 6.8. Chapter Summary

In this Chapter, the nano-SAG of InGaN nanopyramids using nanoporous Type A $SiN_y$ mask templates fabricated on AlN/Si(111) substrates was investigated in detail. Specifically, the influence of MOCVD growth conditions, namely, growth temperature *T*, reactor pressure *P*, growth duration, and gas flow rate are examined. The In content *x*, morphological, structural and PL qualities of the nanopyramid arrays are reported. Reduction in *T* permits increased *x*. However, low *T* (< 750°C) are correlated with lower crystal quality, polycrystalline deposits and In droplet formation. To maintain the quality, a moderately high *T* (~ 775°C) is used in conjunction with lower *P*, which enhances mass transport and suppresses In desorption, to increase *x*. This also enhances the growth rate, and improves nanopyramid and facet size uniformity by mitigating the effects of non-uniform defect exits on sidewall growth rates. Nanopyramid arrays generally exhibit greater

lattice tilt than the corresponding thin film control due to dislocation bending. Notwithstanding this, increase in tilt with reduced *P* and hence increased *x* is slight. While lattice twist increases more notably with higher *x*, it is offset by epitaxial lateral overgrowth (ELO) and coalescence. The degradation of structural quality with *x* is contributed by the greater lattice mismatch. Compared to control samples, nanopyramid samples consistently yielded higher In content, lower average reflectance (< 9%) and a multi-fold increase in photoluminescence intensity with tunable emission energies from 3.05 eV to 1.93 eV.

Increased growth duration promotes ELO and coalescence, and improves structural quality, evident by reduced lattice tilt and twist in the nanopyramid array. Increase in *x* also results due to further strain relaxation. However, roughening of sidewalls during coalescence degrades the anti-reflection properties. On the other hand, for small nanopyramids with little overgrowth, the AlN buffer substantially limits the structural quality. Growth of uncoalesced nanopyramids but with greater overgrowth is thus advocated. This may be achieved through nanoporous mask templates with suitably large ratio of array period : nanopore size. Introduction of $H_2$ in a $H_2$:$N_2$:$NH_3$ flow rate (in slm) of 1:5:18 during MOCVD growth improves morphology and narrows PL emission for InGaN thin films. For both control film and nanopyramid array, structural properties are also improved but at the expense of reduced *x* and growth rate. A $N_2$ environment with no or just a minor fraction of $H_2$ should be used for growth of higher In content InGaN. Reducing the V/III ratio by decreasing $NH_3$ flow rate in a $H_2$:$N_2$:$NH_3$ flow rate (in slm) of 0:12:12, degrades the morphological and structural properties of both sample types but increases *x*. While the increase in *x* is greater in the nanopyramids, the degradation is also more severe. Considering this, a high V/III ratio should be maintained. Lastly, functional InGaN/GaN MQW core-shell structures are successfully grown crack-free on InGaN nanopyramid array in

contrast to the cracked thin film control. The MQW structure also serve as markers elucidating the growth process, and show that dislocation bending towards and exiting the sidewalls of the nanopyramid can influence the sidewall growth rate.

In summary, this Chapter forms a guide for growing InGaN nanopyramids with variable properties through nano-SAG on AlN/Si(111) in MOCVD.

# Chapter 7 Conclusion and Future Work

## 7.1. Conclusion

This work explores the integration of $In_xGa_{1-x}N$ with highly ordered nanostructures on Si substrates for the development of vertically integrated InGaN/Si tandem solar cells. Two nanostructured growth approaches are proposed, namely, (A) nano selective area growth (nano-SAG) of InGaN through a nanoporous $SiN_y$ mask fabricated on Si(111) substrate or Scheme A, and (B) nanoheteroepitaxy on Si nanopillar substrate or Scheme B. Both approaches are postulated to improve crystal quality of high In content InGaN and provide key benefits for the proposed photovoltaic application. For a manageable scope, nano-SAG was selected and explored in detail. Highly ordered arrays of InGaN hexagonal nanopyramids were successfully heteroepitaxially grown on AlN-buffered Si substrates by MOCVD and exhibit improved structural quality, higher In content ($x$ up to ~ 0.42), no phase separation, and substantially lower reflectance (< 9%) than InGaN films. Functional core-shell MQW nanopyramids are also demonstrated. The results support the initial claims and show the validity of the approach. Such a focused approach towards nanostructured InGaN/Si tandem photovoltaics has yet to be attempted by other groups.

Preliminary work involved the development of nanopatterning techniques based on Step and Flash™ Imprint Lithography (S-FIL™), a form of wafer-scale nanoimprint lithography. For Scheme A, uniform, tunable aspect ratio nanoporous $SiN_y$ templates on AlN/Si(111) substrates were fabricated by combining S-FIL™ with angled metal deposition or anodization of aluminum oxide (AAO). For Scheme B, Si nanopillar arrays of variable patterns and adjustable aspect ratio were realized by combining S-FIL™ with metal-catalyzed electroless etching (MCEE). For proof-of-concept and to

ensure a manageable scope, only Type A nanostructured templates were selected for InGaN growth.

Next, scaling of InGaN films into three-dimensional nanostructures on AlN/Si(111) substrate was presented. The results of a MOCVD growth study of InGaN films on the unpatterned substrates were first shown. High temperature in-situ annealing of the AlN/Si(111) substrate in $H_2$ at 1000°C was found to be critical to obtaining epitaxial growth. Further, elevated pressures (~ 300 Torr) aid in obtaining single phase InGaN ($x$ ~ 0.40) at low growth temperatures (~ 655°C), while relatively high temperatures (> 765°C) improves crystal quality albeit at the expense of In content. Taking these factors into consideration, InGaN nanostructured growth via nano-SAG on AlN/Si(111)-based Type A template was performed at 780°C and 300 Torr. Three-dimensional InGaN hexagonal nanopyramids in a dense edge-to-edge array were successfully grown with good growth selectivity. Strain relaxation, dislocation confinement and filtering result in improved InGaN crystalline quality. Only one non-radiative recombination channel ($E_A$ = 72 meV) was detected in the nanopyramid array compared to two ($E_A$ = 14 meV and 131 meV) in the film control. Compared to the film control, the nanopyramid array has higher In content (~ 10.6% vs ~ 6.1%), higher internal quantum efficiency (17.5% vs 4.4%) and substantially lower reflectance (8.3% vs 23.6%). This affirms the initial proposition on the benefits of InGaN nanostructuring for the development of high efficiency InGaN/Si hybrid tandem solar cells.

Subsequently, nano-SAG of InGaN nanopyramids using nanoporous Type A $SiN_y$ mask templates fabricated on AlN/Si(111) substrates was investigated in detail. Specifically, the influence of MOCVD growth conditions, namely, growth temperature $T$, reactor pressure $P$, growth duration, and gas flow rate were examined.

Reduction in *T* permits increased In content *x*. However, low *T* (< 750°C) are correlated with lower crystal quality, polycrystalline deposits and In droplet formation. To maintain the quality, a moderately high *T* (~ 775°C) was used in conjunction with lower *P*, which enhances mass transport and suppresses In desorption, to increase *x*. This also enhances the growth rate, and improves nanopyramid and facet size uniformity by mitigating the effects of non-uniform defect "exits" on sidewall growth rates. Nanopyramid arrays generally exhibit greater lattice tilt than the corresponding thin film control due to dislocation bending. Notwithstanding this, increase in tilt with reduced *P* and hence increased *x* is slight. While lattice twist increases more notably with higher *x*, it is offset by epitaxial lateral overgrowth (ELO) and coalescence. The degradation of structural quality with *x* is contributed by the greater lattice mismatch. Compared to control samples, nanopyramid samples consistently yielded higher In content, lower average reflectance (< 9%) and a multi-fold increase in photoluminescence intensity with tunable emission energies from 3.05 eV to 1.93 eV.

Increased growth duration promotes ELO and coalescence, and improves structural quality. This is evidenced by the reduced lattice tilt and twist in the nanopyramid array with the FWHM of the (0002) and (20.1) $\omega$-scans decreasing below that of the underlying AlN buffer to 0.630° and 1.022° respectively. Increase in *x* also results due to further strain relaxation. However, roughening of sidewalls during coalescence degrades the anti-reflection properties. On the other hand, for small nanopyramids with little overgrowth, the AlN buffer substantially limits the structural quality. Growth of uncoalesced nanopyramids but with greater overgrowth is thus advocated. Introduction of $H_2$ in a $H_2$:$N_2$:$NH_3$ flow rate (in slm) of 1:5:18 during MOCVD growth smoothens the morphology and improves PL characteristics for InGaN films (from broad near-band-edge (NBE) and defect-related PL to narrow NBE PL with

FWHM ~ 110 meV). For both film and nanopyramid array, structural properties are also improved but at the expense of reduced *x* and growth rate. A $N_2$ environment with no or just a minor fraction of $H_2$ should be used for growth of high In content InGaN. Reducing the V/III ratio by decreasing $NH_3$ flow rate in a $H_2$:$N_2$:$NH_3$ flow rate (in slm) of 0:12:12, degrades the morphological and structural properties of both sample types but increases *x*. While the increase in *x* is greater in the nanopyramids, the degradation is severe. Considering this, a high V/III ratio greater than 6100 should be maintained. A V/III ratio of 9200 is commonly used in this work. Lastly, functional InGaN/GaN MQW core-shell structures are successfully grown crack-free on an InGaN nanopyramid array in contrast to the cracked film control. The nanopyramid MQW PL emission is approximately two times as high as the InGaN nanopyramid core but is blue-shifted from ~ 2.85 eV to ~ 3.05 eV due to quantum confinement effects. The MQW structure also serve as markers elucidating the growth process, and show that dislocation bending towards and exiting the sidewalls of the nanopyramid can influence the sidewall growth rate.

As discussed in Section 1.2.3, the technical barriers of InGaN solar cells are related to growth issues which affect structural quality, and polarization effects. We have experimentally shown that improved structural quality and increased In content InGaN nanostructures can be achieved on Si substrates. These further possess reduced reflectance. Growth on the semipolar {1-101} facets (with reduced polarization effects) of functional InGaN/GaN core-shell nanostructures has also been demonstrated. The results (1) support the initial proposition for the integration of InGaN with nanostructures on Si for nanostructured InGaN/Si tandem solar cell applications, and (2) form a guide for tuning the properties of InGaN nanopyramids MOCVD-grown via nano-SAG on AlN/Si(111). These findings are expected to fill a

void in the InGaN/Si photovoltaic community where the growth of InGaN film on Si by MOCVD has met with limited success.

## 7.2. Recommendations for Future Work

The long-term goal extrapolated for this work is the realization of monolithic vertically integrated InGaN/Si tandem solar cells. The results of this work have shown promise in a nanostructuring approach. However, certain areas deserve further investigation. These are listed as follows.

First, relatively high *average* In content $x$ of up to ~ 0.27 has been estimated by XRD in the InGaN nanopyramids. However, the same sample emit PL at energies down to ~ 1.93 eV corresponding to even higher In content of $x$ ~ 0.42. Although this is attributed to efficient luminescent centers, suspected to be located at the ridges formed during coalescence, it also suggests that higher $x$ may be achievable. One way that this can be attained is through further reduction in reactor pressure $P$ to below 70 Torr and/or adjustment of the precursor flow rates. The TMIn flow rate in this work is maintained at 120 sccm for consistency. This is notably lower than that used in separate experiments. As such, future work can investigate the influence of these changes in growth conditions to obtain even broader range of In content.

Second, the nano-SAG pattern used in this work is restricted to a period of 300 nm due to the unavailability of nanoimprint moulds of other patterns. From the results obtained in this work, array patterns with longer period and smaller opening size to increase epitaxial lateral overgrowth (ELO) and nanopyramid size without invoking coalescence can aid in improving structural quality. A reduction in size of the template openings for nano-SAG may be beneficial for enhanced dislocation filtering

and bending. Also, nano-void formation in nanopyramids may be reduced due to a reduction in distance between the core region and mask edges for adatom migration. A coarser, higher relief morphology and smaller template openings is further expected to offer greater strain relaxation for improved In incorporation. By performing growth without coalescence, the smooth sidewalls maintain the light-trapping capabilities of the array. Simulation experiments to investigate the light-trapping properties of different array periods and nanopyramid sizes may be performed to gain a better understanding of the phenomenon.

Third, in Section 6.4.1.3, dark contrast features or notches on the sidewalls of InGaN nanopyramids have been observed. These features have yet to be identified although there is a strong case that they are related to the exit of TDs at the sidewalls. Further investigation is thus suggested.

Fourth, in order to complete the proof-of-concept of a functional nanopyramid InGaN/Si tandem solar cell, some additional work needs to be performed. This includes the development and growth of *p*-type GaN or InGaN as a capping layer on the nanopyramids. Also, suitable designs considering doping, contact formation, device architectures, etc. of the Si bottom cell and GaN/InGaN top cell needs to be worked out. That is, considerable scope still exists for achieving the long-term goal of nanopyramid InGaN/Si tandem solar cell.

Lastly, Type B templates or Si nanostructure arrays have been fabricated from S-FIL$^{TM}$ and metal-catalyzed electroless etching (MCEE). However, these have yet to be utilized for InGaN growth. An analogous approach for nanoheteroepitaxy can be embarked on these templates to gauge their effectiveness in comparison to nano-SAG on Type A templates.

# REFERENCES


[1] Photovoltaics Report, in, Fraunhofer Institute for Solar Energy Systems, 2012.

[2] Technology Roadmaps: Solar photovoltaic energy, in, International Energy Agency, 2010, pp. 48.

[3] A.L. López, V.M. Andreev, Concentrator Photovoltaics, Springer, 2010.

[4] N.R.E. Laboratories, Best Research-Cell Efficiencies, in, National Renewable Energy Laboratory, 2014.

[5] Sharp, Sharp Develops Concentrator Solar Cell with World's Highest Conversion Efficiency of 44.4%, in, 2013.

[6] A. Feltrin, A. Freundlich, Material considerations for terawatt level deployment of photovoltaics, Renew. Energy, 33 (2008) 180-185.

[7] D.C. Law, R.R. King, H. Yoon, M.J. Archer, A. Boca, C.M. Fetzer, S. Mesropian, T. Isshiki, M. Haddad, K.M. Edmondson, Future technology pathways of terrestrial III–V multijunction solar cells for concentrator photovoltaic systems, Sol. Energy Mater. Sol. Cells, 94 (2010) 1314-1318.

[8] M.R. Krames, O.B. Shchekin, R. Mueller-Mach, G.O. Mueller, Z. Ling, G. Harbers, M.G. Craford, Status and Future of High-Power Light-Emitting Diodes for Solid-State Lighting, J. Display Technol., 3 (2007) 160-175.

[9] D.S. Sizov, R. Bhat, A. Zakharian, S. Kechang, D.E. Allen, S. Coleman, Z. Chung-en, Carrier Transport in InGaN MQWs of Aquamarine- and Green-Laser Diodes, Selected Topics in Quantum Electronics, IEEE Journal of, 17 (2011) 1390-1401.

[10] J. Wu, W. Walukiewicz, K.M. Yu, J.W. Ager III, E.E. Haller, H. Lu, W.J. Schaff, Small band gap bowing in $In_{1-x}Ga_xN$ alloys, Appl. Phys. Lett., 80 (2002) 4741-4743.

[11] J. Wu, W. Walukiewicz, K.M. Yu, W. Shan, J.W. Ager, E.E. Haller, H. Lu, W.J. Schaff, W.K. Metzger, S. Kurtz, Superior radiation resistance of $In_{1-x}Ga_xN$ alloys: Full-solar-spectrum photovoltaic material system, J. Appl. Phys., 94 (2003) 6477.

[12] O.J. Christiana Honsberg, Alan Doolittle, Elaissa Trybus, Gon Namkoong Ian Ferguson, David Nicole, Adam Payne, InGaN - A new solar cell material, Proceedings of the 19th European Photovoltaic Science and Energy Conference, Paris, France, (2004) 15 - 20.

[13] J.F. Muth, J.H. Lee, I.K. Shmagin, R.M. Kolbas, H.C. Casey, B.P. Keller, U.K. Mishra, S.P. DenBaars, Absorption coefficient, energy gap, exciton binding energy, and recombination lifetime of GaN obtained from transmission measurements, Appl. Phys. Lett., 71 (1997) 2572-2574.

[14] W. Walukiewicz, I. J. W. Ager, K.M. Yu, Z. Liliental-Weber, J. Wu, S.X. Li, R.E. Jones, J.D. Denlinger, Structure and electronic properties of InN and In-rich group III-nitride alloys, J. Phys. D: Appl. Phys., 39 (2006) R83.

[15] Y. Nanishi, Y. Saito, T. Yamaguchi, RF-Molecular Beam Epitaxy Growth and Properties of InN and Related Alloys, Jap. J. Appl. Phys., 42 2549.

[16] R. Singh, D. Doppalapudi, T.D. Moustakas, L.T. Romano, Phase separation in InGaN thick films and formation of InGaN/GaN double heterostructures in the entire alloy composition, Appl. Phys. Lett., 70 (1997) 1089-1091.

[17] J. Wu, When group-III nitrides go infrared: New properties and perspectives, J. Appl. Phys., 106 (2009) 011101.

[18] Bulk GaN: Too Little, Too Late?, in, Compound Semiconductor, 2013.

[19] T. Paskova, D.A. Hanser, K.R. Evans, GaN Substrates for III-Nitride Devices, Proceedings of the IEEE, 98 (2010) 1324-1338.

[20] G.F. Brown, J.W. Ager, W. Walukiewicz, J. Wu, Numerical simulations of novel InGaN solar cells, in: Photovoltaic Specialists Conference (PVSC), 2009 34th IEEE, 2009, pp. 001958-001962.

[21] G.F. Brown, J.W. Ager, W. Walukiewicz, J. Wu, Finite element simulations of compositionally graded InGaN solar cells, Sol. Energy Mater. Sol. Cells, 94 (2010) 478-483.

[22] L. Hsu, W. Walukiewicz, Modeling of InGaN/Si tandem solar cells, J. Appl. Phys., 104 (2008) 024507.

[23] L.A. Reichertz, I. Gherasoiu, K.M. Yu, J.W. Ager, V.M. Kao, W. Walukiewicz, Progress on III-nitride/silicon hybrid multijunction solar cells, Proceedings of the 35th IEEE Photovoltaic Specialists Conference, (2010) 001044-001047.

[24] L.A. Reichertz, K.M. Yu, Y. Cui, M.E. Hawkridge, J.W. Beeman, Z. Liliental-Weber, J.W. Ager III, W. Walukiewicz, W.J. Schaff, T.L. Williamson, M.A. Hoffbauer, InGaN Thin Films Grown by ENABLE and MBE Techniques on Silicon Substrates, Mater. Res. Soc. Symp. Proc., 1068 (2008).

[25] A. Yamamoto, A. Mihara, K. Sugita, V.Y. Davydov, N. Shigekawa, MOVPE-grown n-$In_xGa_{1-x}N$ (x~0.5)/p-Si(111) template as a novel substrate, Proc. SPIE, 8641 (2013) 86410N.

[26] A. Yamamoto, A. Mihara, D. Hironaga, K. Sugita, A.G. Bhuiyan, A. Hashimoto, N. Shigekawa, N. Watanabe, MOVPE growth of $In_xGa_{1-x}N$ (x ~0.5) on Si(111) substrates with a pn junction on the surface, Phys. Stat. Sol. (c), 10 (2013) 437-440.

[27] J.W. Ager, L.A. Reichertz, K.M. Yu, W.J. Schaff, T.L. Williamson, M.A. Hoffbauer, N.M. Haegel, W. Walukiewicz, InGaN/Si heterojunction tandem solar cells, in: Photovoltaic Specialists Conference, 2008. PVSC '08. 33rd IEEE, 2008, pp. 1-5.

[28] R.R. King, D.C. Law, K.M. Edmondson, C.M. Fetzer, G.S. Kinsey, H. Yoon, R.A. Sherif, N.H. Karam, 40% efficient metamorphic GaInP／GaInAs／Ge multijunction solar cells, Appl. Phys. Lett., 90 (2007) -.

[29] K.J. Russell, H.E. James, M.F. Christopher, R.K. Richard, Evolution of Multijunction Solar Cell Technology for Concentrating Photovoltaics, Jap. J. Appl. Phys., 51 (2012) 10ND01.

[30] D.J. Friedman, Progress and challenges for next-generation high-efficiency multijunction solar cells, Current Opinion in Solid State and Materials Science, 14 (2010) 131-138.

[31] J.W. Nicklas, J.W. Wilkins, Accurate ab initio predictions of III–V direct-indirect band gap crossovers, Appl. Phys. Lett., 97 (2010) -.

[32] J. Wallentin, L. Barrutia Poncela, A.M. Jansson, K. Mergenthaler, M. Ek, D. Jacobsson, L. Reine Wallenberg, K. Deppert, L. Samuelson, D. Hessman, M.T. Borgström, Single GaInP nanowire p-i-n junctions near the direct to indirect bandgap crossover point, Appl. Phys. Lett., 100 (2012) -.

[33] S.P. Bremner, M.Y. Levy, C.B. Honsberg, Analysis of tandem solar cell efficiencies under AM1.5G spectrum using a rapid flux calculation method, Progress in Photovoltaics: Research and Applications, 16 (2008) 225-233.

[34] C. Jih-Yuan, Y. Shih-Hsun, C. Yi-An, L. Bo-Ting, K. Yen-Kuang, Numerical Investigation of High-Efficiency InGaN-Based Multijunction Solar Cell, Electron Devices, IEEE Transactions on, 60 (2013) 4140-4145.

[35] S. Jae-Phil, J. Seong-Ran, J. Yon-Kil, L. Dong-Seon, Improved Efficiency by Using Transparent Contact Layers in InGaN-Based p-i-n Solar Cells, Electron Device Lett., 31 (2010) 1140-1142.

[36] X. Zheng, R.-H. Horng, D.-S. Wuu, M.-T. Chu, W.-Y. Liao, M.-H. Wu, R.-M. Lin, Y.-C. Lu, High-quality InGaN／GaN heterojunctions and their photovoltaic effects, Appl. Phys. Lett., 93 (2008) 261108.

[37] C.J. Neufeld, N.G. Toledo, S.C. Cruz, M. Iza, S.P. DenBaars, U.K. Mishra, High quantum efficiency InGaN/GaN solar cells with 2.95 eV band gap, Appl. Phys. Lett., 93 (2008) 143502.

[38] O. Jani, I. Ferguson, C. Honsberg, S. Kurtz, Design and characterization of GaN／InGaN solar cells, Appl. Phys. Lett., 91 (2007) 132117.

[39] S.W. Zeng, B.P. Zhang, J.W. Sun, J.F. Cai, C. Chen, J.Z. Yu, Substantial photo-response of InGaN p–i–n homojunction solar cells, Semicond. Sci. Technol., 24 (2009) 055009.

[40] X.-m. Cai, S.-w. Zeng, B.-p. Zhang, Fabrication and characterization of InGaN p-i-n homojunction solar cell, Appl. Phys. Lett., 95 (2009) 173504.

[41] B.R. Jampana, A.G. Melton, M. Jamil, N.N. Faleev, R.L. Opila, I.T. Ferguson, C.B. Honsberg, Design and Realization of Wide-Band-Gap (~2.67 eV) InGaN p-n Junction Solar Cell, Electron Device Lett., 31 (2010) 32-34.

[42] S. Yamamoto, M. Mori, Y. Kuwahara, T. Fujii, T. Nakao, S. Kondo, M. Iwaya, T. Takeuchi, S. Kamiyama, I. Akasaki, H. Amano, Properties of nitride-based photovoltaic cells under concentrated light illumination, Phys. Stat. Sol. RRL, 6 (2012) 145-147.

[43] R. Dahal, J. Li, K. Aryal, J.Y. Lin, H.X. Jiang, InGaN/GaN multiple quantum well concentrator solar cells, Appl. Phys. Lett., 97 (2010) 073115.

[44] R. Dahal, B. Pantha, J. Li, J.Y. Lin, H.X. Jiang, InGaN/GaN multiple quantum well solar cells with long operating wavelengths, Appl. Phys. Lett., 94 (2009) 063505.

[45] S.-W. Feng, C.-M. Lai, C.-Y. Tsai, Y.-R. Su, L.-W. Tu, Modeling of InGaN p-n junction solar cells, Optical Materials Express, 3 (2013) 1777-1788.

[46] D.-J. Kim, Y.-T. Moon, K.-M. Song, C.-J. Choi, Y.-W. Ok, T.-Y. Seong, S.-J. Park, Structural and optical properties of InGaN/GaN multiple quantum wells: The effect of the number of InGaN/GaN pairs, J. Cryst. Growth, 221 (2000) 368-372.

[47] C. Jih-Yuan, K. Yen-Kuang, Numerical Study on the Influence of Piezoelectric Polarization on the Performance of p-on-n (0001)-Face GaN/InGaN p-i-n Solar Cells, Electron Device Lett., 32 (2011) 937-939.

[48] J.-Y. Chang, Y.-K. Kuo, Comment on "The impact of piezoelectric polarization and nonradiative recombination on the performance of (0001) face GaN-InGaN photovoltaic devices" [Appl. Phys. Lett. 96, 051107 (2010)], Appl. Phys. Lett., 98 (2011) 036101.

[49] S.D. Hersee, X. Sun, X. Wang, The Controlled Growth of GaN Nanowires, Nano Lett., 6 (2006) 1808-1811.

[50] S. Fündling, S. Li, Ü. Sökmen, S. Merzsch, P. Hinze, T. Weimann, U. Jahn, A. Trampert, H. Riechert, E. Peiner, H.-H. Wehmann, A. Waag, Three-dimensionally structured silicon as a substrate for the MOVPE growth of GaN nanoLEDs, Phys. Stat. Sol. (a), 206 (2009) 1194-1198.

[51] F.Y. Shih, A. Kobayashi, S. Inoue, J. Ohta, H. Fujioka, Fabrication of densely packed arrays of GaN nanostructures on nano-imprinted substrates, J. Cryst. Growth, 319 (2011) 102-105.

[52] C.V. Falub, H. von Känel, F. Isa, R. Bergamaschini, A. Marzegalli, D. Chrastina, G. Isella, E. Müller, P. Niedermann, L. Miglio, Scaling Hetero-Epitaxy from Layers to Three-Dimensional Crystals, Science, 335 (2012) 1330-1334.

[53] S. Luryi, E. Suhir, New approach to the high quality epitaxial growth of lattice - mismatched materials, Appl. Phys. Lett., 49 (1986) 140-142.

[54] A. Alizadeh, P. Sharma, S. Ganti, S.F. LeBoeuf, L. Tsakalakos, Templated wide band-gap nanostructures, J. Appl. Phys., 95 (2004) 8199-8206.

[55] D. Zubia, S.D. Hersee, Nanoheteroepitaxy: The Application of nanostructuring and substrate compliance to the heteroepitaxy of mismatched semiconductor materials, J. Appl. Phys., 85 (1999) 6492-6496.

[56] S.D. Hersee, D. Zubia, X. Sun, R. Bommena, M. Fairchild, S. Zhang, D. Burckel, A. Frauenglass, S.R.J. Brueck, Nanoheteroepitaxy for the integration of highly mismatched semiconductor materials, Quantum Electronics, IEEE Journal of, 38 (2002) 1017-1028.

[57] E. Ertekin, P.A. Greaney, D.C. Chrzan, T.D. Sands, Equilibrium limits of coherency in strained nanowire heterostructures, J. Appl. Phys., 97 (2005) 114325.

[58] R. Colby, Z. Liang, I.H. Wildeson, D.A. Ewoldt, T.D. Sands, R.E. García, E.A. Stach, Dislocation Filtering in GaN Nanostructures, Nano Lett., 10 (2010) 1568-1573.

[59] K. Hiramatsu, K. Nishiyama, M. Onishi, H. Mizutani, M. Narukawa, A. Motogaito, H. Miyake, Y. Iyechika, T. Maeda, Fabrication and characterization of low defect density GaN using facet-controlled epitaxial lateral overgrowth (FACELO), J. Cryst. Growth, 221 (2000) 316-326.

[60] T.S. Zheleva, O.-H. Nam, W.M. Ashmawi, J.D. Griffin, R.F. Davis, Lateral epitaxy and dislocation density reduction in selectively grown GaN structures, J. Cryst. Growth, 222 (2001) 706-718.

[61] K.Y. Zang, Y.D. Wang, S.J. Chua, L.S. Wang, Nanoscale lateral epitaxial overgrowth of GaN on Si (111), Appl. Phys. Lett., 87 (2005) 193106.

[62] J.D. Eshelby, Screw Dislocations in Thin Rods, J. Appl. Phys., 24 (1953) 176-179.

[63] S. Li, S. Fündling, Ü. Sökmen, S. Merzsch, R. Neumann, P. Hinze, T. Weimann, U. Jahn, A. Trampert, H. Riechert, E. Peiner, H.-H. Wehmann, A. Waag, GaN and LED structures grown on pre-patterned silicon pillar arrays, Phys. Stat. Sol. (c), 7 (2010) 84-87.

[64] V. Bousquet, P. Vennéguès, B. Beaumont, M. Vaille, P. Gibart, TEM Study of the Behavior of Dislocations during ELO of GaN, Phys. Stat. Sol. (b), 216 (1999) 691-695.

[65] I.-h. Ho, G.B. Stringfellow, Solid phase immiscibility in GaInN, Appl. Phys. Lett., 69 (1996) 2701-2703.

[66] C. Caetano, L.K. Teles, M. Marques, A. Dal Pino, L.G. Ferreira, Phase stability, chemical bonds, and gap bowing of $In_xGa_{1-x}N$ alloys: Comparison between cubic and wurtzite structures, Phys. Rev. B, 74 (2006) 045215.

[67] N.A. El-Masry, E.L. Piner, S.X. Liu, S.M. Bedair, Phase separation in InGaN grown by metalorganic chemical vapor deposition, Appl. Phys. Lett., 72 (1998) 40-42.

[68] B.N. Pantha, J. Li, J.Y. Lin, H.X. Jiang, Evolution of phase separation in In-rich InGaN alloys, Appl. Phys. Lett., 96 (2010) 232105-232103.

[69] Z. Liliental-Weber, M. Benamara, J. Washburn, J.Z. Domagala, J. Bak-Misiuk, E.L. Piner, J.C. Roberts, S.M. Bedair, Relaxation of InGaN thin layers observed by X-ray and transmission electron microscopy studies, Journal of Elec Materi, 30 (2001) 439-444.

[70] T. Kuykendall, P. Ulrich, S. Aloni, P. Yang, Complete composition tunability of InGaN nanowires using a combinatorial approach, Nat. Mater., 6 (2007) 951-956.

[71] H.J. Xiang, S.-H. Wei, J.L.F. Da Silva, J. Li, Strain relaxation and band-gap tunability in ternary $In_xGa_{1-x}N$ nanowires, Phys. Rev. B, 78 (2008) 193301.

[72] T. Matsuoka, N. Yoshimoto, T. Sasaki, A. Katsui, Wide-gap semiconductor InGaN and InGaALN grown by MOVPE, J. Electron. Mater., 21 (1992) 157-163.

[73] J. Zhao, M.A. Green, Optimized antireflection coatings for high-efficiency silicon solar cells, Electron Devices, IEEE Transactions on, 38 (1991) 1925-1934.

[74] J. Zhu, Z. Yu, G.F. Burkhard, C.-M. Hsu, S.T. Connor, Y. Xu, Q. Wang, M. McGehee, S. Fan, Y. Cui, Optical Absorption Enhancement in Amorphous Silicon Nanowire and Nanocone Arrays, Nano Lett., 9 (2008) 279-282.

[75] L.T. Tan, A.H. Lim, Z.Y. Chee, Y.L. Wong, Y.C. Huang, H.W. Ong, Q.X. Wee, J.W. Ho, R. Steeman, S.J. Chua, Hierarchical nano/microstructures on silicon surface with ultra low reflectance for photovoltaic applications, Phys. Stat. Sol. (c), 9 (2012) 1873-1877.

[76] Y.B. Tang, Z.H. Chen, H.S. Song, C.S. Lee, H.T. Cong, H.M. Cheng, W.J. Zhang, I. Bello, S.T. Lee, Vertically Aligned p-Type Single-Crystalline GaN Nanorod Arrays on n-Type Si for Heterojunction Photovoltaic Cells, Nano Lett., 8 (2008) 4191-4195.

[77] P. Campbell, M.A. Green, Light trapping properties of pyramidally textured surfaces, J. Appl. Phys., 62 (1987) 243-249.

[78] Z. Fan, D.J. Ruebusch, A.A. Rathore, R. Kapadia, O. Ergen, P.W. Leu, A. Javey, Challenges and prospects of nanopillar-based solar cells, Nano Res., 2 (2009) 829-843.

[79] O.K. Varghese, M. Paulose, C.A. Grimes, Long vertically aligned titania nanotubes on transparent conducting oxide for highly efficient solar cells, Nat. Nanotech., 4 (2009) 592-597.

[80] M. Law, L.E. Greene, A. Radenovic, T. Kuykendall, J. Liphardt, P. Yang, ZnO−Al2O3 and ZnO−TiO2 Core−Shell Nanowire Dye-Sensitized Solar Cells, J. Phys. Chem. B, 110 (2006) 22652-22663.

[81] J.-W. Ho, A.A.O. Tay, S.-J. Chua, Numerical modeling of axial junction compositionally graded $In_xGa_{1-x}N$ nanorod solar cells, in: Photovoltaic Specialists Conference (PVSC), 2012 38th IEEE, 2012, pp. 001898-001903.

[82] R. Datta, M.J. Kappers, M.E. Vickers, J.S. Barnard, C.J. Humphreys, Growth and characterisation of GaN with reduced dislocation density, Superlattices Microstruct., 36 (2004) 393-401.

[83] A. Zoroddu, F. Bernardini, P. Ruggerone, V. Fiorentini, First-principles prediction of structure, energetics, formation enthalpy, elastic constants, polarization, and piezoelectric constants of AlN, GaN, and InN: Comparison of local and gradient-corrected density-functional theory, Phys. Rev. B, 64 (2001) 045208.

[84] F. Bernardini, V. Fiorentini, D. Vanderbilt, Accurate calculation of polarization-related quantities in semiconductors, Phys. Rev. B, 63 (2001) 193201.

[85] T. Tetsuya, A. Hiroshi, A. Isamu, Theoretical Study of Orientation Dependence of Piezoelectric Effects in Wurtzite Strained GaInN/GaN Heterostructures and Quantum Wells, Jap. J. Appl. Phys., 39 (2000) 413.

[86] Y.P. Varshni, Temperature dependence of the energy gap in semiconductors, Physica, 34 (1967) 149-154.

[87] I. Vurgaftman, J.R. Meyer, Band parameters for nitrogen-containing semiconductors, J. Appl. Phys., 94 (2003) 3675-3696.

[88] H. Ishikawa, K. Yamamoto, T. Egawa, T. Soga, T. Jimbo, M. Umeno, Thermal stability of GaN on (1 1 1) Si substrate, J. Cryst. Growth, 189–190 (1998) 178-182.

[89] A. Dadgar, A. Strittmatter, J. Bläsing, M. Poschenrieder, O. Contreras, P. Veit, T. Riemann, F. Bertram, A. Reiher, A. Krtschil, A. Diez, T. Hempel, T. Finger, A. Kasic, M. Schubert, D. Bimberg, F.A. Ponce, J. Christen, A. Krost, Metalorganic chemical vapor phase epitaxy of gallium-nitride on silicon, Phys. Stat. Sol. (c), 0 (2003) 1583-1606.

[90] U. Kaiser, P.D. Brown, I. Khodos, C.J. Humphreys, H.P.D. Schenk, W. Richter, The effect of growth condition on the structure of 2H – AlN films deposited on Si(111) by plasma-assisted molecular beam epitaxy, J. Mater. Res., 14 (1999) 2036-2042.

[91] A. Ohtani, K.S. Stevens, R. Beresford, Microstructure and photoluminescence of GaN grown on Si(111) by plasma-assisted molecular beam epitaxy, Appl. Phys. Lett., 65 (1994) 61-63.

[92] H.F. Liu, S.B. Dolmanan, L. Zhang, S.J. Chua, D.Z. Chi, M. Heuken, S. Tripathy, Influence of stress on structural properties of AlGaN/GaN high electron mobility transistor layers grown on 150 mm diameter Si (111) substrate, J. Appl. Phys., 113 (2013) 023510.

[93] J.-W. Ho, S.-b. Dolmanan, C.B. Tay, Q. Wee, A.A.O. Tay, S.-J. Chua, A dual-character InGaN/GaN multiple quantum well device for electroluminescence and photovoltaic absorption of near-mutually exclusive wavelengths, Phys. Stat. Sol. (c), 11 (2014) 635-639.

[94] T. Egawa, B. Zhang, H. Ishikawa, High performance of InGaN LEDs on (111) silicon substrates grown by MOCVD, Electron Device Lett., 26 (2005) 169-171.

[95] S. Raghavan, J. Redwing, Growth stresses and cracking in GaN films on (111) Si grown by metalorganic chemical vapor deposition. II. Graded AlGaN buffer layers, J. Appl. Phys., 98 (2005) 023515.

[96] S. Raghavan, J.M. Redwing, Growth stresses and cracking in GaN films on (111) Si grown by metal-organic chemical-vapor deposition. I. AlN buffer layers, J. Appl. Phys., 98 (2005) 023514.

[97] J.L. Beuth Jr, Cracking of thin bonded films in residual tension, Int. J. Solids Struct., 29 (1992) 1657-1675.

[98] H. Morkoç, Growth and Growth Methods for Nitride Semiconductors, in: Handbook of Nitride Semiconductors and Devices, Wiley-VCH Verlag GmbH & Co. KGaA, 2009, pp. 323-816.

[99] A.F. Wright, Elastic properties of zinc-blende and wurtzite AlN, GaN, and InN, J. Appl. Phys., 82 (1997) 2833-2839.

[100] R.R. Reeber, K. Wang, High Temperature Elastic Constant Prediction of Some Group III-Nitrides, MRS Internet J. Nitride Semicond. Res., 6 (2001) e3.

[101] J. Bläsing, A. Reiher, A. Dadgar, A. Diez, A. Krost, The origin of stress reduction by low-temperature AlN interlayers, Appl. Phys. Lett., 81 (2002) 2722-2724.

[102] D. Armin, B. Jürgen, D. Annette, A. Assadullah, H. Michael, K. Alois, Metalorganic Chemical Vapor Phase Epitaxy of Crack-Free GaN on Si (111) Exceeding 1 μm in Thickness, Jap. J. Appl. Phys., 39 (2000) L1183.

[103] J.-Y. Kim, Y. Tak, J. Kim, H.-G. Hong, S. Chae, J.W. Lee, H. Choi, Y. Park, U.I. Chung, J.-R. Kim, J.-I. Shim, Highly efficient InGaN/GaN blue LED on 8-inch Si (111) substrate, Proc. SPIE, 8262 (2012) 82621D.

[104] M.A. Moram, M.E. Vickers, X-ray diffraction of III-nitrides, Rep. Prog. Phys., 72 (2009) 036502.

[105] L.F.J. Piper, T.D. Veal, C.F. McConville, H. Lu, W.J. Schaff, Origin of the n-type conductivity of InN: The role of positively charged dislocations, Appl. Phys. Lett., 88 (2006) 252109.

[106] V. Cimalla, V. Lebedev, F.M. Morales, R. Goldhahn, O. Ambacher, Model for the thickness dependence of electron concentration in InN films, Appl. Phys. Lett., 89 (2006) 172109.

[107] B. Monemar, B.E. Sernelius, Defect related issues in the “current roll-off” in InGaN based light emitting diodes, Appl. Phys. Lett., 91 (2007) 181103.

[108] Y. Yang, X.A. Cao, C.H. Yan, Electrical and optical characteristics of green light-emitting diodes grown on bulk GaN substrates, Proc. SPIE, 7231 (2009) 72310W.

[109] A. Tabata, L.K. Teles, L.M.R. Scolfaro, J.R. Leite, A. Kharchenko, T. Frey, D.J. As, D. Schikora, K. Lischka, J. Furthmuller, F. Bechstedt, Phase separation suppression in InGaN epitaxial layers due to biaxial strain, Appl. Phys. Lett., 80 (2002) 769-771.

[110] S.Y. Karpov, Suppression of phase separation in InGaN due to elastic strain, MRS Internet J. Nitride Semicond. Res., 3 (1998) e16.

[111] K. Hiramatsu, Y. Kawaguchi, M. Shimizu, N. Sawaki, T. Zheleva, R.F. Davis, H. Tsuda, W. Taki, N. Kuwano, K. Oki, The Composition Pulling Effect in MOVPE Grown InGaN on GaN and AlGaN and its TEM Characterization, MRS Internet J. Nitride Semicond. Res., 2 (1997) e6.

[112] Y. Kawaguchi, M. Shimizu, K. Hiramatsu, N. Sawaki, The Composition Pulling Effect in InGaN Growth on the GaN and AlGaN Epitaxial Layers Grown by MOVPE, Mater. Res. Soc. Symp. Proc., 449 (1996) 89.

[113] J. Tersoff, Enhanced Nucleation and Enrichment of Strained-Alloy Quantum Dots, Phys. Rev. Lett., 81 (1998) 3183-3186.

[114] H. Chen, R.M. Feenstra, J.E. Northrup, T. Zywietz, J. Neugebauer, Spontaneous Formation of Indium-Rich Nanostructures on InGaN(0001) Surfaces, Phys. Rev. Lett., 85 (2000) 1902-1905.

[115] J.E. Northrup, L.T. Romano, J. Neugebauer, Surface energetics, pit formation, and chemical ordering in InGaN alloys, Appl. Phys. Lett., 74 (1999) 2319-2321.

[116] M.K. Behbehani, E.L. Piner, S.X. Liu, N.A. El-Masry, S.M. Bedair, Phase separation and ordering coexisting in $In_xGa_{1-x}N$ grown by metal organic chemical vapor deposition, Appl. Phys. Lett., 75 (1999) 2202-2204.

[117] Y. Narukawa, Y. Kawakami, M. Funato, S. Fujita, S. Fujita, S. Nakamura, Role of self-formed InGaN quantum dots for exciton localization in the purple laser diode emitting at 420 nm, Appl. Phys. Lett., 70 (1997) 981-983.

[118] R.A. Oliver, S.E. Bennett, T. Zhu, D.J. Beesley, M.J. Kappers, D.W. Saxey, A. Cerezo, C.J. Humphreys, Microstructural origins of localization in InGaN quantum wells, J. Phys. D: Appl. Phys., 43 (2010) 354003.

[119] Ö. Tuna, W.M. Linhart, E.V. Lutsenko, M.V. Rzheutski, G.P. Yablonskii, T.D. Veal, C.F. McConville, C. Giesen, H. Kalisch, A. Vescan, M. Heuken, Structural, electrical and optical characterization of MOCVD grown In-rich InGaN layers, J. Cryst. Growth, 358 (2012) 51-56.

[120] H.Y. Omkar Jani, Elaissa Trybus, Balakrishnam Jampana, Ian Ferguson, Alan Doolittle, Christiana Honsberg, Effect of phase separation on performance of III-V nitride solar cells, 22nd European Photovoltaic Solar Energy Conference, (2007) 64 - 67.

[121] C. Tessarek, S. Figge, T. Aschenbrenner, S. Bley, A. Rosenauer, M. Seyfried, J. Kalden, K. Sebald, J. Gutowski, D. Hommel, Strong phase separation of strained $In_xGa_{1-x}N$ layers due to spinodal and binodal decomposition: Formation of stable quantum dots, Phys. Rev. B, 83 (2011) 115316.

[122] T. Matsuoka, Progress in nitride semiconductors from GaN to InN—MOVPE growth and characteristics, Superlattices Microstruct., 37 (2005) 19-32.

[123] S.M. Bedair, F.G. McIntosh, J.C. Roberts, E.L. Piner, K.S. Boutros, N.A. El-Masry, Growth and characterization of In-based nitride compounds, J. Cryst. Growth, 178 (1997) 32-44.

[124] A.B. Erkan, Growth and Fabrication of GaN and $In_xGa_{1-x}N$ Based Optoelectronic Devices in: Materials Science and Engineering, North Carolina State University, Raleigh, North Carolina, 2008.

[125] H.-C. Lin, C.-K. Shu, J. Ou, Y.-C. Pan, W.-K. Chen, W.-H. Chen, M.-C. Lee, Growth temperature effects on $In_xGa_{1-x}N$ films studied by X-ray and photoluminescence, J. Cryst. Growth, 189–190 (1998) 57-60.

[126] K.S. Boutros, F.G. McIntosh, J.C. Roberts, S.M. Bedair, E.L. Piner, N.A. El-Masry, High quality InGaN films by atomic layer epitaxy, Appl. Phys. Lett., 67 (1995) 1856-1858.

[127] D.D. Koleske, A.E. Wickenden, R.L. Henry, M.E. Twigg, Influence of MOVPE growth conditions on carbon and silicon concentrations in GaN, J. Cryst. Growth, 242 (2002) 55-69.

[128] Y. Guo, X.L. Liu, H.P. Song, A.L. Yang, X.Q. Xu, G.L. Zheng, H.Y. Wei, S.Y. Yang, Q.S. Zhu, Z.G. Wang, A study of indium incorporation in In-rich InGaN grown by MOVPE, Appl. Surf. Sci., 256 (2010) 3352-3356.

[129] V.P. Chaly, B.A. Borisov, D.M. Demidov, D.M. Krasovitsky, Y.V. Pogorelsky, A.P. Shkurko, I.A. Sokolov, S.Y. Karpov, Indium droplet formation during molecular beam epitaxy of InGaN, J. Cryst. Growth, 206 (1999) 147-149.

[130] J.W. Ho, L. Zhang, Q. Wee, A.A.O. Tay, M. Heuken, S.-J. Chua, Structural and morphological qualities of InGaN grown via elevated pressures in MOCVD on AlN/Si(111) substrates, J. Cryst. Growth, 383 (2013) 1-8.

[131] A.H. Mueller, E.A. Akhadov, M.A. Hoffbauer, Low-temperature growth of crystalline GaN films using energetic neutral atomic-beam lithography/epitaxy, Appl. Phys. Lett., 88 (2006) 041907-041903.

[132] M.A. Hoffbauer, T.L. Williamson, J.J. Williams, J.L. Fordham, K.M. Yu, W. Walukiewicz, L.A. Reichertz, In-rich InGaN thin films: Progress on growth, compositional uniformity, and doping for device applications, J. Vac. Sci. Technol. B, 31 (2013) 03C114.

[133] M. Moseley, J. Lowder, D. Billingsley, W.A. Doolittle, Control of surface adatom kinetics for the growth of high-indium content InGaN throughout the miscibility gap, Appl. Phys. Lett., 97 (2010) 191902.

[134] M. Moseley, B. Gunning, J. Lowder, W. Alan Doolittle, G. Namkoong, Structural and electrical characterization of InN, InGaN, and p-InGaN grown by metal-modulated epitaxy, J. Vac. Sci. Technol. B, 31 (2013) 03C104.

[135] K. Kumakura, T. Makimoto, N. Kobayashi, High hole concentrations in Mg-doped InGaN grown by MOVPE, J. Cryst. Growth, 221 (2000) 267-270.

[136] P. Vennéguès, B. Beaumont, S. Haffouz, M. Vaille, P. Gibart, Influence of in situ sapphire surface preparation and carrier gas on the growth mode of GaN in MOVPE, J. Cryst. Growth, 187 (1998) 167-177.

[137] E. Frayssinet, B. Beaumont, J.P. Faurie, P. Gibart, Z. Makkai, B. Pécz, P. Lefebvre, P. Valvin, Micro Epitaxial lateral overgrowth of GaN/sapphire by Metal Organic Vapour Phase Epitaxy, MRS Internet J. Nitride Semicond. Res., 7 (2002) e8.

[138] K. Cheng, M. Leys, S. Degroote, M. Germain, G. Borghs, High quality GaN grown on silicon(111) using a SixNy interlayer by metal-organic vapor phase epitaxy, Appl. Phys. Lett., 92 (2008) 192111.

[139] A. Dadgar, M. Poschenrieder, A. Reiher, J. Bläsing, J. Christen, A. Krtschil, T. Finger, T. Hempel, A. Diez, A. Krost, Reduction of stress at the initial stages of GaN growth on Si(111), Appl. Phys. Lett., 82 (2003) 28-30.

[140] Y. Kato, S. Kitamura, K. Hiramatsu, N. Sawaki, Selective growth of wurtzite GaN and AlxGa1−xN on GaN/sapphire substrates by metalorganic vapor phase epitaxy, J. Cryst. Growth, 144 (1994) 133-140.

[141] K. Hiramatsu, K. Nishiyama, A. Motogaito, H. Miyake, Y. Iyechika, T. Maeda, Recent Progress in Selective Area Growth and Epitaxial Lateral Overgrowth of III-Nitrides: Effects of Reactor Pressure in MOVPE Growth, Phys. Stat. Sol. (a), 176 (1999) 535-543.

[142] G. Wulff, XXV. Zur Frage der Geschwindigkeit des Wachsthums und der Auflösung der Krystallflächen, in: Zeitschrift für Kristallographie - Crystalline Materials, 1901, pp. 449.

[143] S.F. Li, S. Fuendling, X. Wang, S. Merzsch, M.A.M. Al-Suleiman, J.D. Wei, H.H. Wehmann, A. Waag, W. Bergbauer, M. Strassburg, Polarity and Its Influence on Growth Mechanism during MOVPE Growth of GaN Sub-micrometer Rods, Cryst. Growth Des., 11 (2011) 1573-1577.

[144] J.E. Northrup, J. Neugebauer, Strong affinity of hydrogen for the GaN(000-1) surface: Implications for molecular beam epitaxy and metalorganic chemical vapor deposition, Appl. Phys. Lett., 85 (2004) 3429-3431.

[145] B.L. VanMil, H. Guo, L.J. Holbert, K. Lee, T.H. Myers, T. Liu, D. Korakakis, High temperature limitations for GaN growth by rf-plasma assisted molecular beam epitaxy: Effects of active nitrogen species, surface polarity, hydrogen, and excess Ga-overpressure, J. Vac. Sci. Technol. B, 22 (2004) 2149-2154.

[146] R.M. Feenstra, Y. Dong, C.D. Lee, J.E. Northrup, Recent developments in surface studies of GaN and AlN, J. Vac. Sci. Technol. B, 23 (2005) 1174-1180.

[147] S. Kitamura, K. Hiramatsu, N. Sawaki, Fabrication of GaN Hexagonal Pyramids on Dot-Patterned GaN/Sapphire Substrates via Selective Metalorganic Vapor Phase Epitaxy, Jap. J. Appl. Phys., 34 (1995) L1184-L1186.

[148] S.-Y. Bae, D.-H. Kim, D.-S. Lee, S.-J. Lee, J.H. Baek, Highly Integrated InGaN/GaN Semipolar Micro-Pyramid Light-Emitting Diode Arrays by Confined Selective Area Growth, Electrochem. Solid-State Lett., 15 (2011) H47-H50.

[149] M. Sugiyama, T. Fujiwara, Y. Nakano, Monolithic integration of semipolar pyramidal LEDs with tailored wavelengths, Phys. Stat. Sol. (c), 9 (2012) 476-479.

[150] S. Gradečak, P. Stadelmann, V. Wagner, M. Ilegems, Bending of dislocations in GaN during epitaxial lateral overgrowth, Appl. Phys. Lett., 85 (2004) 4648-4650.

[151] W. Tim, S. Lukas, N. Carsten, R. Jens, H. Veit, P. Simon, K. Arne, W. Markus, S. Ulrich, K. Michael, Indium incorporation and emission wavelength of polar,

nonpolar and semipolar InGaN quantum wells, Semicond. Sci. Technol., 27 (2012) 024014.

[152] T. Wunderer, M. Feneberg, F. Lipski, J. Wang, R.A.R. Leute, S. Schwaiger, K. Thonke, A. Chuvilin, U. Kaiser, S. Metzner, F. Bertram, J. Christen, G.J. Beirne, M. Jetter, P. Michler, L. Schade, C. Vierheilig, U.T. Schwarz, A.D. Dräger, A. Hangleiter, F. Scholz, Three-dimensional GaN for semipolar light emitters, Phys. Stat. Sol. (b), 248 (2011) 549-560.

[153] J.E. Northrup, GaN and InGaN(11$\bar{2}$2) surfaces: Group-III adlayers and indium incorporation, Appl. Phys. Lett., 95 (2009) 133107.

[154] K. Linthicum, T. Gehrke, D. Thomson, E. Carlson, P. Rajagopal, T. Smith, D. Batchelor, R. Davis, Pendeoepitaxy of gallium nitride thin films, Appl. Phys. Lett., 75 (1999) 196-198.

[155] T. Zheleva, S. Smith, D. Thomson, K. Linthicum, P. Rajagopal, R. Davis, Pendeo-epitaxy: A new approach for lateral growth of gallium nitride films, Journal of Elec Materi, 28 (1999) L5-L8.

[156] A.M. Roskowski, E.A. Preble, S. Einfeldt, P.M. Miraglia, R.F. Davis, Maskless pendeo-epitaxial growth of GaN films, Journal of Elec Materi, 31 (2002) 421-428.

[157] R.I. Barabash, G.E. Ice, W. Liu, S. Einfeldt, A.M. Roskowski, R.F. Davis, Local strain, defects, and crystallographic tilt in GaN(0001) layers grown by maskless pendeo-epitaxy from x-ray microdiffraction, J. Appl. Phys., 97 (2005) 013504.

[158] A. Strittmatter, S. Rodt, L. Reißmann, D. Bimberg, H. Schröder, E. Obermeier, T. Riemann, J. Christen, A. Krost, Maskless epitaxial lateral overgrowth of GaN layers on structured Si(111) substrates, Appl. Phys. Lett., 78 (2001) 727-729.

[159] D. Theeradetch, Y. Masahiro, S. Shigekazu, N. Ryo, M. Shingo, N. Tetsuya, A. Hiroshi, A. Isamu, Heteroepitaxial Lateral Overgrowth of GaN on Periodically Grooved Substrates: A New Approach for Growing Low-Dislocation-Density GaN Single Crystals, Jap. J. Appl. Phys., 40 (2001) L16-L19.

[160] E. Calleja, J. Ristić, S. Fernández-Garrido, L. Cerutti, M.A. Sánchez-García, J. Grandal, A. Trampert, U. Jahn, G. Sánchez, A. Griol, B. Sánchez, Growth, morphology, and structural properties of group-III-nitride nanocolumns and nanodisks, Phys. Stat. Sol. (b), 244 (2007) 2816-2837.

[161] O. Landré, V. Fellmann, P. Jaffrennou, C. Bougerol, H. Renevier, A. Cros, B. Daudin, Molecular beam epitaxy growth and optical properties of AlN nanowires, Appl. Phys. Lett., 96 (2010) 061912.

[162] E. Calleja, M.A. Sánchez-García, F.J. Sánchez, F. Calle, F.B. Naranjo, E. Muñoz, U. Jahn, K. Ploog, Luminescence properties and defects in GaN nanocolumns grown by molecular beam epitaxy, Phys. Rev. B, 62 (2000) 16826-16834.

[163] Y. Masaki, K. Akihiko, M. Masashi, F. Nobuhiko, K. Katsumi, Growth of Self-Organized GaN Nanostructures on $Al_2O_3$(0001) by RF-Radical Source Molecular Beam Epitaxy, Jap. J. Appl. Phys., 36 (1997) L459-L462.

[164] H. Sekiguchi, T. Nakazato, A. Kikuchi, K. Kishino, Structural and optical properties of GaN nanocolumns grown on (0001) sapphire substrates by rf-plasma-assisted molecular-beam epitaxy, J. Cryst. Growth, 300 (2007) 259-262.

[165] C. Yi-Lu, L. Feng, F. Arya, M. Zetian, Molecular beam epitaxial growth and characterization of non-tapered InN nanowires on Si(111), Nanotechnology, 20 (2009) 345203.

[166] N. Hieu Pham Trung, C. Yi-Lu, S. Ishiang, M. Zetian, InN p-i-n Nanowire Solar Cells on Si, Selected Topics in Quantum Electronics, IEEE Journal of, 17 (2011) 1062-1069.

[167] A.P. Vajpeyi, A.O. Ajagunna, K. Tsagaraki, M. Androulidaki, A. Georgakilas, InGaN nanopillars grown on silicon substrate using plasma assisted molecular beam epitaxy, Nanotechnology, 20 (2009) 325605.

[168] K.M. Wu, Y. Pan, C. Liu, InGaN nanorod arrays grown by molecular beam epitaxy: Growth mechanism structural and optical properties, Appl. Surf. Sci., 255 (2009) 6705-6709.

[169] T. Kehagias, Nanoscale indium variation along InGaN nanopillars grown on (111) Si substrates, Physica E: Low-dimensional Systems and Nanostructures, 42 (2010) 2197-2202.

[170] S. Albert, A. Bengoechea-Encabo, P. Lefebvre, M.A. Sanchez-Garcia, E. Calleja, U. Jahn, A. Trampert, Emission control of InGaN nanocolumns grown by molecular-beam epitaxy on Si(111) substrates, Appl. Phys. Lett., 99 (2011) 131108.

[171] T. Tabata, J. Paek, Y. Honda, M. Yamaguchi, H. Amano, Growth of InGaN nanowires on a (111)Si substrate by RF-MBE, Phys. Stat. Sol. (c), 9 (2012) 646-649.

[172] K.D. Goodman, V.V. Protasenko, J. Verma, T.H. Kosel, H.G. Xing, D. Jena, Green luminescence of InGaN nanowires grown on silicon substrates by molecular beam epitaxy, J. Appl. Phys., 109 (2011) 084336.

[173] T. Takuya, P. Jihyun, H. Yoshio, Y. Masahito, A. Hiroshi, Stacking Faults and Luminescence Property of InGaN Nanowires, Jap. J. Appl. Phys., 52 (2013) 08JE06.

[174] M. Gómez-Gómez, N. Garro, J. Segura-Ruiz, G. Martinez-Criado, A. Cantarero, H.T. Mengistu, A. García-Cristóbal, S. Murcia-Mascarós, C. Denker, J. Malindretos, A. Rizzi, Spontaneous core–shell elemental distribution in In-rich $In_xGa_{1-x}N$ nanowires grown by molecular beam epitaxy, Nanotechnology, 25 (2014) 075705.

[175] T. Kouno, A. Kikuchi, K. Kishino, Growth of high-In-content InGaN multiple quantum disk nanocolumns on Si(111) by RF plasma-assisted molecular-beam epitaxy, Phys. Stat. Sol. (b), 243 (2006) 1481-1485.

[176] W. Guo, M. Zhang, A. Banerjee, P. Bhattacharya, Catalyst-Free InGaN/GaN Nanowire Light Emitting Diodes Grown on (001) Silicon by Molecular Beam Epitaxy, Nano Lett., 10 (2010) 3355-3359.

[177] K. Akihiko, K. Mizue, T. Makoto, K. Katsumi, InGaN/GaN Multiple Quantum Disk Nanocolumn Light-Emitting Diodes Grown on (111) Si Substrate, Jap. J. Appl. Phys., 43 (2004) L1524-L1526.

[178] A.L. Bavencove, G. Tourbot, J. Garcia, Y. Désières, P. Gilet, F. Levy, B. André, B. Gayral, B. Daudin, D. Le Si, Submicrometre resolved optical characterization of green nanowire-based light emitting diodes, Nanotechnology, 22 (2011) 345705.

[179] K. Kishino, A. Kikuchi, H. Sekiguchi, S. Ishizawa, InGaN/GaN nanocolumn LEDs emitting from blue to red, Proc. SPIE, 6473 (2007) 64730T.

[180] M. Knelangen, M. Hanke, E. Luna, L. Schrottke, O. Brandt, A. Trampert, Monodisperse (In, Ga)N insertions in catalyst-free-grown GaN(0001) nanowires, Nanotechnology, 22 (2011) 365703.

[181] G. Tourbot, C. Bougerol, F. Glas, L.F. Zagonel, Z. Mahfoud, S. Meuret, P. Gilet, M. Kociak, B. Gayral, B. Daudin, Growth mechanism and properties of InGaN insertions in GaN nanowires, Nanotechnology, 23 (2012) 135703.

[182] R. Armitage, K. Tsubaki, Multicolour luminescence from InGaN quantum wells grown over GaN nanowire arrays by molecular-beam epitaxy, Nanotechnology, 21 (2010) 195202.

[183] C.H. Liang, L.C. Chen, J.S. Hwang, K.H. Chen, Y.T. Hung, Y.F. Chen, Selective-area growth of indium nitride nanowires on gold-patterned Si(100) substrates, Appl. Phys. Lett., 81 (2002) 22.

[184] X.M. Cai, Y.H. Leung, K.Y. Cheung, K.H. Tam, A.B. Djurišić, M.H. Xie, H.Y. Chen, S. Gwo, Straight and helical InGaN core–shell nanowires with a high In core content, Nanotechnology, 17 (2006) 2330.

[185] X.M. Cai, F. Ye, S.Y. Jing, D.P. Zhang, P. Fan, E.Q. Xie, CVD growth of InGaN nanowires, J. Alloys Compd., 467 (2009) 472-476.

[186] F. Ye, X.M. Cai, X.M. Wang, E.Q. Xie, The growth and field electron emission of InGaN nanowires, J. Cryst. Growth, 304 (2007) 333-337.

[187] H.M. Kim, D.S. Kim, Y.S. Park, D.Y. Kim, T.W. Kang, K.S. Chung, Growth of GaN Nanorods by a Hydride Vapor Phase Epitaxy Method, Adv. Mater., 14 (2002) 991-993.

[188] H.-M. Kim, D.S. Kim, D.Y. Kim, T.W. Kang, Y.-H. Cho, K.S. Chung, Growth and characterization of single-crystal GaN nanorods by hydride vapor phase epitaxy, Appl. Phys. Lett., 81 (2002) 2193-2195.

[189] Y.H. Kwon, K.H. Lee, S.Y. Ryu, T.W. Kang, C.H. You, T.W. Kim, Formation mechanisms of GaN nanorods grown on Si(111) substrates, Appl. Surf. Sci., 254 (2008) 7014-7017.

[190] K.H. Lee, Y.H. Kwon, S.Y. Ryu, T.W. Kang, J.H. Jung, D.U. Lee, T.W. Kim, Microstructural properties and atomic arrangements of GaN nanorods grown on Si (111) substrates by using hydride vapor phase epitaxy, J. Cryst. Growth, 310 (2008) 2977-2980.

[191] H.-M. Kim, W.C. Lee, T.W. Kang, K.S. Chung, C.S. Yoon, C.K. Kim, InGaN nanorods grown on (111) silicon substrate by hydride vapor phase epitaxy, Chem. Phys. Lett., 380 (2003) 181-184.

[192] H.-M. Kim, H. Lee, S.I. Kim, S.R. Ryu, T.W. Kang, K.S. Chung, Formation of InGaN nanorods with indium mole fractions by hydride vapor phase epitaxy, Phys. Stat. Sol. (b), 241 (2004) 2802-2805.

[193] H.-M. Kim, Y.-H. Cho, H. Lee, S.I. Kim, S.R. Ryu, D.Y. Kim, T.W. Kang, K.S. Chung, High-Brightness Light Emitting Diodes Using Dislocation-Free Indium Gallium Nitride/Gallium Nitride Multiquantum-Well Nanorod Arrays, Nano Lett., 4 (2004) 1059-1062.

[194] Y. Sun, Y.-H. Cho, H.-M. Kim, T.W. Kang, High efficiency and brightness of blue light emission from dislocation-free InGaN ∕ GaN quantum well nanorod arrays, Appl. Phys. Lett., 87 (2005) 093115.

[195] S. Keating, M.G. Urquhart, D.V.P. McLaughlin, J.M. Pearce, Effects of Substrate Temperature on Indium Gallium Nitride Nanocolumn Crystal Growth, Cryst. Growth Des., 11 (2010) 565-568.

[196] T. Kuykendall, P.J. Pauzauskie, Y. Zhang, J. Goldberger, D. Sirbuly, J. Denlinger, P. Yang, Crystallographic alignment of high-density gallium nitride nanowire arrays, Nat. Mater., 3 (2004) 524-528.

[197] K.-Y. Song, R. Navamathavan, J.-H. Park, Y.-B. Ra, Y.-H. Ra, J.-S. Kim, C.-R. Lee, Selective area growth of GaN nanowires using metalorganic chemical vapor deposition on nano-patterned Si(111) formed by the etching of nano-sized Au droplets, Thin Solid Films, 520 (2011) 126-130.

[198] X.J. Chen, G. Perillat-Merceroz, D. Sam-Giao, C. Durand, J. Eymery, Homoepitaxial growth of catalyst-free GaN wires on N-polar substrates, Appl. Phys. Lett., 97 (2010) 151909.

[199] R. Koester, J.S. Hwang, C. Durand, D.L.S. Dang, J. Eymery, Self-assembled growth of catalyst-free GaN wires by metal–organic vapour phase epitaxy, Nanotechnology, 21 (2010) 015602.

[200] J.L. Mangum, Metalorganic Chemical Vapor Deposition of Indium Nitride and Indium Gallium Nitride Thin Films and Nanostructures for Electronic and Photovoltaic Applications, in: Graduate School of the University of Florida, University of Florida, 2007.

[201] T.R. Kuykendall, III-nitride Semiconductor Nanowires, in: Department of Chemistry, University of California, Berkeley, 2007.

[202] C. Du, T. Wei, H. Zheng, L. Wang, C. Geng, Q. Yan, J. Wang, J. Li, Size-controllable nanopyramids photonic crystal selectively grown on p-GaN for enhanced light-extraction of light-emitting diodes, Opt. Express, 21 (2013) 25373-25380.

[203] A. Winden, M. Mikulics, T. Stoica, M. von der Ahe, G. Mussler, A. Haab, D. Grützmacher, H. Hardtdegen, Site-controlled growth of indium nitride based nanostructures using metalorganic vapour phase epitaxy, J. Cryst. Growth, 370 (2013) 336-341.

[204] K. Kishino, T. Hoshino, S. Ishizawa, A. Kikuchi, Selective-area growth of GaN nanocolumns on titanium-mask-patterned silicon (111) substrates by RF-plasma-assisted molecular-beam epitaxy, Electron. Lett, 44 (2008) 819-821.

[205] K. Kishino, H. Sekiguchi, A. Kikuchi, Improved Ti-mask selective-area growth (SAG) by rf-plasma-assisted molecular beam epitaxy demonstrating extremely uniform GaN nanocolumn arrays, J. Cryst. Growth, 311 (2009) 2063-2068.

[206] K.A. Bertness, A.W. Sanders, D.M. Rourke, T.E. Harvey, A. Roshko, J.B. Schlager, N.A. Sanford, Controlled Nucleation of GaN Nanowires Grown with Molecular Beam Epitaxy, Adv. Funct. Mater., 20 (2010) 2911-2915.

[207] A. Bengoechea-Encabo, F. Barbagini, S. Fernandez-Garrido, J. Grandal, J. Ristic, M.A. Sanchez-Garcia, E. Calleja, U. Jahn, E. Luna, A. Trampert, Understanding the selective area growth of GaN nanocolumns by MBE using Ti nanomasks, J. Cryst. Growth, 325 (2011) 89-92.

[208] Y. Nagae, T. Iwatsuki, Y. Shirai, Y. Osawa, S. Naritsuka, T. Maruyama, Effect of mask material on selective growth of GaN by RF-MBE, J. Cryst. Growth, 324 (2011) 88-92.

[209] H. Sekiguchi, K. Kishino, A. Kikuchi, Emission color control from blue to red with nanocolumn diameter of InGaN/GaN nanocolumn arrays grown on same substrate, Appl. Phys. Lett., 96 (2010) 231104.

[210] H. Sekiguchi, K. Kishino, A. Kikuchi, Formation of InGaN quantum dots in regularly arranged GaN nanocolumns grown by rf-plasma-assisted molecular-beam epitaxy, Phys. Stat. Sol. (c), 7 (2010) 2374-2377.

[211] P. Chen, S.J. Chua, Y.D. Wang, M.D. Sander, C.G. Fonstad, InGaN nanorings and nanodots by selective area epitaxy, Appl. Phys. Lett., 87 (2005) 143111.

[212] Y. Wang, K. Zang, S. Chua, M.S. Sander, S. Tripathy, C.G. Fonstad, High-Density Arrays of InGaN Nanorings, Nanodots, and Nanoarrows Fabricated by a Template-Assisted Approach, J. Phys. Chem. B, 110 (2006) 11081-11087.

[213] P. Deb, H. Kim, V. Rawat, M. Oliver, S. Kim, M. Marshall, E. Stach, T. Sands, Faceted and Vertically Aligned GaN Nanorod Arrays Fabricated without Catalysts or Lithography, Nano Lett., 5 (2005) 1847-1851.

[214] P. Deb, H. Kim, Y. Qin, R. Lahiji, M. Oliver, R. Reifenberger, T. Sands, GaN Nanorod Schottky and p−n Junction Diodes, Nano Lett., 6 (2006) 2893-2898.

[215] Y.D. Wang, K.Y. Zang, S.J. Chua, Nonlithographic nanopatterning through anodic aluminum oxide template and selective growth of highly ordered GaN nanostructures, J. Appl. Phys., 100 (2006) 054306.

[216] Z. Keyan, W. Yadong, C.S. Jin, Low dimensional nanostructured InGaN multi-quantum wells by selective area heteroepitaxy, Phys. Stat. Sol. (c), 6 (2009) S514-S518.

[217] I.H. Wildeson, R. Colby, D.A. Ewoldt, Z. Liang, D.N. Zakharov, N.J. Zaluzec, R.E. García, E.A. Stach, T.D. Sands, III-nitride nanopyramid light emitting diodes grown by organometallic vapor phase epitaxy, J. Appl. Phys., 108 (2010) 044303.

[218] Y.D. Wang, K.Y. Zang, S.J. Chua, S. Tripathy, H.L. Zhou, C.G. Fonstad, Improvement of microstructural and optical properties of GaN layer on sapphire by nanoscale lateral epitaxial overgrowth, Appl. Phys. Lett., 88 (2006) 211908.

[219] G. Liu, H. Zhao, J. Zhang, J. Park, L. Mawst, N. Tansu, Selective area epitaxy of ultra-high density InGaN quantum dots by diblock copolymer lithography, Nanoscale Res. Lett., 6 (2011) 342.

[220] A. Chen, S.J. Chua, P. Chen, X.Y. Chen, L.K. Jian, Fabrication of sub-100 nm patterns in SiO 2 templates by electron-beam lithography for the growth of periodic III–V semiconductor nanostructures, Nanotechnology, 17 (2006) 3903.

[221] P. Chen, A. Chen, S.J. Chua, J.N. Tan, Growth and Optical Properties of Highly Uniform and Periodic InGaN Nanostructures, Adv. Mater., 19 (2007) 1707-1710.

[222] P. Chen, S.J. Chua, J.N. Tan, High-density InGaN nanodots grown on pretreated GaN surfaces, Appl. Phys. Lett., 89 (2006) 023114.

[223] F. Barbagini, A. Bengoechea-Encabo, S. Albert, J. Martinez, M. Sanchez Garcia, A. Trampert, E. Calleja, Critical aspects of substrate nanopatterning for the ordered growth of GaN nanocolumns, Nanoscale Res. Lett., 6 (2011) 632.

[224] H.-S. Chen, Y.-F. Yao, C.-H. Liao, C.-G. Tu, C.-Y. Su, W.-M. Chang, Y.-W. Kiang, C.C. Yang, Light-emitting device with regularly patterned growth of an InGaN/GaN quantum-well nanorod light-emitting diode array, Opt. Lett., 38 (2013) 3370-3373.

[225] K. Wu, T. Wei, H. Zheng, D. Lan, X. Wei, Q. Hu, H. Lu, J. Wang, Y. Luo, J. Li, Fabrication and optical characteristics of phosphor-free InGaN nanopyramid white light emitting diodes by nanospherical-lens photolithography, J. Appl. Phys., 115 (2014) 123101.

[226] Y.-T. Lin, T.-W. Yeh, Y. Nakajima, P.D. Dapkus, Catalyst-Free GaN Nanorods Synthesized by Selective Area Growth, Adv. Funct. Mater., 24 (2014) 3162–3171.

[227] V. Jindal, N. Tripathi, M. Tungare, O. Paschos, P. Haldar, F. Shahedipour-Sandvik, Selective area heteroepitaxy of low dimensional a -plane and c -plane InGaN nanostructures using pulsed MOCVD, Phys. Stat. Sol. (c), 5 (2008) 1709-1711.

[228] Y.-S. Chen, W.-Y. Shiao, T.-Y. Tang, W.-M. Chang, C.-H. Liao, C.-H. Lin, K.-C. Shen, C.C. Yang, M.-C. Hsu, J.-H. Yeh, T.-C. Hsu, Threading dislocation evolution in patterned GaN nanocolumn growth and coalescence overgrowth, J. Appl. Phys., 106 (2009) 023521.

[229] T.-Y. Tang, W.-Y. Shiao, C.-H. Lin, K.-C. Shen, J.-J. Huang, S.-Y. Ting, T.-C. Liu, C.C. Yang, C.-L. Yao, J.-H. Yeh, T.-C. Hsu, W.-C. Chen, H.-C. Hsu, L.-C. Chen, Coalescence overgrowth of GaN nanocolumns on sapphire with patterned metal organic vapor phase epitaxy, J. Appl. Phys., 105 (2009) 023501.

[230] C.-H. Liao, W.-M. Chang, H.-S. Chen, C.-Y. Chen, Y.-F. Yao, H.-T. Chen, C.-Y. Su, S.-Y. Ting, Y.-W. Kiang, C.C. Yang, Geometry and composition comparisons between c-plane disc-like and m-plane core-shell InGaN/GaN quantum wells in a nitride nanorod, Opt. Express, 20 (2012) 15859-15871.

[231] C.-H. Liao, W.-M. Chang, Y.-F. Yao, H.-T. Chen, C.-Y. Su, C.-Y. Chen, C. Hsieh, H.-S. Chen, C.-G. Tu, Y.-W. Kiang, C.C. Yang, T.-C. Hsu, Cross-sectional

sizes and emission wavelengths of regularly patterned GaN and core-shell InGaN/GaN quantum-well nanorod arrays, J. Appl. Phys., 113 (2013) 054315.

[232] T.-W. Yeh, Y.-T. Lin, L.S. Stewart, P.D. Dapkus, R. Sarkissian, J.D. O'Brien, B. Ahn, S.R. Nutt, InGaN/GaN Multiple Quantum Wells Grown on Nonpolar Facets of Vertical GaN Nanorod Arrays, Nano Lett., 12 (2012) 3257-3262.

[233] Y.J. Hong, C.-H. Lee, A. Yoon, M. Kim, H.-K. Seong, H.J. Chung, C. Sone, Y.J. Park, G.-C. Yi, Visible-Color-Tunable Light-Emitting Diodes, Adv. Mater., 23 (2011) 3284-3288.

[234] W. Bergbauer, M. Strassburg, K. Ch, N. Linder, C. Roder, J. Lähnemann, A. Trampert, S. Fündling, S.F. Li, H.H. Wehmann, A. Waag, Continuous-flux MOVPE growth of position-controlled N-face GaN nanorods and embedded InGaN quantum wells, Nanotechnology, 21 (2010) 305201.

[235] W. Bergbauer, M. Strassburg, C. Kölper, N. Linder, C. Roder, J. Lähnemann, A. Trampert, S. Fündling, S.F. Li, H.H. Wehmann, A. Waag, N-face GaN nanorods: Continuous-flux MOVPE growth and morphological properties, J. Cryst. Growth, 315 (2011) 164-167.

[236] S. Li, X. Wang, M.S. Mohajerani, S. Fündling, M. Erenburg, J. Wei, H.-H. Wehmann, A. Waag, M. Mandl, W. Bergbauer, M. Strassburg, Dependence of N-polar GaN rod morphology on growth parameters during selective area growth by MOVPE, J. Cryst. Growth, 364 (2013) 149-154.

[237] X. Wang, S. Li, M.S. Mohajerani, J. Ledig, H.-H. Wehmann, M. Mandl, M. Strassburg, U. Steegmüller, U. Jahn, J. Lähnemann, H. Riechert, I. Griffiths, D. Cherns, A. Waag, Continuous-Flow MOVPE of Ga-Polar GaN Column Arrays and Core–Shell LED Structures, Cryst. Growth Des., 13 (2013) 3475-3480.

[238] C. Tessarek, M. Heilmann, E. Butzen, A. Haab, H. Hardtdegen, C. Dieker, E. Spiecker, S. Christiansen, The Role of Si during the Growth of GaN Micro- and Nanorods, Cryst. Growth Des., 14 (2014) 1486-1492.

[239] K. Choi, M. Arita, Y. Arakawa, Selective-area growth of thin GaN nanowires by MOCVD, J. Cryst. Growth, 357 (2012) 58-61.

[240] L.K. Lee, L.K. Aagesen, K. Thornton, P.C. Ku, Origin of broad luminescence from site-controlled InGaN nanodots fabricated by selective-area epitaxy, Phys. Stat. Sol. (a), 211 (2014) 531-535.

[241] M. Cao, H. Yoshio, Y. Masahito, A. Hiroshi, Growth of InGaN/GaN multiple quantum wells on size-controllable nanopyramid arrays, Jap. J. Appl. Phys., 53 (2014) 030306.

[242] A. Lundskog, J. Palisaitis, C.W. Hsu, M. Eriksson, K.F. Karlsson, L. Hultman, P.O.Å. Persson, U. Forsberg, P.O. Holtz, E. Janzén, InGaN quantum dot formation mechanism on hexagonal GaN/InGaN/GaN pyramids, Nanotechnology, 23 (2012) 305708.

[243] D. Zubia, S.H. Zaidi, S.R.J. Brueck, S.D. Hersee, Nanoheteroepitaxial growth of GaN on Si by organometallic vapor phase epitaxy, Appl. Phys. Lett., 76 (2000) 858-860.

[244] D. Zubia, S.H. Zaidi, S.D. Hersee, S.R.J. Brueck, Nanoheteroepitaxy: Nanofabrication route to improved epitaxial growth, J. Vac. Sci. Technol. B, 18 (2000) 3514-3520.

[245] J. Liang, S.-K. Hong, N. Kouklin, R. Beresford, J.M. Xu, Nanoheteroepitaxy of GaN on a nanopore array Si surface, Appl. Phys. Lett., 83 (2003) 1752-1754.

[246] S.D. Hersee, X.Y. Sun, X. Wang, M.N. Fairchild, J. Liang, J. Xu, Nanoheteroepitaxial growth of GaN on Si nanopillar arrays, J. Appl. Phys., 97 (2005) 124308.

[247] Y.K. Ee, J.M. Biser, W. Cao, H.M. Chan, R.P. Vinci, N. Tansu, Metalorganic Vapor Phase Epitaxy of III-Nitride Light-Emitting Diodes on Nanopatterned AGOG Sapphire Substrate by Abbreviated Growth Mode, Selected Topics in Quantum Electronics, IEEE Journal of, 15 (2009) 1066-1072.

[248] Y.-K. Ee, X.-H. Li, J. Biser, W. Cao, H.M. Chan, R.P. Vinci, N. Tansu, Abbreviated MOVPE nucleation of III-nitride light-emitting diodes on nano-patterned sapphire, J. Cryst. Growth, 312 (2010) 1311-1315.

[249] Y. Li, S. You, M. Zhu, L. Zhao, W. Hou, T. Detchprohm, Y. Taniguchi, N. Tamura, S. Tanaka, C. Wetzel, Defect-reduced green GaInN/GaN light-emitting diode on nanopatterned sapphire, Appl. Phys. Lett., 98 (2011) -.

[250] F. Sönke, S. Ünsal, P. Erwin, W. Thomas, H. Peter, J. Uwe, T. Achim, R. Henning, B. Andrey, W. Hergo-Heinrich, W. Andreas, Gallium nitride heterostructures on 3D structured silicon, Nanotechnology, 19 (2008) 405301.

[251] S. Li, S. Fündling, Ü. Sökmen, R. Neumann, S. Merzsch, P. Hinze, T. Weimann, U. Jahn, A. Trampert, H. Riechert, E. Peiner, H.-H. Wehmann, A. Waag, GaN nanorods and LED structures grown on patterned Si and AlN/Si substrates by selective area growth, Phys. Stat. Sol. (c), 7 (2010) 2224-2226.

[252] D. Won, X. Weng, Y.A. Yuwen, Y. Ke, C. Kendrick, H. Shen, T.S. Mayer, J.M. Redwing, GaN growth on Si pillar arrays by metalorganic chemical vapor deposition, J. Cryst. Growth, 370 (2013) 259-264.

[253] L. Xiao-Hang, Z. Peifen, L. Guangyu, Z. Jing, S. Renbo, E. Yik-Khoon, P. Kumnorkaew, J.F. Gilchrist, N. Tansu, Light Extraction Efficiency Enhancement of III-Nitride Light-Emitting Diodes by Using 2-D Close-Packed $TiO_2$ Microsphere Arrays, Display Technology, Journal of, 9 (2013) 324-332.

[254] W.H. Koo, W. Youn, P. Zhu, X.-H. Li, N. Tansu, F. So, Light Extraction of Organic Light Emitting Diodes by Defective Hexagonal-Close-Packed Array, Adv. Funct. Mater., 22 (2012) 3454-3459.

[255] F.K. Thomas, J.M. Luke, Nanofabrication of III–V semiconductors employing diblock copolymer lithography, Journal of Physics D: Applied Physics, 43 (2010) 183001.

[256] S.Y. Chou, P.R. Krauss, P.J. Renstrom, Imprint of sub‐25 nm vias and trenches in polymers, Appl. Phys. Lett., 67 (1995) 3114-3116.

[257] S.Y. Chou, P.R. Krauss, P.J. Renstrom, Imprint Lithography with 25-Nanometer Resolution, Science, 272 (1996) 85-87.

[258] L.J. Guo, Nanoimprint Lithography: Methods and Material Requirements, Adv. Mater., 19 (2007) 495-513.

[259] W. Zhou, Nanoimprint Lithography: An Enabling Process for Nanofabrication, Springer, Heidelberg, 2013.

[260] Y. Xia, G.M. Whitesides, Soft Lithography, Angew. Chem. Int. Ed., 37 (1998) 550-575.

[261] I. McMackin, J. Choi, P. Schumaker, V. Nguyen, F. Xu, E. Thompson, D. Babbs, S.V. Sreenivasan, M. Watts, N. Schumaker, Step and Repeat UV nanoimprint lithography tools and processes, Proceedings of SPIE, 5374 (2004) 222-231.

[262] M. Colburn, S.C. Johnson, M.D. Stewart, S. Damle, T.C. Bailey, B. Choi, M. Wedlake, T.B. Michaelson, S.V. Sreenivasan, J.G. Ekerdt, C.G. Willson, Step and flash imprint lithography: a new approach to high-resolution patterning, Proceedings of SPIE, 3676 (1999) 379-389.

[263] H.M. Manasevit, SINGLE‐CRYSTAL GALLIUM ARSENIDE ON INSULATING SUBSTRATES, Appl. Phys. Lett., 12 (1968) 156-159.

[264] M. Walter, Z. Gunther, D. Richard, Method of crucible-free production of gallium arsenide rods from alkyl galliums and arsenic compounds at low temperatures, in: U.S. Patents (Ed.), Siemens Ag, 1965.

[265] G.B. Stringfellow, Organometallic Vapor-phase Epitaxy: Theory and Practice, 2nd ed., Academic Press, California, 1999.

[266] SAFC, Hitech Product Catalogue, in, 2008.

[267] A. Koukitu, N. Takahashi, T. Taki, H. Seki, Thermodynamic analysis of the MOVPE growth of $In_xGa_{1-x}N$, J. Cryst. Growth, 170 (1997) 306-311.

[268] K. Akinori, K. Yoshinao, Thermodynamic analysis of group III nitrides grown by metal-organic vapour-phase epitaxy (MOVPE), hydride (or halide) vapour-phase epitaxy (HVPE) and molecular beam epitaxy (MBE), J. Phys.: Condens. Matter., 13 (2001) 6907-6934.

[269] I.G. Joseph, E.N. Dale, E. Patrick, C.J. David, E.L. Charles, L. Eric, S. Linda, R.M. Joseph, Scanning Electron Microscopy and X-ray Microanalysis, Kluwer Academic / Plenum Publishers, New York, 2003.

[270] Bruker, AFM Webinars: An Open and Free Resource for Atomic Force Microscope Owners and Users, in, 2013.

[271] G. Haugstad, Overview of AFM, in: Atomic Force Microscopy, John Wiley & Sons, Inc., 2012, pp. 1-32.

[272] R.F. Egerton, Physical Principles of Electron Microscopy: An Introduction to TEM, SEM, and AEM, Springer, New York, 2005.

[273] D.B. Williams, C.B. Carter, Transmission Electron Microscopy: A Textbook for Materials Science, Springer, New York, 2009.

[274] T. Yao, S.-K. Hong, Oxide and Nitride Semiconductors: Processing, Properties, and Applications, Springer, Berlin Heidelberg, 2009.

[275] D.K. Bowen, K.T. Brian, High Resolution X-Ray Diffractometry And Topography, CRC Press, 1998.

[276] W. Paszkowicz, J. Adamczyk, S. Krukowski, M. Leszczyński, S. Porowski, J.A. Sokolowski, M. Michalec, W. Łasocha, Lattice parameters, density and thermal expansion of InN microcrystals grown by the reaction of nitrogen plasma with liquid indium, Philos. Mag. A, 79 (1999) 1145-1154.

[277] R.R. Reeber, K. Wang, Lattice parameters and thermal expansion of GaN, J. Mater. Res., 15 (2000) 40-44.

[278] J.M. Wagner, F. Bechstedt, Properties of strained wurtzite GaN and AlN: Ab initio studies, Phys. Rev. B, 66 (2002) 115202.

[279] X.H. Zheng, H. Chen, Z.B. Yan, Y.J. Han, H.B. Yu, D.S. Li, Q. Huang, J.M. Zhou, Determination of twist angle of in-plane mosaic spread of GaN films by high-resolution X-ray diffraction, J. Cryst. Growth, 255 (2003) 63-67.

[280] T. Ide, M. Shimizu, X.Q. Shen, K. Jeganathan, H. Okumura, T. Nemoto, Improvement of film quality using Si-doping in AlGaN/GaN heterostructure grown by plasma-assisted molecular beam epitaxy, J. Cryst. Growth, 245 (2002) 15-20.

[281] R. Chierchia, T. Böttcher, H. Heinke, S. Einfeldt, S. Figge, D. Hommel, Microstructure of heteroepitaxial GaN revealed by x-ray diffraction, J. Appl. Phys., 93 (2003) 8918-8925.

[282] G. Pierre, Metal organic vapour phase epitaxy of GaN and lateral overgrowth, Rep. Prog. Phys., 67 (2004) 667.

[283] J. Matthews, Epitaxial Growth, Academic Press, New York, 1975.

[284] J.I. Pankove, Optical Processes in Semiconductors, Dover Publications, New York, 1971.

[285] H.P.D. Schenk, M. Leroux, P. de Mierry, Luminescence and absorption in InGaN epitaxial layers and the van Roosbroeck–Shockley relation, J. Appl. Phys., 88 (2000) 1525-1534.

[286] M. Leroux, N. Grandjean, B. Beaumont, G. Nataf, F. Semond, J. Massies, P. Gibart, Temperature quenching of photoluminescence intensities in undoped and doped GaN, J. Appl. Phys., 86 (1999) 3721-3728.

[287] E.M. Goldys, M. Godlewski, R. Langer, A. Barski, P. Bergman, B. Monemar, Analysis of the red optical emission in cubic GaN grown by molecular-beam epitaxy, Phys. Rev. B, 60 (1999) 5464-5469.

[288] Y. Sun, Y.-H. Cho, H.M. Kim, T.W. Kang, S.Y. Kwon, E. Yoon, Effect of growth interruption on optical properties of In-rich InGaN ／ GaN single quantum well structures, J. Appl. Phys., 100 (2006) 043520.

[289] G. Kortüm, Reflectance spectroscopy: Principles, methods, applications, Springer, New York, 1969.

[290] K. Peng, H. Fang, J. Hu, Y. Wu, J. Zhu, Y. Yan, S. Lee, Metal-Particle-Induced, Highly Localized Site-Specific Etching of Si and Formation of Single-Crystalline Si Nanowires in Aqueous Fluoride Solution, Chem. Eur. J., 12 (2006) 7942-7947.

[291] K.Q. Peng, J.J. Hu, Y.J. Yan, Y. Wu, H. Fang, Y. Xu, S.T. Lee, J. Zhu, Fabrication of Single-Crystalline Silicon Nanowires by Scratching a Silicon Surface with Catalytic Metal Particles, Adv. Funct. Mater., 16 (2006) 387-394.

[292] K. Seeger, R.E. Palmer, Fabrication of silicon cones and pillars using rough metal films as plasma etching masks, Appl. Phys. Lett., 74 (1999) 1627-1629.

[293] P. Mao, J. Han, Massively-parallel ultra-high-aspect-ratio nanochannels as mesoporous membranes, Lab Chip, 9 (2009) 586-591.

[294] Q. Wee, J.-W. Ho, S.-J. Chua, Optimized Silicon Nanostructures Formed by One-Step Metal-Assisted Chemical Etching of Si(111) Wafers for GaN Deposition, ECS J. Solid State Sci. Technol., 3 (2014) P192-P197.

[295] J.-W. Ho, Q. Wee, J. Dumond, L. Zhang, K. Zang, W.K. Choi, A.A.O. Tay, S.-J. Chua, Wafer-Scale, Highly-Ordered Silicon Nanowires Produced by Step-and-Flash Imprint Lithography and Metal-Assisted Chemical Etching, Mater. Res. Soc. Symp. Proc., 1512 (2013).

[296] J.-W. Ho, Q. Wee, J. Dumond, A. Tay, S.-J. Chua, Versatile pattern generation of periodic, high aspect ratio Si nanostructure arrays with sub-50-nm resolution on a wafer scale, Nanoscale Res. Lett., 8 (2013) 506.

[297] Z. Huang, N. Geyer, P. Werner, J. de Boor, U. Gosele, Metal-assisted chemical etching of silicon: a review, Adv. Mater., 23 (2011) 285-308.

[298] P. Lianto, Mechanism and Catalyst Stability of Metal-Assisted Chemical Etching of Silicon, in: Singapore-MIT Alliance, National University of Singapore, Singapore, 2013, pp. 137.

[299] B. Johannes de, G. Nadine, V.W. Jörg, G. Ulrich, S. Volker, Sub-100 nm silicon nanowires by laser interference lithography and metal-assisted etching, Nanotechnology, 21 (2010) 095302.

[300] J. Huang, S.Y. Chiam, H.H. Tan, S. Wang, W.K. Chim, Fabrication of Silicon Nanowires with Precise Diameter Control Using Metal Nanodot Arrays as a Hard Mask Blocking Material in Chemical Etching, Chem. Mater., 22 (2010) 4111-4116.

[301] M.K. Dawood, T.H. Liew, P. Lianto, M.H. Hong, S. Tripathy, J.T.L. Thong, W.K. Choi, Interference lithographically defined and catalytically etched, large-area silicon nanocones from nanowires, Nanotechnology, 21 (2010) 205305.

[302] W.K. Choi, T.H. Liew, M.K. Dawood, H.I. Smith, C.V. Thompson, M.H. Hong, Synthesis of Silicon Nanowires and Nanofin Arrays Using Interference Lithography and Catalytic Etching, Nano Lett., 8 (2008) 3799-3802.

[303] P. Lianto, S. Yu, J. Wu, C.V. Thompson, W.K. Choi, Vertical etching with isolated catalysts in metal-assisted chemical etching of silicon, Nanoscale, 4 (2012) 7532-7539.

[304] K. Peng, M. Zhang, A. Lu, N.-B. Wong, R. Zhang, S.-T. Lee, Ordered silicon nanowire arrays via nanosphere lithography and metal-induced etching, Appl. Phys. Lett., 90 (2007) 163123.

[305] Z. Huang, H. Fang, J. Zhu, Fabrication of Silicon Nanowire Arrays with Controlled Diameter, Length, and Density, Adv. Mater., 19 (2007) 744-748.

[306] S.-W. Chang, V.P. Chuang, S.T. Boles, C.A. Ross, C.V. Thompson, Densely Packed Arrays of Ultra-High-Aspect-Ratio Silicon Nanowires Fabricated using Block-Copolymer Lithography and Metal-Assisted Etching, Adv. Funct. Mater., 19 (2009) 2495-2500.

[307] S.W. King, J.P. Barnak, M.D. Bremser, K.M. Tracy, C. Ronning, R.F. Davis, R.J. Nemanich, Cleaning of AlN and GaN surfaces, J. Appl. Phys., 84 (1998) 5248-5260.

[308] J.G. Highfield, P. Bowen, Diffuse-reflectance Fourier-transform infrared spectroscopic studies of the stability of aluminum nitride powder in an aqueous environment, Anal. Chem., 61 (1989) 2399-2402.

[309] P. Bowen, J.G. Highfield, A. Mocellin, T.A. Ring, Degradation of Aluminum Nitride Powder in an Aqueous Environmet, J. Am. Ceram. Soc., 73 (1990) 724-728.

[310] T. Chung, J. Limb, J.-H. Ryou, W. Lee, P. Li, D. Yoo, X.-B. Zhang, S.-C. Shen, R. Dupuis, D. Keogh, P. Asbeck, B. Chukung, M. Feng, D. Zakharov, Z. Lilienthal-Weber, Growth of InGaN HBTs by MOCVD, J. Electron. Mater., 35 (2006) 695-700.

[311] H. Morkoç, Handbook of Nitride Semiconductors and Devices, Materials Properties, Physics and Growth, John Wiley & Sons, 2009.

[312] M. Jamil, R.A. Arif, Y.-K. Ee, H. Tong, J.B. Higgins, N. Tansu, MOVPE of InN films on GaN templates grown on sapphire and silicon(111) substrates, Phys. Stat. Sol. (a), 205 (2008) 1619-1624.

[313] P.F. Fewster, An Introduction to Semiconductor Materials, in: X-Ray Scattering from Semiconductors, pp. 1-22.

[314] S. Li, A. Waag, GaN based nanorods for solid state lighting, J. Appl. Phys., 111 (2012) 071101.

[315] Y.-H. Cho, G.H. Gainer, A.J. Fischer, J.J. Song, S. Keller, U.K. Mishra, S.P. DenBaars, "S-shaped" temperature-dependent emission shift and carrier dynamics in InGaN/GaN multiple quantum wells, Appl. Phys. Lett., 73 (1998) 1370-1372.

[316] Y.-T. Moon, D.-J. Kim, J.-S. Park, J.-T. Oh, J.-M. Lee, Y.-W. Ok, H. Kim, S.-J. Park, Temperature dependence of photoluminescence of InGaN films containing In-rich quantum dots, Appl. Phys. Lett., 79 (2001) 599-601.

[317] T. Wunderer, J. Hertkorn, F. Lipski, P. Brückner, M. Feneberg, M. Schirra, K. Thonke, I. Knoke, E. Meissner, A. Chuvilin, U. Kaiser, F. Scholz, Optimization of semipolar GaInN/GaN blue/green light emitting diode structures on {1-101} GaN side facets, Proceedings of SPIE: Gallium Nitride Materials and Devices III, 6894 (2008) 68940V.

[318] Z. Liliental-Weber, D.N. Zakharov, K.M. Yu, J.W. Ager, W. Walukiewicz, E.E. Haller, H. Lu, W.J. Schaff, Compositional modulation in $In_xGa_{1-x}N$: TEM and X-ray studies, J. Electron Microsc., 54 (2005) 243-250.

[319] Y. Kawakami, Y. Narukawa, K. Sawada, S. Saijyo, S. Fujita, S. Fujita, S. Nakamura, Recombination dynamics of localized excitons in self-formed InGaN quantum dots, Mater. Sci. Eng. B, 50 (1997) 256-263.

[320] M. Anani, H. Abid, Z. Chama, C. Mathieu, A. Sayede, B. Khelifa, $In_xGa_{1-x}N$ refractive index calculations, Microelectron. J., 38 (2007) 262-266.

[321] D.-J. Kim, Y.-T. Moon, K.-M. Song, I.-H. Lee, S.-J. Park, Effect of growth pressure on indium incorporation during the growth of InGaN by MOCVD, J. Electron. Mater., 30 (2001) 99-102.

[322] A. Lundskog, C.W. Hsu, D. Nilsson, K.F. Karlsson, U. Forsberg, P.O. Holtz, E. Janzén, Controlled growth of hexagonal GaN pyramids by hot-wall MOCVD, J. Cryst. Growth, 363 (2013) 287-293.

[323] G. Nowak, K. Pakuła, I. Grzegory, J.L. Weyher, S. Porowski, Dislocation Structure of Growth Hillocks in Homoepitaxial GaN, Phys. Stat. Sol. (b), 216 (1999) 649-654.

[324] R.M. Farrell, D.A. Haeger, X. Chen, C.S. Gallinat, R.W. Davis, M. Cornish, K. Fujito, S. Keller, S.P. DenBaars, S. Nakamura, J.S. Speck, Origin of pyramidal hillocks on GaN thin films grown on free-standing m-plane GaN substrates, Appl. Phys. Lett., 96 (2010) 231907.

[325] T. Akasaka, Y. Kobayashi, M. Kasu, Supersaturation in nucleus and spiral growth of GaN in metal organic vapor phase epitaxy, Appl. Phys. Lett., 97 (2010) 141902.

[326] M. Ohring, Chapter 1 - A review of materials science, in: M. Ohring (Ed.) Materials Science of Thin Films (Second Edition), Academic Press, San Diego, 2002, pp. 1-56.

[327] J. Farrer, C.B. Carter, Defect structure in GaN pyramids, J. Mater. Sci., 41 (2006) 779-792.

[328] T. Wernicke, S. Ploch, V. Hoffmann, A. Knauer, M. Weyers, M. Kneissl, Surface morphology of homoepitaxial GaN grown on non- and semipolar GaN substrates, Phys. Stat. Sol. (b), 248 (2011) 574-577.

[329] B.W. Jacobs, M.A. Crimp, K. McElroy, V.M. Ayres, Nanopipes in Gallium Nitride Nanowires and Rods, Nano Lett., 8 (2008) 4353-4358.

[330] W.H. Goh, Selective Area Growth and Characterization of GaN Based Nanostructures by Metal Organic Vapor Phase Epitaxy, in: School of Electrical and Computer Engineering, Georgia Institute of Technology, 2013.

[331] P.L. Bonanno, S.M. O'Malley, A.A. Sirenko, A. Kazimirov, Z.-H. Cai, T. Wunderer, P. Brückner, F. Scholz, Intrafacet migration effects in InGaN ⁄ GaN structures grown on triangular GaN ridges studied by submicron beam x-ray diffraction, Appl. Phys. Lett., 92 (2008) 123106.

[332] X.H. Wu, L.M. Brown, D. Kapolnek, S. Keller, B. Keller, S.P. DenBaars, J.S. Speck, Defect structure of metal‐organic chemical vapor deposition‐grown epitaxial (0001) GaN/Al2O3, J. Appl. Phys., 80 (1996) 3228-3237.

[333] I.-H. Kim, H.-S. Park, Y.-J. Park, T. Kim, Formation of V-shaped pits in InGaN/GaN multiquantum wells and bulk InGaN films, Appl. Phys. Lett., 73 (1998) 1634-1636.

[334] O. Schön, B. Schineller, M. Heuken, R. Beccard, Comparison of hydrogen and nitrogen as carrier gas for MOVPE growth of GaN, J. Cryst. Growth, 189–190 (1998) 335-339.

[335] F. Scholz, V. HÄrle, F. Steuber, A. Sohmer, H. Bolay, V. Syganow, A. DÖrnen, J.-S. Im, A. Hangleiter, J.-Y. Duboz, P. Galtier, E. Rosencher, O. Ambacher, D. Brunner, H. Lakner, Metalorganic vapor phase epitaxial growth of GaInN/GaN hetero structures and quantum wells, Mater. Res. Soc. Symp. Proc., 449 (1996).

[336] E.L. Piner, M.K. Behbehani, N.A. El-Masry, F.G. McIntosh, J.C. Roberts, K.S. Boutros, S.M. Bedair, Effect of hydrogen on the indium incorporation in InGaN epitaxial films, Appl. Phys. Lett., 70 (1997) 461-463.

[337] O. Ambacher, Growth and applications of Group III-nitrides, J. Phys. D: Appl. Phys., 31 (1998) 2653.

[338] W. Van der Stricht, I. Moerman, P. Demeester, E.J. Thrush, J.A. Crawley, MOVPE growth of high quality InGaN films and InGaN/GaN quantum wells, in: Vertical-Cavity Lasers, Technologies for a Global Information Infrastructure, WDM Components Technology, Advanced Semiconductor Lasers and Applications, Gallium Nitride Materials, Processing, and Devi, 1997, pp. 27-28.

[339] A. Jain, MOCVD Growth and Study of Thin Films of Indium Nitride, in: Department of Materials Science and Engineering, The Pennsylvania State University, 2006.

[340] D.M. Follstaedt, J. Han, P. Provencio, J.G. Fleming, Microstructure of GaN Grown on (111) Si by MOCVD, Mater. Res. Soc. Symp. Proc., 537 (1998).

# LIST OF PUBLICATIONS

## JOURNALS

1. J.W. Ho, L. Zhang, Q. Wee, A.A.O. Tay, M. Heuken, S.-J. Chua, Structural and Morphological Qualities of InGaN Grown via Elevated Pressures in MOCVD on AlN/Si(111) Substrates, J. Cryst. Growth, 383 (2013) 1-8.

2. J.-W. Ho, S.-b. Dolmanan, C.B. Tay, Q. Wee, A.A.O. Tay, S.-J. Chua, A dual-character InGaN/GaN multiple quantum well device for electroluminescence and photovoltaic absorption of near-mutually exclusive wavelengths, Phys. Stat. Sol. (c), 11 (2014) 635-639.

3. J.-W. Ho, Q. Wee, J. Dumond, A. Tay, S.-J. Chua, Versatile pattern generation of periodic, high aspect ratio Si nanostructure arrays with sub-50-nm resolution on a wafer scale, Nanoscale Res. Lett., 8 (2013) 506.

4. Q. Wee, J.-W. Ho, S.-J. Chua, Optimized Silicon Nanostructures Formed by One-Step Metal-Assisted Chemical Etching of Si(111) Wafers for GaN Deposition, ECS J. Solid State Sci. Technol., 3 (2014) P192-P197.

5. J.W. Ho, H.R. Tan, R.J.N. Tan, J. Huang, K.K. Ansah-Antwi, M. Heuken, A.A.O. Tay and S-J. Chua, Selective Area Heteroepitaxy of Ordered InGaN Nanopyramids on Si Substrates with Enhanced Structural Quality, Indium Incorporation and Luminescence Efficiency. Manuscript in preparation.

6. J.W. Ho, R.J.N. Tan, M. Heuken, A.A.O. Tay and S-J. Chua, Growth of InGaN Nanopyramid Arrays on Si for Potential Photovoltaic Applications. Minor revision required by J. Cryst. Growth (2015).

## CONFERENCES AND PROCEEDINGS

1. J.W. Ho, A.A.O. Tay, S.J. Chua, Numerical Modeling of Axial Junction Compositionally Graded $In_xGa_{1-x}N$ Nanorod Solar Cells, Photovoltaic Specialists Conference (PVSC), 2012 38th IEEE, 2012, Austin, Texas, pp. 001898-001903.

2. L.T. Tan, A.H. Lim, Z.Y. Chee, Y.L. Wong, Y.C. Huang, H.W. Ong, Q.X. Wee, J.W. Ho, R. Steeman, S.J. Chua, Hierarchical Nano/microstructures on Silicon Surface with Ultra Low Reflectance for Photovoltaic Applications, 2011 MRS Fall Meeting & Exhibit, Boston, Massachusetts, USA.

3. L.T. Tan, A.H. Lim, Z.Y. Chee, Y.L. Wong, Y.C. Huang, H.W. Ong, Q.X. Wee, J.W. Ho, R. Steeman, S.J. Chua, Hierarchical Nano/microstructures on Silicon Surface with Ultra Low Reflectance for Photovoltaic Applications, Phys. Stat. Sol. (c), 9 (2012) 1873-1877.

4. J.W. Ho, C.B. Tay, A.A.O. Tay, S.J. Chua, Finite Element Simulation of Compositionally Graded Core-shell Indium Gallium Nitride Nanorod Solar Cells, International Conference of Young Researchers on Advanced Materials 2012, Singapore.

5. J.W. Ho, Q. Wee, J. Dumond, L. Zhang, K. Zang, W.K. Choi, A.A.O. Tay, S.-J. Chua, Wafer-Scale, Highly-Ordered Silicon Nanowires Produced by Step-and-Flash Imprint Lithography and Metal-Assisted Chemical Etching, Mater. Res. Soc. Symp. Proc., 1512 (2013).

6. J.W. Ho, Q. Wee, Z. Li, T.S. Kustandi, J. Dumond, A.A.O. Tay, and S. Chua, Generation of Highly-Ordered Nanoporous Structures Using a Combinatory Approach of Nanoimprinting and Aluminum Anodization, NUS Nanoscience and Nanotechnology Institute – Nanocore Workshop 2012, Singapore. (Best Poster)

7. J.W. Ho, Li. Zhang, Q. Wee, A.A.O. Tay, S.J. Chua, Suppression of Phase Separation and Indium Droplet Formation in the Direct MOCVD Growth of InGaN on AlN/Si(111) Substrate, $10^{th}$ International Conference on Nitride Semiconductors, August 25-30, 2013, Washington D. C., USA.

8. J.W. Ho, S. Dolmanan, Q. Wee, C.B. Tay, A.A.O. Tay, S.J. Chua, A Dual-Character GaN/InGaN Multiple Quantum Well Device for Electroluminescence and Photovoltaic Absorption of Near-Mutually Exclusive Wavelengths, $10^{th}$ International Conference on Nitride Semiconductors, August 25-30, 2013, Washington D. C., USA.

9. J.W. Ho, H.R. Tan, R.J.N. Tan, K.K. Ansah-Antwi, M. Heuken, A.A.O. Tay and S-J. Chua, Dense InGaN Nanopyramid Arrays Grown by Selective Area MOCVD on Si substrate for Tandem Solar Cell Applications, 5th IMRE Scientific Research Forum 2014, Singapore. (Best Poster)

10. J.W. Ho, M. Heuken, A.A.O. Tay and S-J. Chua, Dense InGaN Nanopyramid Arrays Grown by Selective Area MOCVD on AlN/Si(111) Substrates with Intense Green Photoluminescence, 2014 MRS Fall Meeting & Exhibit, Boston, Massachusetts, USA.